JAERI-Research
2005-014

EXPERIMENTAL STUDY ON SECONDARY DEPRESSURIZATION ACTION FOR PWR VESSEL BOTTOM SMALL BREAK LOCA WITH HPI FAILURE AND GAS INFLOW (ROSA-V/LSTF TEST SB-PV-03)

June 2005

Mitsuhiro SUZUKI, Takeshi TAKEDA, Hideaki ASAKA
and Hideo NAKAMURA

日本原子力研究所
Japan Atomic Energy Research Institute

本レポートは、日本原子力研究所が不定期に公刊している研究報告書です。
入手の問合わせは、日本原子力研究所研究情報部研究情報課(〒319-1195 茨城県那珂郡東海村)あて、お申し越し下さい。なお、このほかに財団法人原子力弘済会資料センター(〒319-1195 茨城県那珂郡東海村日本原子力研究所内)で複写による実費頒布を行っております。

This report is issued irregularly.
Inquiries about availability of the reports should be addressed to Research Information Division, Department of Intellectual Resources, Japan Atomic Energy Research Institute, Tokai-mura, Naka-gun, Ibaraki-ken 〒319-1195, Japan.

編集兼発行　日本原子力研究所

JAERI－Research 2005－014

Experimental Study on Secondary Depressurization Action for PWR Vessel Bottom Small Break LOCA with HPI Failure and Gas Inflow (ROSA-V/LSTF Test SB-PV-03)

Mitsuhiro SUZUKI, Takeshi TAKEDA, Hideaki ASAKA and Hideo NAKAMURA

Department of Reactor Safety Research
Nuclear Safety Research Center
Tokai Research Establishment
Japan Atomic Energy Research Institute
Tokai-mura, Naka-gun, Ibaraki-ken

(Received April 14, 2005)

A small break loss-of-coolant accident (SBLOCA) experiment was conducted at the Large Scale Test Facility (LSTF) of ROSA-V program to study effects of accident management (AM) measures on core cooling, which is important in case of high pressure injection (HPI) system failure during an SBLOCA at a pressurized water reactor (PWR). The LSTF is a full-height and 1/48 volume-scaled facility simulating 4-loop Westinghouse-type PWR (3423 MWt). The experiment, SB-PV-03, simulated a PWR vessel bottom SBLOCA with a rupture of ten instrument-tubes which is equivalent to 0.2% cold leg break. Total HPI failure, non-condensable gas inflow from accumulator injection system (AIS) and operator AM actions on steam generator (SG) secondary depressurization at a rate of -55 K/h and auxiliary feedwater (AFW) supply for 30 minutes were assumed as experiment conditions. It is clarified that the AM actions are effective on primary system depressurization until the end of AIS injection at 1.6 MPa, but thereafter become less effective due to inflow of the non-condensable gas, resulting in delay of low pressure injection (LPI) actuation and whole core heatup under continuous water discharge through the bottom break. The report describes these thermohydraulic phenomena related with transient primary coolant mass and AM actions in addition to estimation of non-condensable gas behavior which affected primary-to-secondary heat transfer.

Keywords : SBLOCA Experiment, ROSA-V/LSTF, Instrument-tube Break, PWR, Accident Management (AM), Secondary Depressurization, Core Cooling, HPI Failure, Non-condensable Gas, Heat Transfer Analysis

高圧注入系不作動とガス流入とを想定したＰＷＲ容器底部小破断ＬＯＣＡに及ぼす２次系減圧操作に関する実験考察（ROSA-V / LSTF 実験 SB-PV-03）

日本原子力研究所東海研究所安全性試験研究センター原子炉安全工学部
鈴木　光弘・竹田　武司・浅香　英明・中村　秀夫

(2005年 4月14日受理)

大型非定常試験装置（LSTF）を使用したＲＯＳＡ－Ｖ計画において、加圧水型原子炉（PWR）の小破断冷却材喪失事故（SBLOCA）模擬実験を実施し、高圧注入系（HPI）不作動時に重要なアクシデント・マネージメント（AM）策の炉心冷却効果を調べた。ＬＳＴＦはウェスティングハウス社の４ループＰＷＲ（3423 MWt）を実高、容積比1/48で模擬する装置である。この実験(SB-PV-03)では、ＰＷＲコールドレグ 0.2% 破断に相当する原子炉容器底部計装管10本破断を模擬した。実験条件として、ＨＰＩの不作動と蓄圧注入系（AIS）からの非凝縮性ガス流入を想定するとともに、定率 -55 K/h での２次系減圧と30分間の補助給水（AFW）作動を運転員のＡＭ操作として実施した。その結果、これらのＡＭ操作は、ＡＩＳ注水終了圧力 1.6 MPa までは１次系減圧に効果的であったが、その後、非凝縮性ガスが流入したため減圧効果は低下し、低圧注入系（LPI）の作動開始が遅れ、破断口では水流出が継続していたので全炉心露出に至ったことが分かった。本報では１次系保有水量の推移及びＡＭ操作に関連したこれらの熱流動現象について述べる。さらに、１・２次系間の熱伝達解析をまじえた非凝縮性ガス挙動について述べる。

東海研究所：〒319-1195　茨城県那珂郡東海村白方白根２－４

Contents

目　次

List of Tables and Figures

ROSA/LSTF Acronyms and Abbrebiations

ACC.....Accumulator Tank Connected to Loop A
ACH.....Accumulator Tank Connected to Loop B
AFW.....Auxiliary Feedwater
AIS.....Accumulator Injection System
AM.....Accident Management
AOV.....Air Operated Valve
BU.....Break Unit
CET.....Core Exit Thermocouple, Core Exit Temperature
CL-A, CL-B.....Cold Leg A, Cold Leg B
CP.....Conduction Probe
DP.....Differential Pressure
ECCS.....Emergency Core Cooling System
EL.....Elevation above Core Bottom
HL-A, HL-B.....Hot Leg A, Hot Leg B
HPI.....High Pressure Injection
ICC.....Inadequate Core Cooling
LL.....Liquid Level
LOCA.....Loss-of-Coolant Accident
LPI.....Low Pressure Injection
LS-A, LS-B.....Loop Seal A, Loop Seal B
LSC.....Loopseal Clearing
LSTF.....Large-Scale Test Facility
PORV.....Power-operated Relief Valve
PV.....Pressure Vessel
PWR.....Pressurized Water Reactor
PZR.....Pressurizer
RCS.....Reactor Coolant System
ROSA.....Rig-of-Safety Assessment
RV.....Relief Valve
SBLOCA.....Small Break Loss-of-Coolant Accident
SG-A, SG-B.....Steam Generator A, Steam Generator B
SI Signal.....Safety Injection Signal
ST.....Suppression Tank
TC.....Thermocouple
W-PWR.....Westinghouse-type PWR

This is a blank page.

1. Introduction

1.1 Outline and Background

A small break loss-of-coolant accident (SBLOCA) experiment was conducted at the Large Scale Test Facility (LSTF)[1] in the fifth Rig-of-Safety Assessment (ROSA-V) program to clarify effects of steam generator (SG) secondary depressurization on core cooling, as one of important accident management (AM) measures in case of high pressure injection (HPI) system failure and non-condensable gas inflow from accumulator injection system (AIS) at a pressurized water reactor (PWR). This experiment of SB-PV-03[2] was conducted on November 7 in 2002 simulating a break of ten instrument-tubes at the PWR vessel bottom (see Fig. 1.1) which is equivalent to 0.2% cold leg break.

The LSTF is a full-pressure, full-height and 1/48 volume-scaled integral test facility with an electrically-heated simulated core (up to 14% of the scaled PWR power), major components in both primary and secondary coolant systems, and emergency core cooling systems (ECCSs) simulating a Westinghouse-type four-loop (3423 MWt) PWR. The LSTF is heavily instrumented to measure thermohydraulic behaviors during SBLOCAs or transients in addition to key plant parameters such as core exit thermocouples (CETs) for the AM decision making. In the ROSA-V program, various system integral experiments[3-7] have been conducted to investigate the effects of AM measures for cold or hot leg SBLOCAs with or without influences of the AIS non-condensable gas inflow. It was clarified for a 0.5% cold leg SBLOCA experiment[7] that an SG secondary depressurization action finally established long-term core cooling by the low pressure injection (LPI) actuation irrespective of the AIS non-condensable gas inflow, because most of the gas flowed out through the break at the cold leg.

In case of vessel bottom SBLOCA, however, most of the AIS non-condensable gas which flowed into the primary loops may not flow out through the break until the reactor vessel water level reaches the lower plenum. This means that the gas remains in the primary loops for a longer time in a vessel bottom SBLOCA and causes more significant influences on the primary depressurization resulting in delay of the LPI actuation in comparison with the cold leg SBLOCA. A previous bottom break experiment[8] with equivalent size of 0.5% cold leg break, which was conducted in an early phase of the ROSA-IV program, suggested these break location effects irrespective of no gas inflow nor AM action. Namely, the bottom break experiment (SB-PV-01[9] shortened as SP1) showed unique phenomena in comparison with other SBLOCA experiments of a cold leg break (SCC),

hot leg break (SH3), upper head break (SP2) and pressurizer top break (SB3) as shown in Fig. 1.2; (1) the earliest core heatup under the continuous water discharge through the bottom break and (2) start of steam discharge at the bottom break after whole core uncovery. Therefore, the present experiment of SB-PV-03 was planned to investigate the effects of AM measures on core cooling in case of smaller vessel bottom SBLOCA conditions with HPI failure and AIS gas inflow in comparison with the previous experiment.

AM operator actions in this experiment consist of three steps. The first is a principal AM action to depressurize the SG secondary system to achieve primary loop cooling at a rate of -55 K/h by controlling SG relief valves (RVs), which is assumed to start on the CET temperature responses (CETs $<$ 623 K) with 10 minutes delay after the safety injection (SI) signal actuation in addition to the AFW operation for 30 minutes simulating a turbine-driven AFW operation. The second step is a rapid SG depressurization by fully opening the SGRVs in case of CETs $\geqq$ 623 K, and the third step is to open the PZR power-operated relief valves (PORVs) in case of further increase of the CETs. The first and second depressurization actions based on the CET temperature responses simulated those of a reference PWR.

1.2 Objectives and Contents

Objectives of this study are (1) to clarify general thermohydraulic phenomena observed in the 0.2% vessel bottom SBLOCA experiment focusing on effects of AM actions on core cooling in case of HPI failure and non-condensable gas inflow, and (2) to clarify specific parameters such as transient primary coolant mass, amount of the non-condensable gas flowed into the primary loops, an analysis of primary-to-secondary heat transfer influenced by the gas inflow, and the CET temperature responses during the core heatup process affected by condensed water falling back from the SG U-tubes.

Chapters 2 and 3 describe the LSTF system with instrumentation and test conditions, respectively, and Chapter 4 presents precise experiment results. Chapter 5 presents concluding remarks derived from this experiment. Appendix-A gives a measurement list of all experiment data available for this experiment and the instrumentation locations. Appendix-B presents a measurement list and configuration data base for estimation of regional primary coolant mass. Appendix-C describes an SG heat transfer analysis model with uncertainty estimation.

2. Facility Description

2.1 LSTF System with Fourth Simulated Core Assembly

(1) Overview of LSTF System Description

The LSTF[1] was designed to simulate thermohydraulic phenomena peculiar to SBLOCAs and operational transients in Westinghouse-type PWR (W-PWR). It features prototypical component heights, large loop piping diameters, simulated control systems, simulated ECCS, prototypical thermohydraulic conditions for both primary and secondary systems, and a sufficient core electric power to simulate the scaled PWR decay power. It has a 1/48 volumetric scaling to a typical 4-loop W-PWR (3423 MWt). These major design characteristics of the LSTF are shown in Table 2.1-1 in comparison with the reference PWR. Figure 2.1.1 shows the LSTF configuration compared to the reference PWR. The LSTF has two primary loops and each loop simulates two loops of the reference PWR.

Major differences between the LSTF and the reference PWR exist in cross-sectional configuration of each component, i.e., the LSTF hot leg diameter is approximately 28% of the PWR, and the LSTF upper plenum diameter is approximately 14% of the PWR. Effects of these configurational distortions on three-dimensional fluid behaviors in the LSTF components should be carefully estimated. Additional distorsions of the LSTF system are the relatively large metal stored heat and environmental heat loss per unit coolant volume compared to those of the reference PWR.

Figure 2.1.2 shows a flow diagram of the LSTF of which primary coolant system consists of the pressure vessel (PV) with the fourth simulated fuel assembly and internals, a full-height PZR, two primary loops with an SG and a coolant pump in each one, a break unit (BU) connected to the break flow storage tank (ST), three types of the ECCSs which consist of the HPI system, AIS and LPI system for each loop, and other systems. The LSTF secondary system consists of each SG secondary side with outer downcomer piping, the steam and feedwater systems, the steam condensation system, and the sefety valves (SVs) and RVs in the steam lines.

(2) Pressure Vessel and Steam Generator

Figure 2.1.3 shows vertical cross-sectional view of the LSTF PV compared with that of PWR reactor vessel. Heights of the upper plenum, core and dopwncomer in the LSTF are the same as those of the reference PWR. Top elevation of the hot legs is also the same as that in the reference PWR. Eight control rod guide tubes have flow paths between

the upper head and upper plenum. The downcomer top region and upper head region are connected through eight spray nozzles with 3.4 mm inner diameter (ID). Figure 2.1.4 shows vertical cross-section of the core and internal structures. Heater rods are assembled by nine spacers, lower grid and upper grid in the core barrel. In the lower plenum, each heater rod lead passes through lower plenum spacers and is installed on the vessel flange. A core bypass region surrounding the actual PWR core is simulated in the LSTF downcomer region and thus, the LSTF downcomer volume deviates from a volumeterically scaled PWR downcomer volume. There are two hot leg leak simulation lines which connect the middle downcomer (EL 5.318 m) and two hot legs as shown in Fig.2.1.5.

Figure 2.1.6 shows vertical cross-section of both the primary and secondary sides of SG-A/B. The SG primary side consists of inlet and outlet plena, and U-tube inner volumes. The LSTF SG inlet plenum volume is more than twice larger than that of reference PWR SG, while the LSTF SG outlet plenum consisting of compartment and vertical sleeve approximately simulates the PWR SG outlet plenum volume. The SG secondary side consists of a boiling region around the 141 U-tubes, steam separator, steam dryer, main steam line nozzles, main and auxiliary feedwater line nozzles, and downcomer regions. The upper downcomer includes a feedwater ring with sparger nozzles, while the lower downcomer annulus in the PWR SG is simulated by four downcomer pipes in the LSTF to enable measurements for the U-tube fluid behaviors. Two SGs are sufficient to remove scaled core decay heat and capable of AM depressurization by controlling the SGRVs in addition to the AFW supply.

(3) Simulated Core Assembly

Figure 2.1.7 shows horizontal cross-section of the core and arrangement of electric heater rods. The heater rods have the same diameter and heated length as the reference PWR and are arranged in twenty four bundles with 7×7 array except for peripheral regions. Total numbers of the heater rods, non-heating tie rods and dummy rods are 1008, 96 and 40, respectively. Four tie rods in one bundle simulate the PWR control rods. Eight differential pressure (DP) measurements at the peripheral core were not used.

Three kinds of heater rods are assembled in the LSTF core, i.e., high, middle and low power rods with respect to the power levels supplied to the rod bundles. Figure 2.1.8 shows axial power distribution of the high power rod in bundles No.13 through No.20 with an axial peaking factor of 1.4945. A nine-step axial power distribution simulates a cosine curve around the core center. All these heater rods have similar axial power profiles. Figure 2.1.9 shows radial power profile of "case 3" which gives radial peaking factor of 1.51 for the high power rod bundles, 1.00 for the middle power bundles

(bundles No. 21 through No. 24) and 0.66 for the peripheral low power bundles (bundles No. 1 through No. 12), respectively.

(4) Accumulator Injection System (AIS) Pressurized by Nitrogen Gas

AIS injection line connects each AIS tank and cold legs, i.e., one from the ACC tank to CL-A, and another from ACH tank to CL-B. These tanks have the same geometry shown in Fig. 2.1.10. Heater rods are installed in both tanks to establish initial AIS water temperature (320 K in most cases). Normal water level is set at EL 14.604 m to simulate both initial gas volume and water volume above the stand pipe top (EL 13.024 m) as in the reference PWR. The AIS tank is pressurized at 4.5 MPa prior to the test initiation by supplying nitrogen cover gas from the gas supplying system. The Gas volumes above water levels in the ACC and ACH tanks are estimated as 0.4644 and 0.4652 m^3, respectively including pipe volumes connected to the top shell of the tanks. A ratio between the gas volume and water volume above the stand pipe is approximately 1:2 for each AIS tank.

Figures 2.1.11 (a) and (b) show AIS water injection lines to CL-A and CL-B, respectively. In a case of nitrogen gas inflow into the primary system, gas passes these lines and sweeps water out of these lines. Thus, initially remained water in these injection lines are added to the AIS injection mass estimated by the tank level change. The gas volume expansion is determined by measurements of pressure, water level change and gas phase temperature. A total volume in the standpipe and injection line upstream side of the air operated valve (AOV) is estimated as 0.1979 m^3 and 0.1402 m^3 for the ACC and ACH injection lines, respectively.

Figures 2.1.12 (a) and (b) show vertical and plane views, respectively of a discharge line between the BU and ST tank. The discharge line consists of eight-inch pipes with a total length of 15.84 m and is connected to a steam blow pipe with many holes in the ST tank. The ST tank water level prior to the experiment initiation is set higher than the steam blow pipe level.

2.2 Instrumentation and Data Processing

2.2.1 Measurements

There are two kinds of data or measurements for the LSTF experiments, i.e., the first level data (1760 in total for this experiment) listed in Table 2.2-1, and the second

level data with tagged identification symbol (ID) of RC derived from the first level data. The first level data include fluid temperatures (noted Tag ID of TE or TC), wall temperatures (ibid. TW), differential temperatures (DT), pressures (PE), differential pressures (DP), liquid levels (LE), gamma-densitometers (DE), flow rates (FE), conductance probe data (CP) for local water level detection and power (WE). These are grouped in eight general locations such as the PV, PZR, primary loops and SGs. Detail of the major measurement locations is shown in figures of Appendix-A.

The DP data and corresponding fluid temperature data at each primary region are used to calculate the water levels and primary mass distribution. The primary coolant mass dischrged from the break into ST tank is estimated by this calculation and the break flow rate is reduced from the ST tank mass increasing rate. Therefore, primary mass balance can be checked between two methods (see Section 4.2), i.e., one is a sum of regional fluid mass remaining in the primary system and another one is counting the discharged fluid mass, injected coolant mass and the initial primary coolant mass. The energy balance in the SG secondary system is also estimated by using the measurement data as shown in Section 4.2 and Appendix-C.

Nine thermocouples were axially embedded at each power step of one instrumented heater rod to measure transient thermal responses of the core. The axial thermocouple locations are designated like as Position 1 (bottom of core; EL 0.15 m), Position 5 (middle height of core; EL 1.86 m) and Position 9 (top of core; EL 3.61 m). In this experiment, these heater rod surface temperatures were not only recorded by the data logger but also monitored during the experiment to detect core heatup phenomena.

Twenty CETs located on the upper core plate, six thermocouples in the upper plenum and the hot leg fluid temperature measurements can be also used to detect the core heatup phenomena during the experiment. Characteristic responses of these core heatup detection instruments are described in Section 4.1.3.

2.2.2 Data Reduction and Qualification

All the measurement signals are sent to the data acquisition system, converted to digital form and recorded on magnetic disks. The instrument signals recorded on the data loggers are converted from volts into engineering units using the appropriate conversion equations, and the first level data are produced. These first level data are corrected and qualified. For example, the readings from DP transducers are corrected to compensate for the effect of pressure. The corrections are based on instrument read-

ings that were obtained at low and high system pressure, with zero DP across the instrument. Also, the readings from gamma-densitometers are corrected, if necessary, based on data taken during the test preparation procedure. The corrected data are then manually qualified, that is, each data channel is reviewed and placed into one of the categories which include,

Good: The data have been reviewed manually and are believed to lie within a stated span and uncertainty values during the test.

Qualitative: In general, these data can be used for trend only. The absolute magnitude cannot be verified and uncertainty is unkown. This normally results from lack of calibration.

All the available experiment data which consist of the "**Good**" and "**Qualitative**" data in the experiment SB-PV-03 are shown in Table A.1 (20 sheets) in Appendix-A. This excludes data of other categories of "**Bad**" which should not be used because of a failure in the measurement channel, and "**Unused**" which should not be used because the sensor was not connected or installed in the environment to be measured or perhaps the region was not included in the experiment. Table A.1 includes a function ID, a tag name, an output range (low and high ranges) and an uncertainty (absolute value and relative uncertainty in %) of each available measurement data and RC data. The data qualification for the experiment SB-PV-03 reduced available data of 1559 in total.

3. Test Procedures and Boundary Conditions

3.1 Test Preparation Procedure to Set Up Initial Conditions

The LSTF system was necessarily drained prior to the test preparation procedures, so any instrument calibration normally done under voided conditions was also performed at that time. All the DP transducers were zero checked while voided. The next action was to fill and vent the air from the primary system in several steps. First, the system was filled with demineralized water up to the bottom of the loops. The system was then vented using three vacuum pumps connected to the PZR top and the SG outlet plena. The vacuum pumps were operated until the air space pressure reached 735 mmHg absolute.

Next, the remaining air was purged by injecting steam into the system gas spaces. The steam was generated in ACH using the electric heater and was injected into both the SG outlet plena and the pump discharge side in both loops. The vacuum pumps were continuously operated during the steam injection process. This purging process was continued until well after the primary system gas phase temperatures had reached the vapor saturation temperature.

The system was next filled with water and pressurized. Under the pressurized condition, the primary coolant pumps were operated repeatedly at full capacity to ultimately transport any remaining air bubbles to the PZR where the air could be vented.

After these steps, the system was depressurized and drained slightly to lower the PZR water level. The amount of air remaining in the system was then measured by pressurizing the system by injecting air into the PZR gas space and measuring the decrease in PZR water level in response to this pressure increase. This water level decrease is thus an indication of air remaining in the primary system at a room temperature condition. In the preparation process of the experiment SB-PV-03, the PZR water level dropped by 3.0 cm (corresponding volume; $\Delta V = 0.00326$ m^3) when the primary fluid (290.5 K) was pressurized from $P_1 = 0.19$ MPa to $P_2 = 0.803$ MPa. When an initial air volume is V_1 [m^3] at the pressure of P_1, a remained air volume of Vr [m^3] in this experiment was estimated at the atmospheric pressure condition ($P_a = 0.1013$ MPa) as,

$$P_1 \times V_1 = P_2 \times (V_1 - \Delta V) = P_a \times Vr, \text{ thus}$$
$$Vr = \Delta V \times P_2 / (P_2 - P_1) \times (P_1 / P_a) = 0.008 \text{ m}^3.$$

With the primary system satisfactorily filled with water and clear of air, the gamma densitometers and the conductance probes were again calibrated. Zero adjustments on the DP transducers checked under full conditions were completed. The system was then pressurized in steps to five different elevated pressures. The system was held for four minutes at each level to check the instrument drift. A check of all thermocouple outputs was made to verify that each was reading at a room temperature.

Most of the above procedures were performed during two weeks prior to the experiment. During the heatup period on the day of experiment, output from the gamma densitometers was recorded at six different times to provide calibration data.

The primary and secondary systems were maintained at the full initial conditions for approximately 98 minutes before the start of experiment SB-PV-03. Immediately before the test initiation, the three-way valves connecting the sense lines of certain DP transducers were opened for two minutes. The three-way valves were again opened for two minutes at the end of experiment. These data are used for post test correction on the measurement data. In this experiment, the data recording was initiated at 366 s prior to the break signal and terminated at 12399 s after the break initiation.

3.2 Boundary and Initial Conditions

Major boundary conditions for the primary and secondary systems of this experiment are shown below in addition to the initial experiment conditions.

(1) Failure Assumptions and Accident Management (AM) Measures

This experiment assumed total failure of the HPI system in case of a break at 10 instrument-tubes at the reference PWR vessel bottom. Thus, core cooling can be conducted by actuation of the AIS and LPI in this test. Two motor-driven AFW pumps in the reference PWR[10] were assumed to fail and only a turbine-driven AFW pump in the PWR was assumed to be available. The turbine-driven AFW pump has a design capability to remove core decay power for 30 minutes.

AM actions in this experiment were planned to start at 10 minutes after the SI signal actuation and consisted of three steps depending on the CET indication, as one of the key plant parameters for the reference PWR as shown below.

・The first step AM action is the SG feed and bleed, i.e., to depressurize the pri-

mary coolant system by controlling the SGRVs to achieve a primary temperature decreasing rate at - 55 K/h and to operate the turbine-driven AFW pump (scaled flow rate of 0.72 kg/s per one SG) when the CETs are less than 350 ℃ (623 K).

- The second step AM action is the rapid SG depressurization, i.e., to fully open the SGRVs when the CETs reached temperatures equal to or higher than 350 ℃ at the time of AM action start or in a process of the first step AM action.

- The third step is an additional AM action to fully open the power-operated relief valves (PORVs) at the PZR when the CETs indicated further increase (≧ 500 ℃). This AM action does not simulate the PWR AM measures but is an attempt unique for this experiment to promote the primary depressurization.

(2) Control Logics

The control logics used in this experiment are shown in Table 3.2-1. The trip logics shown in Table 3.2-1 simulates those of the reference PWR. The break signal is the first signal of the experiment start. The primary coolant pumps were powered after the break to simulate the pump coastdown characteristics from the normal operating speed.

The scram and SI signals were generated when the PZR pressure decreased to setpoints at 12.97 and 12.27 MPa, respectively. In this experiment, the scram signal tripped to initiate the primary pump coastdown, core power decay and isolation of two SGs by closing their steam and feedwater lines. The SGRVs were automatically controlled to maintain the secondary pressure between 8.03 and 7.82 MPa before the AM action started.

(3) Break Unit (BU)

The break was initiated at the lower plenum break unit (BU) by quickly opening the break valve (AOV300) shown in Fig. 3.2.1. The break direction was horizontal and the break orifice shown in Fig. 3.2.2 had an inner diameter of 4.6 mm. The break orifice and the measuring instruments including the three-beam gamma-densitometer in the spool piece were set in upstream-side of the break valve. The break flow was finally lead to the ST and its flow rate was measured by a Venturi flow meter located in the BU line in addition to the ST mass estimation. Air was injected into the discharge line (see Fig. 2.1.12) to mitigate effects of condensation-induced pressure spikes in these areas.

(4) Core Power

The core power was regulated by the system control computer (CENTUM) to simulate the post-scram core power decay shown in Table 3.2-2. The decay curve used in this test,

designated the "New Power Curve"[11], was developed for SBLOCA experiments by correcting the old "JAERI Power Curve". Since the maximum electric core power of the LSTF is limited to 10 MW, i.e., approximately 14% of the 1/48-scaled PWR rated power, the "New Power Curve" maintained the 10 MW core power until the scaled PWR core power decreased to 10 MW at 17.87 s after the scram signal actuation. After this timing, the LSTF core power was regulated to follow the scaled PWR core power decay. Figure 3.2.3 (a) shows the core power during this experiment.

An additional core power control is usually programmed to protect the heater rods from overheat in case of core heatup, i.e., the core power decreases to 75% at the maximum heater rod temperature of 908 K, to 50% power at 918 K, to 25% power at 919 K, to 10% power at 920 K and finally to 0% power at 923 K, respectively. In this experiment, the core power was degraded as shown in Fig. 3.2.3 (b) and the final core power was 10% of the programmed core power given in Table 3.2-2.

(5) Pump Coastdown

The coastdown of the primary coolant pumps was controlled by the CENTUM accoding to a programmed characteristics as shown in Table 3.2-3 and Fig. 3.2.4. The initial pump speed is generally maintained at a certain low level so that the primary coolant temperature distribution can meet the rated PWR conditions under the limited LSTF core power (14% of the 1/48-scaled PWR thermal output). Immediately after the break initiation, the pumps were quickly powered to speed at 25 rps. The pump coastdown characteristics are common in the LSTF SBLOCA experiments.

(6) Pressurizer Heaters and Trace Heaters

The LSTF PZR heaters consist of three proportional heater rods (3.33 kW per one rod) and six backup heater rods (18.75 kW, ibid) with the same heated length of 2.023 m. Thus, their maximum powers are 10.0 kW and 112.5 kW, respectively. The proportional heater power was automatically controlled so that the primary pressure was kept constant at the initial setpoint as long as the water level was higher than 2.3 m. The backup heaters were used to compensate the environmental heat loss from the PZR system and other primary system as long as the PZR liquid level was higher than 2.3 m. In addition to these, trace heater powers were supplied to the PZR surge and spray lines. Figure 3.2.5 shows these heater powers in this experiment. Initial powers before the break start for the proportional heater, backup heater, surge line heater and spray line heater were 2.7, 33.6, 2.7 and 3.0 kW, respectively (see Table 3.2-4). On the other hand, the proportional and base heaters were powered to 8.2 and 86.8 kW, respectively after the break due to the pressure control logics and tripped off at 181 and

183 s, respectively due to the low PZR water level signal.

In addition to the PZR, the LSTF primary and secondary systems are equipped with trace heaters intending to compensate for environmental heat losses. In this experiment, the trace heaters were initially powered as shown in Table 3.2-4 (81.3 kW in total) and tripped off immediately after the break. Thus, the total initial heater power for the primary and secondary systems including the PZR was 123.3 kW. Trace heaters attached to the AIS injection lines were maintained during the test period.

(7) ECCS Injection

As shown in the failure assumptions, both of the AIS and LPI systems were available in this experiment. The AIS started to inject water when the primary pressure decreased below 4.51 MPa in this experiment (see Table 3.2-4). A ratio of both AIS injection flow rates at CL-A (ACC) and CL-B (ACH) was planned to 2 : 2. The initial AIS tank water temperatures were approximately 322 K. The nitrogen gas in each AIS tank was planned to flow into the cold legs after the water injection terminated at approximately 1.6 MPa. The LPI system was planned to inject water into both cold legs when the lower plenum pressure decreased below 1.24 MPa.

(8) Pressurizer PORVs

The PZR PORVs were originally planned for this experiment to open by detecting further increase of the CET values ($\geqq$ 500 ℃) as the third step of the AM actions. In the experiment, the CETs showed saturation temperatures during the core heatup process. Thus the PORVs were manually opened not with the CET responses but with the monitored core heatup temperatures. The orifice diameter was 10.18 mm simulating three PORVs. The PORVs discharge flow, however, was not measured in this experiment.

(9) Initial Test Conditions

Most of the measured initial test conditions agreed well with the specified conditions within each measurement accuracy as shown in Table 3.2-4. The primary and secondary pressures, hot leg temperatures, fluid temperature increase across the core simulated those of the rated PWR conditions. Initial pressurizer water level was 7.26 m above the bottom (DL 0.08 m). The total primary coolant mass in the initial conditions was estimated as 5418 kg (see Section 4.2). The SG secondary sides were almost saturated except for a lower part where the subcooled downcomer flows entered. The steam and feedwater flow rates in the initial condition were controlled to maintain both secondary pressure and SG water levels at each constant level. Data base for initial coolant mass distribution in primary and secondary systems are shown in Appendices B and C.

4. Test Results of Experiment SB－PV－03

Described in this chapter are results of the experiment SB-PV-03 including (1) general thermohydraulic behaviors in both primary and secondary coolant systems with respect to effects of the AM actions on vessel bottom SBLOCA phenomena in case of the HPI failure and the AIS gas inflow (Section 4.1) and (2) experiment data analyses on primary mass balance and primary-to-secondary heat transfer (Section 4.2).

4.1 General Thermohydraulic Behaviors in Three Typical Phases

General thermohydraulic behaviors during the whole test period are characterized in three phases, i.e., Phase I (①), an initial transient after the break (0－945 s) with the scram, SGs isolation and automatic SGRVs operation at about 8 MPa, Phase II (②), a long primary cooling process (SG feed & bleed) lead by the first AM action at a rate of -55 K/h including the AIS actuation (945－7190 s) and Phase III (③), inadequate core cooling (ICC) conditions under degraded primary depressurization caused by non-condensable gas inflow from the AIS tanks, in addition to succeeding water discharge through the break (7190－9880 s). The third phase includes the second AM action to fully open the SGRVs, the third AM action to fully open the PORVs, and the LPI actuation after the core power limitation. Typical experiment results are shown in Sections 4.1.1 through 4.1.3. After end of this experiment, the second test (④) was conducted with no core power under a pressurizing process by the HPI injection to characterize a non-condensable gas volume remained in the primary system (9880－11741 s).

These typical phases and major events are compactly shown in figures of the primary and secondary pressures (Fig. 4.1.1), a discharged coolant mass and a break flow rate (Fig. 4.1.2), collapsed water levels in both upper plenum and core (Fig. 4.1.3) and representative heater rod surface temperatures in the core (Fig. 4.1.4). A chronology of events and AM actions is shown in Table 4.1-1.

4.1.1 Initial Transient after Break (0－945 s)

(1) Immediate System Responses after Break

The experiment SB-PV-03 was initiated by quickly opening the break valve (AOV-300) in the lower plenum BU line at t＝0 s with the initial conditions (see Table 3.2-4). The break immediately caused the PZR level decrease and primary depressurization as shown

in Fig. 4.1.5. The proportional and base PZR heaters were immediately powered to compensate the pressure decrease and were finally tripped off at 181 s by the low water level setpoint. At the time of break, each primary coolant pump (PC) was powered up to the specified speed to simulate an initial pump speed of the reference PWR. The core electric power was maintained at 10 MW for a time after the break.

(2) Scram Signal to Trip Core Power Decay, Pump Coast-down and SG Isolation

The scram signal was sent at 250 s on the PZR pressure setpoint of 12.97 MPa and actuated the following logics, i.e., core power decay along the decay heat simulation curve (see Table 3.2-2) and the PC pump coastdown along the coastdown curve in Table 3.2-3. The core power started to decrease from 10 MW at 280 s. The PC pump started coastdown at 252 s and caused rapid decrease of the forced primary coolant flows as shown in Fig. 4.1.6. Natural circulation flow more than 8 kg/s continued in Phase I process after the PC pumps stopped at 500 s.

The scram signal also caused turbine trip, main feedwater pump trip and resulting SG isolation at each secondary system. The SG isolation resulted in rapid pressure rise in each SG secondary side. Automatic RV operation started at 302 s to control the secondary pressure between the setpoints of 8.03 and 7.82 MPa (Fig. 4.1.5). The secondary pressure, fluid temperatures, steam flow rates at both main steam and RV lines, feedwater flow rate during the cyclic RV operation at SG-B are shown in detail in Figs. 4.1.7 and 4.1.8. The secondary water levels at two SGs showed gradual decrease after the main feedwater trip and remained above 9 m at the end of Phase I (see Fig. 4.1.9).

(3) Safety Injection (SI) Signal

The SI signal was generated at 340 s on the PZR pressure setpoint at 12.27 MPa and it caused the first AM action to initiate the SG feed & bleed operation with 10 minutes delay. The HPI was assumed to fail in this experiment while the LPI was activated by the SI signal to start later at the pressure setpoint of 1.24 MPa.

(4) Core Cooling Conditions under Void Formation in Primary Loops

Core cooling conditions were adequately established in the first phase with sufficient water levels in the core (see Fig. 4.1.3) and the forced and/or natural circulation flows (see Fig. 4.1.6). The core decay power was transported by the primary circulation flows to the SG secondary sides. Figure 4.1.10 shows typical temperature difference between the SG-A inlet and outlet plena indicating heat removal at the SG U-tubes during the first phase. The SG-A inlet plenum temperatures indicate an abrupt decrease after the PC pumps were powered at the time of break, a rapid recovery corresponding

to the pump coastdown, and gradual decrease after the core power decreased.

The collapsed water level in the upper plenum (see Fig. 4. 1. 3) started to decrease at approximately 380 s indicating void accumulation in the upper space, and reached the hot leg nozzle level at the end of the first phase. Corresponding to this void accumulation in the upper plenum, steam phase was observed in the hot legs. Figure 4. 1. 11 presents the three-beam HL-A fluid density data (refer Fig. A. 14 in Appendix-A). The beam A density data started to decrease at 350 s indicating generation of steam phase in the HL-A upper region. The beam B and beam C density data, on the other hand, showed nearly water solid condition during the first phase. These fluid density conditions were similarly found in the HL-B. It is shown that the steam flow passed through the hot leg top region above the water level in the first phase.

The CL-A fluid density data are shown in Fig. 4. 1. 12. The Beam A density data started to decrease at 655 s indicating water level formation in the cold leg. The Beam B and Beam C also started to decrease within 350 s from the Beam A density decrease. Similar cold leg density data were found in the CL-B. Thus, the cold leg water level decreased earlier than those of hot legs in the first phase.

Collapsed water levels in the SG U-tube inlet sides were measured in six tubes with DP measurements at SG-A and SG-B as shown in Figs. 4. 1. 13 and 4. 1. 14, respectively. These data included effects of frictional pressure losses in the initial forced circulation flow, which abruptly changed after the break according to the PC pump speed-up and became negligibly small after the primary pump stopped at 500 s. In the initial 800 s, these level data showed that almost all U-tubes were filled with solid water. This indicates that the steam flowed into the U-tubes from each hot leg was well condensed in the U-tube inlet region during the first phase.

4. 1. 2 Secondary Depressurization Process and AIS Actuation (945－7190 s)

The primary system cooldown was conducted in the second phase by initiating the first AM action to depressurize the SG secondary systems at 945 s. During this phase, the AIS started to inject water into the CL-A at 3241 s and CL-B at 3264 s, respectively and the core cooling was almost maintained except for a short time (5455－5784 s) with temporary ICC condition at a limited core top region.

(1) Effects of the First AM Action

The first AM action was initiated at 945 s on the SI signal with 10 minutes delay by

controlling RV steam flow at both SGs which caused the primary cooling rate at -55 K/h. The AIS was actuated approximately 38 minutes after this AM action started. The AM action lead the primary pressure decrease from approximately 8 MPa to 1.6 MPa (end of the AIS) within 105 minutes (refer Fig. 4.1.1). The primary depressurization also contributed to decrease the break flow and to delay the primary mass decrease in comparison with a case of no AM action, in which the primary pressure should be kept at the SG secondary pressures of 8 MPa and larger break flow rate would cause earlier primary mass decrease.

The AFW was simultaneously supplied to each SG secondary side in the first AM action simulating a turbine-driven AFW pump capability of the reference PWR for 30 minutes. The AFW flow rate at each SG was approximately 0.7 kg/s but was slightly different between two SGs to cause different water level transients as shown in Fig. 4.1.9. After the AFW stopped at 2753 s, both SG secondary water levels turned to decrease due to the succeeding steam discharge through the RVs.

(2) Primary Coolant Mass Depletion in U-tubes and SG plena

Collapsed water levels in the SG-A U-tube inlet sides started to decrease at approximately 800 s and reached zero level at approximately 2390 s (see Fig. 4.1.13) while those in the SG-B U-tubes similarly decreased but reached zero level at approximately 2950 s (see Fig. 4.1.14). This later drainage in the SG-B U-tubes than in the SG-A U-tubes can be ascribed to longer condensation period under the higher secondary water level in the former. It is also shown that drainage in the U-tubes occurred differently with respect to the tube length, i.e., drainage in the shortest tubes (No. 1 and 6) was the earliest while that of the middle length tubes (No. 2 and 5) was the latest among the six instrumented U-tubes in both SGs.

Figure 4.1.15 shows that collapsed water levels in SG inlet plena started to decrease at 2408 and 2975 s in the SG-A and SG-B, respectively. These level decreases in inlet plena followed the U-tubes drainage in each SG shown above.

Figure 4.1.16 shows collapsed water levels in SG-A/B outlet regions including the outlet plenum and downflow-sides of the cross-over legs. The SG-A outlet plenum water level started to decrease at 2359 s and stopped at 3000 s at a level of 3.9 m corresponding to EL 5.6 m (nearly at the cold leg top) in the loopseal downflow-side. This water level in the loopseal downflow-side gradually decreased after the AIS was actuated at 3241 s and rapidly decreased after 5670 s with fluctuation during an oscillatory AIS injection period shown later. The SG-B outlet plenum water level started to

decrease at 2967 s and reached the same water level of SG-A outlet region at 3650 s. Thereafter, these water levels in both SG outlet regions showed similar responses in the loopseal downflow-sides.

(3) AIS Actuation and Temporary Coolant Mass Recovery in Primary System

The AIS injection started at 3241 s from the ACC tank to CL-A and at 3264 s from the ACH tank to CL-B, respectively. According to the slow primary depressurization (approximately 1.2－0.7 kPa/s) during the first 2500 s of the AIS injection period, the AIS injection flow rates were very low (0.1－0.4 kg/s) as shown in Figs. 4.1.17 and 4.1.18. In a later period between 5700 and 7100 s, these flow rates gradually increased with intermittent injection at both AISs, which were caused by intermittent pressure decrease and recovery in the primary system. The AIS pressures and water levels at both tanks changed simultaneously corresponding to these primary pressure transients. When each AIS tank water level reached top of the stand pipe (see Fig. 2.1.10), water discharge from the AIS tank was terminated. This timing was 6710 s at the ACC tank and 7080 s at the ACH tank, respectively. Tank pressure at this timing was 1.57 MPa in the ACC and 1.54 MPa in the ACH, respectively.

Hereafter, a water sweep-out behavior started in each injection line (see Fig. 2.1.11) by expansion of the nitrogen gas during the depressurization process. A free volume of the ACC injection line to CL-A is 0.1979 m^3 and that of the ACH injection line to CL-B is 0.1402m^3, respectively. When the sweep-out behavior completed, i.e., the gas fully filled the injection line, at 7190 s for ACC and 7477 s for ACH, respectively, the nitrogen gas started to flow into each cold leg (see Section 4.2.2) and then both AIS tank pressures gradually decreased according to the lasting gas expansion.

The AIS injection contributed to temporarily recover the primary coolant mass. The water level in the core, which had decreased to the core top level in the early phase of AIS injection period, recovered during the intermittent AIS injection period (see Fig. 4.1.3). The upper plenum water level also recovered to the hot leg elevation. During a period of the low core water level between 5455 and 5784 s, limited core heatup was detected only at the top of one high power rod (B17, Position 9, see Fig. 4.1.43). This maximum temperature rize above the saturation temperature was only 7 K and diminished in the core water level inceasing period. These water levels in PV turned to decrease again after the AIS injection terminated.

A coolant mass distribution map was made for each primary region, SG-A/B secondary regions, AIS tanks and ST tank by estimating each regional coolant mass at times of both

initial and last phases of the AIS injection (t = 3295 and 7000 s) as shown in Figs. 4.1.19 and 4.1.20, respectively. A shaded region indicates existence of coolant mass under a collapsed water level, and a white region indicates steam or gas space. Amount of the coolant mass in each region (including steam mass) and total value of the primary system are noted in these figures. It is shown that most of the primary regions above the cold leg level were filled with steam and the upper plenum level formed at the hot leg level at these two times. The total coolant masses in the primary system at 3290 and 7000 s were approximately 39 and 33% of an initial coolant mass, respectively (see Section 4.2.1).

(4) Two-phase Discharge through Vessel Bottom Break

Figure 4.1.21 shows fluid density data measured by three beam gamma-ray densitometer at the horizontal break line connected to a PV lower plenum nozzle (EL -1.735 m). The beam locations are also shown in this figure. It should be noted that these fluid densities before break initiation were slightly different each other because of initial fluid temperature distribution in vertical direction of the break line, i.e., 551.4 K at the pipe top (TE 651) and 505.2 K at the pipe bottom (TE 652). The initial density of each beam was estimated at each middle cord-length by assuming linearity of the fluid temperature distribution in the vertical direction.

It is shown in this figure that (1) single phase water initially flowed through the BU line, (2) two-phase flow discharge started at approximately 1350 s, which was detected only by Beam A density at the top of break line, (3) bubble flow or steam phase gradually increased resulting in decrease of Beam B density at approximately 4420 s, (4) the steam phase did not reach middle height of the horizontal pipe as shown in the Beam C density data, which showed saturated water density up to 9200 s, and (5) single phase water flow was detected again in the break line at approximately 9500 s. It is concluded from these results that single phase steam discharge did not occur at the break line, but single phase water flow or two-phase flow with low quality was detected during this experiment.

(5) Super-heated Fluid Temperatures in Primary Cooldown Process

When the core was well cooled under water level during the primary cooldown process, various degrees of super-heated steam temperatures were detected in the primary region due to surrounding hot metal walls. These super-heated steam temperatures, however, should be distinguished from those of super-heated steam which generated in the over-heated core during the thirrd phase of this experiment (see Section 4.1.3) on the view point of accident management methodlogy using the CETs.

Figures 4.1.22, 4.2.23, 4.2.24 and 4.2.25 show fluid temperatures in the HL-A, CL-A, upper plenum and lower plenum, respectively. The lower plenum temperatures were kept in saturation conditions in the second phase. Fluid temperatures in the HL-A showed almost saturated conditions except for the top part (TE 1) which showed slight deviation above the saturation temperature (less than 14 K) after 3800 s when steam both from the upper plenum and pressurizer passed the hot leg upper region and condensed water from the SG flowed the lower part at the same time. Middle and bottom region of the upper plenum were covered by two-phase mixture or saturated steam during the second phase while the top region was filled with super-heated steam after approximately 1400 s because steam in the top region was stagnant and heated by thick metal wall of the upper core support plate. A degree of maximum super-heat at the upper plenum top was less than 18 K in the second phase.

The CL-A fluid temperatures in Fig. 4.1.23, on the other hand, became super-heated conditions after 2200 s except for the cold leg bottom (TE 24). A degree of super-heat in the CL-A was within 25 K during the second phase. These temperature rises in both cold legs are due to stagnant steam which was heated by the cold leg metal walls. It is also shown in Fig. 4.1.23 that the CL-A fluid temperatures showed large subcooling indicating AIS water in the lower part when the super-heated steam was detected in the upper part. The lowest subcooling was -96 K at approximately 6650 s. Thus, the largest temperature difference between the top and bottom of CL-A reached more than 120 K.

Significantly higher steam temperatures were detected in the downcomer upper region as shown in Fig. 4.1.26. Downcomer fluid temperatures measured below the cold leg nozzle (EL 3.6, 1.8 and 0.0 m) showed almost saturated temperatures while those at the downcomer top (EL 6.7 and 7.1 m) were kept higher than 540 K indicating significant hot wall effects on the stagnant steam. A maximum degree of super-heat was 64 K at the downcomer top in the second phase.

The highest fluid temperatures were detected in the pressurizer as shown in Fig. 4.1.27. Most of these fluid temperatures were kept higher than 550 K in the second phase but some parts (TE 961 and TE 963) showed larger temperature decrease down to saturation temperature probably due to fall back condensed water from the steam lines or spray line piping. On the other hand, the surge line temperature showed almost saturated con dition except for a later period of the second phase when super-heated steam in PZR intermittently flowed down to the HL-A passing through the surge line.

4.1.3 Degraded Depressurization under Gas Inflow and Core Heatup (7190－9880 s)

Described here are degradation of the primary depressurization caused by nitrogen gas inflow from the AIS tanks, resulting delay of the LPI actuation, succeeding water discharge through the break, and significant core heatup irrespective of the second and thirrd AM actions in a time period after the gas inflow (7190 s) to an end of the core power supply (9880 s). In addition, described are estimated gas mass flowed into the primary loops, local gas accumulation in the SG U-tubes, effects of fall-back condensed water on local core cooling, and CET responses during the core heatup process.

(1) Degraded Primary Depressurization after Gas Inflow

Figure 4.1.28 shows later pressure transients in primary and SG secondary systems in addition to related timing of the gas inflow and AM actions. It is shown here that the primary depressurization rate was significantly lowered after the gas inflow started (7190 s at ACC, 7477 s at ACH, respectively) irrespective of the continued secondary depressurization actions at both SGs. It is shown in Table 4.1-2 that the PZR depressurization rate after the gas inflow start became only 22 ± 6% of the SG secondary depressurization rates in the same period.

The non-condensable gas flowed into the primary loops contributed to lower the primary depressurization rate in three ways, i.e., one is the addition of gas volume to the primary loops, and next one is thermal gas expansion when the gas at initially 322 K in the AIS tanks was heated up to primary saturation temperature (for example, 469.5 K at 7200 s) increasing the gas volume to 1.46 times of the original gas volume. The third one is degradation of steam condensation heat transfer coefficient at the SG U-tubes when the gas flowed into the U-tubes (see Section 4.2.2 (2)).

Due to the degraded primary depressurization rate, the LPI actuation at 1.24 MPa was delayed until 9280 s as shown in Fig.4.1.28. The LPI actuation delay caused core heatup at 8573 s under succeeding coolant mass depletion from the pressure vessel and no mass recovery (see Section 4.2.1 (2)). The second and third AM actions which were initially planned to actuate by detecting CET increases (CET ≫ 623 K) corresponding to the core heatup, were differently actuated by operators at 8970 s with the SGRVs full-open and at 9060 s with the PORVs full-open, respectively, which were decided with information of the heater rod temperature monitoring. The core electric power was finally degraded to 10% of the planned core power curve at 9200 s in order to protect the heater rods from overheat more than 920 K.

It is easily derived from these results that if a methodlogy to prevent gas inflow by closing valves in the AIS injection lines were associated with the first AM action, it could result in earlier LPI actuation at 1.24 MPa (probably before 8000 s) and therefore no core heatup could be resulted. Moreover, additional AM actions to fully open the SGRVs and PORVs, if they were associated with the first AM action, could promote the primary depressurization and contribute to earlier primary mass recovery.

(2) Nitrogen Gas Flowed into Primary Loops

The nitrogen gas volumes flowed into the primary loops from the AIS tanks were finally estimated through two steps, i.e., the first step by determining actual gas expansion characteristics during the AIS water level decrease, and the second step by extraporating the gas expansion characteristics to gas inflow states after the tank water level became constant at the stand pipe top level.

In the first step, actual change of gas state during the water level decrease was characterized for ACC and ACH tanks as shown in Table 4.1-3. A correct gas volume of V_G^* [m^3] was determined by estimating a gas volume of V_G [m^3] in each tank volume, adding free volumes of V_{PO} [m^3] for pipe lines connected to the tank top, and correcting a measurement error caused by a water level shift ($\triangle V_G$) [m^3] as,

$$V_G^* = V_G + \triangle V_G + V_{PO}. \tag{4.1}$$

By using V_G^*, pressure P [MPa] and gas phase temperature T_G [K], a ratio of gas constant was reduced at each time compared to those at initial state with suffix "$_o$" as,

$$R = (P \times V_G^*/T_G)/(P_o \times V_{Go}^*/T_{Go}). \tag{4.2}$$

Figure 4.1.29 shows that the "R" shifted in both negative and positive sides from the initial value (R＝1.0) as a pressure difference of (P_o－P) [MPa] increased in both AIS tanks, and that the shift to positive side at ACH tank was significantly large. Reasons of this variation can be ascribed to (1) local gas temperature affected by the surrounding tank wall temperature which remained higher than the gas temperature under the gas expansion (a negative shift on "R") and (2) release of dissolved gases in water remained in the tank and related pipe lines as the tank pressure decreased (a positive shift on "R"). It was confirmed after the experiment SB-PV-03 that there was always inependent water volume of 0.044 m^3 in a 4-inch downward pipe connected only to the ACH tank top, which had been processed with no de-gas treatment but contacted to air in a long time prior to the experiment. As the solubility of oxygen gas in water

is approximately as twice as that of nitrogen gas, volume of air gas release is larger than a case of pure nitrogen gas release.

In the second step, the gas expansion characteristics was extraporated to low pressure range at constant AIS water level ($P_0 - P \geqq 2.9$ MPa) by using a relation of,

$$R = a \times (P_0 - P) + b, \tag{4.3}$$

$a = 0.01088$ [MPa^{-1}], $b = 0.9696$ for ACC,

$a = 0.03583$ [MPa^{-1}], $b = 0.9387$ for ACH.

Table 4.1-4 shows total gas volumes of V_{GE}^* [m^3] estimated for both sweep-out and gas inflow process after the water level became constant at two AIS systems as,

$$V_{GE}^* = R \times C_0 \times (T_G/P), \tag{4.4}$$

$$C_0 = P_0 \times V_{G0}^*/T_{G0} \quad [\text{MPa} \cdot \text{m}^3/\text{K}]. \tag{4.5}$$

The sweep-out process in the AIS injection lines started when the tank water level decrease stopped at 6710 s in ACC and 7080 s in ACH, respectively. This process ended when the expanded gas volume reached end of the injection pipe, i.e., location at the check valve, at 7190 s for ACC system and 7477 s for ACH system, respectively. After these times, the gas inflow started from each AIS line. A gas mass of $\triangle M_{GE}$ [mol] flowed into the primary loop was estimated as shown in Table 4.1-4 by subtracting a volume of V_L [m^3] in the AIS injection line at upstream-side of the check valve and gas volumes remaining both in the tank (V_{GSP} [m^3]) and tank top piping (V_{P0} [m^3]) from a total gas volume of V_{GE}^*, and by transforming the gas volume to a gas mass as,

$$\triangle M_{GE} = 1.20271 \times 10^5 \times P \times (V_{GE}^* - V_{P0} - V_{GSP} - V_L)/T_G \ . \tag{4.6}$$

A total gas mass flowed into the primary loops was only 26 mol until 7500 s, and it increased to 72, 200, 295 and 570 mol until 8000, 9000, 9300 and 9900 s, respectively. These gas inflow phenomena continued until the primary pressure turned to increase by the break valve closure at 9935 s.

Figure 4.1.30 shows transient total gas volume of V_G^* in a period of AIS tank level decrease, V_{GE}^* during both sweep-out and gas inflow process, and gas volumes flowed into the cold legs estimated at conditions of AIS tank pressure at each time. These gas expansion transients were mainly dependent of the primary depressurization process. It is shown in this figure that the gas expansion after 7190 s was suppressed by the

degraded primary depressurization indicating significant influence of small amount of gas in the early phase of gas inflow process. A faster gas expansion in a later phase (after 9300 s) was due to rapid primary depressurization caused by steam condensation promoted by the LPI actuation (9280 s) under the largely limited core power supply.

(3) Steam Heating above Secondary Water Level in the Third Phase

Figure 4.1.31 shows fluid temperatures measured in the SG-A secondary boiler region in comparison with saturation temperatures in both primary (RC 200) and SG-A secondary systems (RC 202). These fluid temperatures under the SG secondary water level were kept at a saturation condition and those above the water level became super-heated. Moreover, most of the steam temperatures measured above Pos. 8 were higher than the primary saturation temperature during the third phase (7190－9880 s). Similar results were observed in the SG-B secondary side. The reason of super-heated steam in the SG secondary sides is the hot wall effects of the surrounding metal structures such as the SG vessel and U-tubes which were uncovered by the secondary water level in early phase after the AFW stop (2753 s) during the depressurization process.

Figure 4.1.32 shows primary fluid temperatures in SG-A No. 2 U-tube inlet region. Steam temperature at the U-tube top (Pos. 9) which was maintained at saturation condition, started to deviate into super-heated condition at approximately 4600 s and those at Pos. 8 and Pos. 7 also deviated into superheated conditions in the later period. Thus, the primary fluid temperatures in the U-tubes followed similar trends as the secondary side temperatures shown in Fig. 4.1.31. Some of the temperatures measured in the lower U-tube region, however, showed subcooling compared to the primary saturation temperature after the AIS gas inflow started.

The non-condensable gas flowed into the downcomer diffused or flowed into the hot legs through the downcomer-to-hot leg leak simulation lines (see Fig. 2.1.5, from nozzles at EL 5.3178 m in the downcomer to hot legs at EL 5.5028 m) and was transported to SG U-tubes by the hot leg steam flows resulting in gas accumulation in U-tubes.

(4) Gas Accumulation in SG U-tubes Detected by Subcooled Temperatures

The gas accumulation detected by the U-tube fluid temperatures is discussed below. In general, existence of non-condensable gas in a steam gas mixture at thermal equilibrium condition can be detected by thermocouples applying the ideal gas theory to this steam gas mixture only when steam is in a saturation condition at its partial pressure.

Namely, a gas volume (V_G) at a measured total pressure of P [MPa] and a measured fluid

temperature of T_G [K] is given as,

$$V_G = V \times P_G/P = V \times (P-P_S)/P \tag{4.7}$$

where V ($=V_G+V_S$) is a regional volume, P_G ($=P-P_S$) and P_S are partial pressures of gas and steam, and suffices "$_G$" and "$_S$" indicate gas and steam, respectively. P_S corresponds to the saturated steam temperature of T_S ($=T_G$) and P corresponds to a saturated steam temperature of T with no non-condensable gas. Therefore, a subcooling temperature of $\triangle T$ ($=T-T_G$) is one of the important parameters indicating existence of non-condensable gas accumulation in a phase of steam condensation.

On the other hand, the equation (4.7) does not hold when the steam is not saturated or in a super-heated condition in which steam gas mixture temperature of T_G is higher than a saturated steam temperature of T_S determined from a partial steam pressure of P_S, namely in a case of $T_G > T_S$ even if the measured mixture temperature indicates a subcooling as $T > T_G$. In this case, however, a saturated steam temperature of T_S can not be measured or determined and therefore mass fraction of steam or gas is not determined. In a case of definite super-heated steam condition ($T_G > T$), it is clear that it is impossible to determine mass fraction of the non-condensable gas or steam from the measurement data of temperature and pressure.

Figures 4.1.33 through 4.1.39 show precise temperatures measured at several elevations both inside and outside of a representative U-tube (No.2 tube) of the SG-A inlet side in comparison with saturation temperatures at both primary and secondary systems. The following are found in these typical experimental data.

(1) Due to a main heat flow direction of primary-to-secondary sides during the SG depressurization, measured fluid temperatures and saturation temperature in the primary side were higher in general than those in the secondary side, and metal wall temperatures were within primary and secondary temperatures. The heat transfer was mainly conducted at U-tubes under the SG secondary water level while the upper U-tube region uncovered by the water level showed super-heated temperatures as shown previously. In addition to these, subcooling temperatures indicating existence of non-condensable gas were measured in the lower U-tube region, and primary fluid temperatures lower than tube wall temperature were measured at the upper U-tube region indicating local hot wall heating as shown below.

(2) Even before the gas inflow started at 7190 s, small subcooling was detected in

several times in the U-tube outlet at Pos. 1 (TE 337) as shown in Fig. 4. 1. 33 and Pos. 3 (TE 351) in Fig. 4. 1. 34 indicating gas existence in these regions. This gas existence can be ascribable to dissolved gas release from the AIS injection water. The subcooling observed was within -2 K. On the other hand, fluid temperatures at Pos. 1 and Pos. 3 of the U-tube inlet side were kept at a saturation condition before 7190 s indicating saturated steam supply from the hot leg. Moreover, subcooling was not detected before 7190 s in any U-tube region except for the U-tube outlet regions shown above. It is probable that a part of the gas released from the AIS water which flowed into the loopseal to SG outlet region through mixing with hot remained water during the oscillatory (intermittent) AIS injection under the SG depressurization process.

(3) After the gas inflow started, subcooling was detected in the primary regions of U-tube outlet side at Pos. 1 after 7210 s, Pos. 3 after 7545 s, Pos. 5 (temperatures at tubes No. 1, 4 and 6 were used instead of failed T/C at No. 2 tube) after 7560 s and Pos. 6 after 8635 s. These temperatures followed the secondary saturation temperature below the secondary water level and those above the water level showed less subcooling at Pos. 5 and Pos. 6. In U-tube regions higher than or equal to Pos. 7, no subcooling was detected and higher fluid temperatures were detected in the higher U-tube regions during the third experiment phase.

On the other hand, subcooling was detected in the U-tube inlet side in a slightly different way from the U-tube outlet side. Namely, Pos. 3 and Pos. 5 showed subcools after 7545 and 7531 s, respectively in the similar times as in the outlet region, while Pos. 1 was maintained at saturation condition until 9000 s. In the higher U-tube inlet regions, no subcooling was detected and their fluid temperatures were relatively lower than the outlet fluid temperatures. These indicate that gas mass fraction was low in the steam-rich condition at the U-tube inlet lower region in which steam condensation continued, the gas mass fraction increased as the steam condensed along the tube length, and steam gas mixture was transported to higher regions with heating effects from the hot surrounding tube walls, which resulted in super-heated fluid conditions irrespective of the gas existence. The super-heated fluid flowed into the U-tube outlet side through the top bend were then gradually cooled by the tube walls at lower temperatures in the lower regions. The thermal interaction shown above between the fluid and U-tube walls is confirmed by clarifying horizontal temperature distribution around U-tubes as shown below.

(4) In the U-tube upper regions, primary-to-secondary temperature distribution across

the tube wall was different between upflow and downflow sides as a result of mixture flow as shown below. For example, Fig. 4. 1. 38 shows fluid and wall temperatures at Pos. 9 (EL 16. 3039 m corresponding to water level of 8. 34 m) of the No. 2 tube in addition to the saturation temperatures. As this location was already uncovered by the secondary water level before 5000 s, the secondary fluid temperature (TE 435) turned to super-heated condition at apprximately 5380 s and the temperatures for both primary fluid (noted by TE) and tube walls (noted by TW) were all super-heated for a period between 5000 and 7600 s indicating temperature distribution along a tube flow direction at the same horizontal domain as,

TE 415 (outlet) > TW 492 (outlet) > TW 491 (inlet) > TE 414 (inlet).

This means that fluid mixture in the Pos. 9 inlet-side was heated by the tube wall and that in the outlet-side was cooled by the tube wall. The highest fluid temperature among these four temperatures at the outlet region was a result of hotter tube walls at a higher elevation than that of Pos. 9. Although the tube wall temperature at the No. 2 tube top (Pos. 10) was not measured, the highest temperature was confirmed by No. 3 tube wall temperature at Pos. 11 (EL 18. 5839 m) as shown in TW 497 in Fig. 4. 1. 39 for comparison. In the later period after 7600 s, difference between the fluid and wall temperatures became small indicating that smaller mixture flowed in the U-tube by degradation of steam condensation.

(5) Primary coolant Mass Decrease and Core Heatup

In the third phase of this experiment, the primary coolant mass decreased linearly by the break flow at a constant rate of approximately 0. 46 kg/s (refer Fig. 4. 1. 2) after termination of the AIS water injection at 7477 s. Due to this mass decrease, collapsed water level in the upper plenum started to decrease again from the hot leg elevation at 7747 s and that in the core rapidly decreased at 8320 s (see Fig. 4. 1. 3). As there was no more way of coolant mass recovery until the LPI actuation at 9280 s, the boil-off core heatup started at 8573 s.

Figures 4. 1. 40 and 4. 1. 41 show coolant mass distribution in both primary and secondary systems at the times of core heatup start and before PORV open (t = 9015 s). In these cases, the primary system was almost empty of water except for the vessel lower region and two loopseal regions indicating smaller coolant mass in both primary and secondary systems in the later phase.

Core heatup phenomena were detected by heater rod surface temperatures measured at

several regions as shown in Table 4.1-5 (a). Figure 4.1.42 shows the high power rod (B13) temperatures including the maximum temperature of 920 K detected at Pos.6 (above the middle core level) at 9200 s, which tripped the core power to 10 % of decay heat for heater rod protection. Thermocouple at Pos.8 started to heatup at first (8573 s), lower regions started later and finally Pos.2 (EL 0.612 m) started heatup at 9282 s.

Figure 4.1.43 also shows the high power rod (B17) temperatures including the temporary core heatup observed during the AIS injection (see Section 4.1.2) at a limited region of the core top (Pos.9) and no heatup at the core bottom (Pos.1). Figure 4.1.44 shows the temperatures at middle power rod (B22) and non-heated tie rod (B21) in the central core region indicating slower temperature increasing rate at B22 rod Pos.5 compared to the B17 rod Pos.5 (see Fig.4.1.43) and better cooling conditions at B22 rod Pos.9 compared to that of B17 rod Pos.9. This core heatup phenomena with wide variation even in the same core height is precisely described below.

(6) Effects of Fall-back Water on CETs and Local Core Cooling

The core exit temperatures measured at the upper core plate top surface (EL 4.044 m) did not detect any symptoms of the core heatup phenomena during the core heatup period until 9100 s as shown in Fig.4.1.45. Therefore, the second and third AM actions which had been planned to actuate on the CET values higher than 623 K, were not actuated by the CET indications but were manually decided to actuate by direct monitoring of the heater rods surface temperatures. At start times of the second and third AM actions, the maximum heater rod surface temperature were 751.03 K and 811.29 K, respectively at Pos.7 of the high power rod. Irrespective of the second and third AM actions, the core heatup continued and the core power was degraded to 10% at 9200 s.

A principal reason of no core heatup detection by the CETs can be ascribed to water fall-back from the two SGs at which steam condensation continued. Namely, the fall-back water directly covered a part of CETs on the upper core plate, secondly the water locally cooled the heater rods especially at the upper core region contributing to prevent generation of super-heated steam in the upper region, and thirdly the fall-back water in the core region generated saturated steam by contacting the heated core as shown below.

The water fall-back phenomena was detected by the heater rod temperatures indicating local cooling above the core water level. Figures 4.1.46 through 4.1.53 show all the surface temperatures measured at heater rods and tie rods at Pos.9 (EL 3.610m) through Pos.2 (EL 0.612 m) with both rod bundle locations and directions of hot legs in the

core cross section. Measurement location of all tie rods (non-heated rods) are shown in Table 4.1-5 (b). The measured heater rod bundles are distinguished by bundle number in a circle from the measured tie rod bundles. The primary saturation temperature (RC 200) is shown in these figures for comparison.

From these rod temperature data, local core cooling behavior caused by fall-back water from the hot legs during the SG depressurization actions was confirmed as shown below. Figure 4.1.54 shows heatup and quench times of six heater rods at elevations of Pos.9 (Top) through Pos.2 in comparison with the collapsed water levels in both upper plenum (RC 140) and core (RC 139). Additional heatup and quench times are shown in the figure for a tie rod at B12 (2,6) which showed the latest heatup behavior among five instrumented tie rods. The following findings were obtained.

(1) The earliest heatup was detected at the high-power rods in Bundles 13 and/or 17 at each vertical elevation. This earliest heatup front can be equivallent to a core mixture level, which swelled above the collapsed water level (RC 139) by an average void fraction (for example 0.27 at 8650s and 0.22 at 8860s). The latest heatup among the heater rods was detected at a low-power rod in peripheral region (Bundle No.3) which located just below the HL-B. When the heater rod in Bundle 3 Pos.8 started heatup at 9158 s, the earliest heatup front (equivallent mixture level) was more than 2 m below the elevation of Pos.8. A heatup time of Bundle 3 heater rod at Pos.8 was later more than 580 s from that of the earliest heatup front. Other heater rods in Bundles 8, 10 and 22 showed later heatup behaviors in comparison with those of the earliest heatup front above the middle height of core. These results strongly support water fall-back into the heated core especially in bundles below or close to the hot leg nozzles. These local cooling effects due to water fall-back were significant especially in the upper half core region. On the other hand, the fall-back water did not cool the bundles which located far from the hot legs as in the Bundles 13 and 17 in the LSTF core with 0.514 m diameter.

(2) It should be noted that steam generated in the cooled core below the water level in addition to the local cooling above the water level rose up the core to upper plenum through the upper core plate. Namely, there were two-dimensional flows at the upper core plate, i.e., a fall-back water flow in two regions below or close to the hot legs and an uprizing steam flow in the regions far from the hot leg directions (two regions close to the cold legs) in the LSTF core region. As the steam generated in the local cooling regions especially at the upper core part was in a saturated condition, the saturated steam could affect the CETs to detect the

saturation temperature during the core dryout process of this experiment.

(3) The tie rod temperature data showed better cooling than those of the heater rods. For example, a tie rod in Bundle 8 (2,2) showed heatup between 9115 s (Pos.4) and 9193 s (Pos.8), and its heatup time at Pos.5 was 261 s later than that of heater rod in the same bundle (4,3) as shown in Fig.4.1.50. Similar differences were also found between the heatup times of a tie rod in Bundle 21 (6,6) and a heater rod in Bundle 22 (4,4) which were closely located in the central core region. This indicates local water flow paths along the non-heating tie rods which simulated control rod guide thimbles in a PWR. Figure 4.1.54 shows the latest heatup behaviors at Pos.8 through Pos.4 of the tie rod in Bundle 12 (2,6) among all instrumented tie rods, which were later than those of the tie rod in Bundle 8 (2,2) shown above by more than 20 s.

(4) In the reflooding process after the LPI actuation at 9280 s, the core region was rather quickly filled with water, and a quench front of all heater rods (except for a Bundle 3) and all tie rods agreed completely to the reflooding collapsed water level as shown in Fig.4.1.54. This indicates no horizontal distribution of quench front in the core. The core power was already degraded to 10 % of the core power curve in the reflooding process.

4.2 Mass Balance and SG Heat Transfer Analysis

Estimation of primary coolant mass and primary-to-secondary heat transfer rates for experiment SB-PV-03 is discussed in this Section.

4.2.1 Mass Balance in Primary System

(1) Improved Methodlogy on Primary Coolant Mass Estimation

A transient primary coolant mass during an LSTF experiment has been estimated [Ref.12] by two methods, i.e., one is a directly-estimated mass of M_C [kg] which is a cumulated value of transient regional mass (M_i) in region (i), and the other one is a remained coolant mass of M_R [kg] in the primary system, which is indirectly-estimated by a mass balance equation. These methodlogies are applied for this experiment with some modifications shown below.

A regional mass of M_i [kg] is calculated by a collapsed water level reduced from cor-

responding DP data or by a gamma-densitometer data (only for the cold and hot legs), pressure and average fluid temperature in a region (i) (see Table B.1 in Appendix-B) with an LSTF configuration data base (Table B.2, ibid). Thus M_C is given as,

$$M_C = \Sigma_i M_i . \tag{4.8}$$

It should be noted that the DP data, however, generally include a frictional pressure loss in the forced circulation mode and an accerelation pressure loss in a rapid pressure transient. These result in increase of mass uncertainty especially in the early phase including the forced circulation. Therefore, the primary mass of M_C [kg] should be carefully treated in order to lower these mass uncertaunties. Additionally, some modifications were made for this mass estimation method, i.e., (1) one is a modification of average temperature corresponding to rejection of some failed thermocouples in two SG U-tube regions, (2) the second one is correction of the configurational data base for the lower plenum and both cold legs including ECCS lines to meet for the new one given in Table B.2. (3) Thirdly, improvements were made for the AIS tank water level estimation on six points, i.e., (a) correction of zero level used in the AIS tank level data base to meet for the correct level of EL 7.795 m, (b) correction of nitrogen gas density, (c) addition of gas volume in the piping connected to the AIS tank top head, (d) correction of the stand pipe top elevations to meet for the correct one which was lately measured at the ACC and ACH tanks, (e) improvement of water level estimation to account for the water density change in the pressure impulse lines between the calibration period at atomospheric pressure and the initial test conditions at 4.5 MPs, and (f) a zero level drift of the initial water level in the test period, which was found in a discrepancy between the final AIS tank water level during the gas inflow process and the correct stand pipe top elevation. The third improvement on the AIS water level measurement is not only important for estimation of the accurate water injection flow rate but also for estimation of gas expansion process including the gas inflow to the primary loops (see Section 4.1.3).

An initial primary coolant mass of M_0 for the experiment SB-PV-03 was determined as shown in Table B.1 (Appendix-B) by using equation (4.8) at an initial state before the break initiation, when each region was filled with only water and each water mass was easily calculated by a maximum volume and an average fluid density except for the PZR in which water level data did not include any frictional pressure loss. Thus, an initial mass in the primary system was obtained as $M_0 = 5418$ kg.

On the other hand, a transient primary coolant mass of M_R [kg] was obtained by using a

following mass balance equation with a total discharged primary mass of M_D [kg], a total injected ECCS mass of M_I [kg] and an initial primary mass of M_0 [kg] as,

$$M_R = M_0 - M_D + M_I. \tag{4.9}$$

The M_D is a sum of masses discharged from the break unit (M_{D1}:RC 191 in Fig. 4.1.2) and from the PORVs after 9060 s (M_{D2}), while the M_I is a sum of injected water masses from the AIS tanks (M_{IA}) and the LPI system after 9280 s (M_{IL}). The M_{IA} includes a water mass remained in each injection line.

$$M_D = M_{D1} + M_{D2}, \tag{4.10}$$

$$M_I = M_{IA} + M_{IL}. \tag{4.11}$$

In the experiment SB-PV-03, the discharged steam mass through the PORVs was not measured. Therefore, the primary mass of M_R shown in Table 4.2-1 after 9100 s is slightly over-estimated due to lack of the discharged steam mass through the PORVs. Moreover, the mass of M_R does not include a total mass of the nitrogen gas flowed into the primary loops after 7190 s. A total water mass injected from the LPI system during 20 s after 9280 s was approximately estimated as M_{IL} = 40 kg and it was included in the value of M_R at 9300 s .

(2) Transient Primary Coolant Mass Related to Major Events in Experiment SB-PV-03

Table 4.2-1 and Fig. 4.2.1 show the transient primary coolant mass of M_R in 9300 s after the break initiation. The following major events are related to the transient primary mass inventory.

(1) Water level in the upper plenum which started to decrease from the hot leg nozzle elevation at 3949 s corresponds to the primary mass inventory of M_R/M_0 = 0.329, that in the core started at 4750 s corresponds to M_R/M_0 = 0.284, that at the second upper plenum level decrease (7747 s) corresponds to M_R/M_0 = 0.330, start of the overall core heatup (8573 s) corresponds to M_R/M_0 = 0.259, start of the second and third AM actions at 8970 and 9060 s correspond to M_R/M_0 = 0.228 and 0.219, respectively, and the least mass ratio of M_R/M_0 = 0.20 was estimated at 9300 s just after the LPI actuation.

(2) As it was already shown in Fig. 4.1.2, water or two-phase discharge continued and no steam single-phase discharge occurred at the break in this experiment. This is a result of the specific break location at the lower plenum which is the lowest

in the primary system.

(3) The effects of AIS on the primary mass recovery in this experiment are clearly shown in Fig. 4.2.1. Namely, mass decrease in the primary system was gradually lowered after the AIS injection at 3241 s, stopped at approximately 5100 s at the minimum mass ratio of $M_R/M_0 = 0.275$, turned to increase until the sweep-out behaviors in the AIS injection lines almost completed at 7200 s (mass recovery to $M_R/M_0 = 0.375$) and started again at a faster rate after the AIS injection stopped.

(3) A Map of Primary Pressure - Coolant Mass Inventory for Accident Management

Figure 4.2.2 shows a trajectory map of the primary pressure and coolant mass ratio of M_R/M_0 during the test period of experiment SB-PV-03, which are given in Table 4.2.1. Each data point noted by a circle in the figure was plotted at every 100 s from the starting point at t = 0 s (P = 15.5 MPa and $M_R/M_0 = 1.0$) to the final state at 9300 s (P = 1.21 MPa and $M_R/M_0 = 0.200$). This map includes two important pressure setpoints, i.e., 4.5 MPa for the AIS actuation and 1.24 MPa for the LPI actuation in addition to a critical mass ratio of $M_R/M_0 = 0.25$ which is a reference mass ratio at the time of core heatup start in the experiment SB-PV-01 [Ref. 9].

This pressure - mass inventory map is useful for indication of key plant parameters in a case of accident management at a PWR system, which aims to depressurize the primary system to actuate the LPI system ($P < 1.24$ MPa) for long-term primary system cooling, and to establish adequate core cooling conditions ($M_R/M_0 > 0.25$) or re-establish core cooling conditions after a limited core heatup. This is shown in Fig. 4.2.2 that the AM actions aim to go into a left-upper region with sufficient mass ($M_R/M_0 > 0.25$) and under low pressure ($P < 1.24$ MPa) conditions.

In the experiment SB-PV-03, the first AM action started at 945 s (P = 8.21 MPa, $M_R/M_0 = 0.782$) contributed to moderately decrease the primary pressure as shown in Fig. 4.2.2 and the primary mass ratio at the temporary core heatup (5455 - 5784 s) was approximately $M_R/M_0 = 0.28$ which was more than 10 % higher than the critical mass ratio of $M_R/M_0 = 0.25$. This discrepancy between the mass ratios for the core heatup start between the experiments SB-PV-03 and SB-PV-01 can be ascribed to difference in water mass in the primary loops. On the other hand, the mass ratio at the start of overall core heatup at 8573 s in the experiment SB-PV-03 was rather close to the critical mass ratio of $M_R/M_0 = 0.25$. It is also shown in this P-M map that the mass ratio finally became lower than $M_R/M_0 = 0.25$ at a pressure higher than the LPI actuation pressure indicating inadequate core cooling conditions for this experiment.

4.2.2 Heat Transfer Analysis for SG-A and SG-B

Steam generator heat removal rates or primary-to-secondary heat transfer rates at two SGs were derived using an SG heat transfer model in addition to the secondary coolant mass inventory estimation for this experiment. A methodlogy to estimate the secondary coolant masses and the heat transfer model are shown in Appendix-C. First, discussed here is mass consistency between loss of the secondary mass inventory during the SG depressurization period (1000－9000 s) and a net coolant mass discharged from the secondary system. It is important for the SG heat transfer analysis to use these fluid mass data confirmed in good consistency. Secondly, discussed here are the estimated heat removal rates, average heat transfer coefficients at the SG U-tube inner surfaces and a total mass flow rate of the steam condensation at two SGs during the depressurization period.

(1) Mass Consistency in SG Secondary System

The secondary coolant mass inventory was estimated by using a DP data, average fluid temperature data and pressure data at each region of the secondary system (Appendix-C). Table 4.2-2 shows transient total secondary coolant masses in SG-A/B and their ratios compared to each initial coolant mass of M_0 (2552.1 kg for SG-A and 2555.9 kg for SG-B, respectively). As shown in Appendix-C, an overall accuracy of total secondary coolant mass was estimated as ±65.8 kg for SG-A and ±66.6 kg for SG-B, respectively. Temporary mass recovery shown in the table between 1000 and 3000 s is due to the AFW supply at both SGs. The mass recovery in the SG-B was larger than that in the SG-A as a result of larger AFW flow rate. The AM action to depressurize the secondary systems by controlling the SGRV steam flow rates resulted in the continuous mass decrease after the AFW stopped at 2753 s and a total mass remained in each secondary side was less than 15% of the initial mass at the last stage of SG depressurization (t＝9000 s).

On the other hand, a steam mass flow rate discharged through the RVs and a water mass supplied from the AFW system were separately measured at two SGs with accuracies of ±0.07 kg/s for the former and ±0.05 kg/s for the latter. This means large mass uncertainty in the total masses; for example ±0.07 [kg/s]×8000 [s]＝±560 [kg] for the RV steam flow during the depressurization period between 1000 and 9000 s. Moreover, the measured data of RV steam flow rates at two SGs had each zero shift all through the test period (see Fig.4.1.8). Thus, mass balance was checked between the decrease of secondary mass inventory and net mass discharge from the secondary systems, and an excess mass flow rate included in the RV steam flow data was estimated as shown below.

Table 4.2-3 compares a coolant mass decreased in the secondary side ($\triangle M$ [kg]), a supplied AFW water mass (M_F [kg]) and a steam mass (M_D [kg]) discharged through the SGRVs in each 500 s between 1000 and 9000 s. It is shown that a total RV steam mass (ΣM_D) subtracted by a total AFW water mass (ΣM_F) during 8000 s is significantly larger than a total mass of ($\Sigma \triangle M$) at two SGs as a result of the excess RV steam flow rates. Thus,

$\{\Sigma M_D - \Sigma M_F\} - \Sigma \triangle M = 737.1$ kg for SG-A and 414.3 kg for SG-B, respectively.

An average excess steam mass flow rate ($\triangle W_S$ [kg/s]) was determined as,

$$\triangle W_S = \{(\Sigma M_D - \Sigma M_F) - \Sigma \triangle M\}/8000 , \quad (4.12)$$

and $\triangle W_S$ was 0.0921 [kg/s] for SG-A and 0.0518 [kg/s] for SG-B, respectively. Then a corrected steam mass (M_D^*) discharged though the RVs during each 500 s was defined as,

$$M_D^* = M_D - C , \quad (4.13)$$

$$C = \triangle W_S \times 500 \text{ [kg]}. \quad (4.14)$$

These corrected steam masses during each 500 s for the SG-A and SG-B are also shown in Table 4.2-3. The excess steam mass flow rate at SG-A was higher than the accuracy of ± 0.07kg/s and that at SG-B was within the accuracy. In the following heat transfer analysis, the corrected steam masses of M_D^* for two SGs are used instead of M_D on the view point of secondary mass consistency.

(2) Primary-to-secondary Heat Transfer Model in SG Depressurization Process

A total primary-to-secondary heat transfer rate at one SG and an average heat transfer coefficient at U-tube inner surfaces were estimated at SG-A/B by using a calculation program developed for this purpose (see Appendix-C). A rough model used to estimate the primary-to-secondary heat transfer rate in the LSTF previous report [Ref.12] was modified for this experiment as briefly shown below.

A total energy of Q_U [kJ] transfered from the primary fluid to the SG U-tubes during a time period of $\triangle t$ [s] is given by a total steam enthalpy of Q_D [kJ] discharged from the main steam line, RV line and SV line, a total water enthalpy of Q_F [kJ] supplied to secondary side from the main and auxiliary feedwater systems, a total enthalpy increase of $\triangle Q_H$ [kJ] in the secondary fluid system, an external work of $V \times \triangle P$ [kJ], a metal energy increase of $\triangle Q_T$ [kJ] stored in the U-tube walls, a metal energy decrease of $\triangle Q_W$ [kJ] in both of SG vessel walls and internal structures, and an environmental

energy loss of Q_L [kJ] from the SG outer surfaces as,

$$Q_U = Q_{UA} + Q_{UB} , \tag{4.15}$$

$$Q_{Uj} = Q_{Dj} - Q_{Fj} + \triangle Q_{Hj} - V_j \times \triangle P_j + \triangle Q_{Tj} - \triangle Q_{Wj} + Q_{Lj} , \tag{4.16}$$

where j=A, B means SG-A and SG-B, respectively. An uncertainty of the total energy of $\triangle Q_{Uj}$ was estimated as $\pm 1.21 \times 10^5$ [kJ] for SG-A and $\pm 1.28 \times 10^5$ [kJ] for SG-B, respectively. An average heat removal rate during a time period of $\triangle t$ at each SG is given by $Q_{Uj}/\triangle t$ [kW] with an uncertainty of ± 242 [kW] for SG-A and ± 256 [kW] for SG-B, respectively (see C.3.2 in Appendix-C).

Then, an average heat transfer coefficient of h_T [kW/m^2/K] at the whole U-tube inner surfaces ($A_T = 171.0$ m^2) can be given as follows with an average value of saturation temperature difference of $\triangle T$ [K] between the primary system (represented by RC 200) and the secondary systems (RC 202 for SG-A and RC 203 for SG-B) in addition to the average heat removal rate during a time period of $\triangle t$ as,

$$h_{Tj} = (Q_{Uj}/\triangle t)/(A_T \times \triangle T_j) , \quad j=A, B \tag{4.17}$$

and $h_T = 0.78$ [kW/m^2/K] $\pm$ 3.2 % for the forced circulation mode in the initial steady state of two SGs.

In the case of secondary depressurization process during this experiment, most of the SG heat removal can be conducted in a steam condensation heat transfer mode at the U-tube inner walls below the secondary water level, and heat transfer between the superheated steam phases in both primary and secondary sides above the secondary water level can be less important compared to the former mode. Then, an average heat transfer coefficient of h_{cj} [kW/m^2/K] in steam condensation mode can be approximated by using a total heat transfer rate of ($Q_{Uj} / \triangle t$) and U-tube inner surface area of A_{cj} [m^2] below the secondary water level as,

$$h_{cj} = (Q_{Uj}/\triangle t)/(A_{cj} \times \triangle T_j) , \tag{4.18}$$

$$A_{cj} = 17.364 \times L_{cj} , \quad j=A, B \tag{4.19}$$

where L_{cj} [m] is a collapsed water level in the secondary side and $A_{cj} = A_T$ in case of $L_{cj} \geqq 9.866$ m.

(3) Results of Heat Transfer Estimation at Two SGs

Tables 4.2-4 (1) and (2) include estimated results of $Q_{Uj}/\triangle t$, a collapsed water level in SG secondary side of L_{cj} [m], $\triangle T_j$ and h_{cj} during each 500 s after the break at SG-A and SG-B, respectively. Figure 4.2.3 compares a total heat removal rate at two SGs ($Q_U/\triangle t$) during each 500 s with the transient core power and an additional enthalpy discharge ($Q_B/\triangle t$ [kW]) through the break, which was estimated by assuming saturated water enthalpy (h' [kJ/kg]) for the break flow of $\triangle M_B$ [kg] during each 500 s as,

$$Q_B = \triangle M_B \times h' \ [kJ]. \tag{4.20}$$

Figure 4.2.4 shows average heat transfer coefficient (h_{cj}) at U-tube inner surfaces below each secondary water level. Table 4.2-5 and Fig. 4.2.3 compares the total heat removal rate at two SGs ($Q_U/\triangle t$) and the break ($Q_B/\triangle t$ [kW]) with the core power of Q_C [kW]. On the other hand, contribution of the stored heat release from the U-tube walls ($\triangle Q_T$), SG vessel walls ($\triangle Q_W$) including internal structures, and environmental heat loss (Q_L) during each 500 s were estimated in comparison with the heat removal rate ($Q_{Uj}/\triangle t$) at each SG as shown in Table 4.2-6.

The following are derived from these results.

(1) The first AM action to depressurize the SG secondary systems had a major contribution to cool down the primary system. Namely, total heat removal rate at two SGs was more than 20% higher than the core power during the earlier phase before 4000 s and thereafter it became comparable or higher than approximately 80% of the core power. On the other hand, heat removal rate from the break was approximately 50 to 90% of the core power during the AM action with an assumption of saturated water break flow.

(2) Figure 4.2.4 shows that an average heat transfer coefficient at the U-tube inner surfaces was more than approximately 2 kW/m^2/K before the non-condensable gas inflow in the steam condensation mode under the secondary water level. This value accounts to more than two times of a heat transfer coefficient (0.78 kW/m^2/K) in the initial state of forced circulation mode. After the non-condensable gas flowed into the primary loops, however, negative influence of the gas inflow on the SG heat transfer coefficient was clearly shown. Namely, the average heat transfer coefficients largely decreased after 7500 s and finally became less than 50 % of those before the gas inflow at the end of this experiment. The increased temperature differences between the primary and secondary saturation temperatures after

the gas inflow covered the decreased heat transfer coefficients and contributed to maintain the SG heat removal rates (see Fig. 4.2.3 and Tables 4.2-4 (1) and (2)).

(3) It should be noted, however, that contribution of heat transfer rate at the U-tubes above the secondary water level could not be negligiblly small compared to the steam condensation heat transfer rate when the secondary water level became significantly low and U-tube surface areas above the secondary water level became significantly larger than those below the water level. In addition, some negative influences of the non-condensable gas dissolved in the injected AIS water can be included in the estimated SG heat transfer coefficients in 6000－7000 s before the gas inflow start.

(4) Contribution of the metal stored heat release on the SG heat removal rate was estimated in Table 4.2-6. Namely, metal stored heat release from the vessel walls and internal structures in each SG during each 500 s was approximately 10－30% of Q_{Uj} during the SG depressurization action. This influence is typical in the LSTF facility which has larger SG metal mass ratio to the secondary fluid mass than the reference PWR because of smaller-scaled system than the actual plant. A ratio of metal stored heat release from the U-tube walls compared with the heat removal rate was approximately 4－10% which is influenced by thick U-tube wall compared with that in the reference PWR. Thus, these metal stored heat effects on the SG heat removal rate are 15 to 40% in total at each SG. The environmental heat loss was approximately 3 to 6% of the heat removal rate in most of the time periods.

(4) Condensed Water Flowed down to the Upper Plenum and Core

The SG heat transfer analysis also gives an important information on the fall-back water flow from two SGs to the upper plenum, which is described with respect to the local core cooling and CET responses during the core heatup process (Section 4.1.3 (6)). Table 4.2-7 shows a total mass rate of condensed water, W_C [kg/s], and an equivalent steam volumetric flow rate of V_S [m^3/s] during each 500 s in the SG depressurization period, which were derived from the total heat removal rate ($Q_U / \triangle t$) using an average value of latent heat of q_L [kJ/kg] and saturated steam density of ρ'' [kg/m^3] at an average pressure in each time period with an assumption that all the condensed water flowed down to the upper plenum as,

$$W_C = (Q_U/\triangle t)/q_L \ , \tag{4.21}$$

$$V_S = W_C/\rho''. \tag{4.22}$$

It is shown that the total condensed water flow was 0.68 kg/s in average and an uncertainty of this flow rate was ± 0.18 kg/s (see Section C.3.2 in Appendix-C) during the depressurization process. It became 0.32 kg/s in the last period (8500-9000 s) which is equivalent to approximately 70% of the average break flow rate, and the corresponding total heat removal rate is equivalent to 79% of the core power. Thus, the condensed water flow can contribute to cool most of the heated core above the water level when the fall-back water flowed uniformely on all the heater rod surfaces. This water flow rate can generate a saturated steam flow rate of 0.05 m^3/s in this last phase of core heatup process. Consequently, the local core cooling observed during the core heatup process after 8573 s (Section 4.1.3 (6)) can be ascribable to the effects of fall-back condensed water on the view point of cooling capability, and a generated steam flow at the core exit can affect the CETs to maintain saturated temperatures during the core heatup process.

The total mass rate of W_C, however, includes a condensed water flow at the lower parts of the U-tube outlet sides (SG outlet plenum sides) but this heat transfer analysis can not determine a ratio of these mass flow rates at inlet and outlet sides. The fluid temperatures measured in both sides of U-tube lower regions (see Fig.4.1.33) shows that U-tube inlet side Pos.1 was maintained at a saturation temperature until 9000 s indicating a larger steam flow rate than in the outlet side, and larger heat transfer rate can be caused by a larger temperature difference between the primary and secondary systems in comparison with the U-tube outlet side. Moreover, the hot leg fluid density data (see Fig.4.1.11) show existence of a condensed water layer in a period of 8000 and 9000 s while the cold leg density data (Fig.4.1.12) show almost steam phase. These thermohydraulic conditions support that most of the condensed water passed the hot legs and flowed down to the upper plenum in the core heatup period.

5. Concluding Remarks

A small break loss-of-coolant accident (SBLOCA) experiment of SB-PV-03 was successfully conducted at the Large Scale Test Facility (LSTF) of ROSA-V program simulating a break of 10 instrument-tubes at vessel bottom of a 4-loop pressurized water reactor (PWR) to clarify effects of accident management (AM) measures on core cooling in case of high pressure injection (HPI) system failure and non-condensable gas inflow from the accumulator injection system (AIS) tanks. The break size is equivalent to a 0.2% cold leg break. Steam generator (SG) secondary-side depressurization as the principal AM action was initiated 10 minutes after the safety injection (SI) signal at two SGs by controlling relief valves (RVs) to achieve a primary system cooling rate at -55 K/h and supplying auxiliary feedwater (AFW) for 30 minutes. The second and third AM actions were conducted in the last phase of experiment with different initiation logics from the initial experiment plan based on the core exit thermocouple (CET) measurement.

The followings are conclusions obtained with respect to (1) three typical phases in the experiment, (2) effects of AM actions on core cooling, (3) primary coolant mass depletion typical for the vessel bottom SBLOCA, (4) condensation heat transfer coefficient at SG U-tubes degraded by non-condensable gas inflow, and (5) CET responses and local core cooling affected by fall-back condensed water from SG U-tubes.

(1) Three Typical Phases in Chronology of Experiment SB-PV-03

Observed three typical phases are; (a) an initial transient after break with core cooling by forced or natural circulation flow in the primary loops (0－945 s), (b) a long-term primary cooldown process lead by the principal AM action resulting in the AIS actuation and cooling at most part of the core (945－7190 s) and (c) a low pressure transient below 1.6 MPa with non-condensable gas in the primary loops resulting in overall core heatup due to delay of low pressure injection (LPI) start and continuing water discharge at the break (7190－9880 s).

(2) Effects of AM Actions on Core Cooling under AIS Gas Inflow

The principal AM action to obtain the primary depressurization at -55 K/h became less effective immediately after the initiation of AIS gas inflow at 1.6 MPa and the LPI actuation at 1.24 MPa was about 34 minutes later than the gas inflow start. Overall core heatup started about 12 minutes before the LPI start but the CETs did not detect any super-heated steam temperature at the core exit. Therefore, the additional AM actions as the second step to fully open the SGRVs and the third step

to open the pressurizer power-operated relief valves (PORVs) were conducted by the operators monitoring core heatup behaviors instead of the CET responses (see fifth conclusion shown below), but these were also less effective to promote the primary depressurization. It is concluded that these AM actions in this LSTF experiment were not sufficient to achieve early LPI actuation for adequate core cooling under the AIS gas inflow conditions.

(3) Effects of Bottom Break Location on Core Cooling

The vessel bottom break resulted in no steam or gas discharge but continuous water discharge during the experiment. This caused two typical results in comparison with a 0.5% cold leg SBLOCA experiment [7] performed with similar AM actions. Steam discharge took place at the cold leg break causing a large depressurization rate but with small mass decreasing rate. Most of AIS gas flowed out through the break either. Both of these gas-phase discharge from the break resulted in effective core cooling by early actuation of the LPI. The PV bottom break with single-phase liquid discharge, on the contrary, resulted slow depressurization while fast loss of primary mass inventory, causing very slow primary mass recovery after the AIS actuation. Meanwhile, a part of core experienced inadequate core cooling during the AIS injection. The fast loss of primary mass inventory caused a rapid core uncovery after the termination of coolant injection from the AIS.

(4) Degradation of SG Heat Transfer due to Non-condensable Gas Inflow

An SG heat transfer model was developed to estimate total heat removal rate and average heat transfer coefficients at the U-tubes (see Appendix-C). It was clarified that a sum of total primary-to-secondary heat transfer rate and heat removal rate at the break was sufficient to cool the primary system with more than 40% higher power than the core power during the principal AM action before the gas inflow time. It was also clarified that steam condensation heat transfer coefficient at the U-tube insides below the secondary water level, however, rapidly decreased soon after the gas inflow started from the AIS tank, and thereafter the primary depressurization was significantly degraded while the SG secondary pressures further decreased by the AM actions.

(5) CET Temperature Responses and Local Core Cooling during SG Depressurization Action

The CET temperatures are one of the key plant parameters to detect core heatup for PWR AM decision making, and were attempted to use in this experiment to start AM actions in three steps. The CETs, however, showed saturation temperatures even during the core heatup period. It was thus expected that the CETs were mainly af-

fected by condensed water fall-back from two SGs as shown below. Namely, one reason is a direct contact effect of water falling onto the CETs installed at upper surfaces of the upper core plate. Next one is the cooling of the heated core top region by the falling condensate water. The third one is the generation of steam in the core cooled by the falling water. As the total SG heat transfer rate in the core heatup period was comparable to the core power, the falling water flow had a cooling capablity for the whole core when the condensed water uniformly fell onto all the heater rods. On the other hand, it should be noted that CET temperature responses in a PWR may be differently influenced by condensed water fall-back from the experiment results in the LSTF which has atypical upper plenum configuration compared with the PWR. This issue is remained to be clarified.

Acknowledgment

The authors are grateful to Messrs. M. SUZUKI deputy director of Department of Reactor Safety Research and M. HIRANO director of Department of Reactor Safety Research for their useful comments on the report, to Messrs. H. OHSAKI, M. OGAWA, A. OHWADA and T. NISHIKIZAWA in Thermohydraulic Safety Engineering Laboratory and T. OHWADA in Department of Reactor Safety Research for their technical supports of conducting the experiment and some characterization tests, and to Ms. K. TOYODA of ITJ Inc. for her contribution to experimental data analysis and processing.

References

(1) The ROSA-V Group, "ROSA-V Large Scale Test Facility (LSTF) System Description for the Third and Fourth Simulated Fuel Assemblies", JAERI-Tech 2003-037, Mar. 2003.

(2) M. SUZUKI, et al., "ROSA/LSTF Experiments on PWR Reactor Vessel Bottom Very-small Break LOCA - Effects of Secondary Depressurization and Influences of Non-condensable Gas-", Proceed. of 1997 Fall Meeting of AESJ, C44, 2003 (in Japanese).

(3) H. ASAKA, et al., "Intentional Depressurization of Steam Generator Secondary Side during a PWR Small-Break Loss-of-Coolant Accident", J. Nucl. Sci. Technol., Vol. 32, No. 2, Feb. 1995.

(4) T. YONOMOTO, et al., "PWR Small Break Loss-of-Coolant-Accident Experiment at ROSA-V/LSTF with a Combination of Secondary-Side Depressurization and Gravity-Driven Safety Injection", J. Nucl. Sci. Technol., Vol. 34, No. 6, June 1997.

(5) H. KUMAMARU, et al., "RELAP5/MOD3 Code Analyses of LSTF Experiments on Intentional Primary-side Depressurization Following SBLOCAs with Totally Failed HPI", Nucl. Technol., Vol. 126, No. 3, 1998.

(6) H. ASAKA, et al., "Secondary-Side Depressurization during PWR Cold Leg Small Break LOCAs Based on ROSA-V/LSTF Experiments ans Analyses", J. Nucl. Sci. Technol., Vol. 35, No. 12, Dec. 1998.

(7) I. OHTSU, et al., "N_2 Gas Behavior from ACC during PWR Small Break LOCA", Proceed. of 1997 Fall Meeting of AESJ, G12, 1997 (in Japanese).

(8) M. SUZUKI, et al., "Simulation Test of PWR Instrument Tube Break LOCA in ROSA-IV Program", J. Nucl. Sci. Technol., Vol. 24, No. 12, Dec. 1987.

(9) M. SUZUKI, "Break Location Effects on PWR Small Break LOCA Phenomena - Inadequate Core Cooling in Lower Plenum Break Test at LSTF -", JAERI-M 88-271, Jan. 1989.

(10) Japan Nuclear Power Company, "Tsuruga Hatsudensho genshiro-secchihenkou-kyokashin seisho (#2 zousetsu)", 1979 (in Japanese).

(11) H. KUMAMARU, et al., "Recalculation of Simulated Post-scram Core Power Decay Curve for Use in ROSA IV/LSTF Experiments on PWR Small-break LOCAs and Transients", JAERI-M 90-142, Aug. 1990.

(12) M. SUZUKI, et al., "ROSA/LSTF Experiment Report for RUN SB-CL-24, Repeated Core Heatup Phenomena during 0.5% Cold Leg Break LOCA", JAERI-Tech 2000-016, 2000.

(13) A. MORISHIMA, et al., "Design for Power Reactor Fuel Assemblies Vol. 1 (2nd Revision), Design Data of Temperature, Heat-flux Distribution, and Mechanical Strength", JAERI-M 4881, July 1972 (in Japanese).

(14) Private Communication, R. Shaw, et al., "Summary of the LSTF Characterization Tests Performed in Conjunction with the ROSA/AP600 Experiments", Feb. 1995.

Table 2.1-1 Major design characteristics of LSTF compared with four-loop PWR

Item	(Unit)	LSTF*1	PWR	Ratio
Rated Condition				
Pressure	(MPa)	16	16	1 / 1
Hot Leg Temperature	(K)	598	598	1 / 1
Primary Fluid Volume (V)*2	(m^3)	7.83	347	1 / 44.3
Pressure Vessel Fluid Volume	(m^3)	2.67	131.7	1 / 49.4
Core Thermal Design				
Number of Fuel Rods		1008	50952	1 / 50.55
Thermal Core Power (P)	(MW)	10	3423	1 / 342
(P/V)	(MW/m^3)	1.28	9.9	1 / 7.7
Core Inlet Flow Rate	(kg/s)	48.8	16700	1 / 342
Core Height	(m)	3.66	3.66	1 / 1
Core Flow Area	(m^2)	0.1134	4.75	1 / 41.9
Downcomer Gap	(m)	0.053	0.260	1 / 4.91
Primary Loop Design				
Number of Primary Loops		2	4	1 / 2
Hot Leg Diameter (D)	(m)	0.207	0.737	1 / 3.56
Hot Leg Length (L)	(m)	3.69	6.99	1 / 1.89
$(L/\sqrt{D})$	($m^{1/2}$)	8.15	8.15	1 / 1
$\pi D^2L/4$	(m^3)	0.124	2.98	1 / 24
Hot Leg Top Elevation*3	(m)	EL 5.606	EL 5.606	1 / 1
Loopseal Bottom Elevation*3	(m)	EL 1.701	EL 1.7	1 / 1
Pressurizer Design				
Pressurizer Fluid Volume	(m^3)	1.2	51	1 / 42.5
Pressurizer Height	(m)	11.092	15.5	1 / 1.40
Steam Generator Design				
Number of SGs		2	4	1 / 2
One SG Vessel Fluid Volume	(m^3)	7.0	163.1	1 / 23
Number of U-tubes per One SG		141	3382	1 / 24
U-tube Inner Diameter	(mm)	19.6	19.6	1 / 1
Average U-tube Length	(m)	20.2	20.2	1 / 1

*1 Large-scale Test Facility (LSTF) with the fourth core assembly.
*2 Steam lines and active dead volumes are not included.
*3 Elevation above the core bottom (EL 0.0 m).

Table 2.2-1 Summary of measurement types and locations

Instrument / Measurement	Pressure Vessel	Pressurizer	Primary System	Steam Generator	Secondary System	ECCS	Blowdown System	Utility	Total		Tag ID
									3rd	4th	
Fluid Temperature	219 (234)	12 (12)	98 (108)	225 (248)	24 (28)	57 (58)	19 (26)	23 (23)	737	677	TE
Wall Temperature	152 (301)	18 (20)	13 (39)	86 (86)	12 (12)	2 (2)	2 (7)		467	285	TW
Differential Temperature	81 (104)	2 (2)	24 (24)	66 (70)					200	173	DT
Conductance Probe	13 (57)		57 (58)	67 (87)	1 (1)	4 (6)	1 (2)	0 (2)	213	143	CP
BICOTH Liquid Level[a]	0 (24)								24	0	TE
HTC Liquid Level[a]	11 (12)								12	11	TE,DT,CP
Liquid Level	2 (2)	2 (2)		16 (16)	2 (2)	8 (8)	8 (8)		38	38	LE
Pressure	5 (5)	7 (8)	11 (11)	8 (8)	7 (7)	7 (7)	11 (15)		61	56	PE
Differential Pressure	17 (18)	8 (8)	38 (38)	54 (54)	8 (8)	5 (5)	8 (9)		140	138	DP
Gamma Densitometer (1 beam)		2 (2)	2 (2)	0 (2)	1 (1)				7	5	DE
Gamma Densitometer (3 beam)		3 (3)	18 (18)		3 (3)		3 (3)		27	27	DE
Flowrate	2 (2)	1 (1)	14 (16)	8 (8)	22 (22)	39 (39)	6 (8)	2 (2)	98	94	FE
Pitot-tube or Turbine Meter	0 (4)	1 (1)	0 (9)						14	1	MI
Drag Disk Flowmeter (MFE)	0 (4)	0 (2)	26 (26)				4 (5)		37	30	MF
Drag Disk Flowmeter (MFT)			22 (22)						22	22	MF
Rotational Speed			2 (2)						2	2	MI
Pump Oscillation			2 (2)						2	2	MI
Pump Torque			2 (2)						2	2	MI
Power	11 (11)	4 (4)	8 (8)	16 (16)		4 (4)			43	43	MI
Input Current			2 (2)						2	2	MI
Break Signal							1 (3)		3	1	CP
Valve Position		2 (2)			4 (4)	2 (2)			8	8	MI
Regional Total	513 (778)	62 (67)	339 (387)	546 (595)	84 (88)	128 (131)	63 (86)	25 (27)	2159	1760	

* Number of instruments in the 3rd core is shown in bracket for each column.

[a] The BICOTH liquid level meter includes 3 TEs for each of 8 instruments, and the HTC liquid level meter includes 2 TEs, 1 DT, and 1 CP for each of 3 instruments in the 3rd core.

Table 3.2-1 Control logic for experiment SB-PV-03

Event	Cause	Delay Time
Break and Trace Heaters Power Off	Time = 0.0 s	
Pressurizer Heater Power Off	L_{PZR} < 2.3 m	
Scram Signal	P_{PZR} ≦ 12.97 MPa	
SI Signal	P_{PZR} ≦ 12.27 MPa	
Core Power Tripped to Decay Curve	Scram Signal	
Core Power Control on Decay Curve	75% for Rod Temp. ≧ 908 K 50% for Rod Temp. ≧ 918 K 25% for Rod Temp. ≧ 919 K 10% for Rod Temp. ≧ 920 K 0% for Rod Temp. ≧ 923 K	
Primary Pumps Speed-up Primary Pumps Tripped to Decay Primary Pumps Stopped	Break Signal Scram Signal Pump Decay Start	 16.2 s 250 s
Turbine Trip	Scram Signal	
Main Feedwater Valve Closed	Scram Signal	
SG-RV Setpoint to Open SG-RV Setpoint to Close SG-SV Setpoint to Open SG-SV Setpoint to Close	P_{SG} ≧ 8.03 MPa P_{SG} ≦ 7.82 MPa P_{SG} ≧ 8.68 MPa P_{SG} ≦ 7.69 MPa	
SG-RV Control for Primary Cooling (dT/dt = −55 K/h) SG-RV Fully Open Pressurizer 3 PORVs Open	SI Signal Operator Action*1 Operator Action*2	600 s
High Pressure Injection System	All Systems Failed	
Low Pressure Injection System	SI Signal & P ≦1.24 MPa	17 s
Auxiliary Feedwater Operation Auxiliary Feedwater Termination*3	SI Signal Operation Start	600 s 1800 s

*1 Initially planned to start after detection of the core heatup, i.e., when a maximum core exit templerature (CET) reached 623 K after AISs actuation. In SB-PV-03, the SGRV was actually opened at 8970 s by detecting core heat-up (TW≧750 K) instead of the fixed CET at the saturation temperature.

*2 Initially planned to start after the operator action to full-open the SG-RVs, if necessary. In the experiment, PORVs were actually opened at 9060 s by detecting higher core temperature TW ≧810 K.

*3 Actuation of a turbine-driven auxiliary feedwater pump within 1800 s.

Table 3.2-2 JAERI new core power curve after the scram

Time (s)	Power (MW)	Time (s)	Power (MW)	Time (s)	Power (MW)	Time (s)	Power (MW)
0	10.000	80	3.0425	600	1.8317	5000	0.93648
17.87	10.000	100	2.7633	800	1.5768	6000	0.88612
20	8.1497	150	2.4228	1000	1.4872	8000	0.81362
30	5.3662	200	2.2631	1500	1.3417	10000	0.76272
40	4.5044	300	2.0795	2000	1.2378	20000	0.62943
50	3.9056	400	2.0000	3000	1.0960	50000	0.49122
60	3.5384	500	1.9127	4000	1.0029	100000	0.40466

Table 3.2-3 Primary pump coastdown curve after the scram

Time (s)	Pump Speed Ratio	Time (s)	Pump Speed Ratio	Time (s)	Pump Speed Ratio
0	1.000	30	0.280	80	0.125
2	0.850	40	0.220	90	0.110
5	0.730	50	0.185	100	0.100
10	0.540	60	0.160	250	0.000
20	0.370	70	0.140		

The pump speed ratio is normarized by the maximun pump speed of 1500 rpm.
A time delay of 16.2 s is assumed after the scram.

Table 3.2-4 Initial conditions in experiment SB-PV-03

Region and Items	(Unit)	Specified	Measured	(Accuracy*1)
Pressure Vessel:				
Core Power	(MW)	10.0	10.1*2	(± 0.07)
Primary Loops (A-Loop / B-Loop):				
Hot Leg Temperature	(K)	598.1	600.4 / 598.9	(± 2.75)
Cold Leg Temperature	(K)	562.4	564.3 / 565.7	(± 2.75)
Mass Flow Rate	(kg/s/loop)	24.3	24.7 / 24.3	(± 1.25)
Downcomer-to-HL Byp.Flow	(kg/s/loop)	0.049	0.049 (Estimated*3)	
Pressurizer:				
Pressure	(MPa)	15.5	15.54	(± 0.108)
Water Level above Bottom*4	(m)	7.2	7.26	(± 0.25)
Steam Generators (A-Loop / B-Loop):				
Pressure	(MPa)	7.3	7.37 / 7.39	(± 0.054)
Water Level	(m)	10.3	10.22/10.22	(± 0.38)
Main Feedwater Flow Rate	(kg/s)	2.74	2.67 / 2.59	(± 0.05)
Main Feedwater Temperature	(K)	495.2	495.7/495.7	(± 2.63)
Auxiliary Feedwater Temperature	(K)	310	309.5	(± 2.37)
Accumulators (ACC to CLA / ACH to CLB)				
Flow Distribution Ratio (A:B)		2 : 2	2 : 2	
Injection Pressure	(MPa)	4.51 / 4.51	4.55 / 4.54	(± 0.054)
Water Temperature	(K)	320 / 320	321.8/322.7	(± 2.3/2.4)
Water Level above Bottom*5	(m)	5.87 / 6.54	6.75 / 6.75	(±0.12/0.15)
Low Pressure Injection System:				
Flow Distribution Ratio (A:B)		2 : 2	2 : 2	
Actuation Pressure	(MPa)	1.24	1.24	(± 0.064)
Water Temperature	(K)	310	309.5	(± 2.63)
Trace Heater Power before Break:				
Pressurizer Heater Power	(kW)		36.3	(± 0.63)
Pressurizer Surge Line	(kW)		2.7	(± 0.01)
Pressurizer Spray Line	(kW)		3.0	(± 0.01)
Pressure Vessel	(kW)		37.1	(± 0.08)
A-Loop	(kW)		8.6	(± 0.023)
B-Loop	(kW)		8.0	(± 0.023)
SG-A Vessel and Downcomer	(kW)		13.8	(± 0.05)
SG-B Vessel and Downcomer	(kW)		13.8	(± 0.05)

*1 Reference [1]
*2 Actual power supplied to the core is 1% lower than the recorded MI 17 data because the data included the 1% electric loss outside the pressure vessel.
*3 The downcomer-to-HL leak flow in each loop is controlled by the flow control valve (HCV010 or HCV150).
*4 Bottom of the pressurizer level meter (DL 0.08 m).
*5 Bottom of the ACC/ACH vessels, which is 2.112 m lower than the zero point of water level measurement data (LE 14, LE 15).

Table 4.1-1 Sequence of events in experiment SB-PV-03

Event	Time (s)
·Break initiation	0.0
Primary pump speed started to increase	0
·Trace heater powers tripped off	2
·PZR heaters tripped on low PZR level	181
·Scram signal setpoint (12.97 MPa)	250
SG-A/B steam and feedwater lines were closed	250
·Primary coolant pumps started to coast down	252
·Core power decay started from 10 MW	280
·SG-B relief valve started to cyclicly open	302
·Pressure reached to SI setpoint (12.27 MPa)	340
·PZR water level reached lower end	348
·Boiling started in HL-A	350
·Primary coolant pumps stopped	500
·Water level formed in cold legs	655
·1st AM action start (Secondary feed & bleed)	945
·Level decrease start in SG-A outlet plenum	2359
·Level decrease start in SG-A inlet plenum	2408
·Auxiliary feedwater stopped at SG-A/B	2753
·Level decrease start in SG-B outlet plenum	2967
·Level decrease start in SG-B inlet plenum	2975
·ACC injection start to CL-A	3241
·ACH injection start to CL-B	3264
·Upper plenum water level decreased	3949
·Hot legs became almost empty	3980
·Core water level started to decrease	4750
·Temporary heatup at the top of core	5455 - 5784
·Gas discharge starts from ACC tank to CL-A	7190
·Gas discharge starts from ACH tank to CL-B	7477
·Upper plenum water level decreased again	7747
·Core water level started to decrease again	8320
·Core heatup start at Pos.8 (High-power Rod)	8573
·2nd AM action (SG-RVs full-open)	8970
·3rd AM action (PORVs full-open)	9060
·Core decay power degraded to 75%	9179
·Core power degraded to 10%	9200
·LPI injection	9280 - 10525
·Final core quench	9680
·Core power supply termination	9880
·PORV closure	9920
·Break valve closure	9935
·ACH and ACC lines isolation	9956
·Charging system operation for second test	10706 - 11741
·Data recording termination	12399

Table 4.1-2 Degraded primary depressurization after gas inflow

Item	Time Period (s)				
	5450-6450	6450-7200	7200-7700	7700-8300	8300-8900
Time duration (s)	1000	750	500	600	600
a:dP/dt(kPa/s) at PZR	- 0.687	- 0.527	- 0.111	- 0.060	- 0.092
b:dP/dt(kPa/s) at SGs	- 0.673	- 0.539	- 0.401	- 0.385	- 0.385
Ratio (a/b)	1.02	0.98	0.28	0.16	0.28

Table 4.1-3 AIS gas volume expansion under injection process

Time (s)	Gas in ACC Tank				Gas in ACH Tank			
	PE 31 P (MPa)	TE 965 T_G (K)	V_G^* (m^3)	R (-)	PE 32 P (MPa)	TE 780 T_G (K)	V_G^* (m^3)	R (-)
3200*1	4.5456	317.37	0.5632	1.000	4.5417	318.41	0.5294	1.000
3400	4.3155	314.33	0.5947	0.995	4.3564	315.95	0.5467	0.998
3600	4.0844	312.82	0.6140	0.994	4.1262	314.61	0.5751	0.999
3800	3.8674	312.54	0.6477	0.994	3.9098	314.09	0.6074	1.001
4000	3.6841	312.70	0.6799	0.993	3.7273	314.02	0.6383	1.003
4200	3.5000	312.77	0.7166	0.994	3.5439	314.04	0.6731	1.006
4400	3.3084	312.70	0.7580	0.994	3.3528	314.04	0.7123	1.007
4600	3.1246	312.66	0.8024	0.994	3.1696	314.08	0.7546	1.009
4800	2.9640	312.86	0.8478	0.996	3.0101	314.13	0.7973	1.012
5000	2.7896	312.70	0.9002	0.996	2.8357	314.16	0.8469	1.012
5200	2.6253	312.68	0.9574	0.997	2.6702	314.14	0.9018	1.015
5400	2.4528	312.60	1.0245	0.997	2.4966	313.80	0.9660	1.018
5600	2.3131	312.91	1.0904	0.999	2.3586	314.22	1.0285	1.022
5800	2.1631	312.54	1.1662	1.001	2.2067	313.79	1.1014	1.026
6000	2.0157	313.00	1.2475	0.996	2.0608	313.89	1.1776	1.024
6100	1.9550	313.00	1.2872	0.997	2.0003	314.20	1.2148	1.024
6200	1.9347	313.78	1.3129	1.004	1.9797	315.15	1.2418	1.033
6300	1.8234	312.33	1.3833	1.001	1.8717	313.80	1.3073	1.033
6400	1.7525	312.43	1.4415	1.002	1.8023	313.90	1.3615	1.035
6500	1.7458	314.26	1.4598	1.005	1.7931	315.55	1.3805	1.039
6600	1.7569	315.78	1.4604	1.007	1.8022	316.77	1.3810	1.040
6700	1.5960	312.31	1.5777	1.000	1.6724	313.71	1.4912	1.034
6800	--	--	--	--	1.5799	313.77	1.5605	1.041
6900	--	--	--	--	1.5921	315.85	1.5671	1.032
7000	--	--	--	--	1.6005	317.08	1.5671	1.048

$V_G^* = V_G + \Delta V_G + V_{PO}$,

V_G^* [m^3] : Corrected gas volume,

V_G [m^3] : AIS tank gas volume above water level,

ΔV_G[m^3] : Correction on level shift (0.0294 for ACC and -0.0074 for ACH),

V_{PO} [m^3] : Gas volume in top piping (0.0078 for ACC and 0.0144 for ACH).

$R = (P \cdot V_G^*/T_G)/(P_O \cdot V_{GO}^*/T_{GO})$: Ratio of gas constant to initial state.

*1 : Gas state in ACH at 3250 s.

Table 4.1-4 Estimation of AIS gas volume flowed into primary loops

Time (s)	Gas from ACC Tank				Gas from ACH Tank			
	PE 31 P (MPa)	TE 965 T_G (K)	V_{GE}^* (m^3)	ΔM_{GE} (mol)	PE 32 P (MPa)	TE 780 T_G (K)	V_{GE}^* (m^3)	ΔM_{GE} (mol)
6700	1.5960	312.31	1.5811	--	--	--	--	--
6800	1.5663	313.24	1.6164	--	--	--	--	--
6900	1.5783	315.27	1.6143	--	--	--	--	--
7000	1.5856	316.37	1.6123	--	--	--	--	--
7100	1.5010	314.62	1.6953	--	1.5359	315.71	1.6242	--
7200	1.4094	312.63	1.7959	5.5	1.4529	314.42	1.7149	--
7300	1.4201	314.71	1.7940	5.5	1.4670	316.16	1.7070	--
7400	1.4276	315.97	1.7916	5.5	1.4734	317.00	1.7036	--
7500	1.3981	315.57	1.8276	22.3	1.4457	316.86	1.7371	3.2
7600	1.3774	315.42	1.8547	36.2	1.4253	316.67	1.7623	16.8
7700	1.3721	315.94	1.8650	41.4	1.4203	317.05	1.7708	21.3
7800	1.3730	316.40	1.8665	42.1	1.4214	317.58	1.7723	22.1
7900	1.3739	316.81	1.8676	42.7	1.4225	318.02	1.7734	22.7
8000	1.3695	316.89	1.8743	46.0	1.4178	317.98	1.7793	25.8
8100	1.3572	316.69	1.8903	53.9	1.4055	317.78	1.7946	33.7
8200	1.3442	316.46	1.9074	62.1	1.3925	317.61	1.8110	42.1
8300	1.3366	316.49	1.9186	67.5	1.3853	317.71	1.8215	47.4
8400	1.3326	316.73	1.9260	70.9	1.3813	317.84	1.8277	50.4
8500	1.3262	316.81	1.9358	75.5	1.3749	317.90	1.8371	55.1
8600	1.3164	316.61	1.9492	81.7	1.3653	317.76	1.8497	61.2
8700	1.3049	316.54	1.9663	89.5	1.3539	317.69	1.8656	68.9
8800	1.2923	316.45	1.9851	97.9	1.3410	317.54	1.8836	77.4
8900	1.2820	316.39	2.0009	104.8	1.3310	317.59	1.8985	84.3
9000	1.2748	316.59	2.0136	110.3	1.3238	317.68	1.9100	89.6
9100	1.2656	316.65	2.0289	116.9	1.3148	317.73	1.9239	95.9
9200	1.2488	316.26	2.0540	127.4	1.2983	317.39	1.9596	112.4
9300	1.2000	315.07	2.1306	157.9	1.2494	316.28	2.0199	137.2
9900	0.9529	312.65	2.6696	324.0	1.0003	314.22	2.3727	245.6

$V_{GE}^* = R \cdot C_0 \cdot (T_G/P)$,

V_{GE}^* [m^3]: Gas volume estimated for sweep-out and loop-inflow process,

$R = a \cdot (P_0 - P) + b$: Ratio to initial gas state with

$a = 0.01088$ [MPa^{-1}] and $b = 0.9696$ for gas expansion at ACC,

$a = 0.03583$ [MPa^{-1}] and $b = 0.9387$ for gas expansion at ACH and

$C_0 = P_0 \cdot V_{G0}^*/T_{G0}$ [$MPa \cdot m^3/K$] : Gas constant for initial state.

$\Delta M_{GE} = 1.20271 \cdot 10^5 \cdot P \cdot (V_{GE}^* - V_{P0} - V_{GSP} - V_L)/T_G$,

ΔM_{GE} [mol] : Gas mass flowed into primary loops,

P [MPa] : Gas pressure in AIS tank,

V_{GSP} [m^3]: AIS tank volume above stand pipe (1.5801 in ACC and 1.5766 in ACH),

V_L [m^3] : Free volume in injection line and stand pipe (0.1979 for ACC and 0.1402 for ACH).

Table 4.1-5 List of rod surface temperature measurement in core

(a) Heater Rods

Location	B03(4, 3)	B08(4, 3)	B10(4, 4)	B13(4, 4)	B17(4, 4)	B22(4, 4)	Total No.
Pos. 9		○			○	○	3
Pos. 8	○		○	○			3
Pos. 7	○	○	○	○	○	○	6
Pos. 6	○		○	○			3
Pos. 5		○			○	○	3
Pos. 4	○		○	○			3
Pos. 3		○			○	○	3
Pos. 2	○		○	○			3
Pos. 1		○			○	○	3
Total No.	5	5	5	5	5	5	30

(b) Tie Rods (Non-heated Rods)

Location	B01(2, 2)	B04(2, 2)	B08(2, 2)	B11(2, 2)	B12(2, 6)	B16(2, 2)	B21(6, 6)	Total
Pos. 9		○				○		2
Pos. 8			○		○			2
Pos. 7							○	1
Pos. 6		○	○	○	○	○	○	6
Pos. 5	○		○	○	○			4
Pos. 4			○		○		○	3
Pos. 3						○		1
Pos. 2			○		○		○	3
Pos. 1		○				○		2
Total	1	3	5	2	5	4	4	24

Table 4.2-1 Estimated primary mass inventory in experiment SB-PV-03

Time (s)	M_D (kg)	M_I (kg)	M_R (kg)	$M^*=M_R/M_o$
- 50	0	0	5418	1.000
0	0	0	5418	1.000
100	160	0	5258	0.970
200	306	0	5112	0.944
300	438	0	4980	0.919
400	562	0	4856	0.896
500	684	0	4734	0.874
600	799	0	4619	0.853
700	914	0	4504	0.831
800	1023	0	4395	0.811
900	1131	0	4287	0.791
1000	1235	0	4183	0.772
1100	1340	0	4078	0.753
1200	1438	0	3980	0.735
1300	1543	0	3875	0.715
1400	1637	0	3781	0.698
1500	1740	0	3678	0.679
1600	1841	0	3577	0.660
1700	1937	0	3481	0.642
1800	2029	0	3389	0.626
1900	2128	0	3290	0.607
2000	2227	0	3191	0.589
2100	2316	0	3102	0.573
2200	2413	0	3005	0.555
2300	2501	0	2917	0.538
2400	2586	0	2832	0.523
2500	2678	0	2740	0.506
2600	2766	0	2652	0.489
2700	2854	0	2564	0.473
2800	2935	0	2483	0.458
2900	3009	0	2409	0.445
3000	3099	0	2319	0.428
3100	3189	0	2229	0.411
3200	3267	0	2151	0.397
3300	3347	12	2083	0.384
3400	3427	39	2030	0.375
3500	3504	65	1979	0.365
3600	3584	96	1930	0.356
3700	3650	132	1900	0.351
3800	3735	162	1845	0.340
3900	3804	189	1803	0.333
4000	3876	224	1766	0.326
4100	3956	260	1722	0.318
4200	4025	295	1688	0.312
4300	4093	333	1658	0.306
4400	4168	375	1625	0.300
4500	4232	416	1602	0.296
4600	4302	461	1577	0.291
4700	4371	505	1552	0.286
4800	4438	549	1529	0.282
4900	4499	598	1517	0.280
5000	4558	650	1510	0.279
5100	4630	702	1490	0.275
5200	4689	761	1490	0.275
5300	4745	822	1495	0.276
5400	4807	891	1502	0.277
5500	4863	961	1516	0.280
5600	4933	1018	1503	0.277
5700	4984	1078	1512	0.279
5800	5048	1165	1535	0.283
5900	5098	1246	1566	0.289
6000	5164	1321	1575	0.291
6100	5214	1397	1601	0.296
6200	5270	1449	1597	0.295
6300	5315	1584	1687	0.311
6400	5375	1695	1738	0.321
6500	5425	1732	1725	0.318
6600	5478	1733	1673	0.309
6700	5528	1958	1848	0.341
6800	5578	2065	1905	0.352
6900	5621	2069	1866	0.344
7000	5677	2069	1810	0.334
7100	5732	2206	1892	0.349
7200	5772	2385	2031	0.375
7300	5818	〃	1985	0.366
7400	5862	〃	1941	0.358
7500	5911	2401	1908	0.352
7600	5960	〃	1859	0.343
7700	6007	〃	1812	0.334
7800	6057	〃	1762	0.325
7900	6102	〃	1717	0.317
8000	6149	〃	1670	0.308
8100	6192	〃	1627	0.300
8200	6242	〃	1577	0.291
8300	6290	〃	1529	0.282
8400	6330	〃	1489	0.275
8500	6385	〃	1434	0.265
8600	6429	〃	1390	0.257
8700	6473	〃	1346	0.248
8800	6515	〃	1304	0.241
8900	6556	〃	1263	0.233
9000	6598	〃	1221	0.225
9100	6651	〃	1168	0.216
9200	6696	〃	1123	0.207

$M_R = M_o - M_D + M_I$, where $M_o = 5418$ kg, M_D is a discharged mass from the break, M_I is a total AIS injected mass but a mass discharged through PORVs is not accounted.

Table 4.2-2 Estimated secondary mass inventory in experiment SB-PV-03

Time (s)	M_A (kg)	M_A/M_0 (－)	M_B (kg)	M_B/M_0 (－)
0	2552.1	1.000	2555.9	1.000
500	2345.4	0.919	2405.7	0.941
1000	2076.1	0.813	2125.3	0.832
1500	2064.4	0.809	2294.2	0.898
2000	2111.1	0.827	2496.6	0.977
2500	2254.5	0.883	2691.4	1.053
3000	2132.5	0.836	2642.8	1.034
3500	1903.0	0.746	2371.6	0.928
4000	1699.4	0.666	2123.5	0.831
4500	1514.7	0.594	1860.7	0.728
5000	1354.5	0.531	1630.0	0.638
5500	1202.8	0.471	1425.7	0.558
6000	1073.0	0.420	1248.5	0.488
6500	952.7	0.373	1089.6	0.426
7000	836.6	0.328	939.5	0.368
7500	700.2	0.274	778.3	0.305
8000	562.4	0.220	619.1	0.242
8500	434.8	0.170	465.8	0.182
9000	298.2	0.117	373.0	0.146
9500	234.2	0.092	322.2	0.126
10000	208.9	0.082	293.8	0.115
Accuracy	±65.8 [kg]		±66.6 [kg]	

Table 4.2-3 Correction of RV steam flow rates in experiment SB-PV-03

Time Range (s)	SG-A Secondary System				SG-B Secondary System			
	Decrease of Mass ΔM (kg)	Supplied AFW Mass M_F (kg)	Disch. St. Mass M_D (kg)	Correc. St. Mass M_D^* (kg)	Decrease of Mass ΔM (kg)	Supplied AFW Mass M_F (kg)	Disch. St. Mass M_D (kg)	Correc. St. Mass M_D^* (kg)
1000 - 1500	11.7	294.9	329.1	283.0	-168.9	373.9	235.9	210.0
1500 - 2000	- 46.7	299.0	259.4	213.3	-202.4	378.3	205.3	179.4
2000 - 2500	-143.4	297.9	247.1	201.0	-194.8	381.7	186.4	160.5
2500 - 3000	122.0	146.2	298.7	252.6	48.6	189.9	277.2	251.3
3000 - 3500	229.5	-	320.0	273.9	271.2	-	341.2	315.3
3500 - 4000	203.6	-	259.1	213.0	248.1	-	303.8	277.9
4000 - 4500	184.7	-	225.7	179.6	262.8	-	280.5	254.6
4500 - 5000	160.2	-	209.0	162.9	230.4	-	264.1	238.2
5000 - 5500	151.7	-	197.7	151.6	204.6	-	244.1	218.2
5500 - 6000	129.8	-	182.7	136.6	177.2	-	213.5	187.6
6000 - 6500	120.3	-	166.2	120.1	158.9	-	192.3	166.4
6500 - 7000	116.1	-	159.5	113.4	150.1	-	177.5	151.6
7000 - 7500	136.4	-	179.3	133.2	161.2	-	162.8	136.9
7500 - 8000	137.8	-	173.6	127.5	159.2	-	152.9	127.0
8000 - 8500	127.6	-	159.2	113.1	153.3	-	154.3	128.4
8500 - 9000	136.6	-	187.1	141.0	92.8	-	98.6	72.8
Total	1777.9	1038.1	3553.1	2816.0	1752.3	1323.8	3490.4	3076.1
Accuracy	±65.8	±25	±35		±66.6	±25	±35	

$\Sigma \Delta M_j = \Sigma M_{Dj}^* - \Sigma M_{Fj}$, j=A, B.
$M_{Dj}^* = M_{Dj} - C$, C＝46.07 kg for SG-A, 25.90 kg for SG-B, respectively.

Table 4.2-4 Primary-to-secondary heat transfer coefficients at two SGs

(1) Heat transfer coefficient at SG-A U-tubes

Time Period (s)	Average Heat Trans. Rate*1 $Q_{UA}/\Delta t$ [kW]	Secondary Water Level L_{CA} [m]	Temperature Difference ΔT_A [K]	Average Heat Trans. Coef. h_{CA}[kW/K/m^2]
0- 500	4063.0	10.72*2	25.03	0.95
500-1000	1954.3	9.90*2	9.33	1.22
1000-1500	1080.9	9.14	3.72	1.83
1500-2000	845.5	9.41	2.85	1.82
2000-2500	908.1	9.60	2.27	2.40
2500-3000	844.9	9.57	2.05	2.48
3000-3500	612.5	9.05	1.82	2.07
3500-4000	467.4	8.11	1.58	2.10
4000-4500	367.2	7.11	1.55	1.92
4500-5000	401.8	6.22	1.62	2.30
5000-5500	335.2	5.43	1.76	2.03
5500-6000	363.5	4.73	1.81	2.45
6000-6500	268.2	4.11	2.14	1.76
6500-7000	315.5	3.55	2.88	1.78
7000-7500	361.3	2.96	3.80	1.86
7500-8000	416.7	2.31	8.09	1.28
8000-8500	358.9	1.75	15.23	0.78
8500-9000	481.4	1.19	23.39	1.00

$h_{Cj} = (Q_{Uj}/\Delta t) / (17.364 \times L_{Cj} \times \Delta T_j)$ [kW/K/m^2], j=A, B.

*1 Uncertainty of $(Q_{UA}/\Delta t)$ was estimated as ±242 kW.

*2 A total U-tube surface area is 171 m^2 for $L_{CB} \geqq 9.85$ m.

(2) Heat transfer coefficient at SG-B U-tubes

Time Period (s)	Average Heat Trans. Rate*3 $Q_{UB}/\Delta t$ [kW]	Secondary Water Level L_{CB} [m]	Temperature Difference ΔT_B [K]	Average Heat Trans. Coef. h_{CB}[kW/K/m^2]
0- 500	3256.0	10.15*2	23.77	0.80
500-1000	1063.0	9.65	8.62	0.74
1000-1500	924.9	9.43	3.66	1.55
1500-2000	1001.2	10.15*2	2.86	2.05
2000-2500	871.8	10.96*2	2.22	2.30
2500-3000	855.5	11.29*2	1.96	2.56
3000-3500	807.5	10.39*2	1.75	2.71
3500-4000	808.6	9.46	1.52	3.24
4000-4500	584.3	8.62	1.49	2.62
4500-5000	592.8	7.53	1.57	2.89
5000-5500	537.8	6.48	1.72	2.79
5500-6000	566.2	5.53	1.76	3.35
6000-6500	493.4	4.69	2.10	2.89
6500-7000	438.5	3.95	2.82	2.27
7000-7500	307.4	3.22	3.73	1.48
7500-8000	320.9	2.50	8.05	0.92
8000-8500	423.8	1.80	15.67	0.87
8500-9000	156.1	1.25	25.59	0.28

*3 Uncertainty of $(Q_{UB}/\Delta t)$ was estimated as ±256 kW.

Table 4.2-5 Energy removal at SGs and break compared to core power

Time Period (s)	Average Core Power Q_C*1 [kW]	Total Heat Tran. Rate*2 $Q_U/\Delta t$ [kW]	Ratio $\frac{Q_U/\Delta t}{Q_C}$	Break Flow Enthalpy*3 $Q_B/\Delta t$ [kW]	Ratio $\frac{Q_B/\Delta t}{Q_C}$
0- 500	6086	7319.0	1.20	2075.6	0.34
500-1000	1793	3017.3	1.68	1507.3	0.84
1000-1500	1495	2005.8	1.34	1320.8	0.88
1500-2000	1360	1846.6	1.36	1223.4	0.90
2000-2500	1261	1779.9	1.41	1093.0	0.87
2500-3000	1180	1700.4	1.44	985.0	0.83
3000-3500	1106	1420.0	1.28	914.6	0.83
3500-4000	1058	1276.0	1.21	811.4	0.77
4000-4500	1006	951.5	0.95	750.2	0.75
4500-5000	974	994.6	1.02	663.0	0.68
5000-5500	946	873.0	0.92	597.2	0.63
5500-6000	916	929.7	1.01	566.6	0.62
6000-6500	896	761.6	0.85	473.2	0.53
6500-7000	873	754.0	0.86	442.2	0.51
7000-7500	854	668.7	0.78	397.2	0.47
7500-8000	834	737.6	0.88	394.8	0.47
8000-8500	810	782.7	0.97	388.8	0.48
8500-9000	802	637.5	0.79	347.8	0.43

*1 Core power at middle time except for initial 1000s in which mean value of core powers at initial and final times was adopted.
*2 Uncertainty of ($Q_U/\Delta t$) was estimated as ±352 kW.
*3 $Q_B = \Delta M \times h'$ [kJ] : Average enthalpy of break flow with
h' : Saturated water enthalpy [kJ/kg] at average pressure and
ΔM : Discharged mass during each time period (Δt=500 s).

Table 4.2-6 Effects of metal stored heat release on SG heat removal estimation

Time Period (s)	SG-A Secondary System				SG-B Secondary System			
	$Q_{UA}/\Delta t$ [kW]	$\Delta Q_T/Q_{UA}$ [－]	$\Delta Q_W/Q_{UA}$ [－]	Q_L/Q_{UA} [－]	$Q_{UB}/\Delta t$ [kW]	$\Delta Q_T/Q_{UB}$ [－]	$\Delta Q_W/Q_{UB}$ [－]	Q_L/Q_{UB} [－]
1000-1500	1080.9	-0.043	0.107	0.028	924.9	-0.051	0.131	0.038
1500-2000	845.5	-0.046	0.138	0.033	1001.2	-0.038	0.109	0.033
2000-2500	908.1	-0.042	0.130	0.029	871.8	-0.043	0.138	0.036
2500-3000	844.9	-0.047	0.158	0.029	855.5	-0.047	0.146	0.034
3000-3500	612.5	-0.062	0.174	0.038	807.5	-0.047	0.136	0.034
3500-4000	467.4	-0.078	0.247	0.047	808.6	-0.046	0.134	0.032
4000-4500	367.2	-0.090	0.286	0.056	584.3	-0.064	0.185	0.041
4500-5000	401.8	-0.084	0.156	0.049	592.8	-0.060	0.185	0.038
5000-5500	335.2	-0.104	0.182	0.057	537.8	-0.067	0.164	0.040
5500-6000	363.5	-0.076	0.208	0.051	566.2	-0.058	0.108	0.036
6000-6500	268.2	-0.103	0.276	0.067	493.4	-0.056	0.119	0.040
6500-7000	315.5	-0.076	0.224	0.055	438.5	-0.054	0.175	0.044
7000-7500	361.3	-0.088	0.188	0.047	307.4	-0.103	0.311	0.060
7500-8000	416.7	-0.053	0.175	0.039	320.9	-0.069	0.152	0.056
8000-8500	358.9	-0.062	0.106	0.044	423.8	-0.055	0.177	0.041
8500-9000	481.4	-0.055	0.138	0.032	156.1	-0.114	0.326	0.106

Refer metal stored heats and SG heat removal rate in Section 4.2.2 (2).

Table 4.2-7 Estimation of condensed water flows from two SGs

Time Period (s)	Primary Pressure [MPa]	Total Heat Trans. Rate $Q_U/\Delta t$ [kW]	Condensed Water Flow W_C*1 [kg/s]	Sat. Steam Flow Rate V_S*2 [m^3/s]
1000-1500	7.806	2005.8	1.38	0.033
1500-2000	6.780	1846.6	1.21	0.034
2000-2500	5.965	1779.9	1.13	0.037
2500-3000	5.248	1700.4	1.05	0.039
3000-3500	4.604	1420.0	0.85	0.037
3500-4000	4.044	1276.0	0.75	0.037
4000-4500	3.549	951.5	0.54	0.031
4500-5000	3.100	994.6	0.56	0.036
5000-5500	2.676	873.0	0.48	0.036
5500-6000	2.296	929.7	0.50	0.043
6000-6500	1.983	761.6	0.40	0.040
6500-7000	1.744	754.0	0.39	0.045
7000-7500	1.529	668.7	0.34	0.044
7500-8000	1.395	737.6	0.38	0.053
8000-8500	1.359	782.7	0.40	0.058
8500-9000	1.311	637.5	0.32	0.049

*1: $W_C = (Q_U / \Delta t) / q_L$, q_L :Average latent heat [kJ/kg].
Uncertainty of W_C was estimated as ± 0.24 kg/s.

*2: $V_S = W_C / \rho''$, ρ'' :Average saturated steam density [kg/m^3].
Uncertainty of V_S was estimated as ± 0.037 m^3/s.

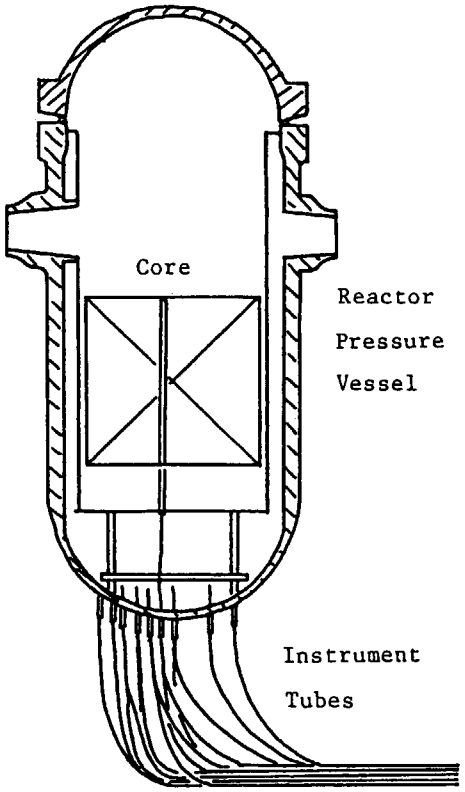

Fig. 1.1 Location of PWR instrument tubes

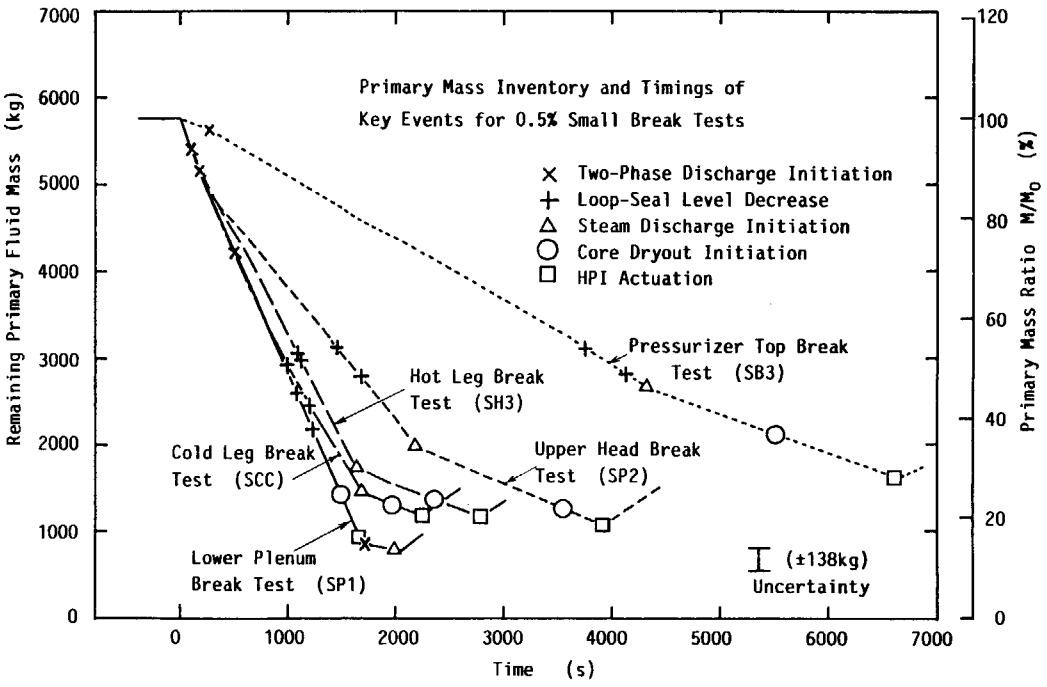

Fig. 1.2 Primary coolant mass inventory and key events of 0.5% break location parameter experiments (Ref. 9)

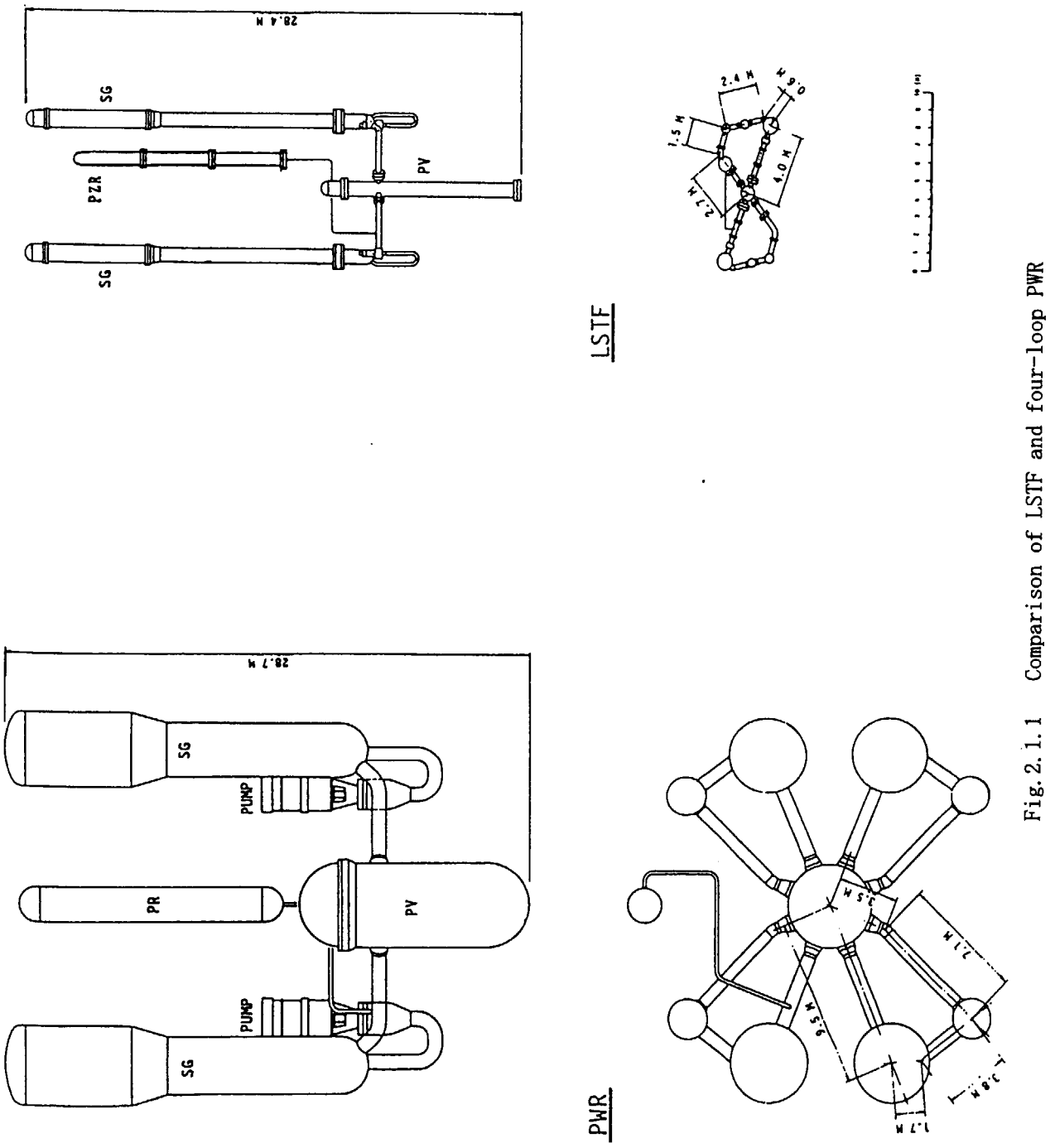

Fig. 2.1.1 Comparison of LSTF and four-loop PWR

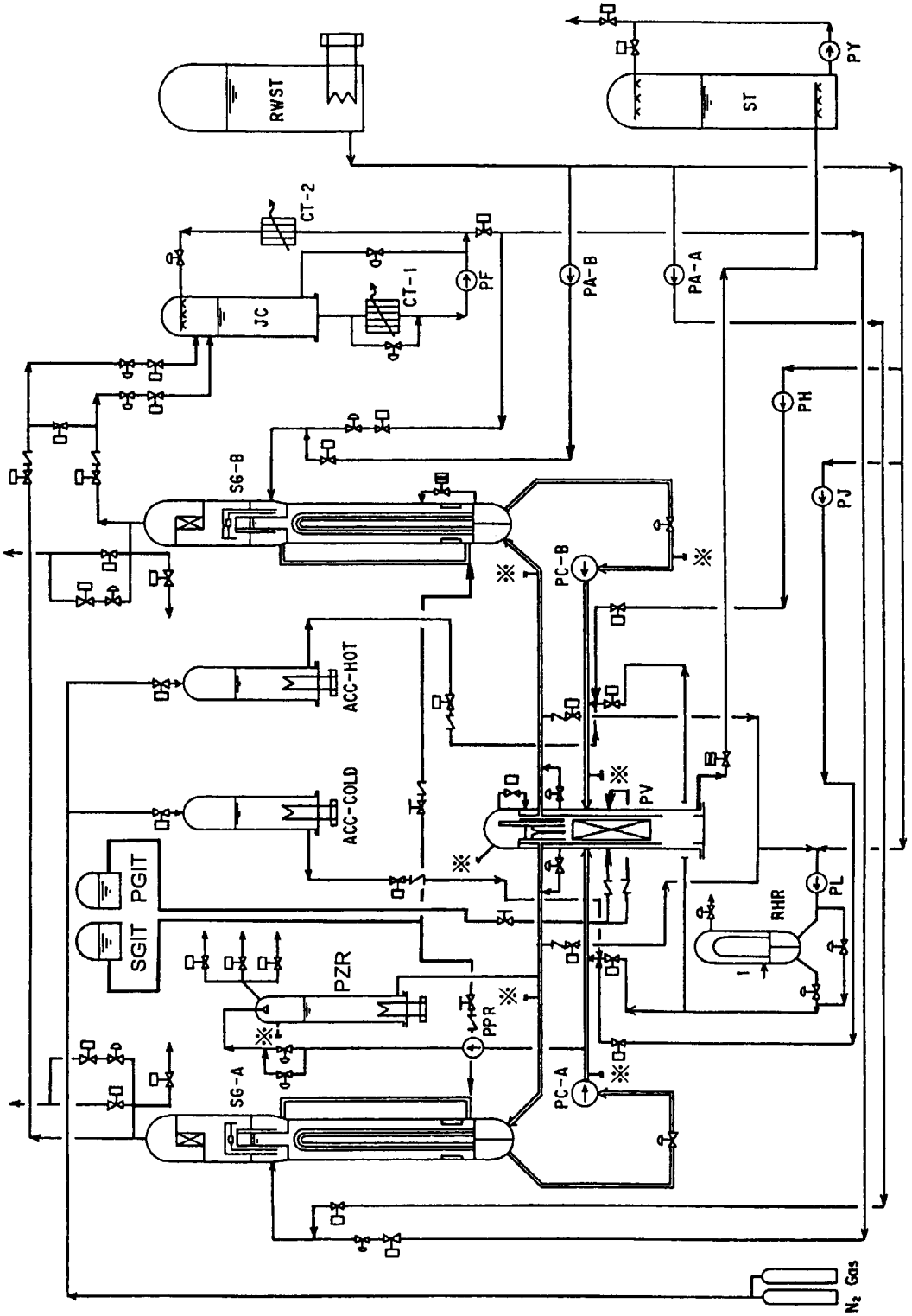

Fig. 2.1.2 Flow diagram of LSTF

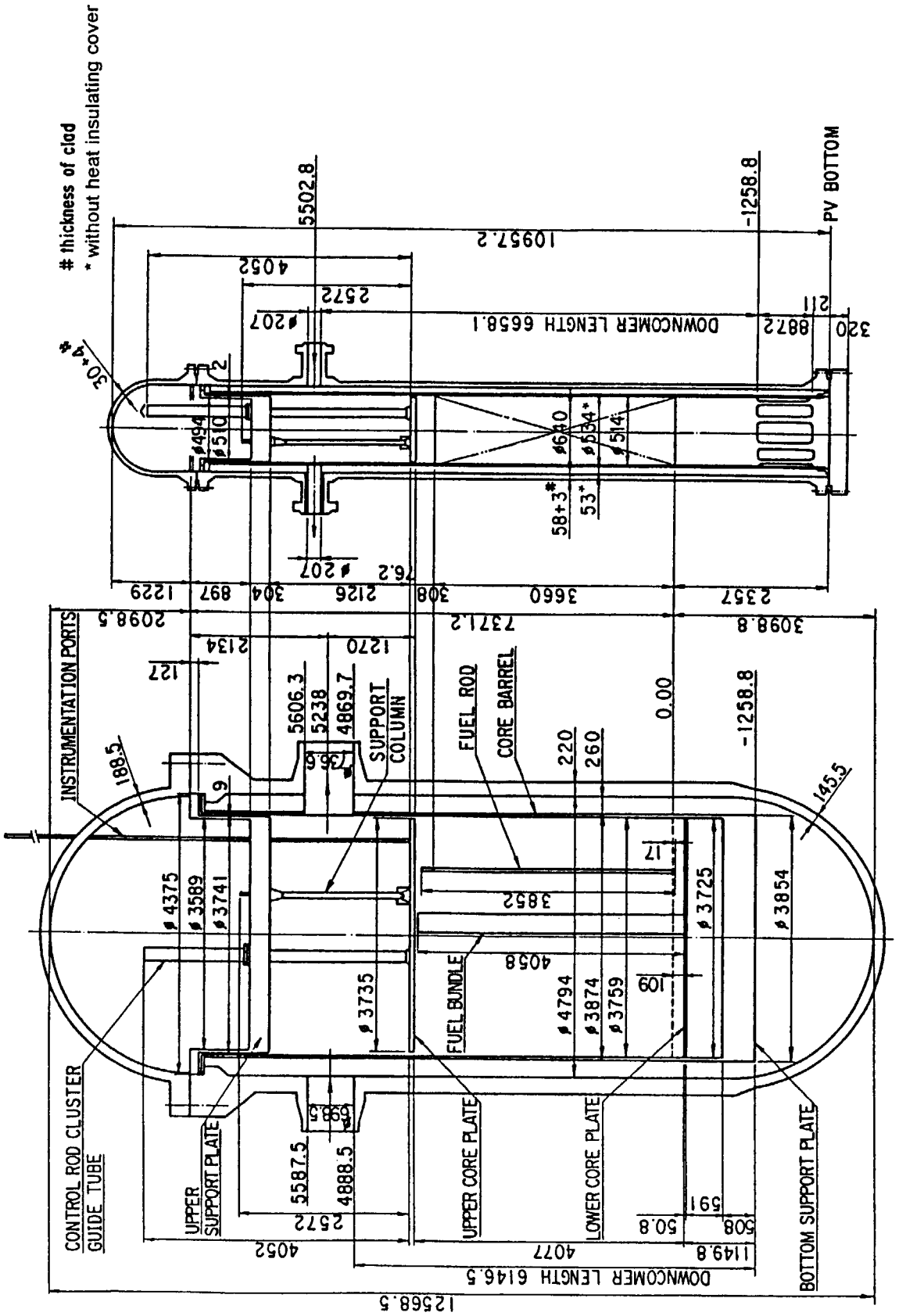

Fig. 2.1.3 Comparison of reactor vessel dimensions between LSTF and PWR

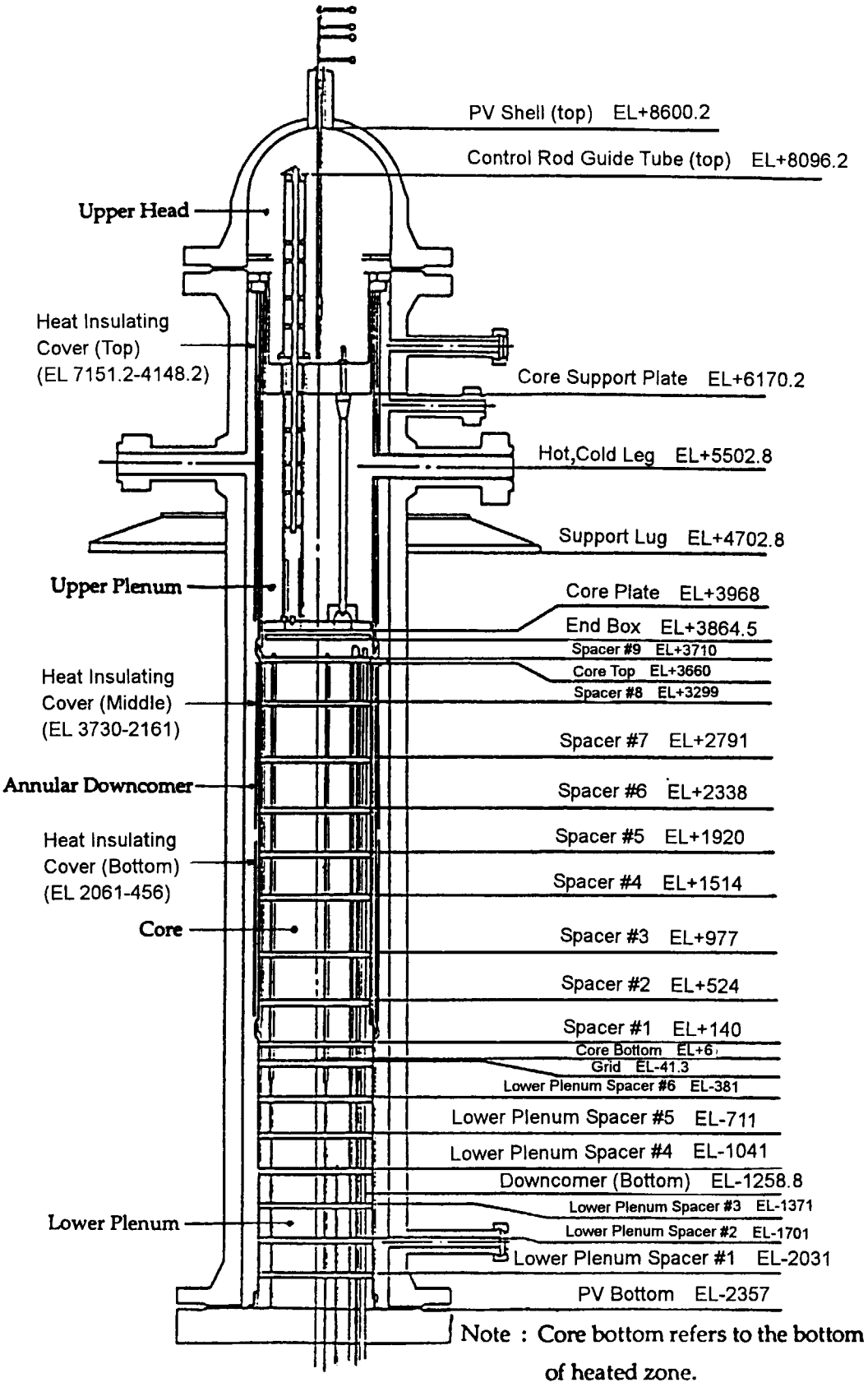

Fig. 2. 1. 4 LSTF Pressure vessel with internal assembly

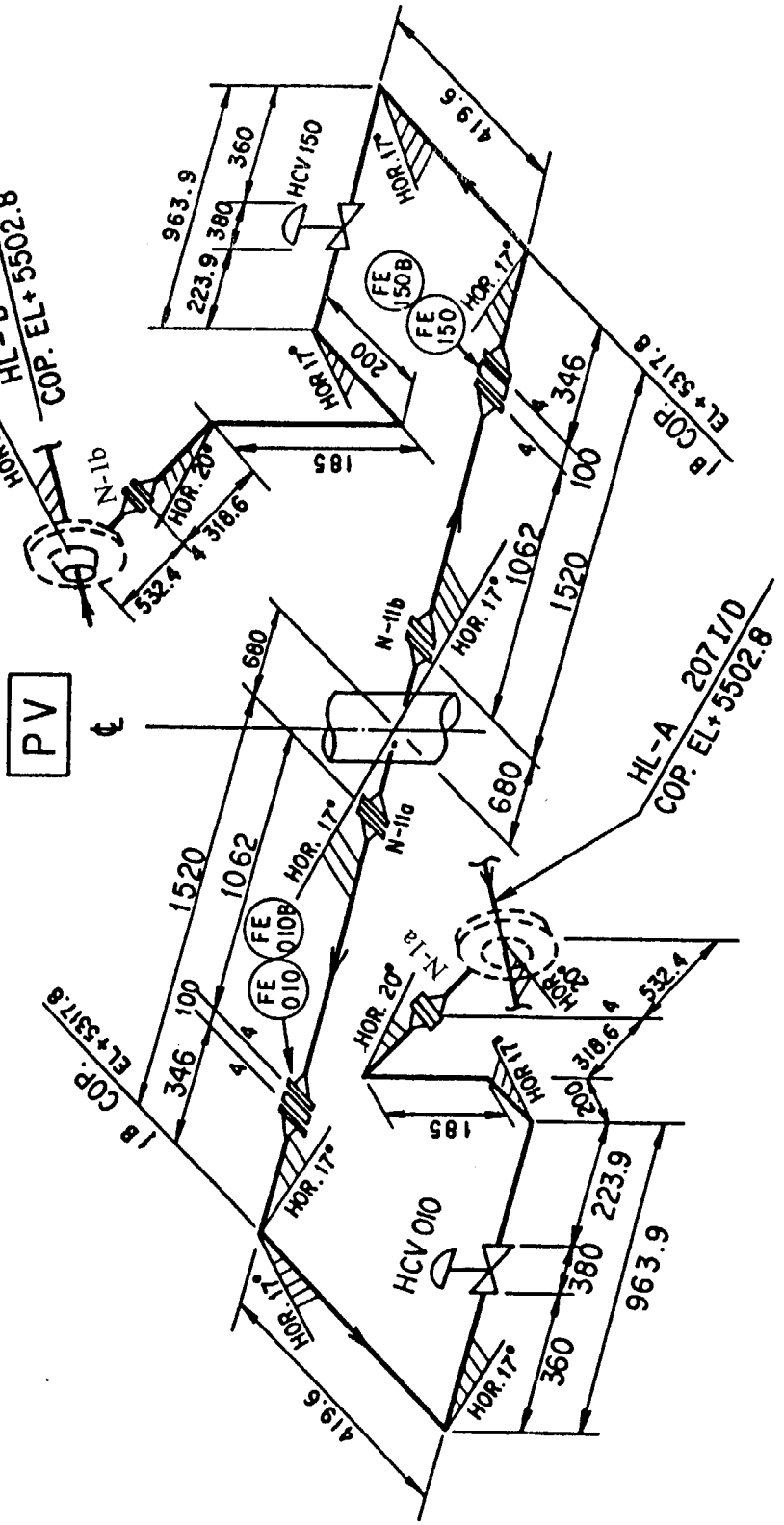

Fig. 2.1.5 Hot leg leak simulation lines

List of Nozzle at SG Vessel

Nozzle No.	Size	Nozzle Name	Location(direction*)
N-1	206 mm I.D.	P. Coolant Inlet Nozzle	SG Inlet Plenum(36.5)
N-2	168.2 mm I.D.	P. Coolant Outlet Nozzle	SG Outlet Plenum(143.5)
N-3	3B Sch.80	Feedwater Inlet Nozzle	EL+19761.4(326.5)
N-4	8B 〃	Steam Outlet Nozzle	Top of Steam Dome
N-5	2B 〃	Safety Valve Nozzle	〃 〃
N-6	4B 〃	FW Break Line	EL+19846.6(146.5)
N-7a-d	〃 〃	Downcomer Piping Nozzle	EL+19163.9(4, 69,184,249)
N-7e-h	〃 〃	Downcomer Piping Nozzle	EL+ 8843.9 (4, 69,184,249)
		(249° downcomer connected to GDIS)	
N-8	1/2B Sch.160	Vacuum Vent Nozzle	EL+ 7761.9(180)
N-9	1B Sch.80	Level Instrumentation Nozzle	EL+7843.9(180)

Nozzle No.	Size	Nozzle Name	Location(direction*)
N-10	4B Sch.160	U tube Break Nozzle	EL+6363.9(325)
		or Gas Vent Nozzle for SG-B	
N-11	1 1/2B Sch.80	U tube Break Nozzle	EL+ 7843.9(90)
N-21a	PT1/2	Air supply	EL+ 6263.9(36.5)
		or Vacuum Vent Nozzle	
N-22a	〃	Level Instrumentation Nozzle	Top of Steam Dome
N-22b	〃	〃 〃	EL+19161.4(216.5)
N-23a,b	〃	〃 〃	EL+18518.9(90, 270)
N-23c,d	6B Sch.80	〃 〃	EL+17663.9(90, 270)
N-23e,f	〃 〃	〃 〃	EL+17011.9(90, 270)
N-24	1 1/2B Sch.160	〃 〃	EL+19386.9(216.5)

*: The direction zero indicated -16.5° from P.N. for SG-A and 163.5° for SG-B, respectively.

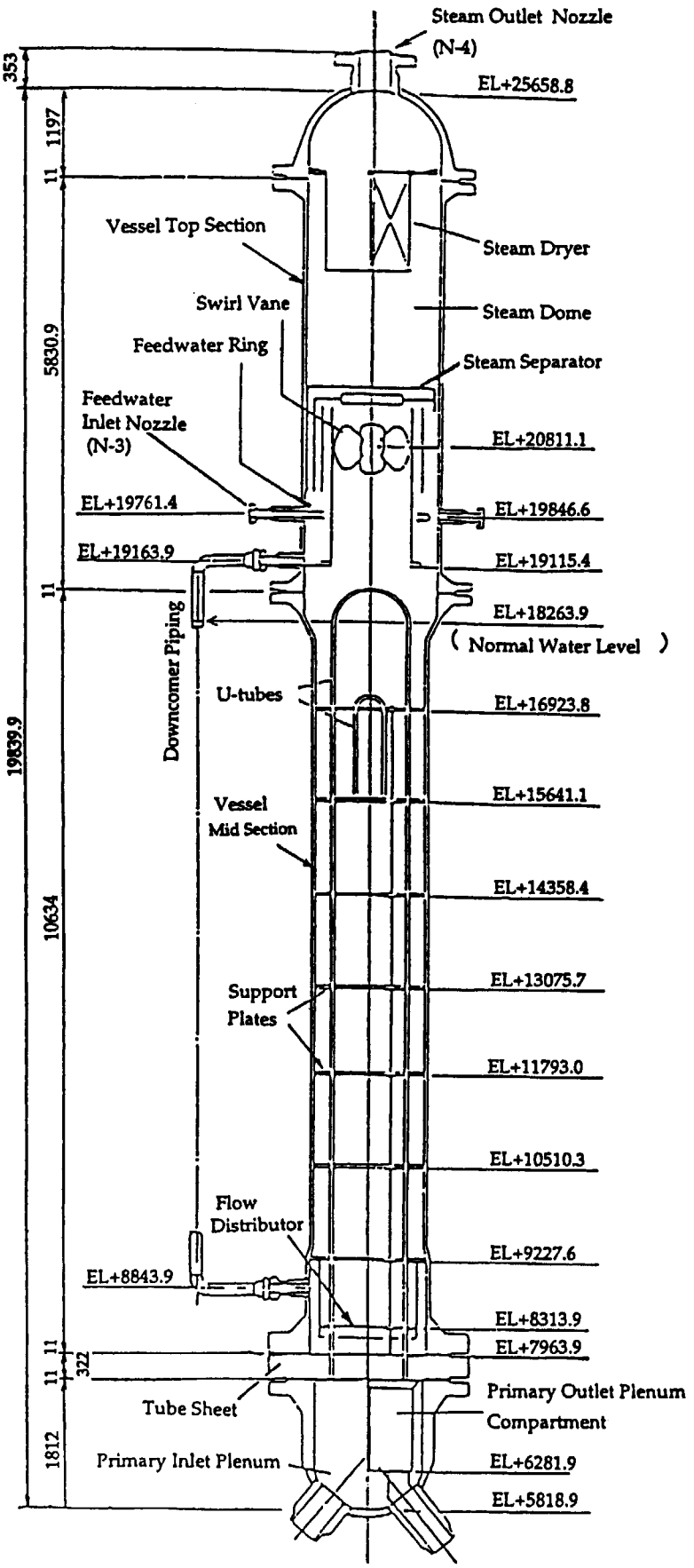

Fig. 2. 1. 6 Primary and secondary sides of steam generators (SG-A and SG-B)

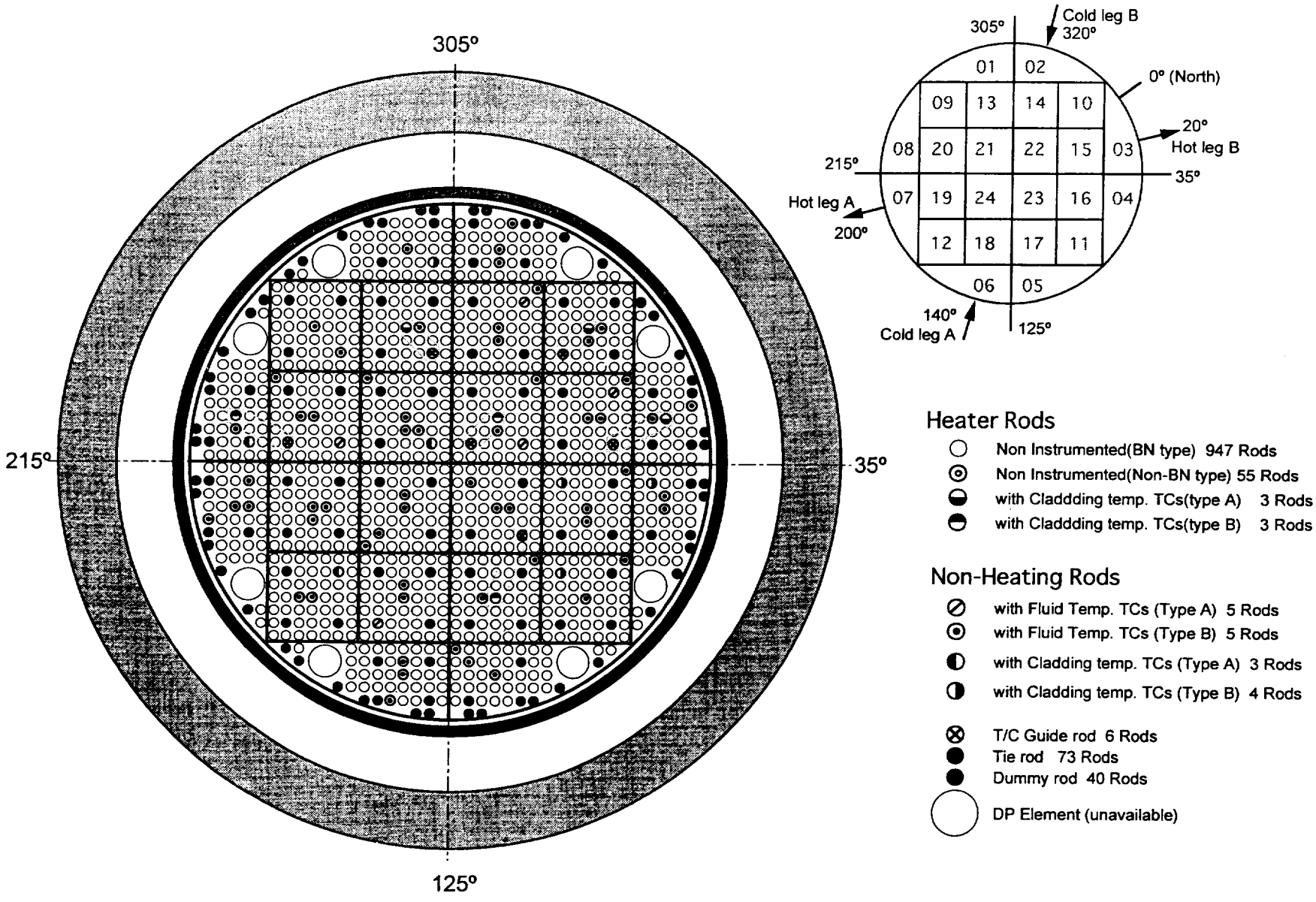

Fig. 2.1.7 Cross-section of core heater rod assembly

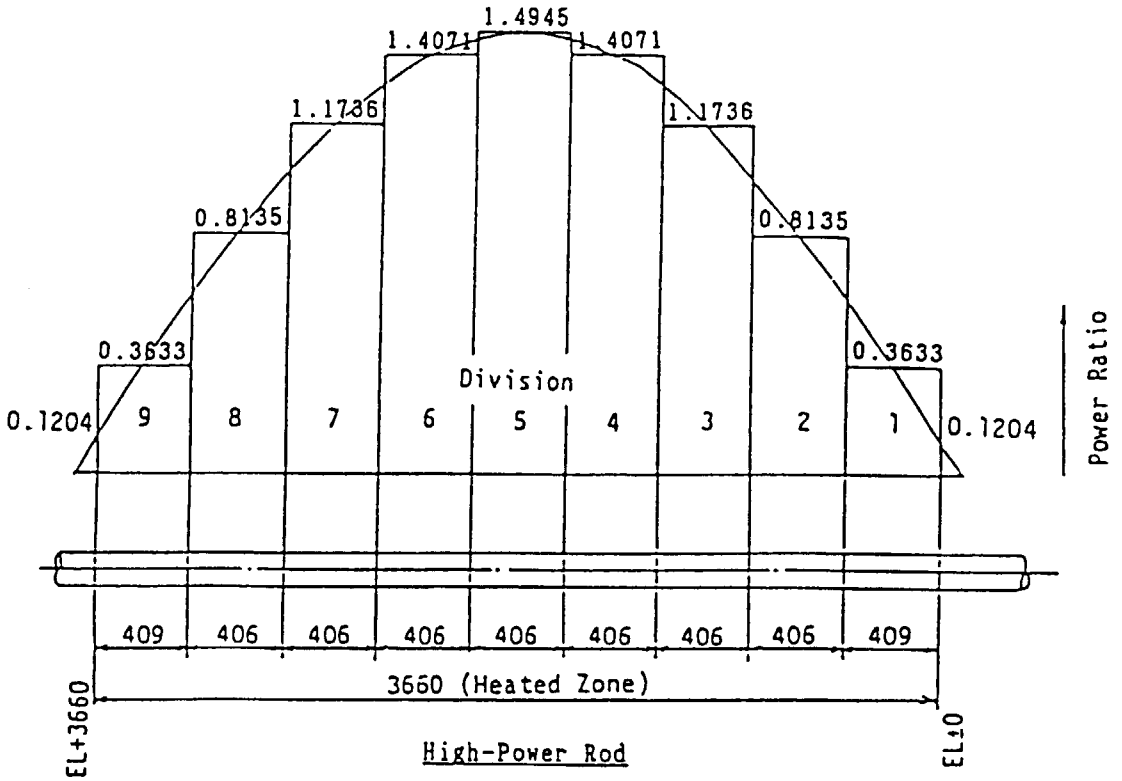

Fig. 2. 1. 8 Axial power distribution for high-power rod

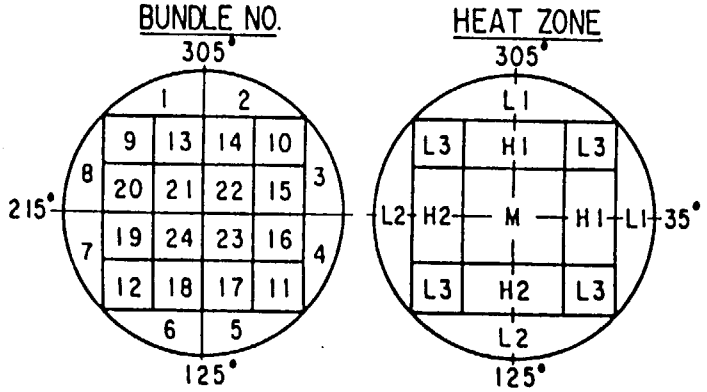

HEAT ZONE		MAX. HEATER OUTPUT (DESIGN VALUE)
LOW	L1 L3	11.0kW/ROD x468ROD= 5.148 MW
HIGH	H1 H2	16.6kW/ROD x360ROD= 5.976 MW
MEAN	M	11.0kW/ROD x180ROD= 1.980 MW
TOTAL		1008 ROD 13.104 MW

HEAT ZONE	PIECE	CASE 3	
		PEAK FACTOR	HEATER OUTPUT
L 1	144	0.66	9.69kW/ROD ×0.66×144 =921kW
L 2	144		9.69kW/ROD ×0.66×144 =921kW
L 3	180		9.69kW/ROD ×0.66×180 =1151kW
H 1	180	1.51	9.69kW/ROD ×1.51×180 =2634kW
H 2	180		9.69kW/ROD ×1.51×180 =2634kW
M	180	1.00	9.69kW/ROD ×1.00×180 =1744kW
TOTAL	1008	10.005MW	

Fig. 2. 1. 9 Radial core power distribution in experiment SB-PV-03

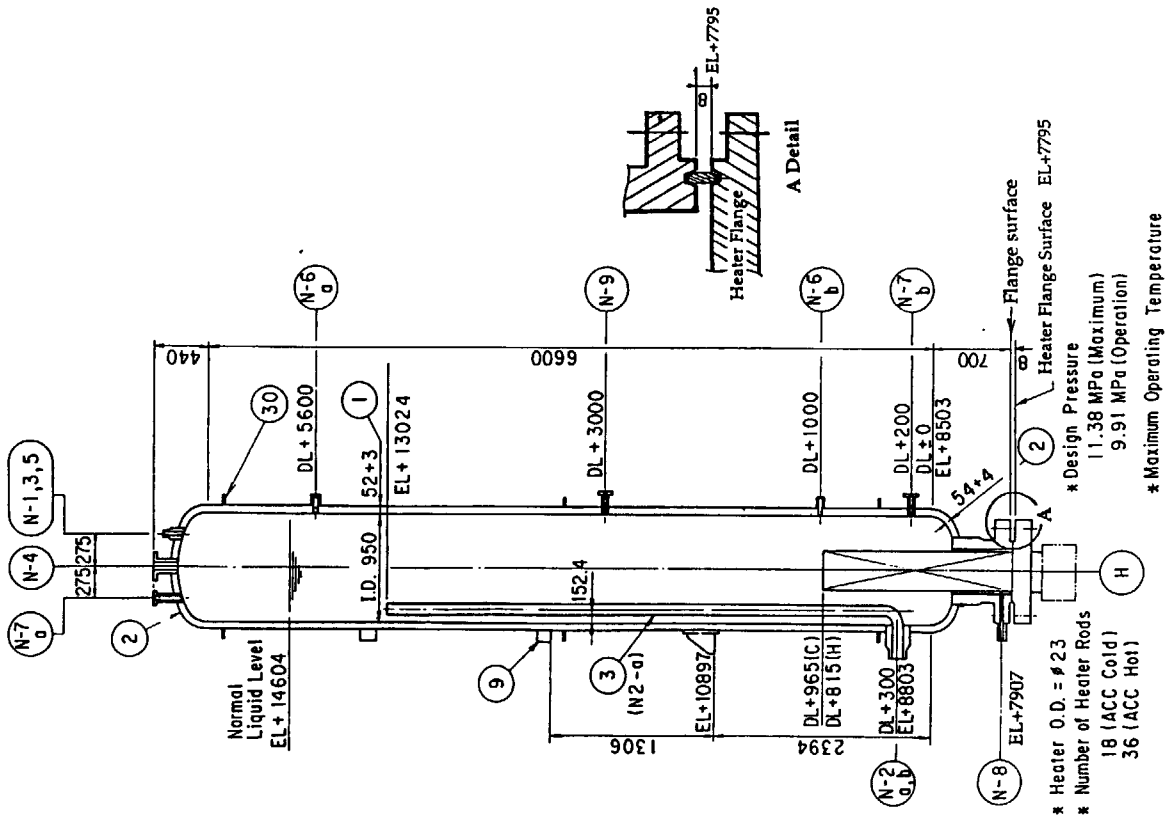

Location	Description	Material
1	Shell (I.D.950)	SB49+SUS316L Clad
2	Elliptical Head (2:1)	SB45+SUS316L Clad
3	Stand Pipe (Nozzle N2-a only)	4B Sch.20s
9	Name Plate	SS41
30	Ring	SS41

Location	Service of Nozzle	Size	Pipe Sch.
N-1	Liquid Inlet	1B	80
N-2a,b	Liquid Outlet	4B	80
N-3	N2 Gas Inlet	1B	80
N-4	Safety Valve Line	1 1/2B	80
N-5	Relief Valve Line	1B	80
N-6a	Thermometer	PT1/8	80
N-6b(ACH)	Dissolved Oxygen-gas Sampling	PT1/8	80
N-7a	Liquid Level Meter	1/2B	80
N-7b(ACC)	Dissolved Oxygen-gas Sampling	1/2B	80
N-8	Liquid Level Meter & Drain	1B	80
N-9	Pressure Gauge	1/2B	80
H	Heater Unit	18B	80

a) Liquid volume in the tank between the normal liquid level (EL 14604) and the stand pipe top level (EL 13024) is 1.120 m³ for ACC and ACH.

b) Tank gas volume above the normal water level is as follows.
0.4652 m³ for ACH
0.4644 m³ for ACC

Fig. 2. 1. 10 Accumulator tank geometry

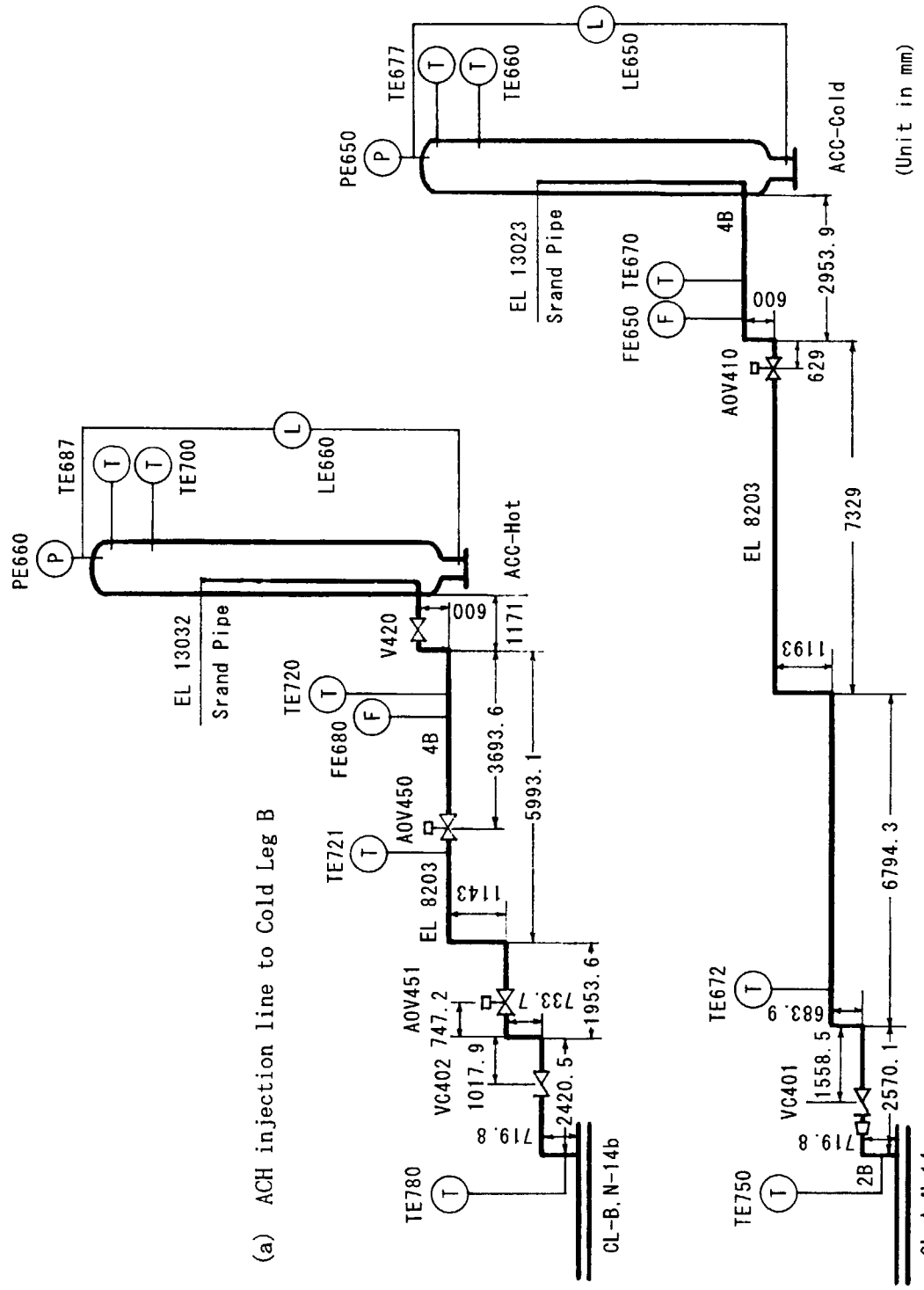

Fig. 2.1.11 Scheme of accumulator injection lines

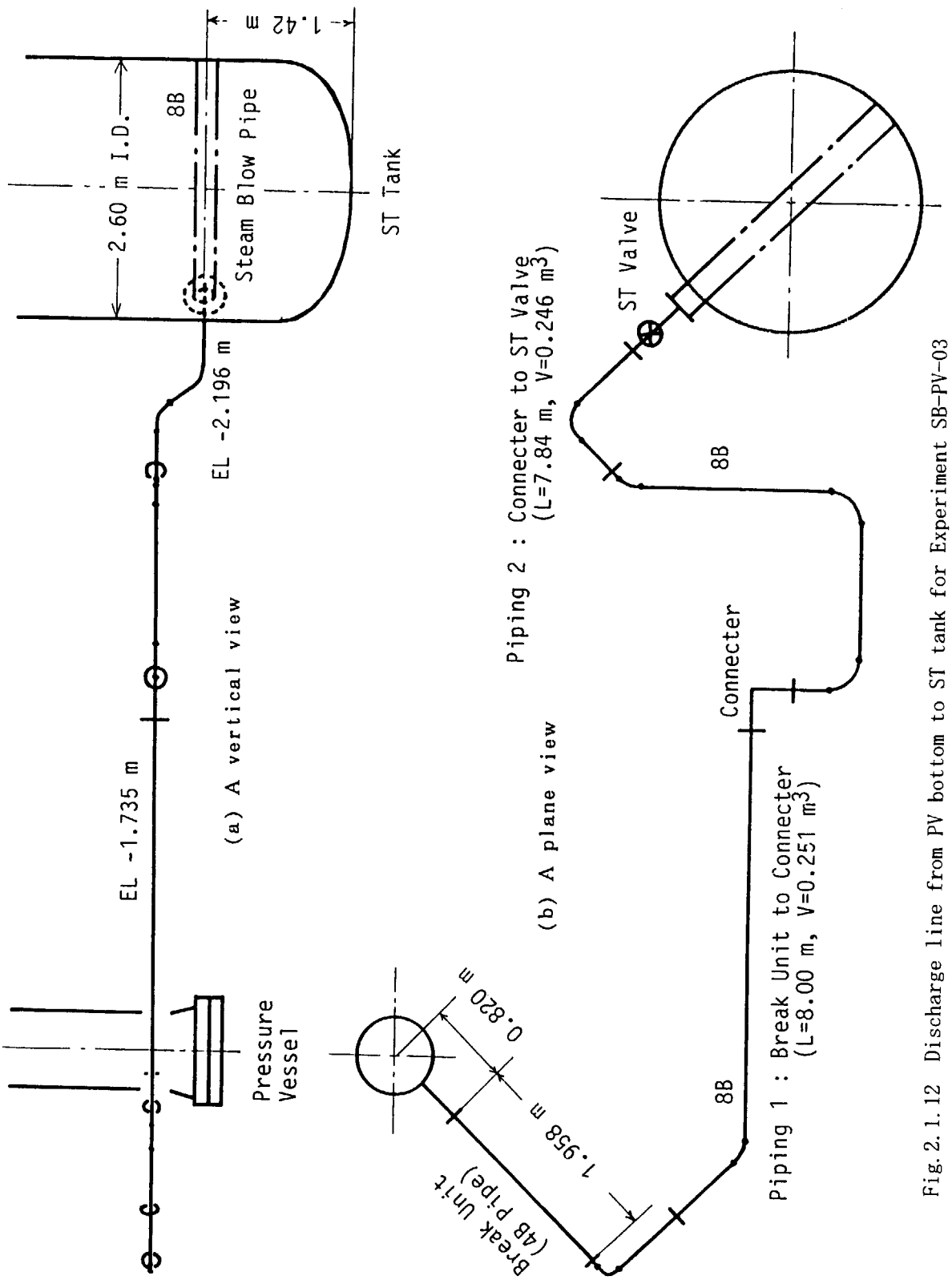

Fig. 2.1.12 Discharge line from PV bottom to ST tank for Experiment SB-PV-03

Location	Description	Material
1	Venturi Flow Meter	SUSF316
2	Spool Piece	SUS316L
3	R.O. Piece 1/2	SUS316L
4	R.O. Piece 2/2	SUS316L
5	Break Valve	SCS13

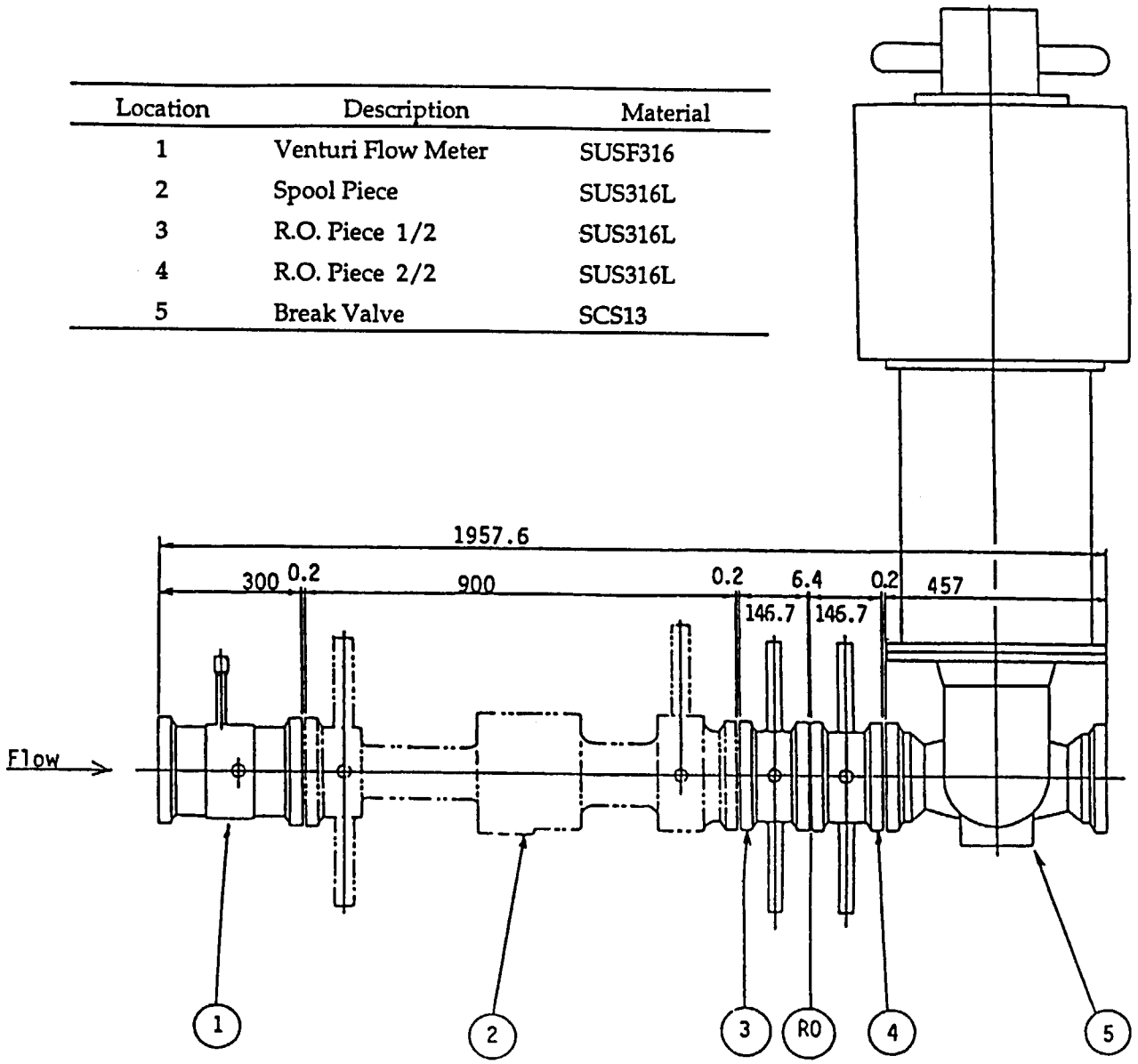

Fig. 3.2.1 Configuration and instrumentation of break unit

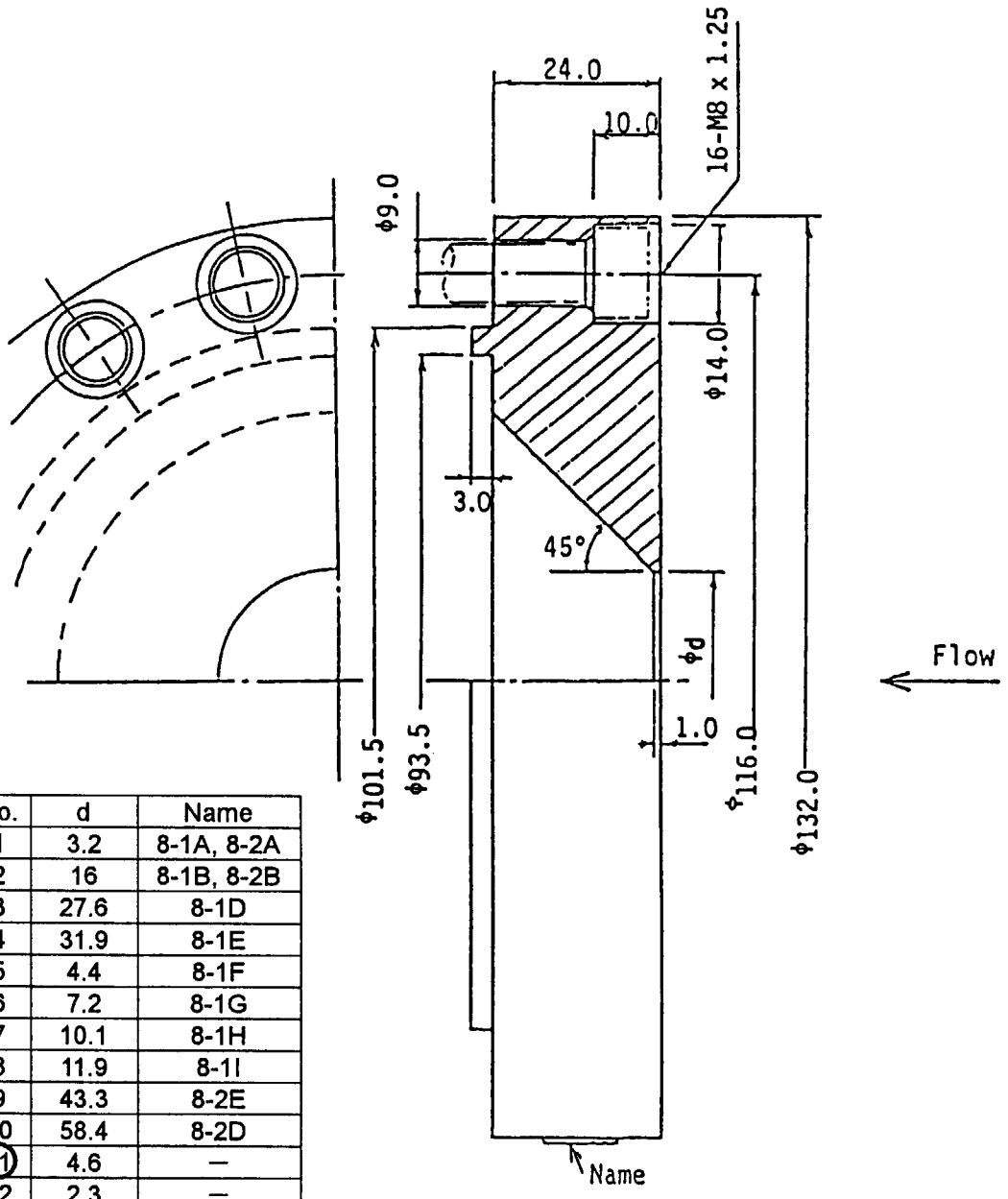

No.	d	Name
1	3.2	8-1A, 8-2A
2	16	8-1B, 8-2B
3	27.6	8-1D
4	31.9	8-1E
5	4.4	8-1F
6	7.2	8-1G
7	10.1	8-1H
8	11.9	8-1I
9	43.3	8-2E
10	58.4	8-2D
(11)	4.6	—
12	2.3	—
13	9.2	—
14	31.34	—
15	32.2	—
16	6.8	—
17	49.6	8-2C
18	35.82	—
19	13.8	—
20	18.4	—
21	22.5	8-1C

(Unit in mm)

Fig. 3. 2. 2 Geometry of break orifice

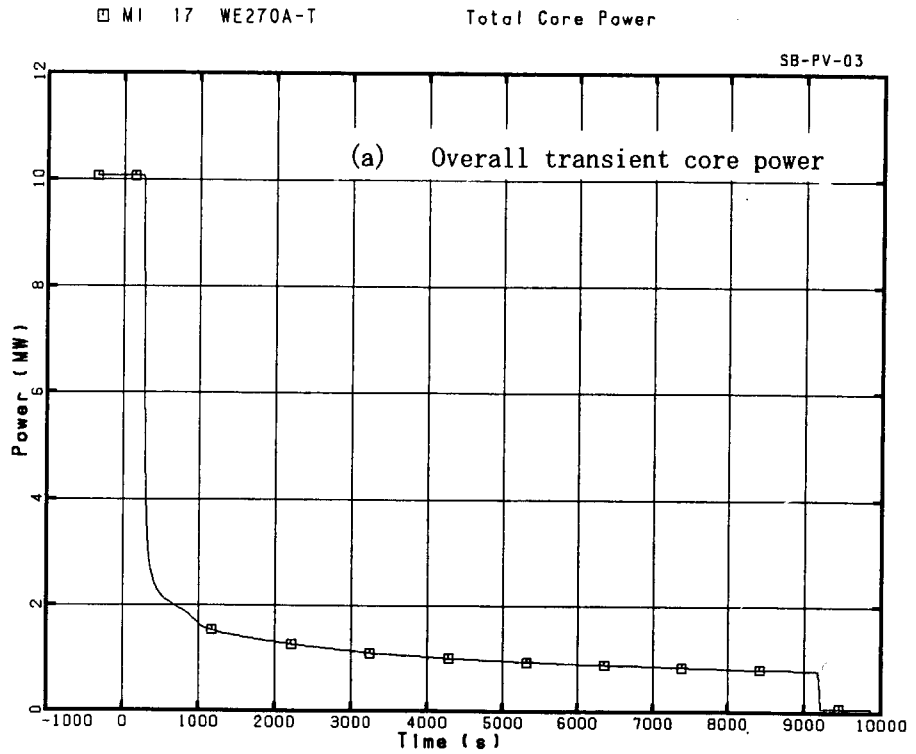

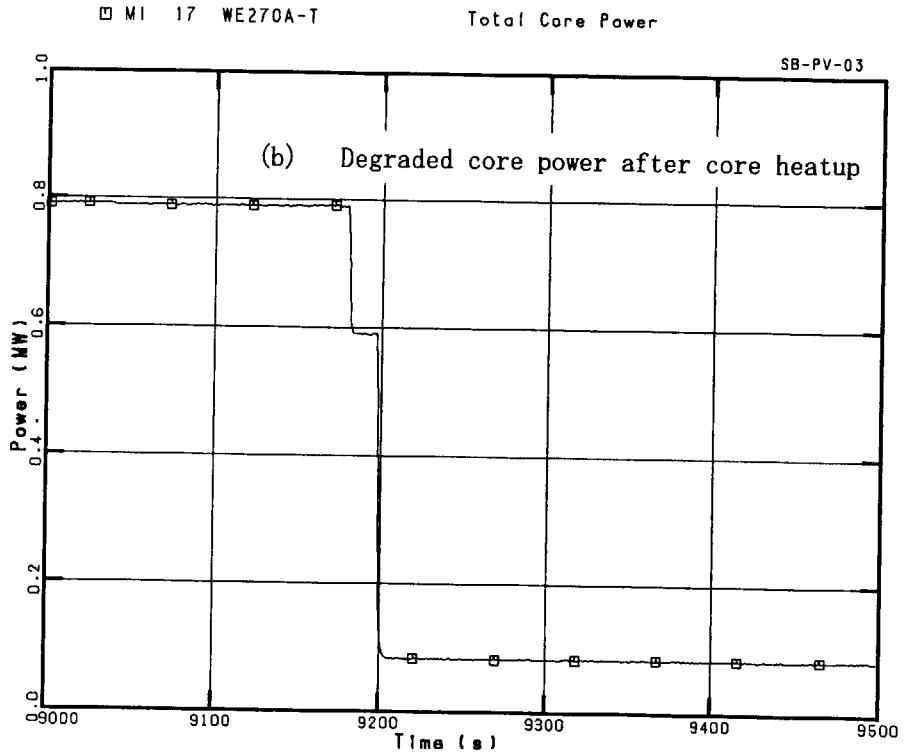

Fig. 3.2.3 Core power curve in experiment SB-PV-03

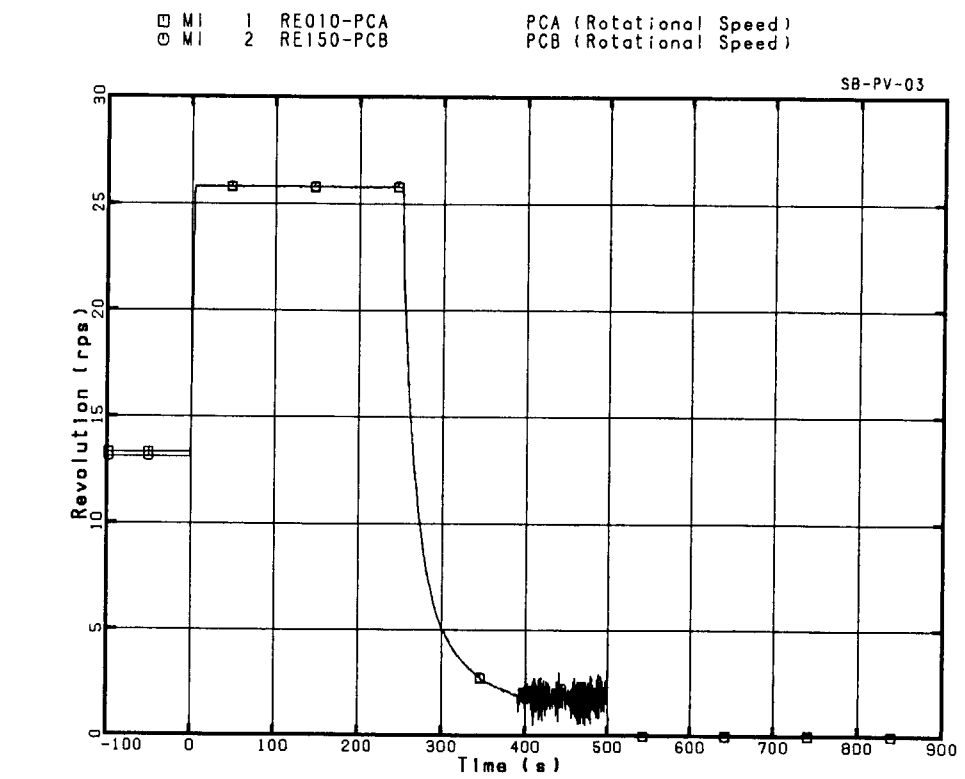

Fig. 3.2.4 Primary coolant pump speeds

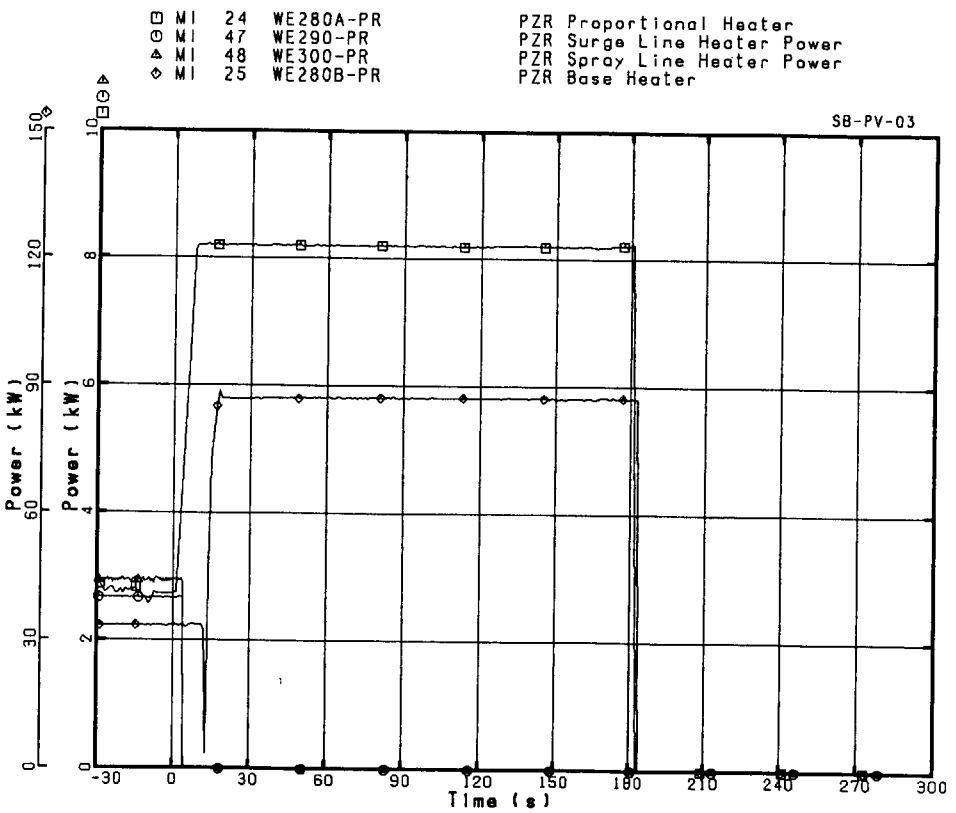

Fig. 3.2.5 Pressurizer heater powers

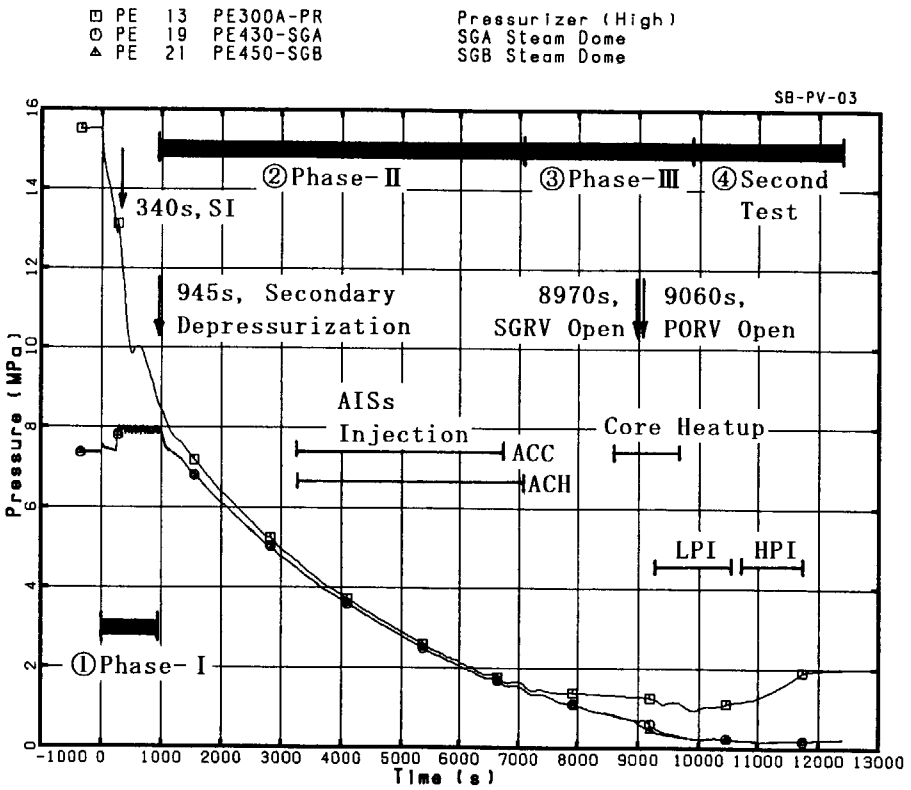

Fig. 4.1.1 Transient system pressures and major events in whole test period

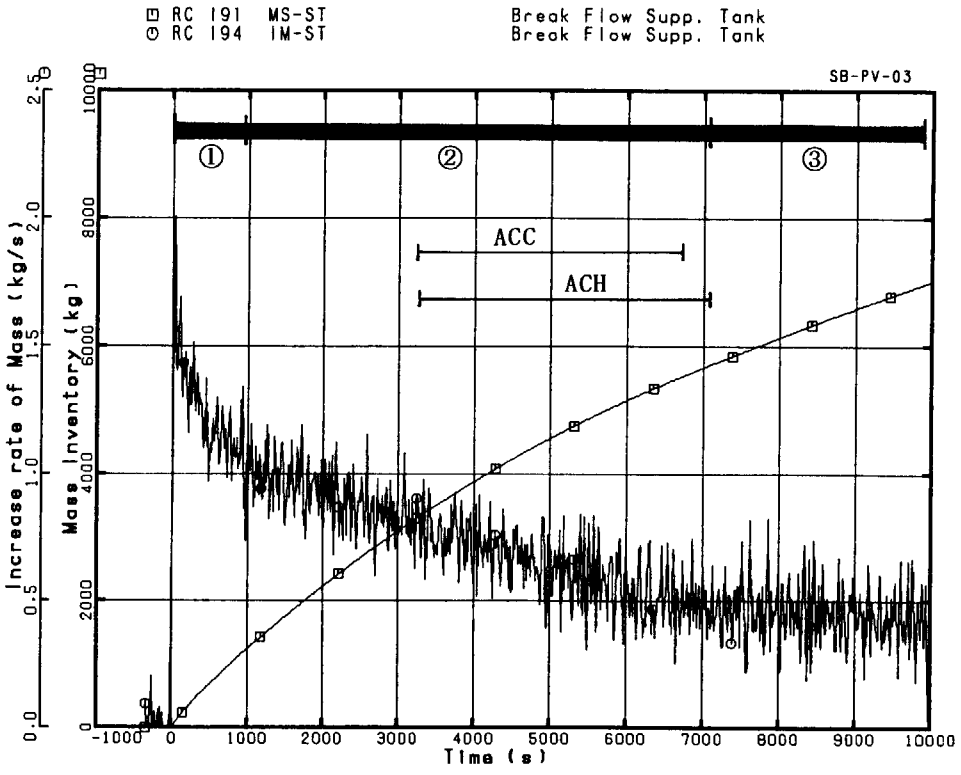

Fig. 4.1.2 Discharged mass and break flow rate in three test phases

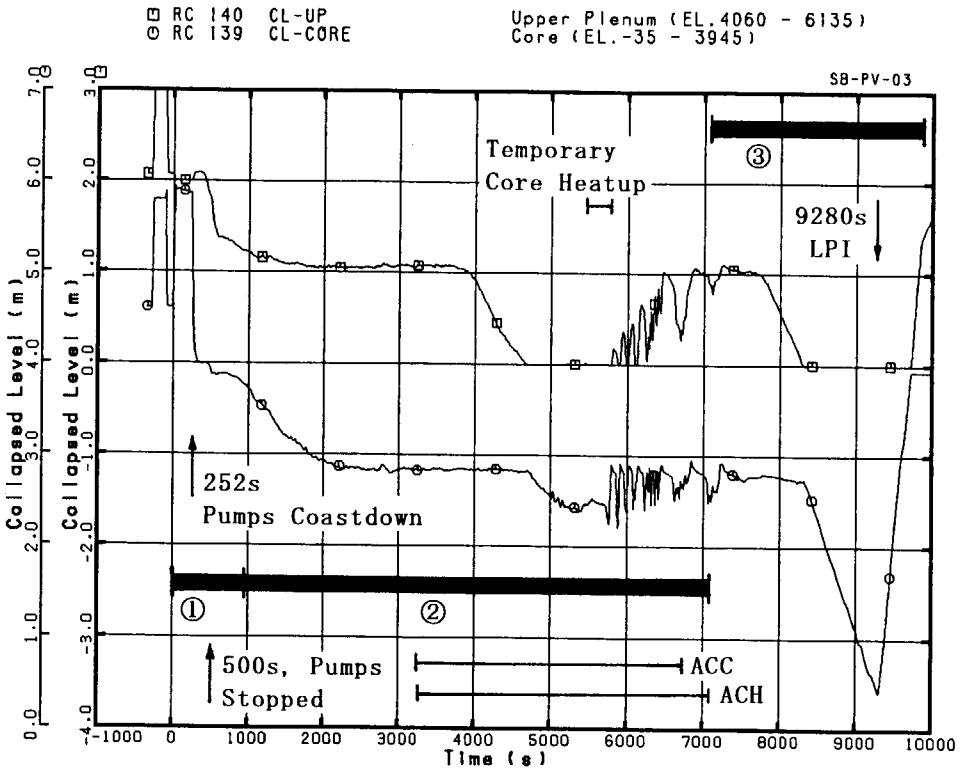

Fig. 4.1.3 Collapsed liquid levels in upper plenum and core in three test phases

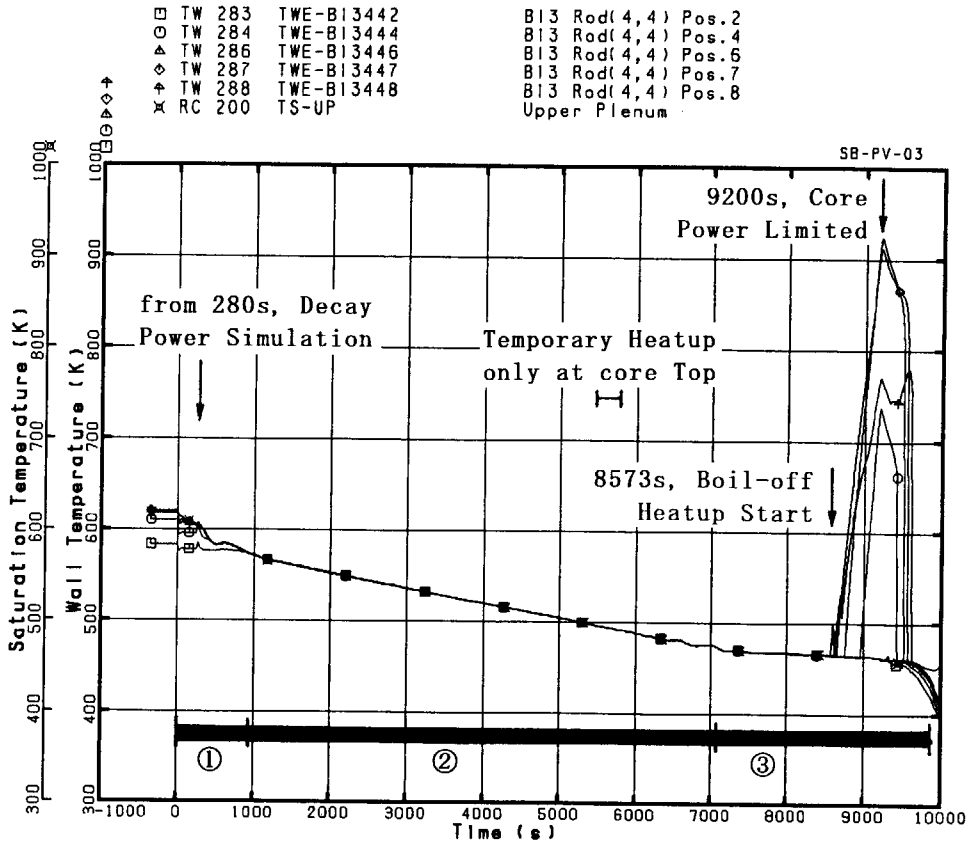

Fig. 4.1.4 Representative heater rod temperatures in three test phases

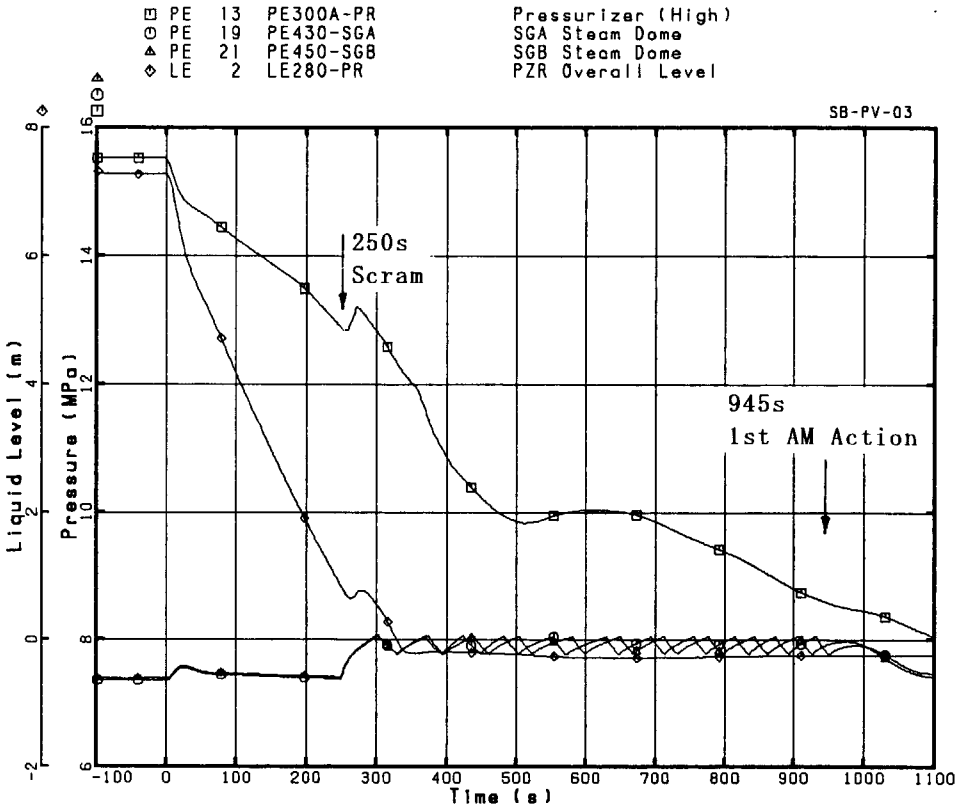

Fig. 4. 1. 5 Primary and secondary pressures and PZR level in early phase

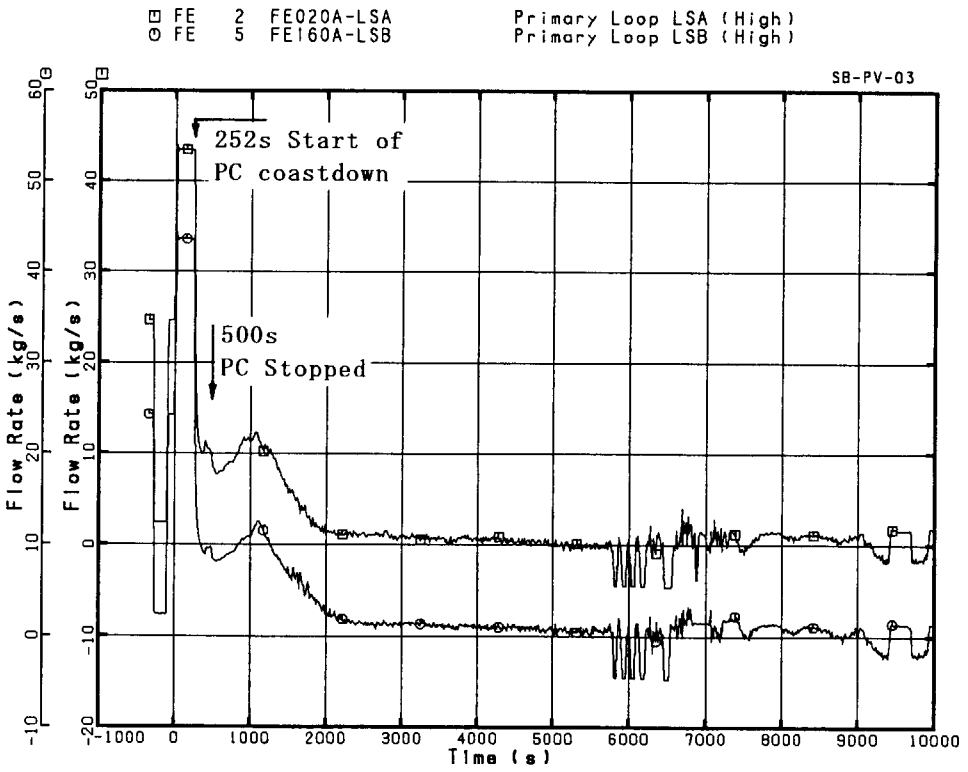

Fig. 4. 1. 6 Primary loop flow rates during test period

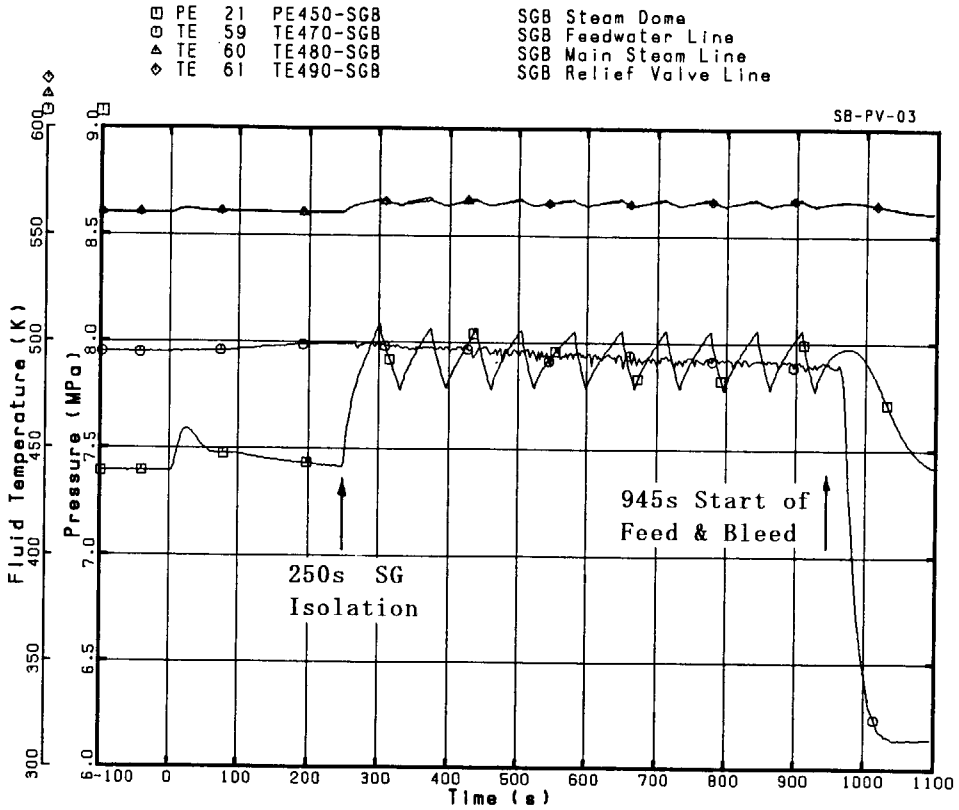

Fig. 4.1.7 Typical pressure and temperature responses at SG-B in early phase

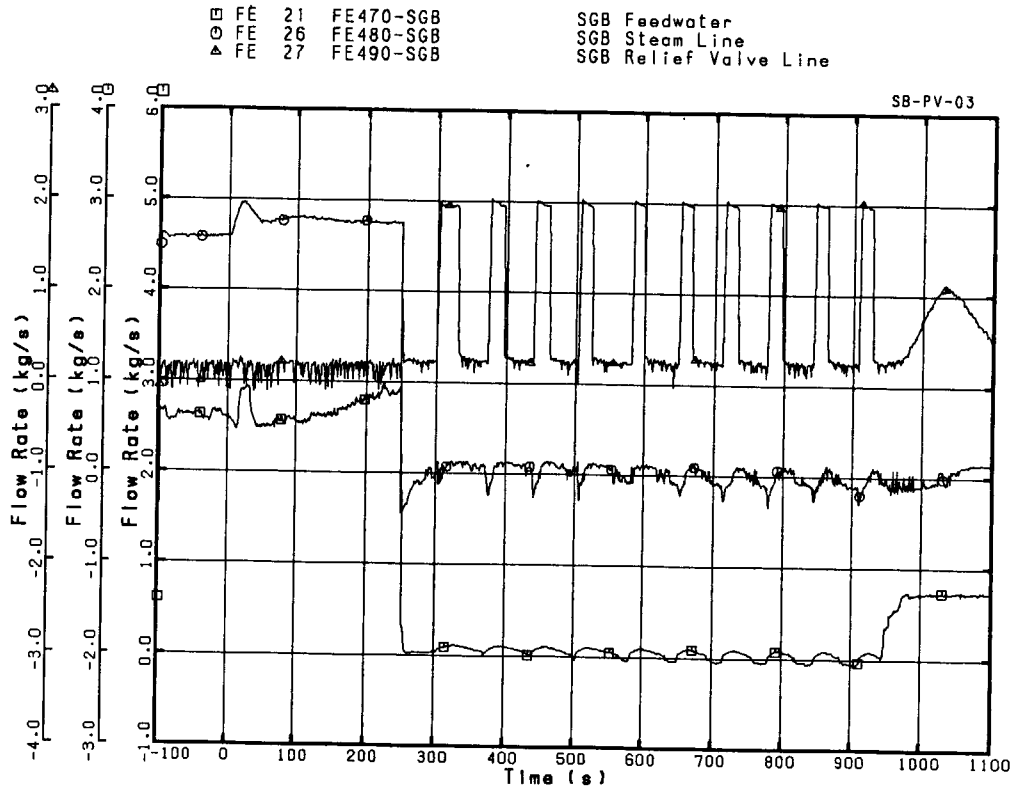

Fig. 4.1.8 Typical mass flow rates at SG-B feedwater, steam and RV lines

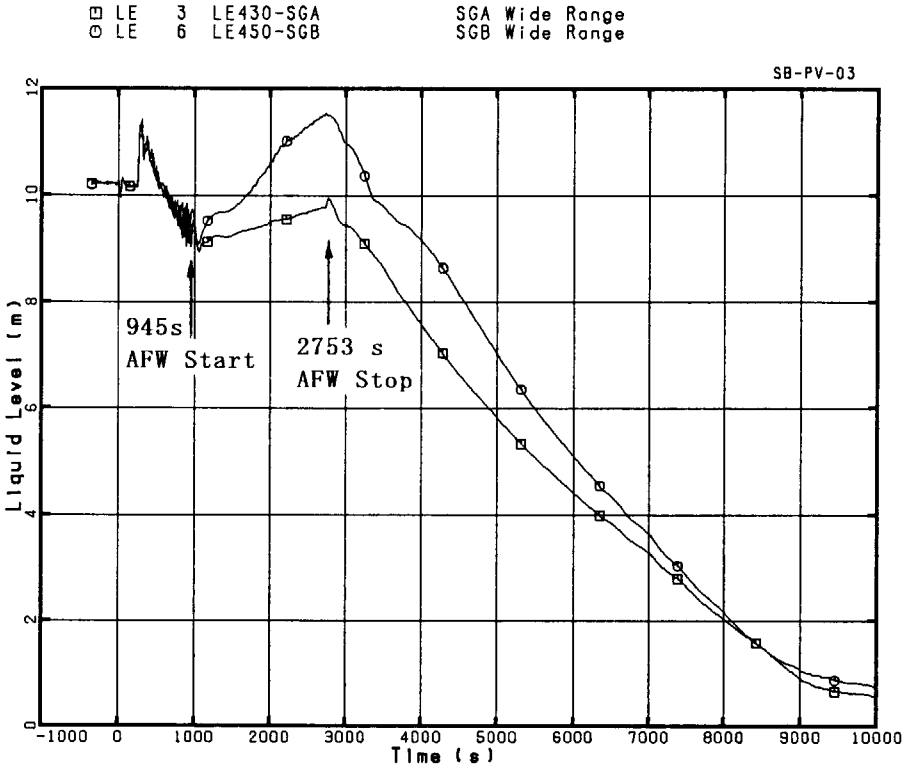

Fig. 4. 1. 9 Secondary water levels in two SGs during test period

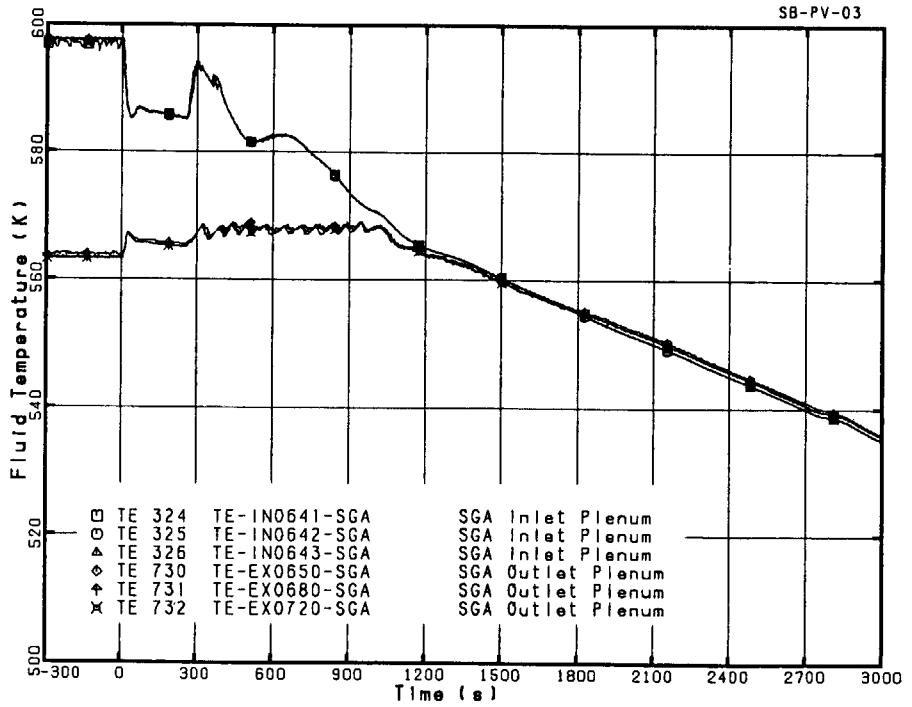

Fig. 4. 1. 10 Primary fluid temperatures at inlet and outlet plena of SG-A

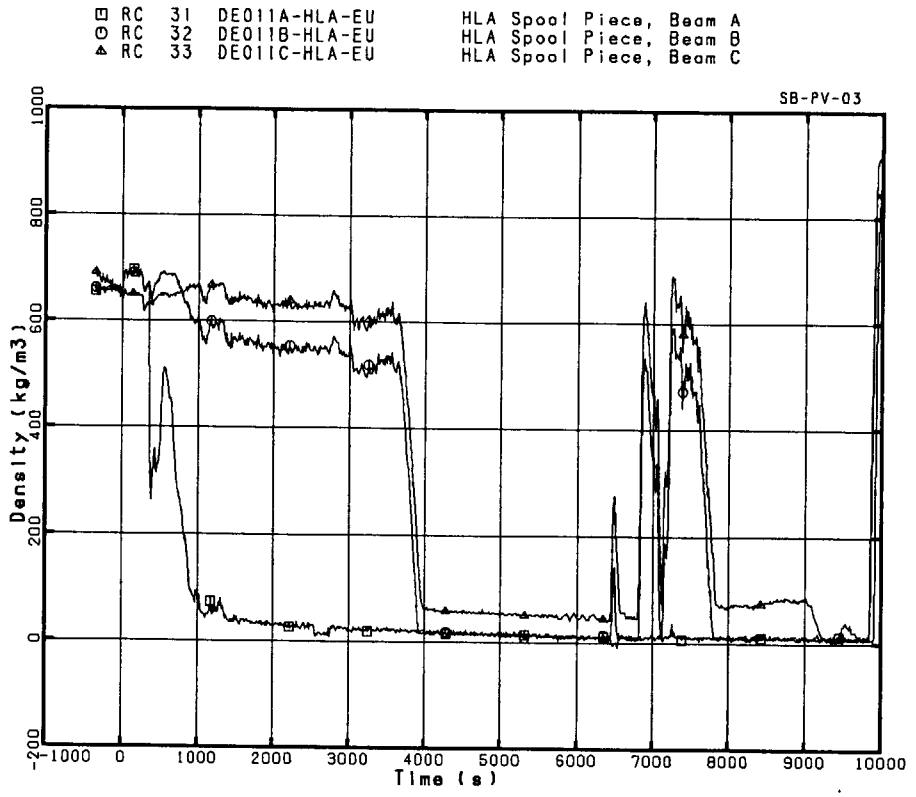

Fig. 4. 1. 11 Typical three-beam density data at hot leg A during test period

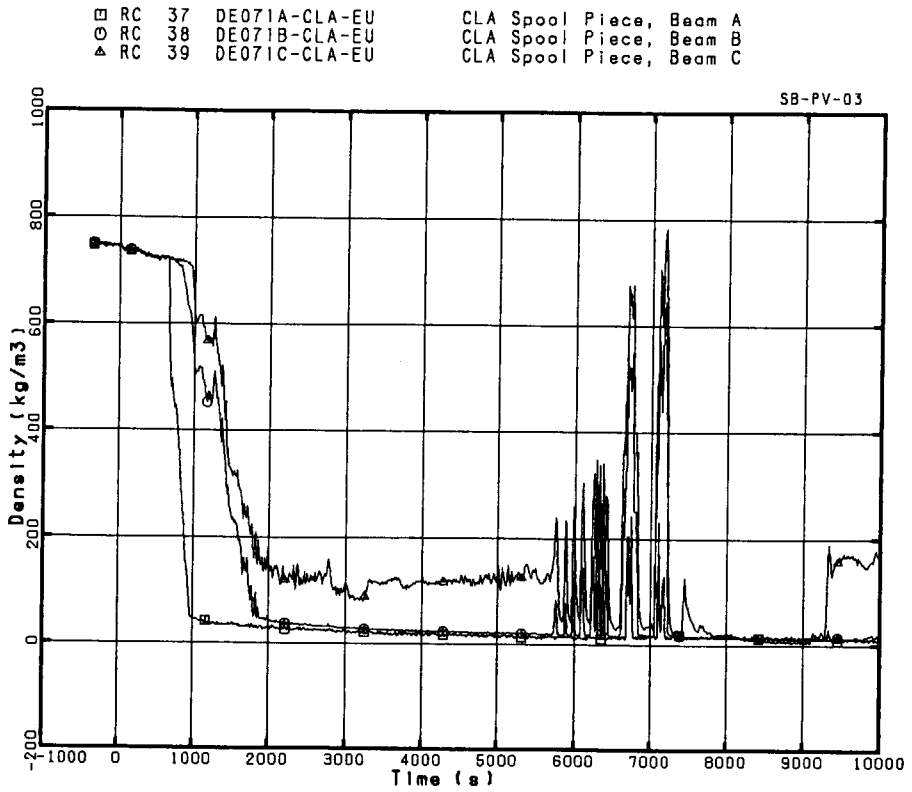

Fig. 4. 1. 12 Typical three-beam density data at cold leg A during test period

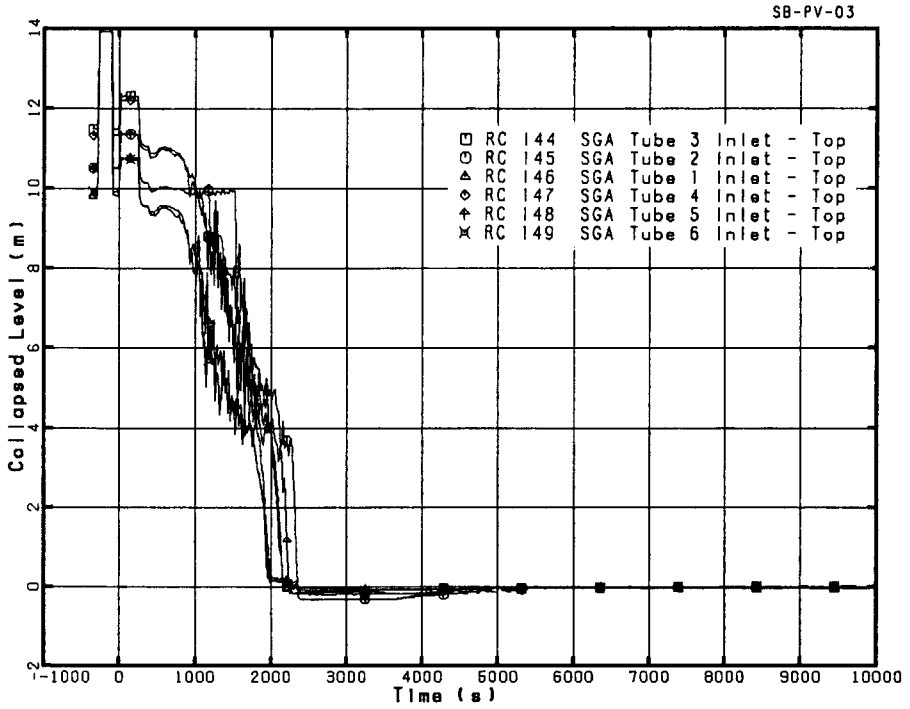

Fig. 4. 1. 13 Collapsed water levels in SG-A U-tube inlet sides

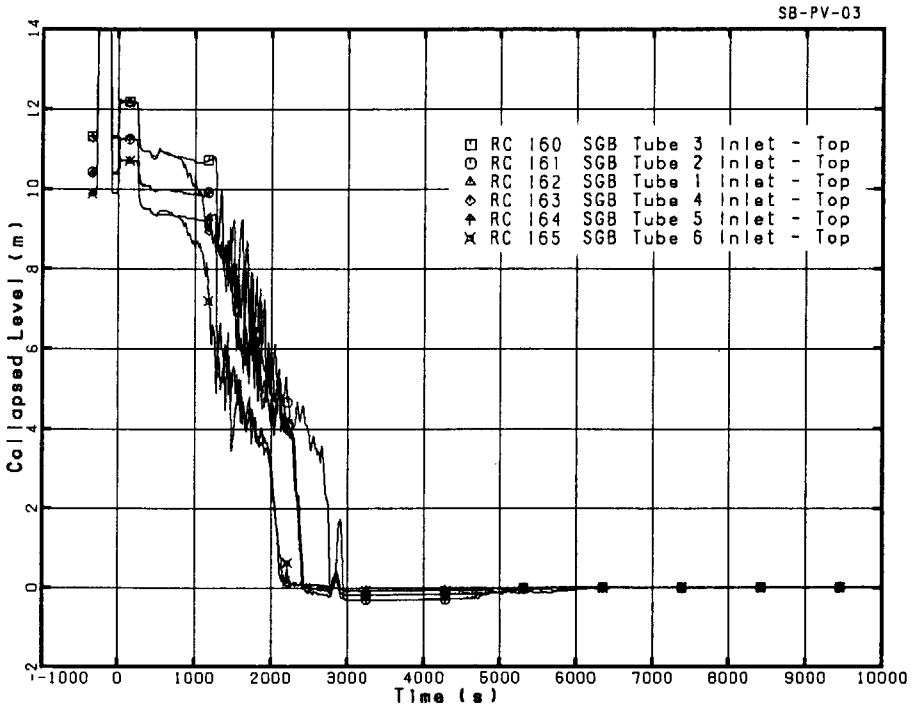

Fig. 4. 1. 14 Collapsed water levels in SG-B U-tube inlet sides

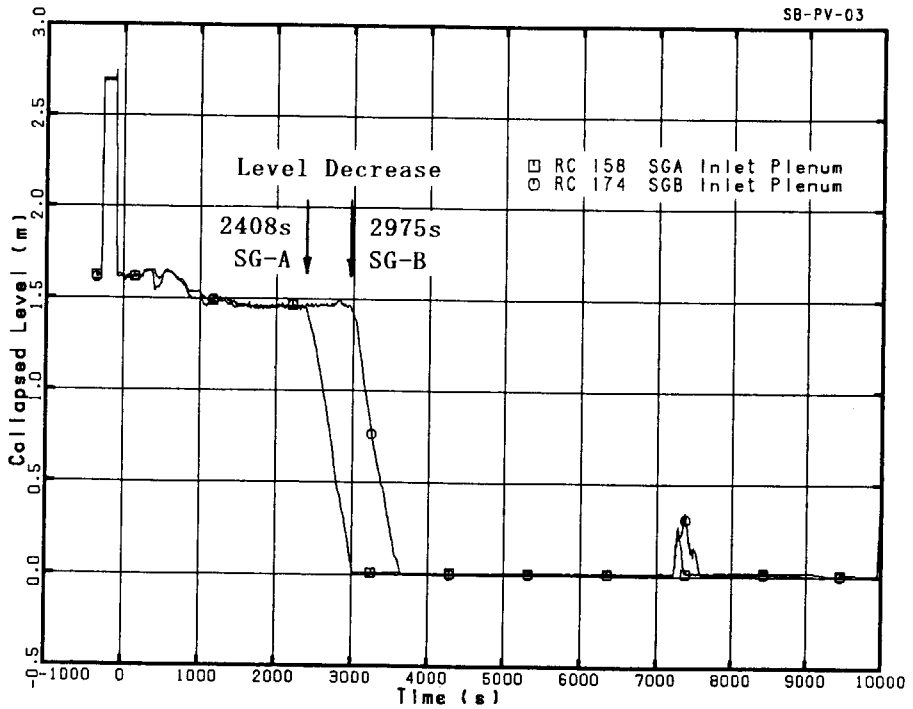

Fig. 4. 1. 15 Collapsed water levels in inlet plena of SG-A and SG-B

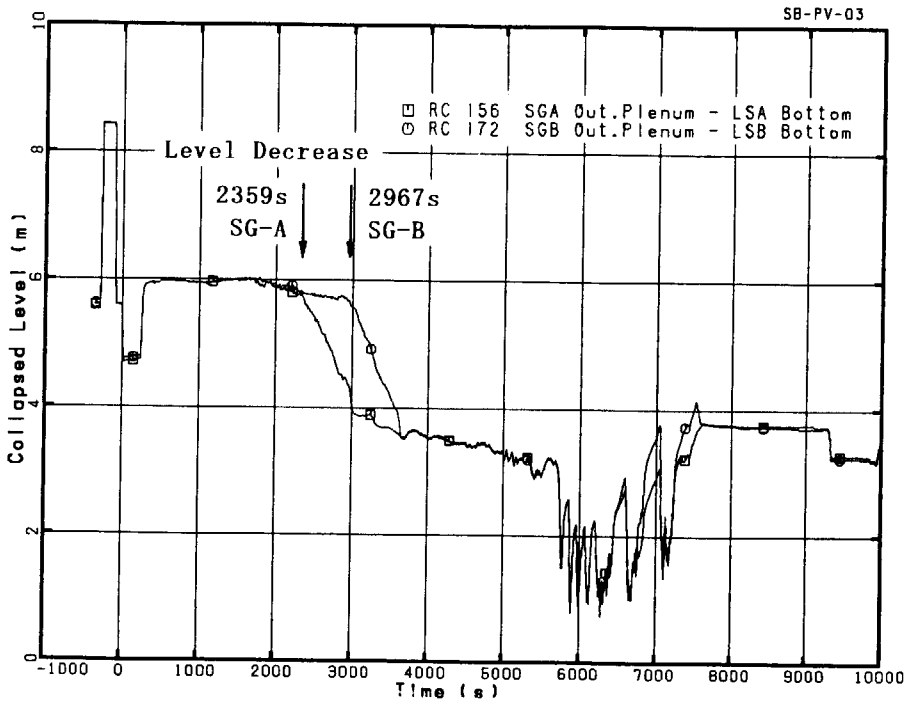

Fig. 4. 1. 16 Collapsed water levels in outlet regions of SG-A and SG-B

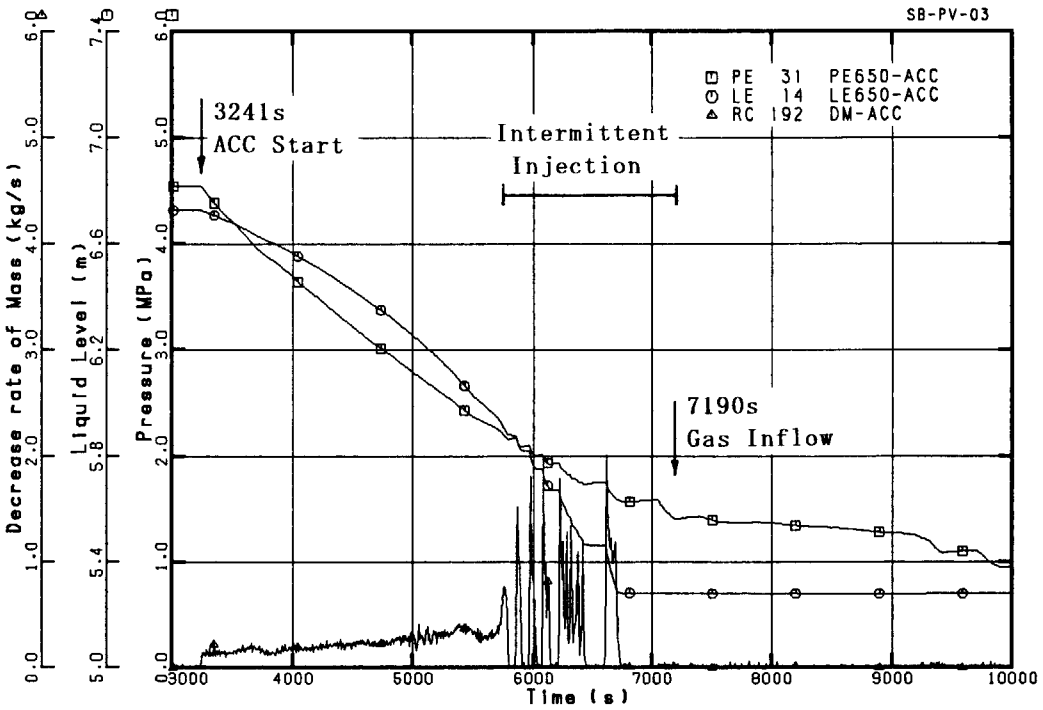

Fig. 4. 1. 17 Injection flow rate, water level and pressure responses in ACC tank

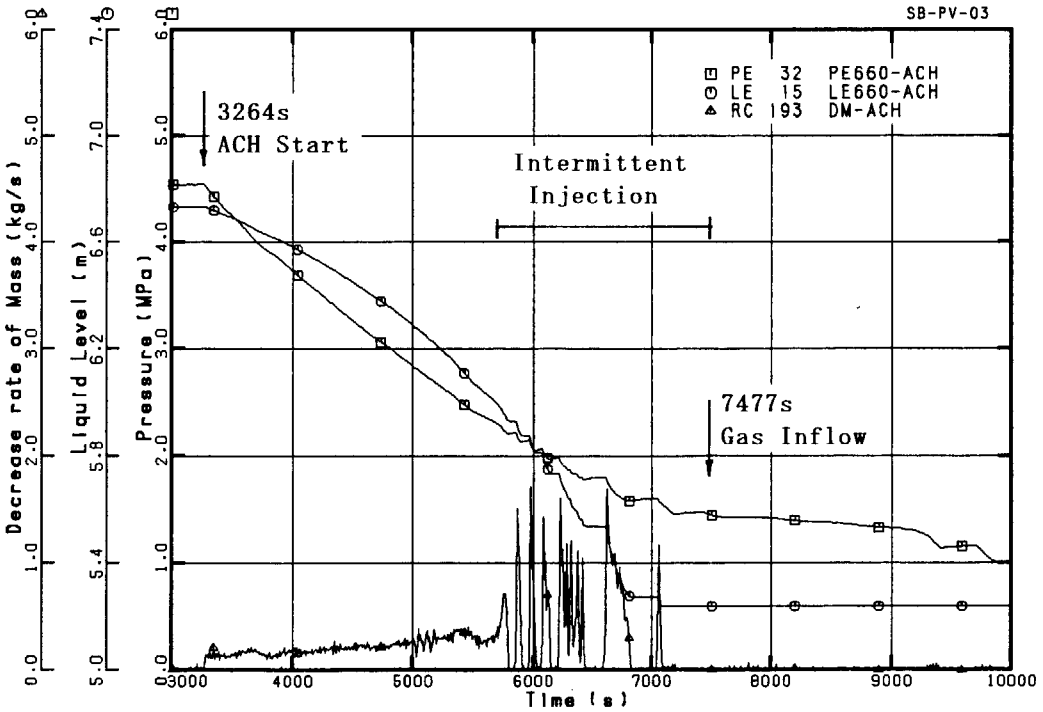

Fig. 4. 1. 18 Injection flow rate, water level and pressure responses in ACH tank

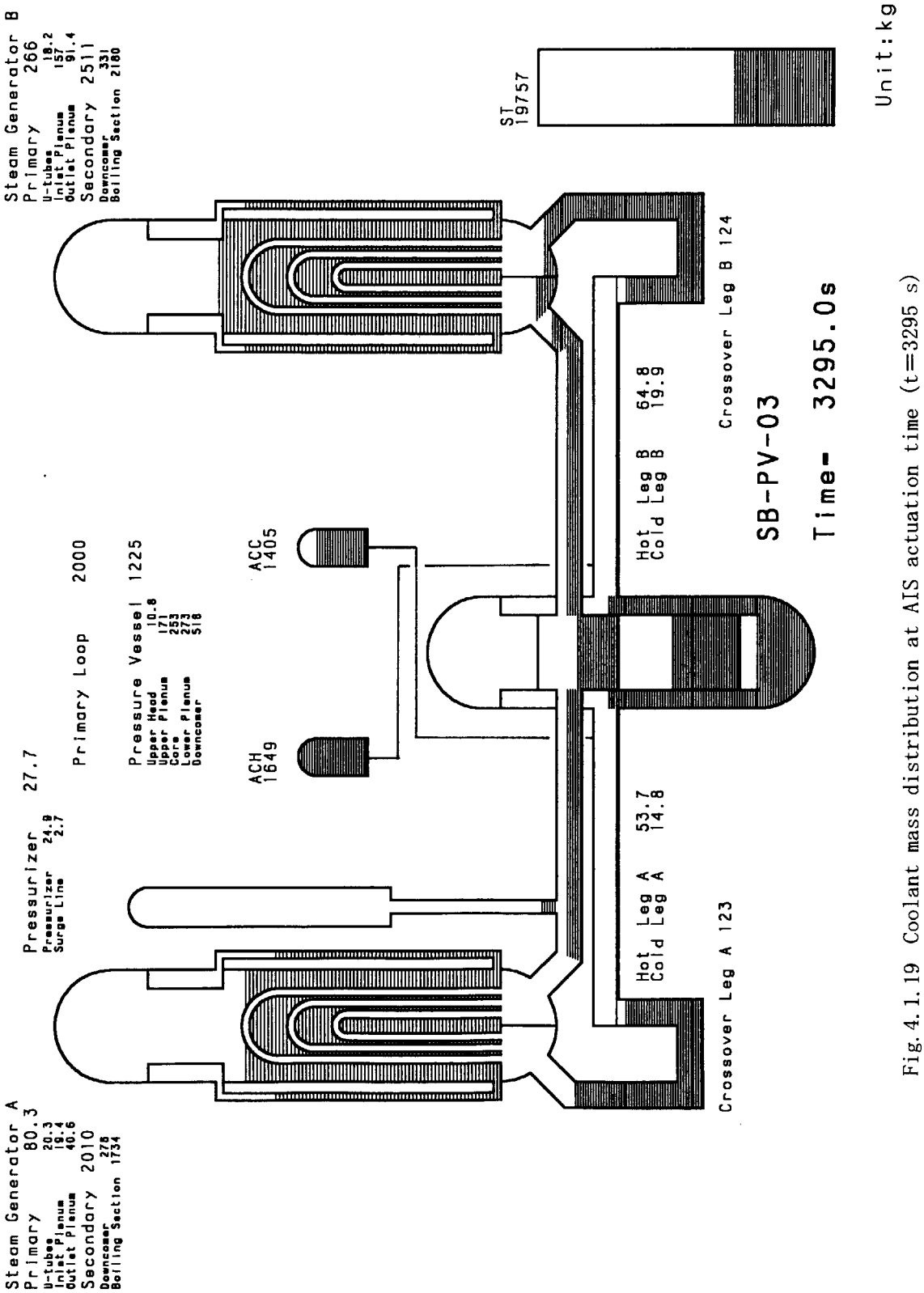

Fig. 4.1.19 Coolant mass distribution at AIS actuation time (t=3295 s)

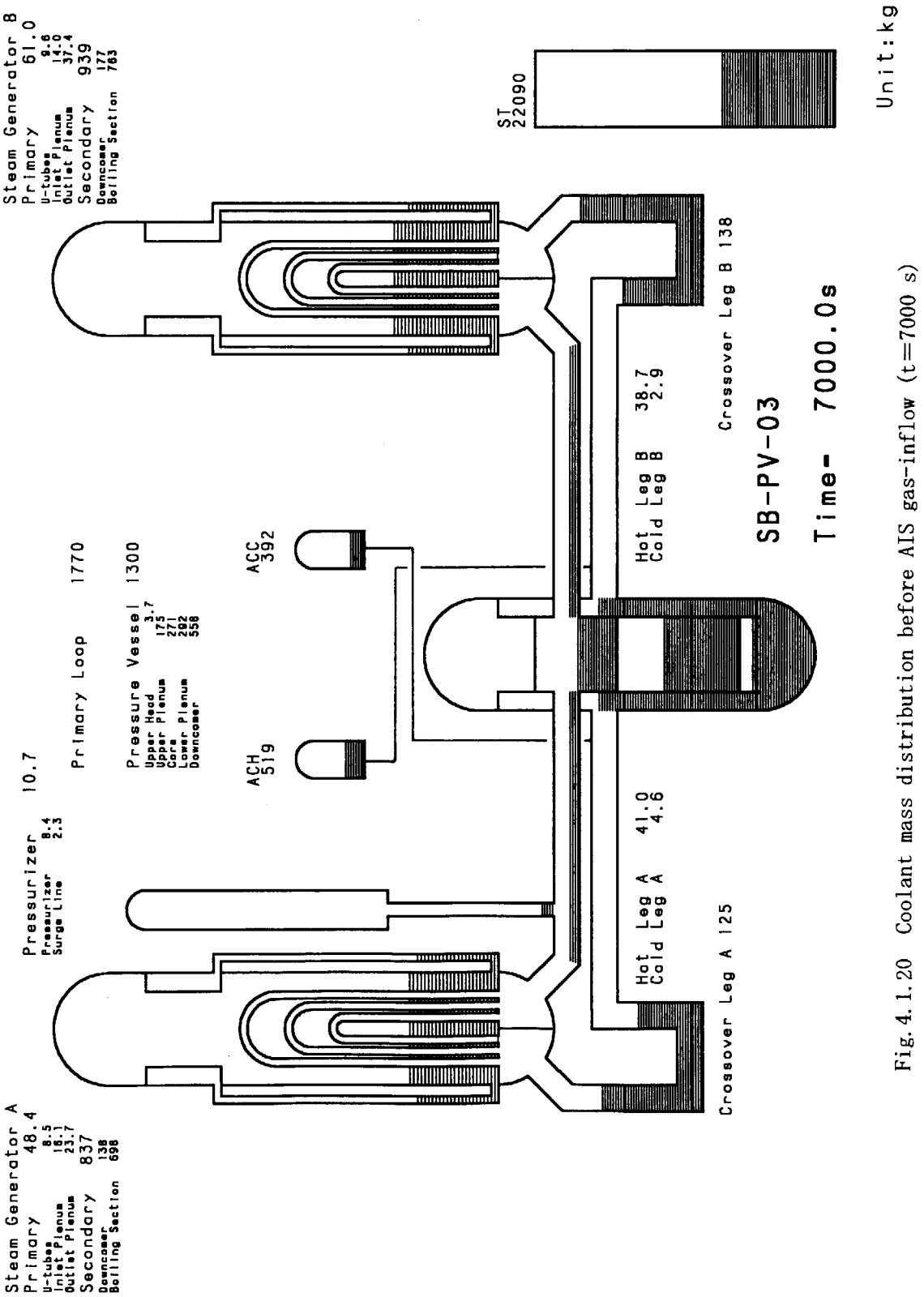

Fig. 4.1.20 Coolant mass distribution before AIS gas-inflow (t=7000 s)

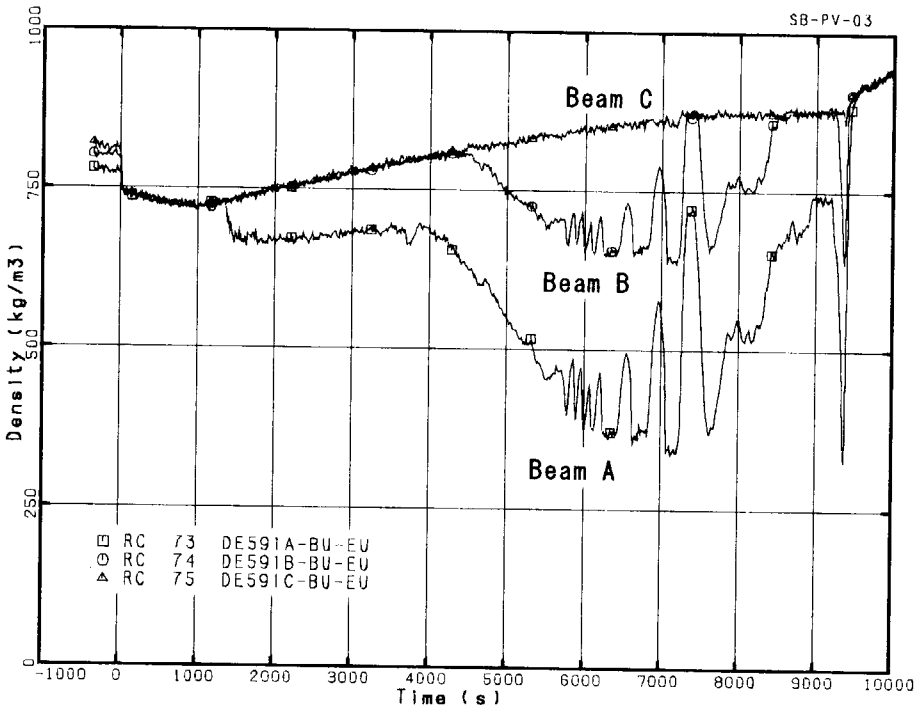

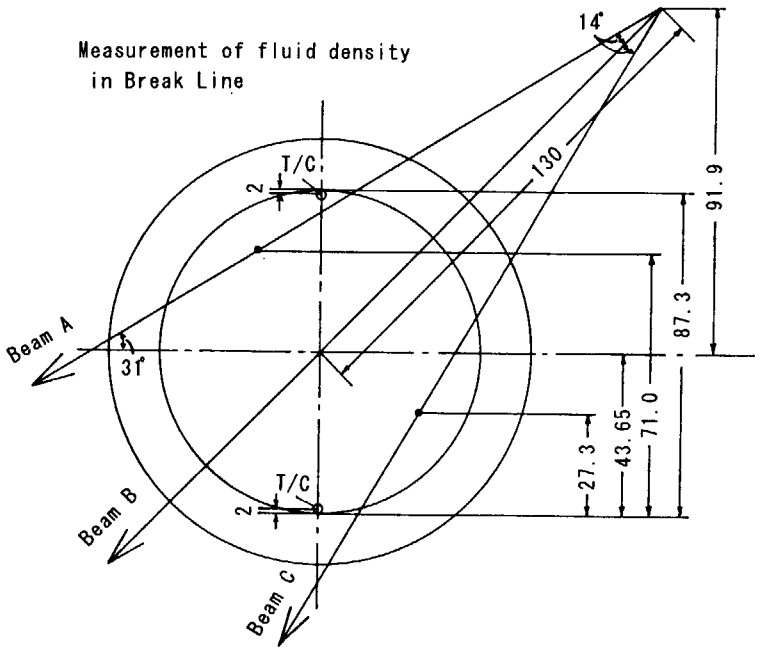

Fig. 4.1.21 Typical three-beam density data at break unit

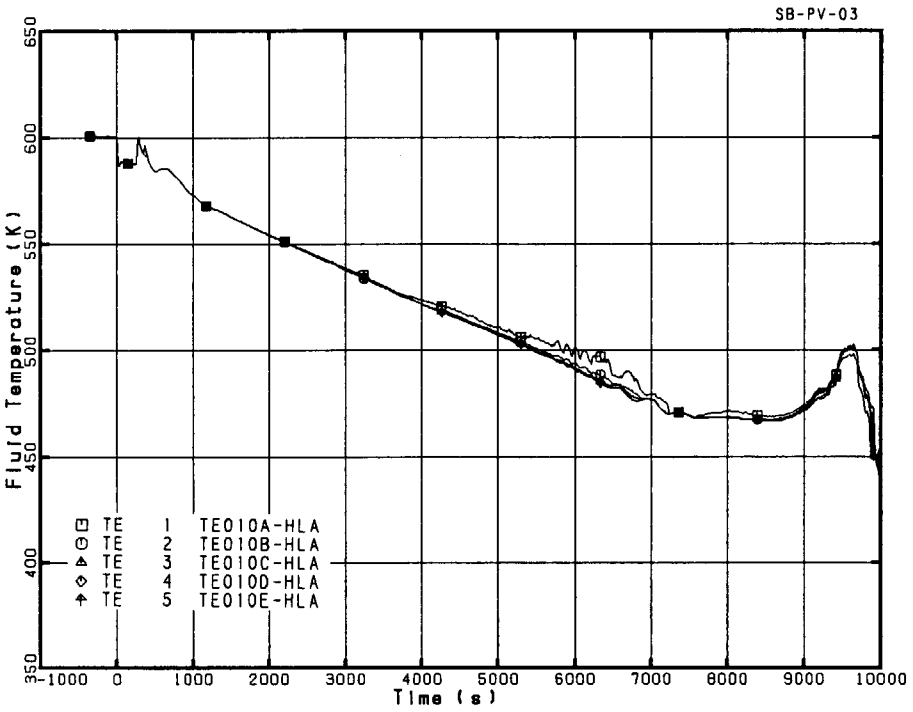

Fig. 4. 1. 22 Primary fluid temperatures at hot leg A during test period

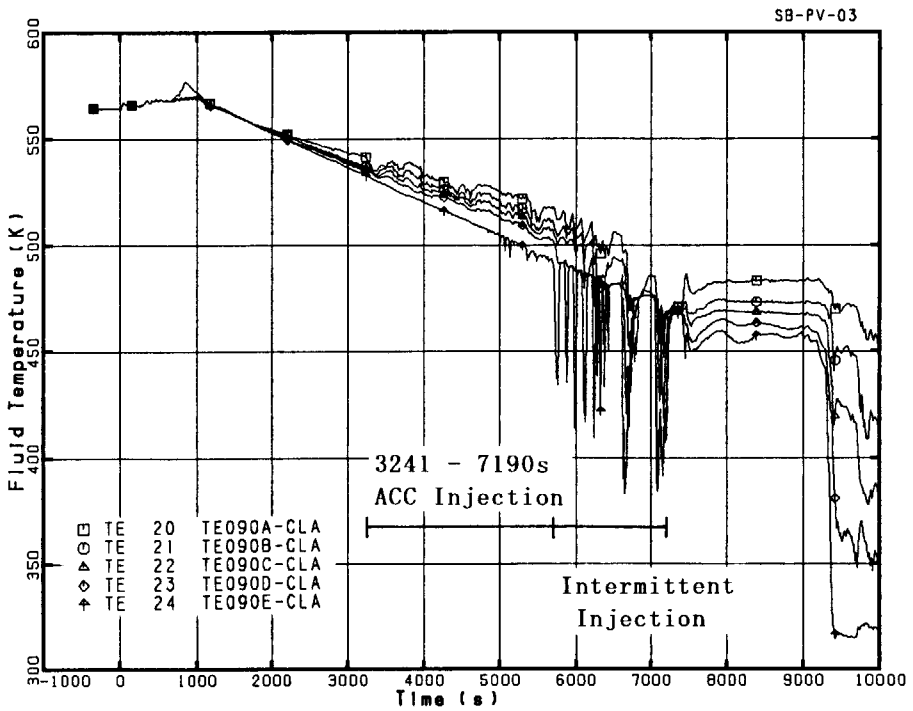

Fig. 4. 1. 23 Primary fluid temperatures at cold leg A during test period

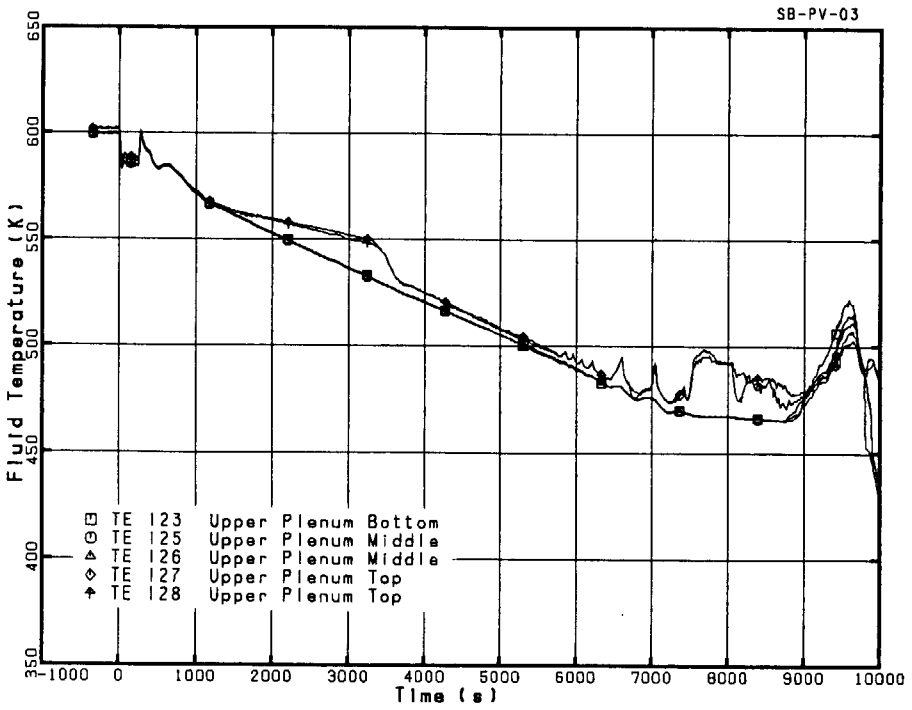

Fig. 4. 1. 24 Primary fluid temperatures in upper plenum during test period

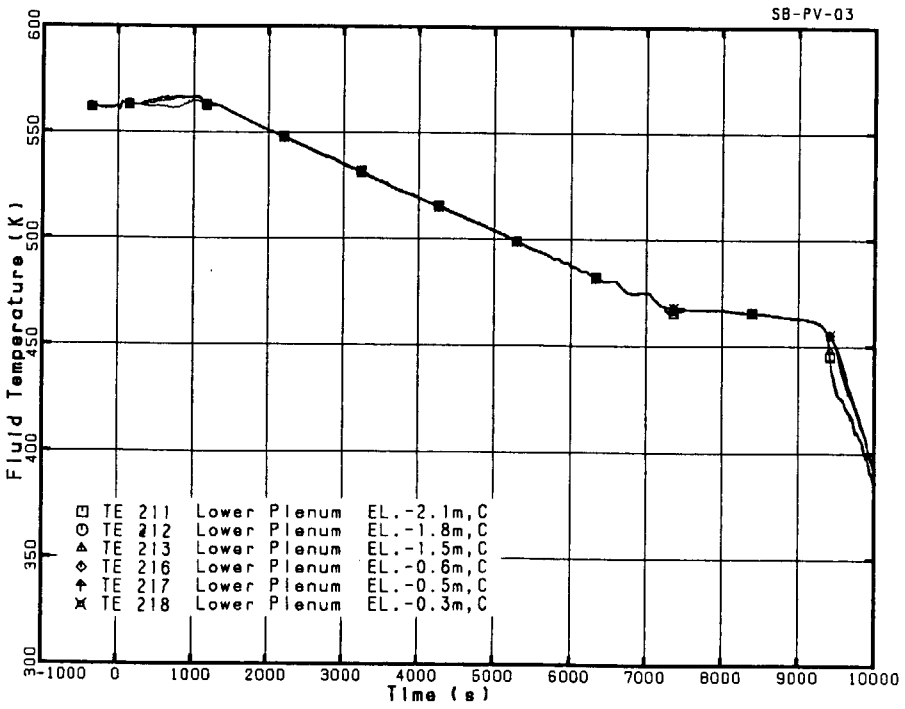

Fig. 4. 1. 25 Primary fluid temperatures in lower plenum during test period

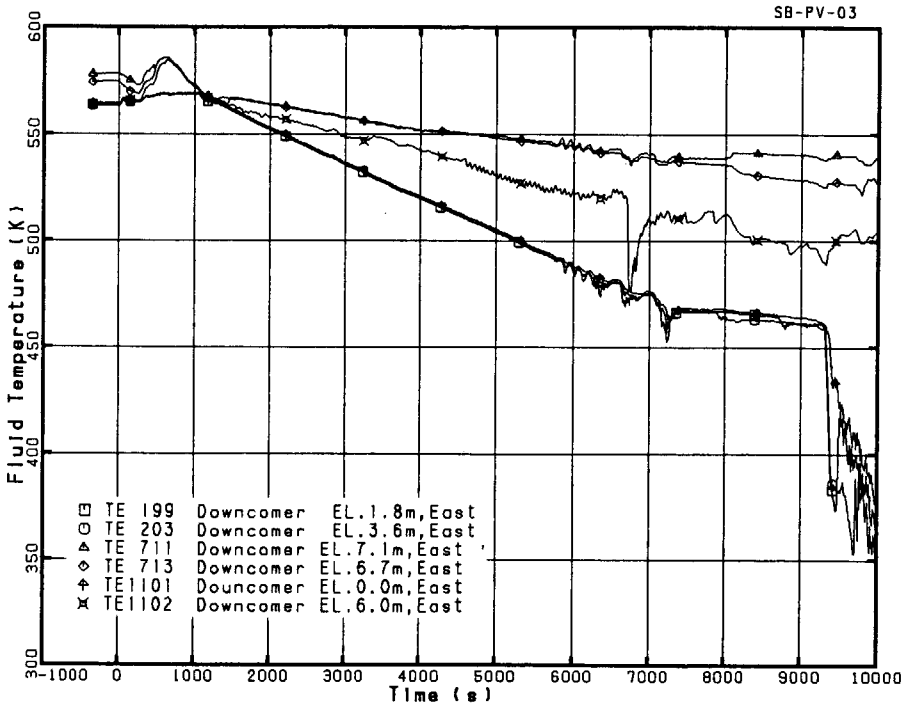

Fig. 4. 1. 26 Primary fluid temperatures in downcomer during test period

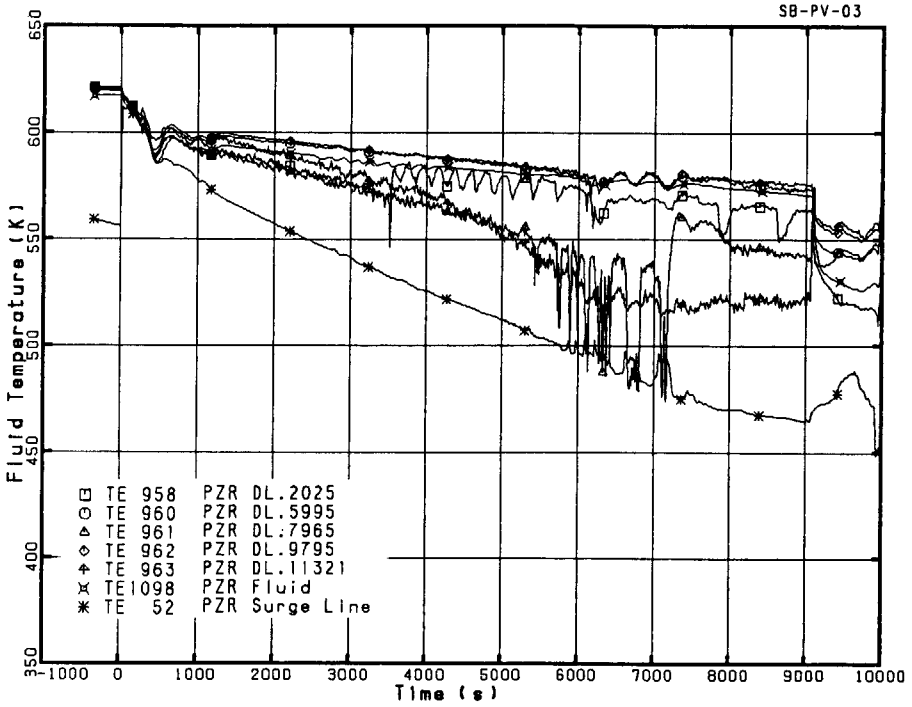

Fig. 4. 1. 27 Pressurizer fluid temperatures during test period

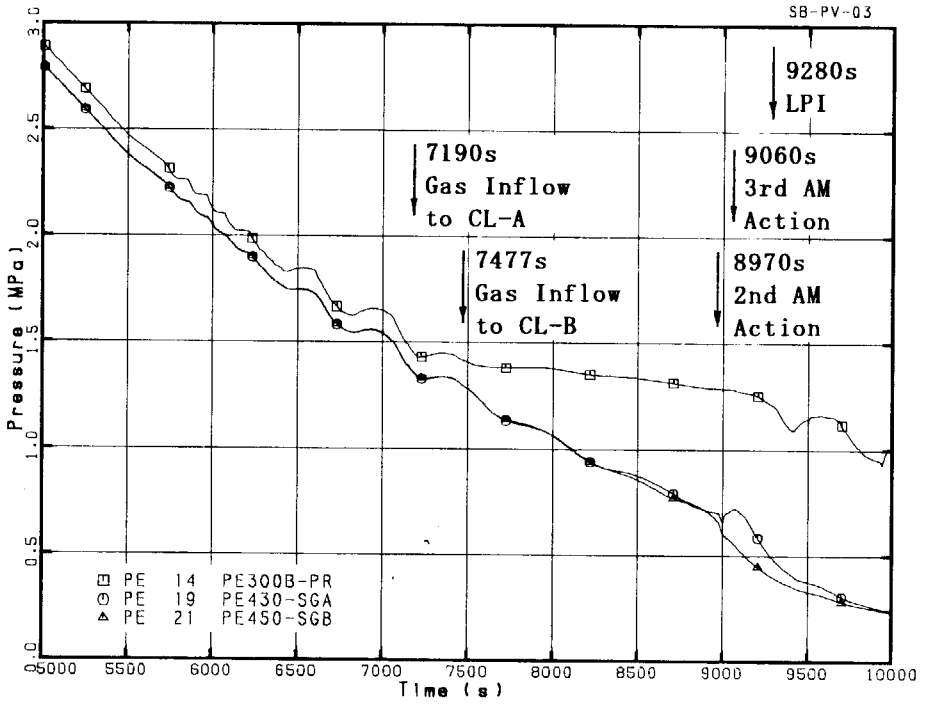

Fig. 4.1.28 Degraded primary depressurization under gas inflow in the third phase

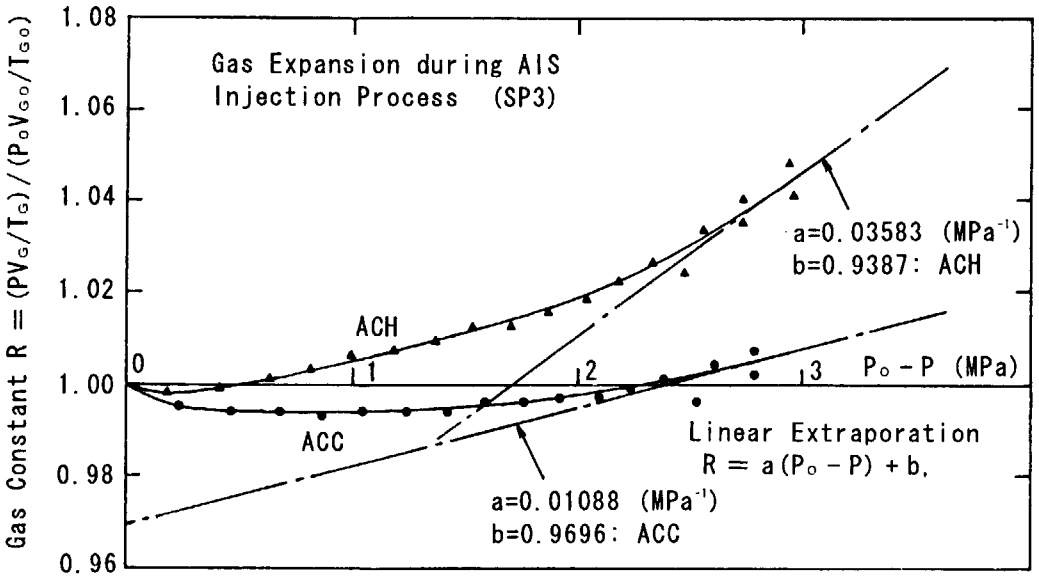

Fig. 4.1.29 Gas constants in two AIS tanks under depressurization process

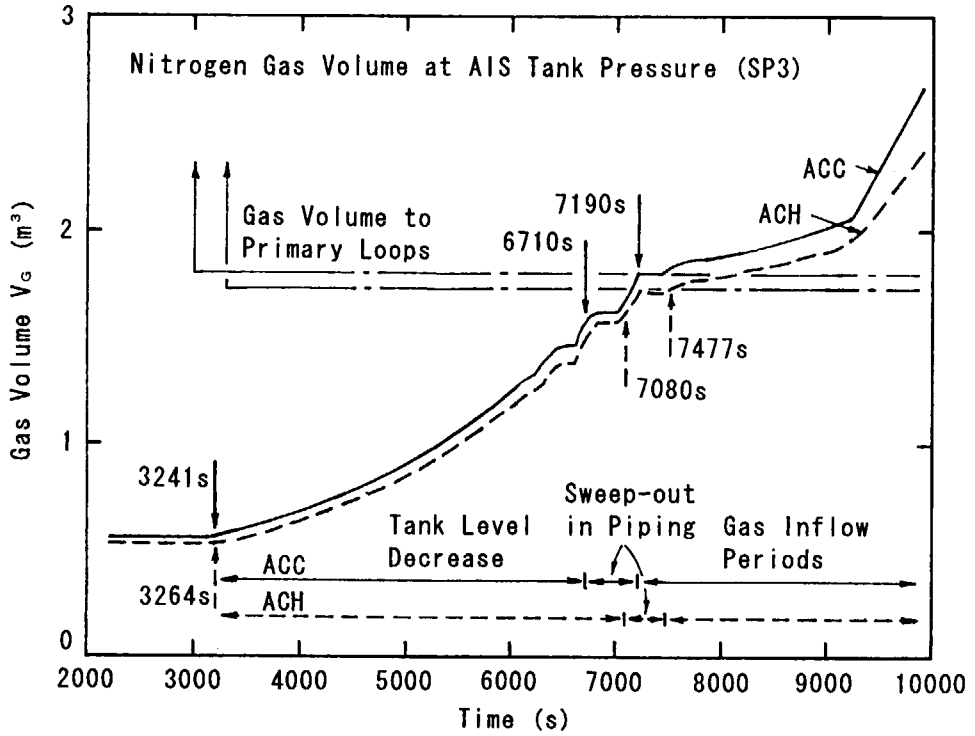

Fig. 4.1.30 Gas volume expansion in two accumulator injection systems

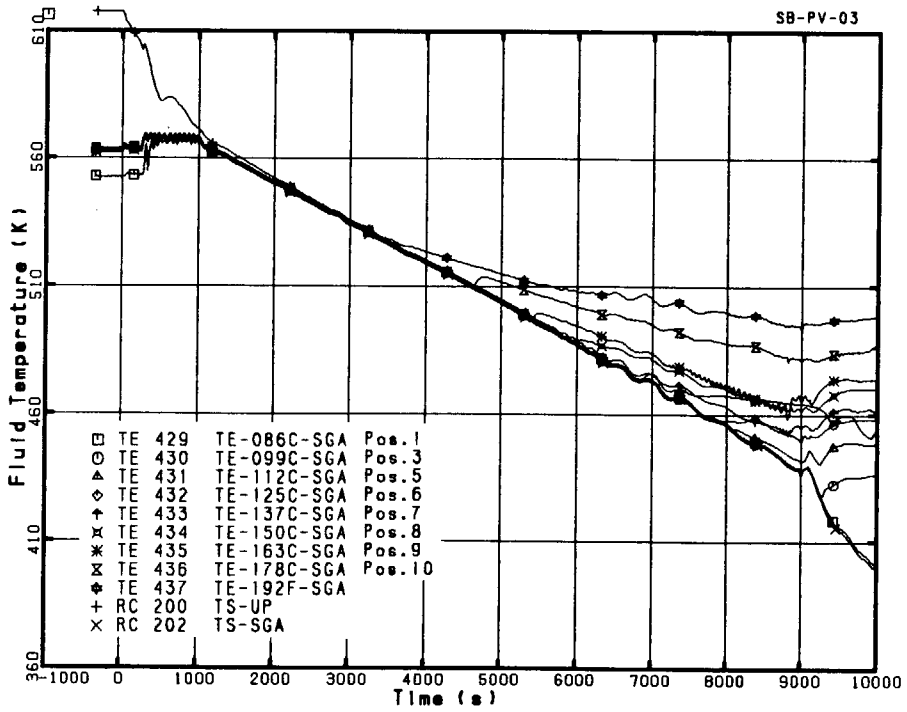

Fig. 4.1.31 Secondary fluid temperatures in SG-A boling section

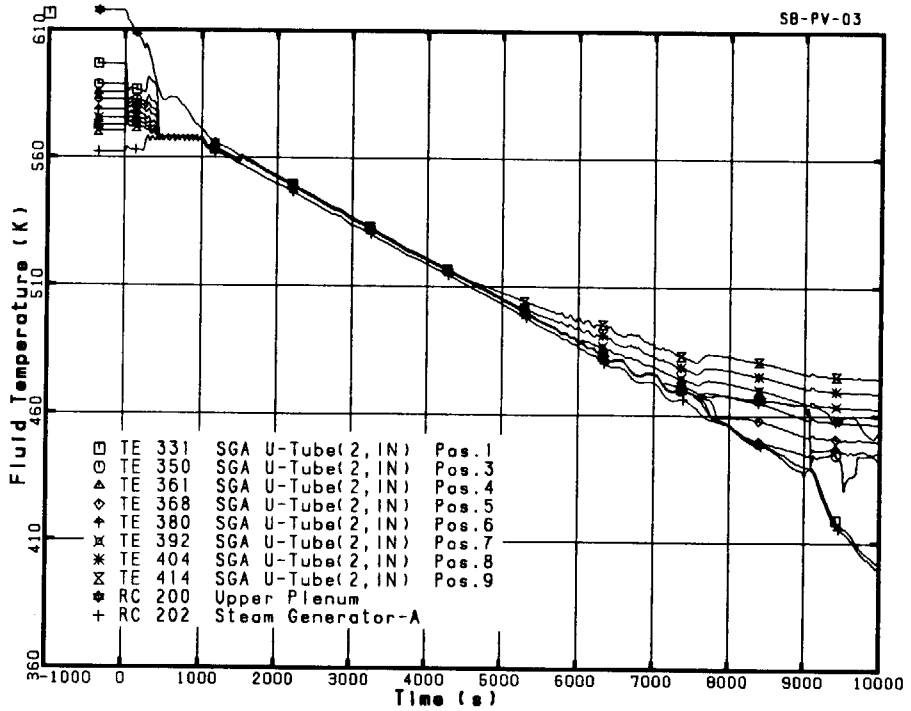

Fig. 4. 1. 32 Primary fluid temperatures in SG-A U-tube inlet side (Tube 2)

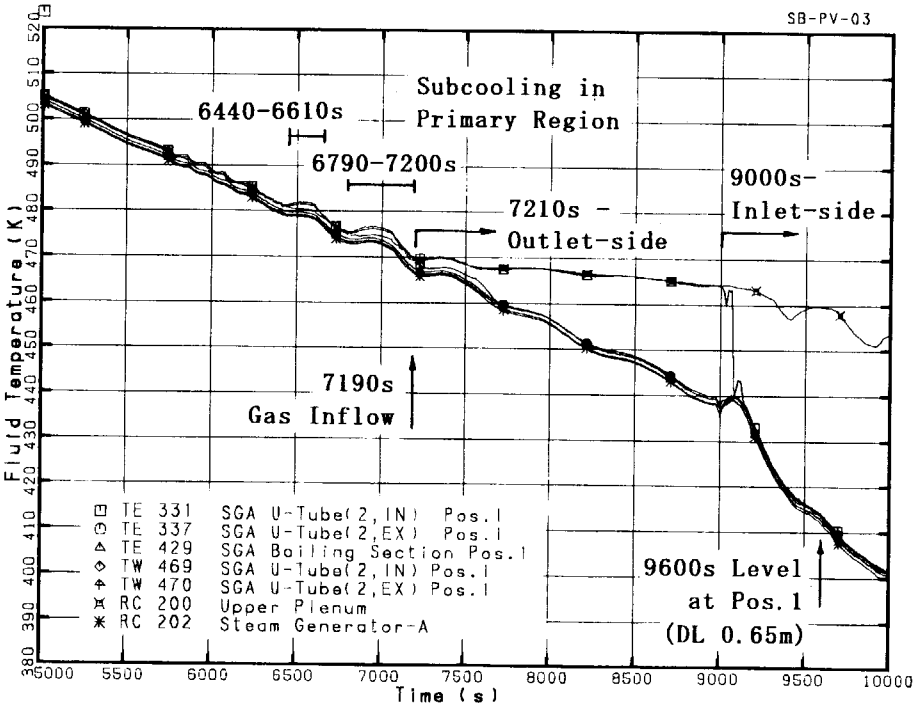

Fig. 4. 1. 33 Primary-to-secondary temperatures across SG-A U-tube 2 (Pos. 1, Bottom)

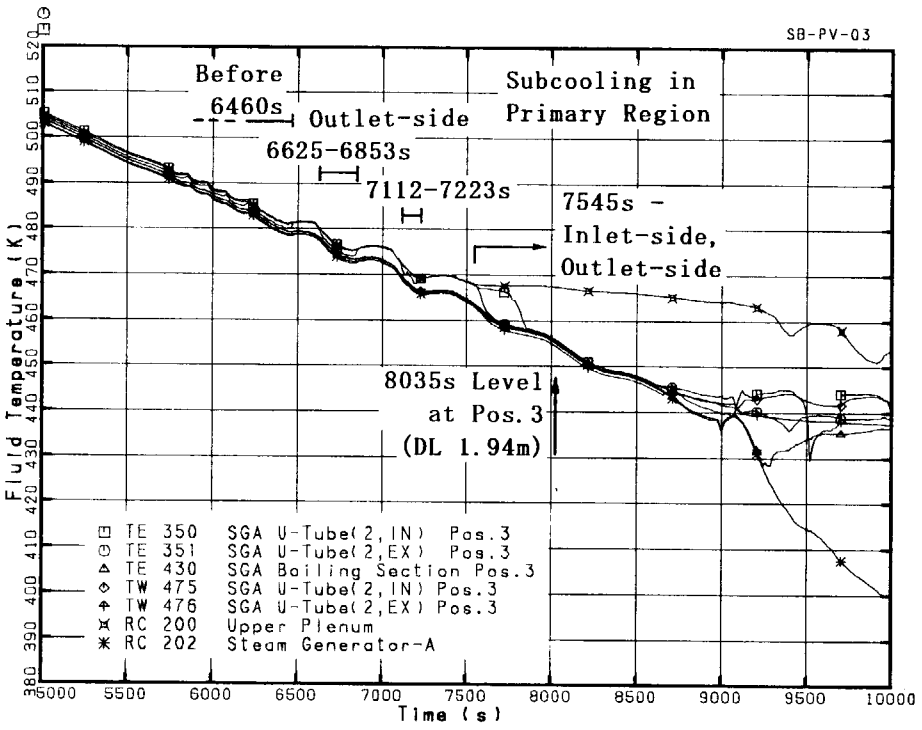

Fig. 4. 1. 34 Primary-to-secondary temperatures across SG-A U-tube 2 (Pos. 3)

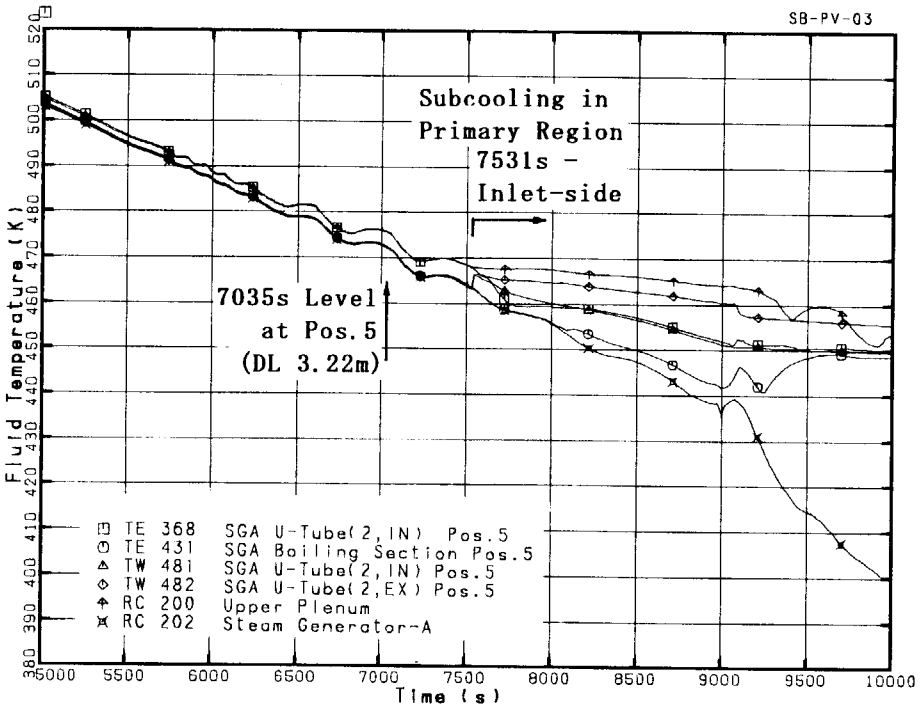

Fig. 4. 1. 35 Primary-to-secondary temperatures across SG-A U-tube 2 (Pos. 5)

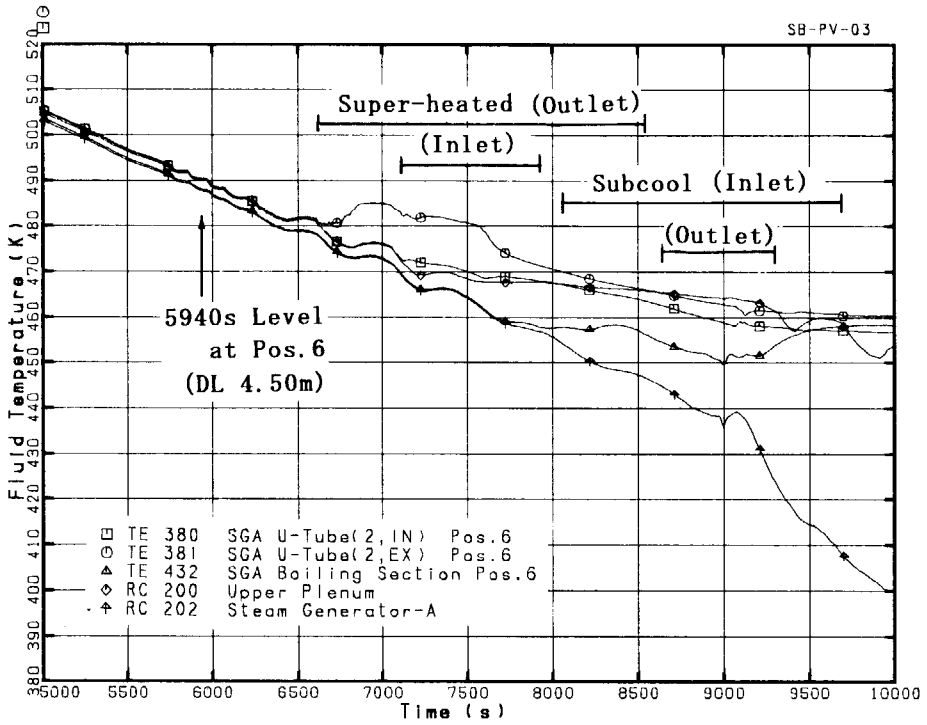

Fig. 4. 1. 36 Primary-to-secondary temperatures across SG-A U-tube 2 (Pos. 6, Middle)

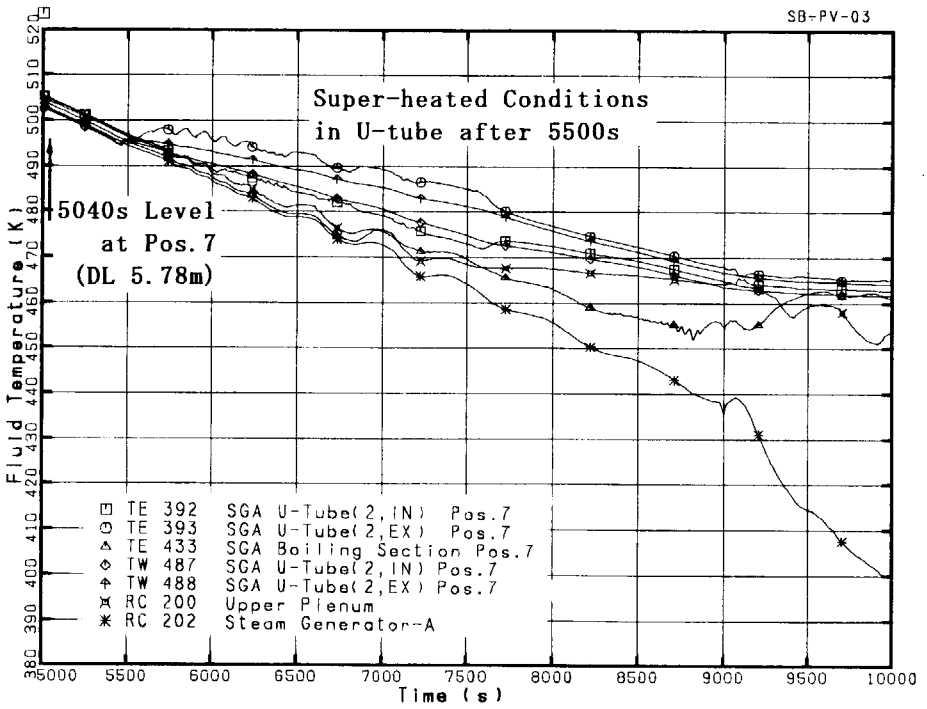

Fig. 4. 1. 37 Primary-to-secondary temperatures across SG-A U-tube 2 (Pos. 7)

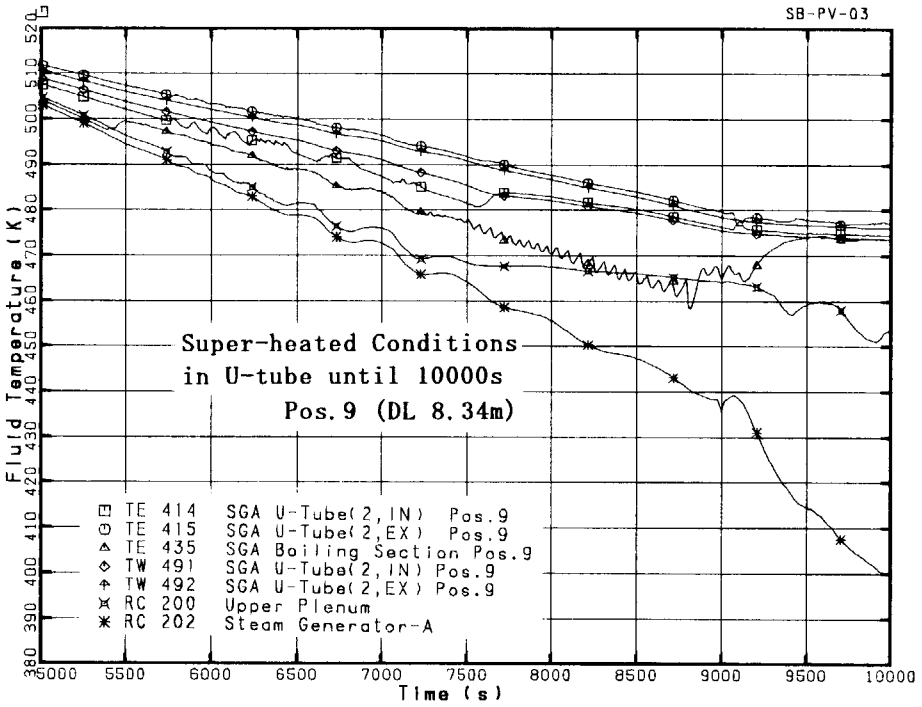

Fig. 4. 1. 38 Primary-to-secondary temperatures across SG-A U-tube 2 (Pos. 9)

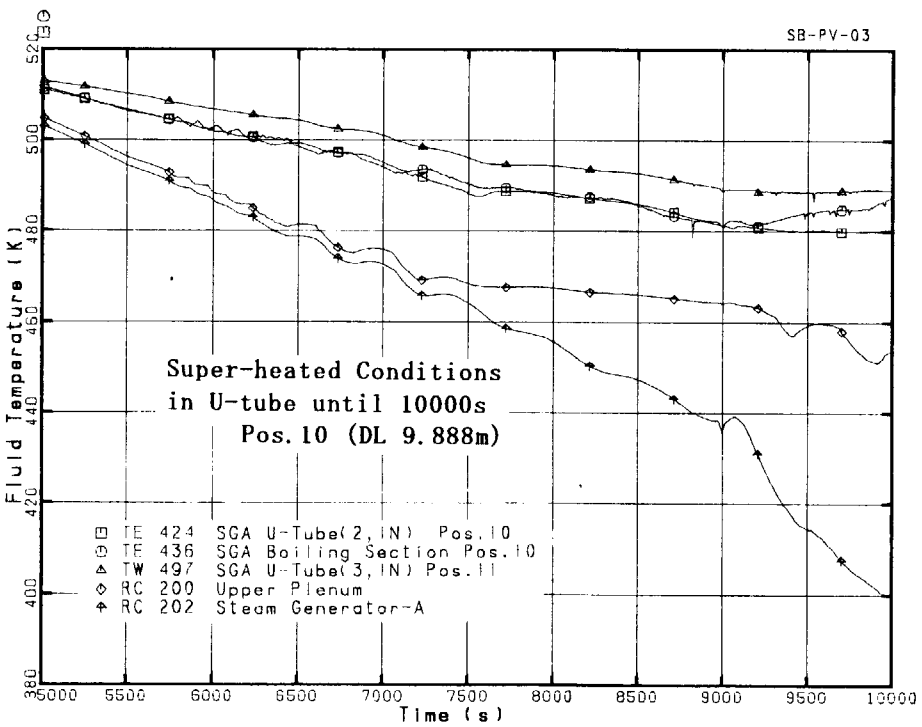

Fig. 4. 1. 39 Primary-to-secondary temperatures across SG-A U-tube 2 (Pos. 10, Top)

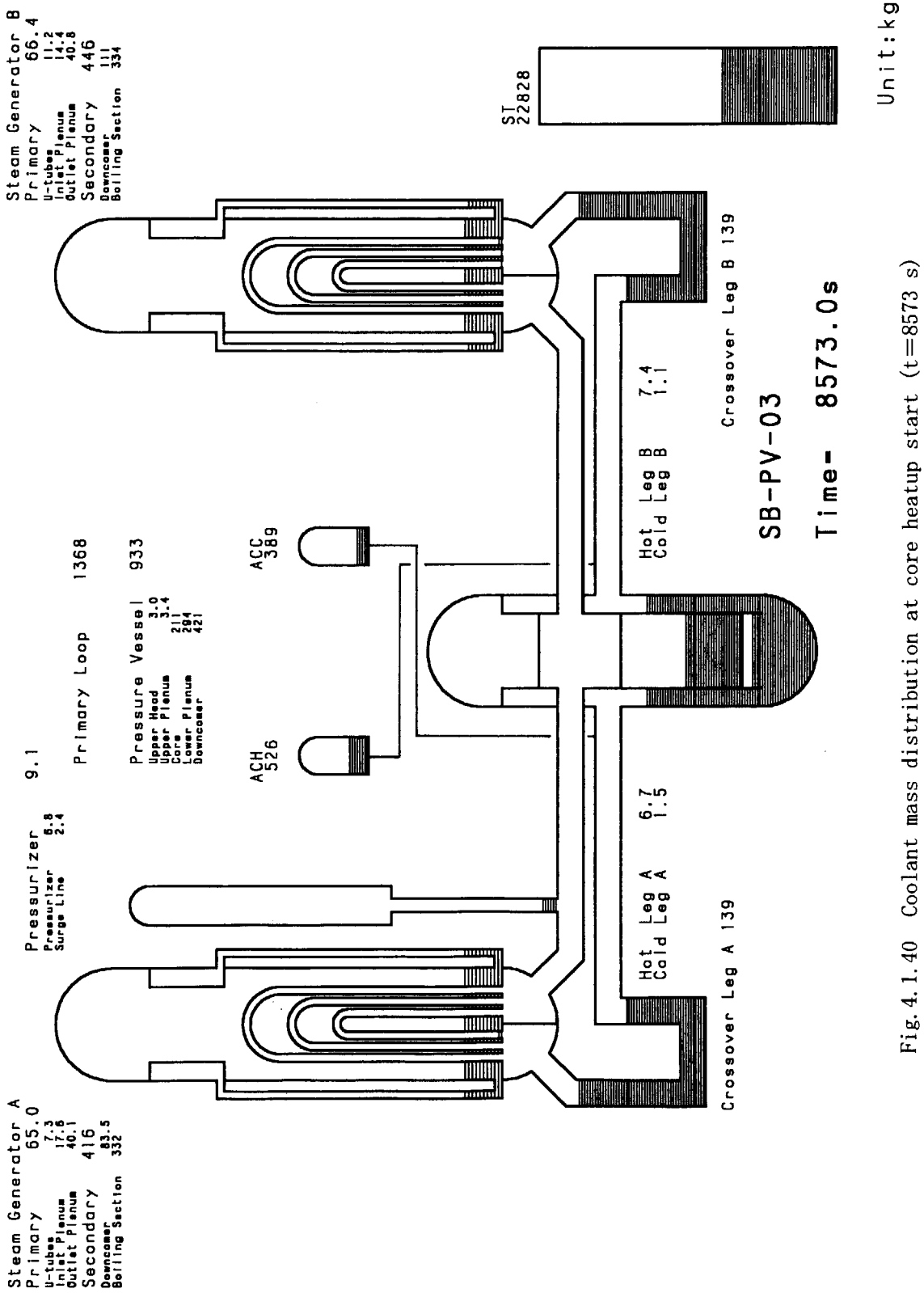

Fig. 4.1.40 Coolant mass distribution at core heatup start (t=8573 s)

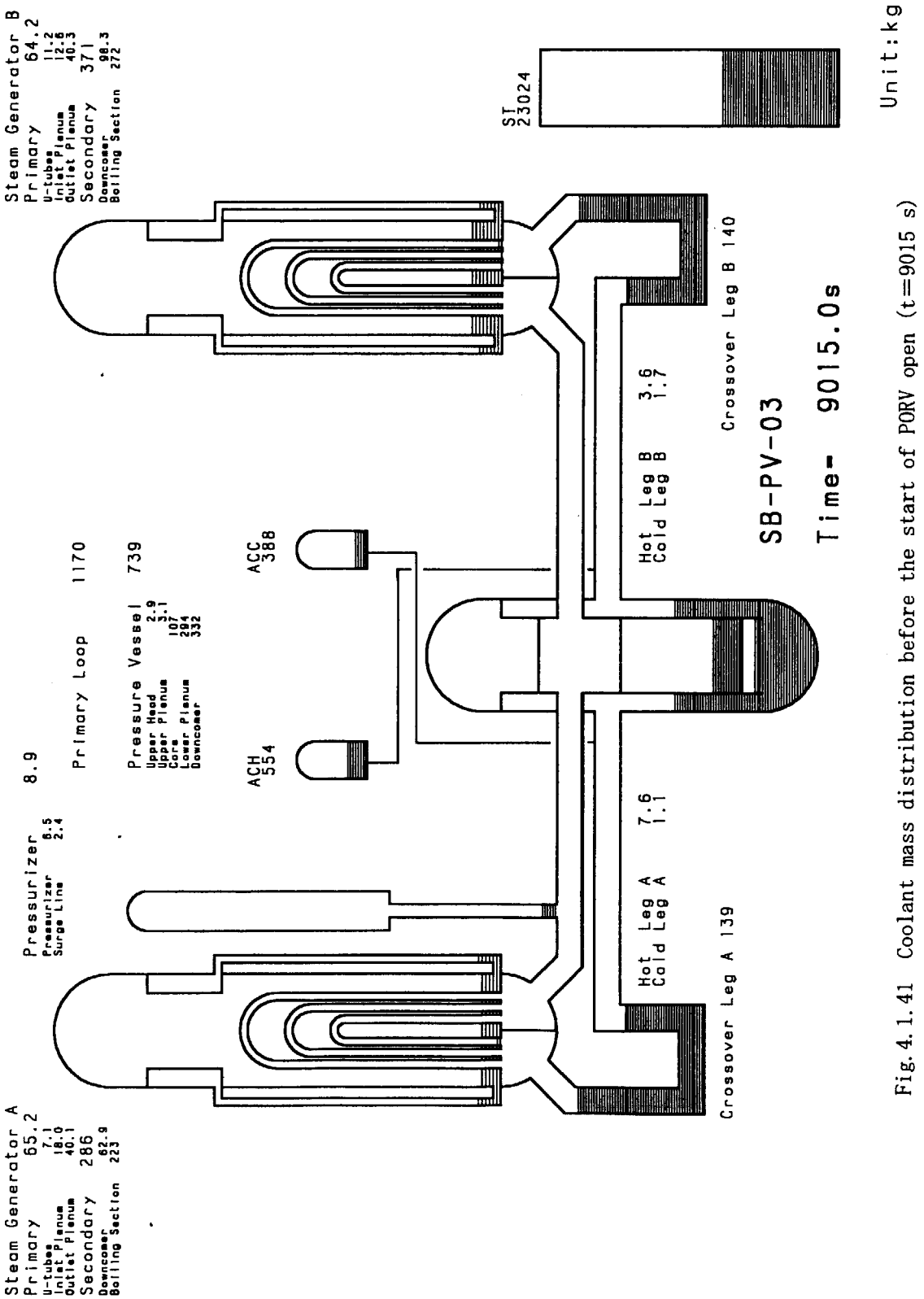

Fig. 4.1.41 Coolant mass distribution before the start of PORV open (t=9015 s)

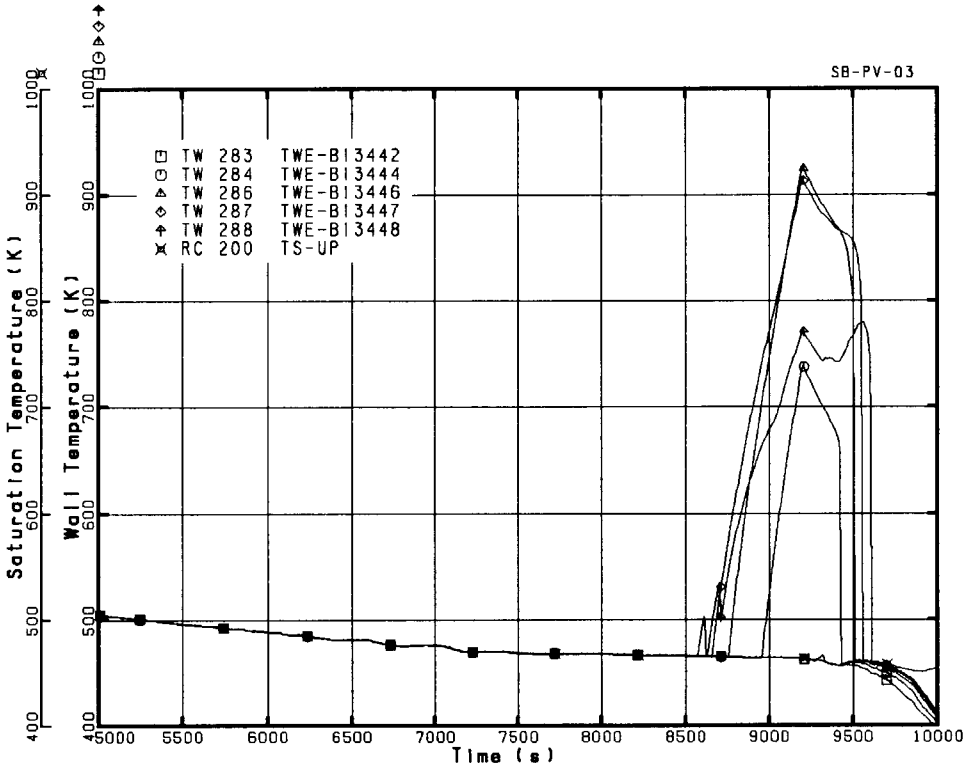

Fig. 4. 1. 42 Heater rod temperatures at high power rod (B13) including Maximum temperature reached 920 K at Pos. 6 (9200 s))

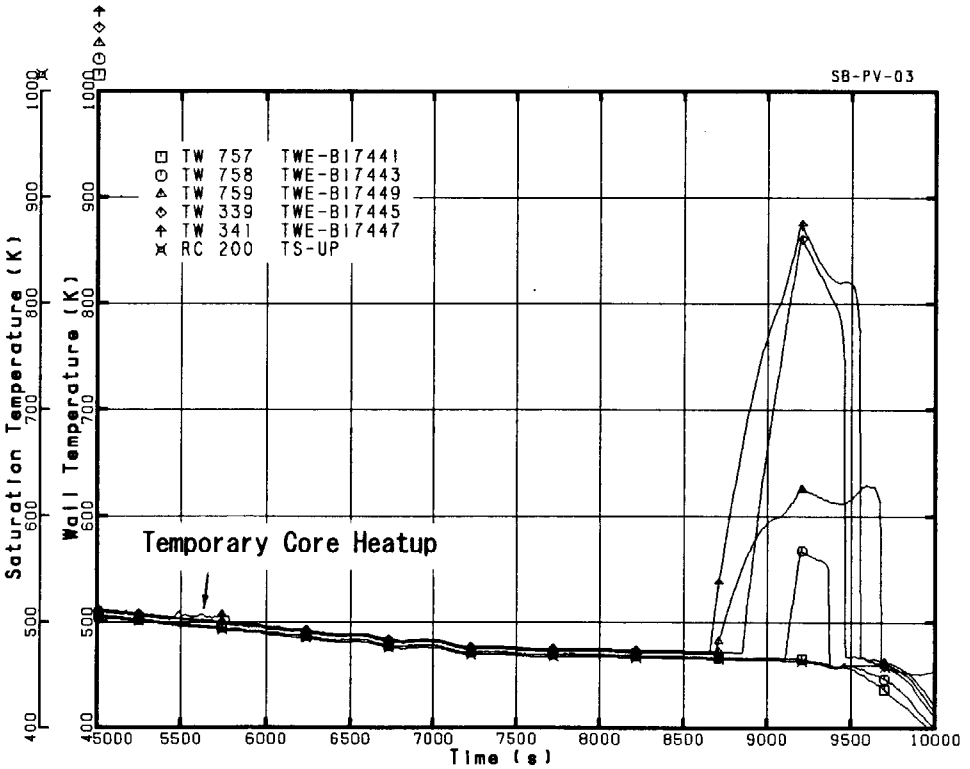

Fig. 4. 1. 43 Heater rod temperatures at high power rod (B17) including temporary heatup behavior at core top (5455 - 5784 s)

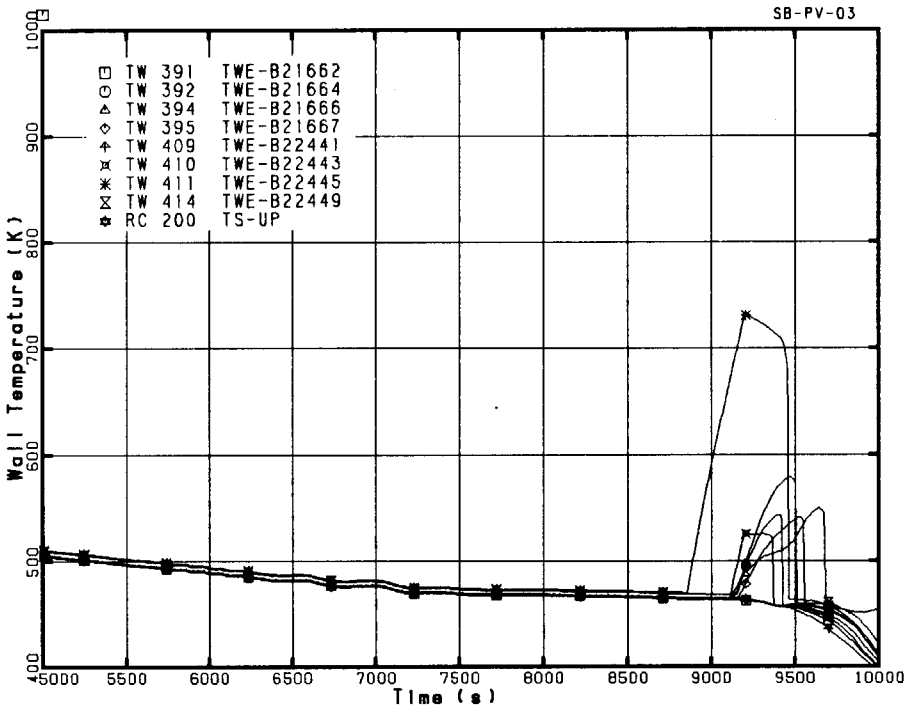

Fig. 4. 1. 44 Surface temperatures at middle-power rod (B22) and tie rod (B21)

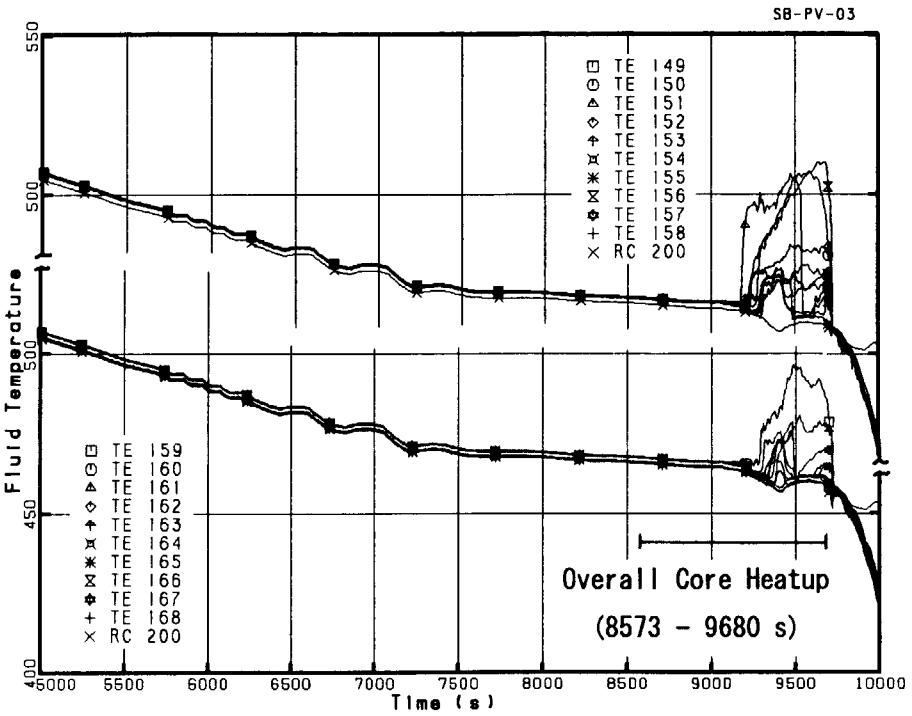

Fig. 4. 1. 45 No detection of core heatup at core exit temperatures (CETs) before PORV opening at 9060 s

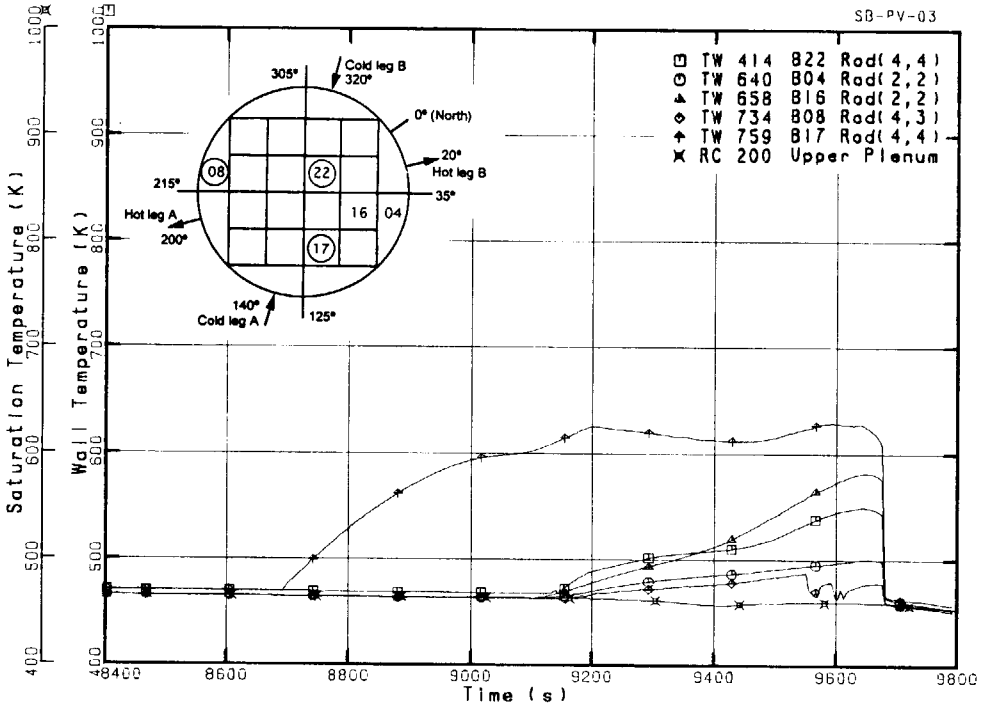

Fig. 4. 1. 46 Distribution of surface temperatures measured on heaters (in circle) and tie rods at Pos. 9 (EL 3.610 m) compared with saturation temperature

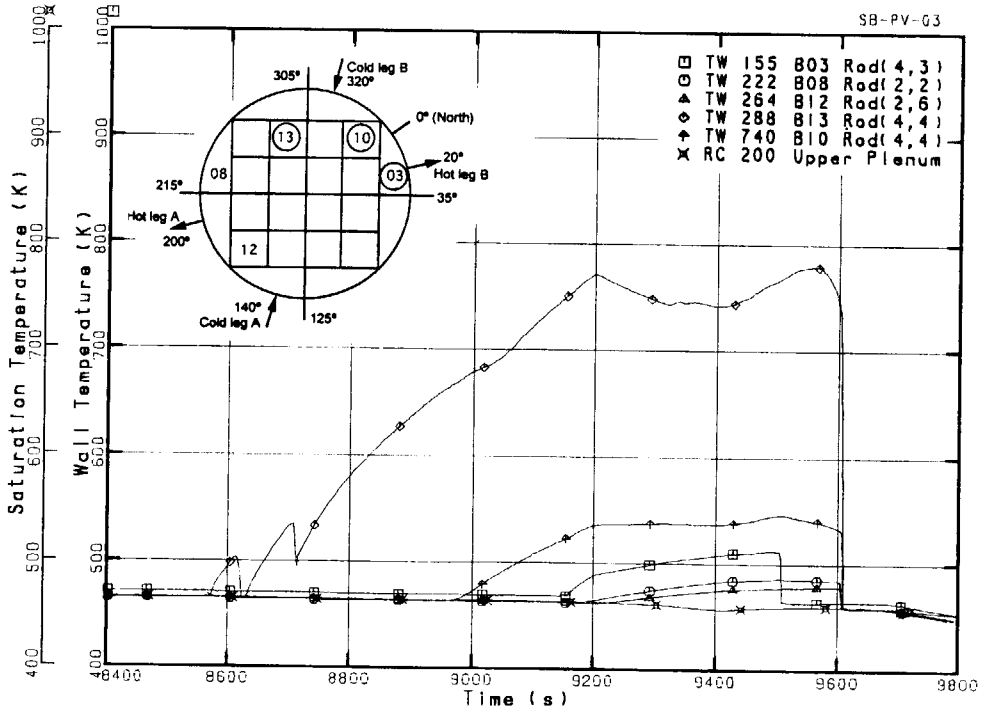

Fig. 4. 1. 47 Distribution of surface temperatures measured on heaters (in circle) and tie rods at Pos. 8 (EL 3.048 m) compared with saturation temperature

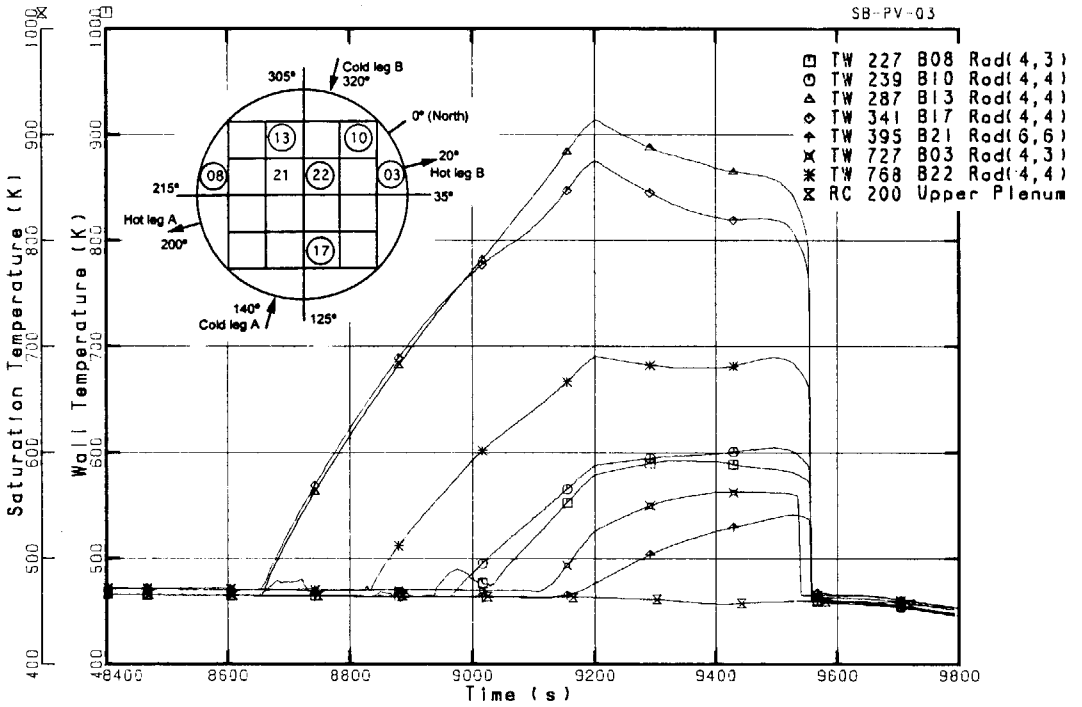

Fig. 4. 1. 48 Distribution of surface temperatures measured on heaters (in circle) and tie rod at Pos. 7 (EL 2. 642 m) compared with saturation temperature

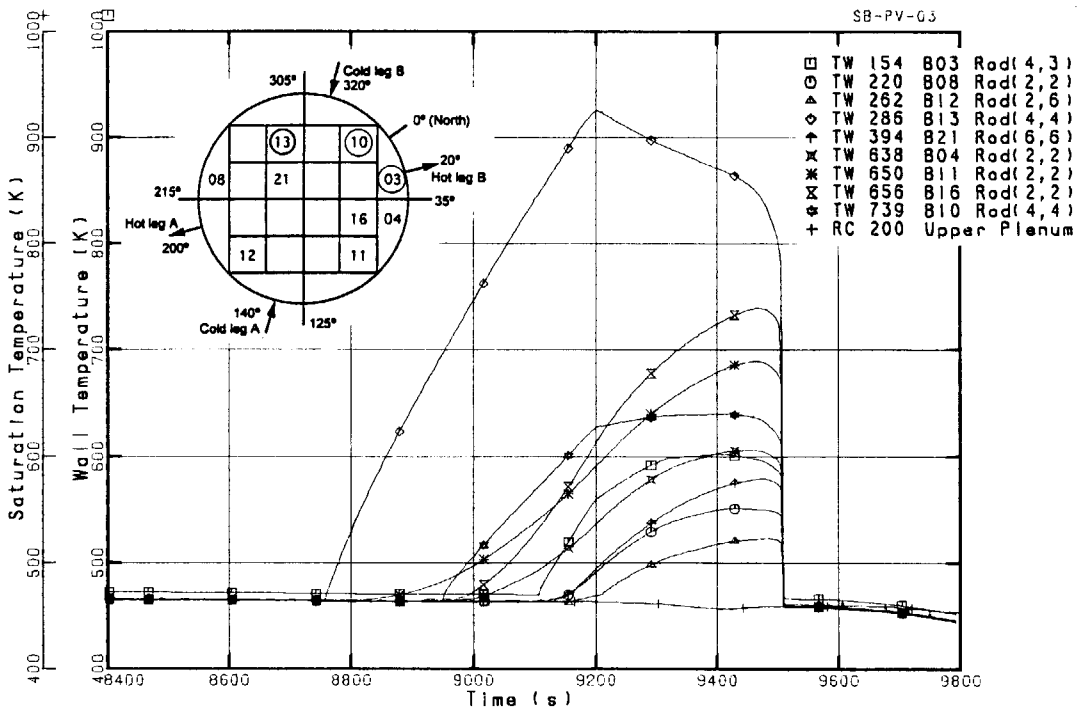

Fig. 4. 1. 49 Distribution of surface temperatures measured on heaters (in circle) and tie rods at Pos. 6 (EL 2. 236 m) compared with saturation temperature

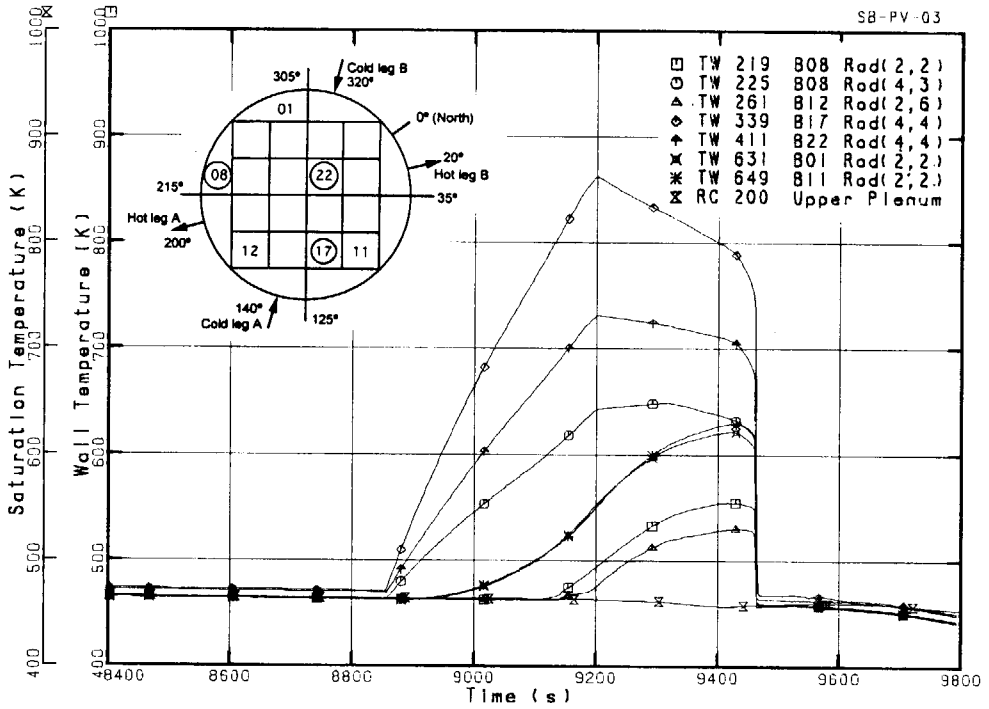

Fig. 4. 1. 50 Distribution of surface temperatures measured on heaters (in circle) and tie rods at Pos. 5 (EL 1. 830 m) compared with saturation temperature

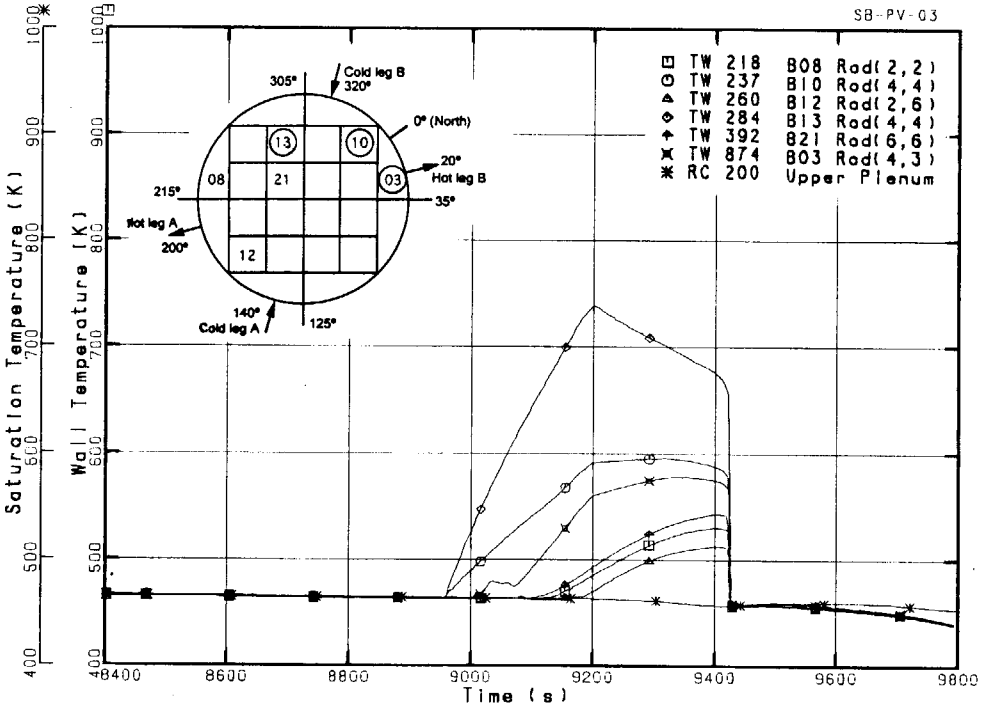

Fig. 4. 1. 51 Distribution of surface temperatures measured on heaters (in circle) and tie rods at Pos. 4 (EL 1. 424m) compared with saturation temperature

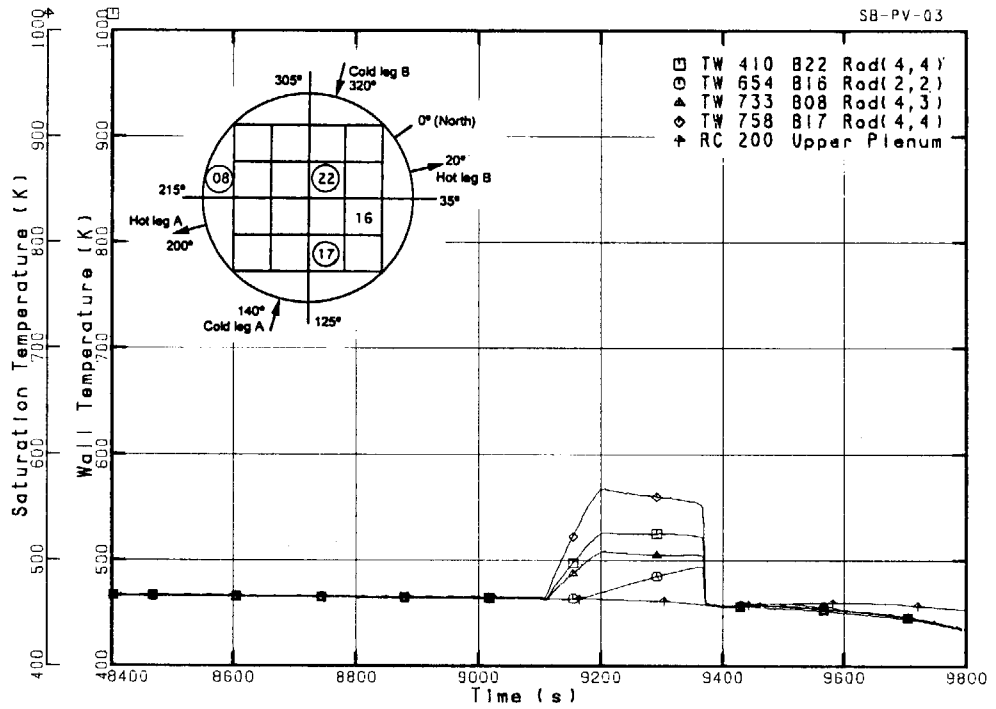

Fig. 4. 1. 52 Distribution of surface temperatures measured on heaters (in circle) and tie rod at Pos. 3 (EL 1.018 m) compared with saturation temperature

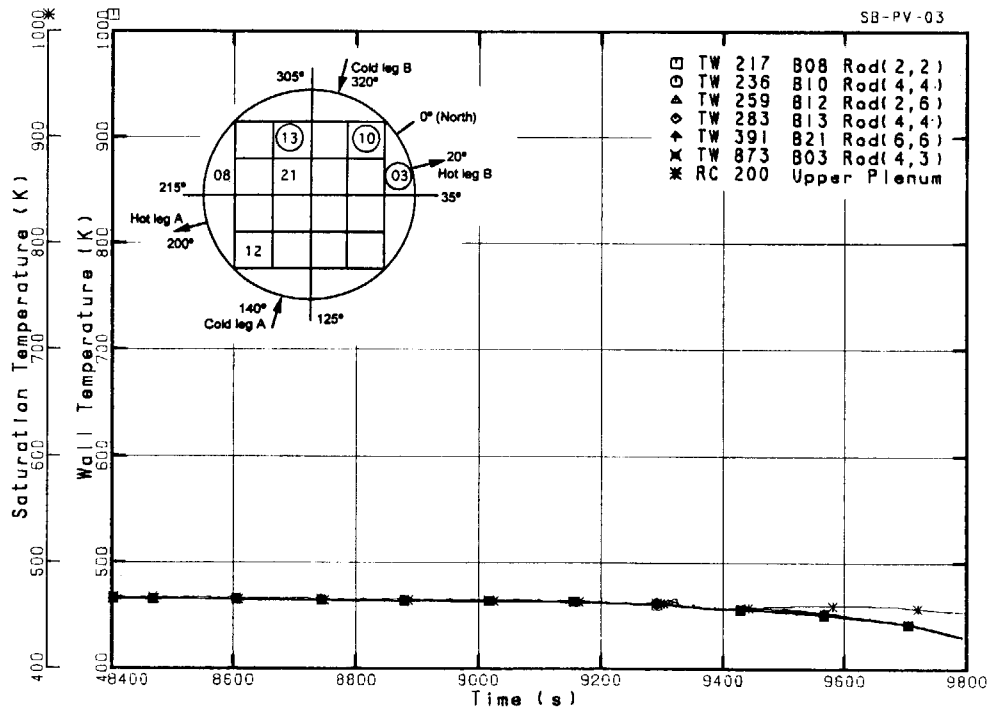

Fig. 4. 1. 53 Distribution of surface temperatures measured on heater (in circle) and tie rods at Pos. 2 (EL 0.612 m) compared with saturation temperature

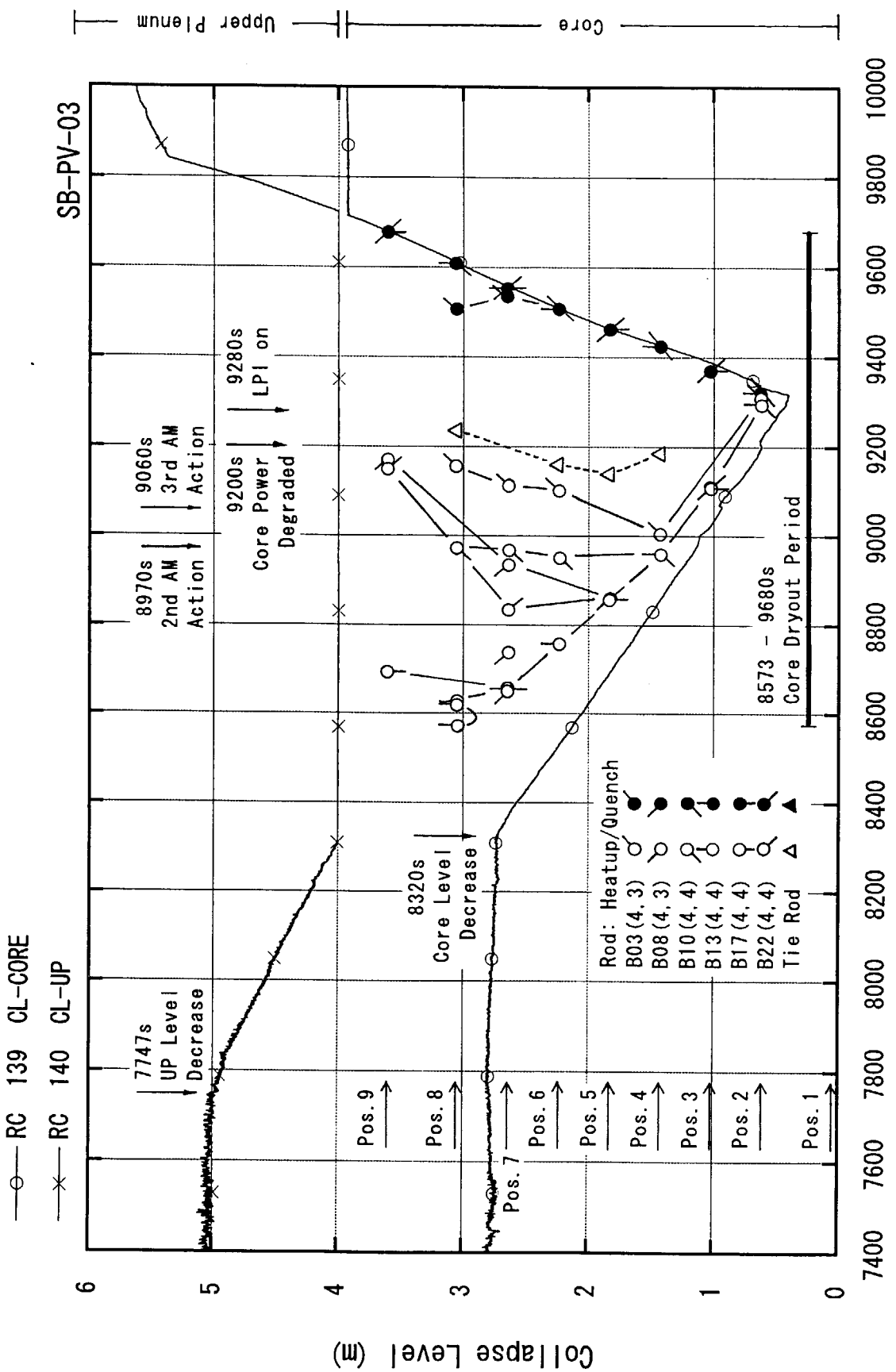

Fig. 4. 1. 54 Typical core heatup and quench phenomena compared with collapsed water levels indicating local core cooling under SG depressurization action

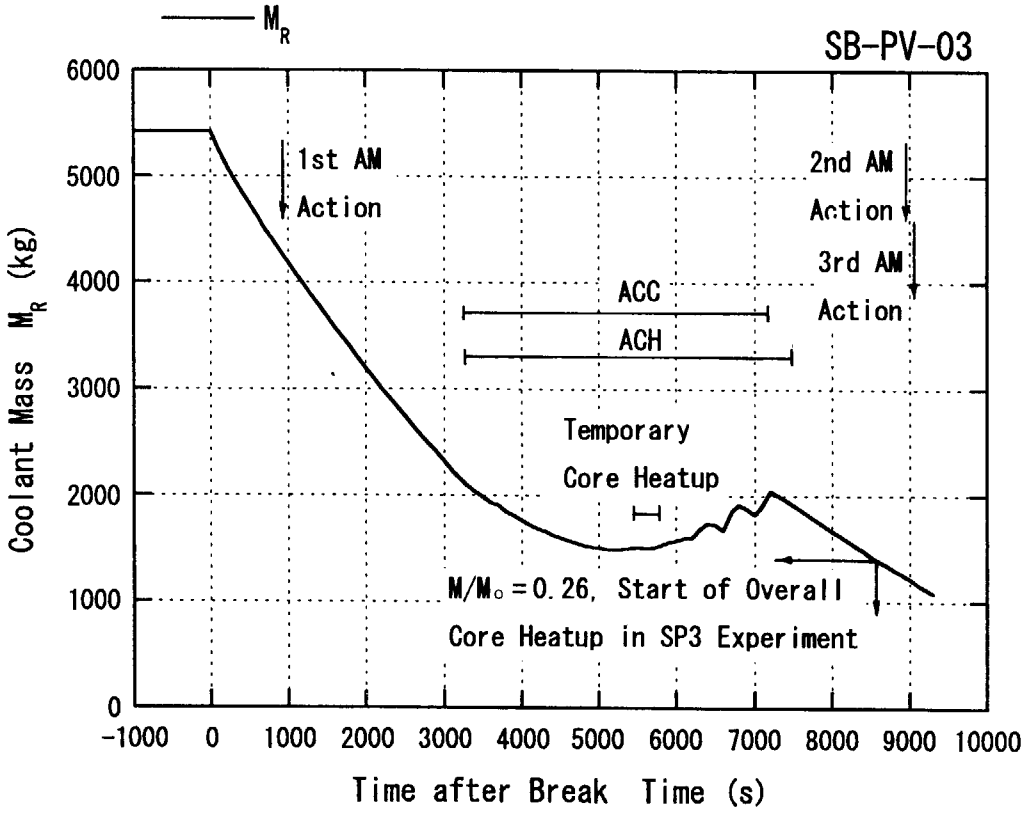

Fig. 4.2.1 Primary mass inventory related to major events in experiment SB-PV-03

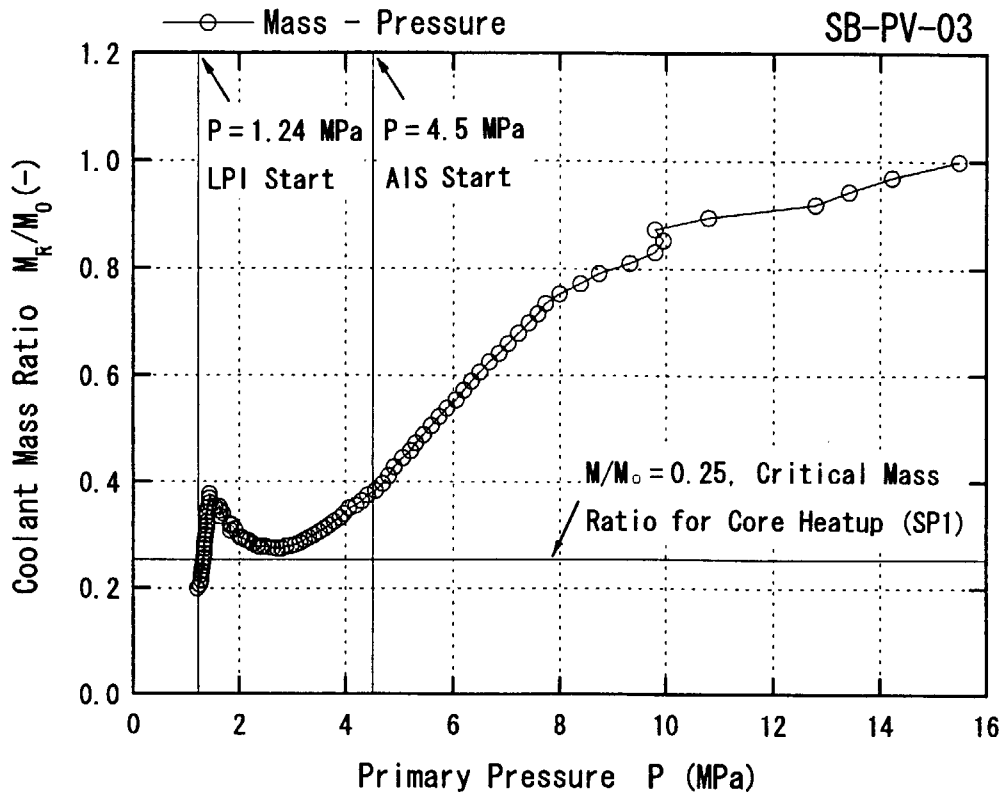

Fig. 4.2.2 Primary pressure - Mass inventory Map for experiment SB-PV-03

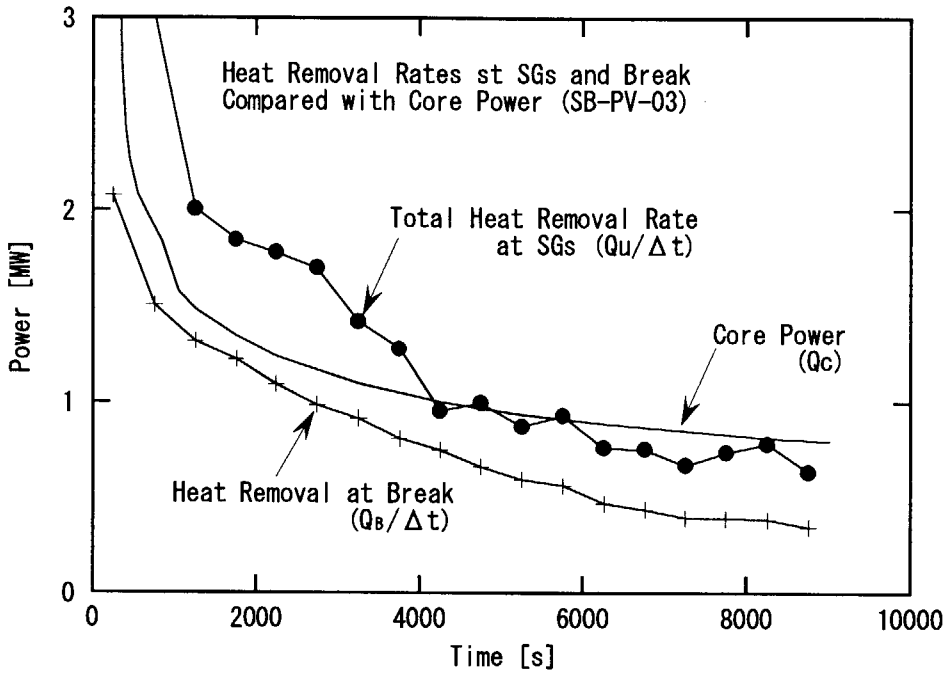

Fig.4.2.3 Heat removal rates at SGs and break compared to core power

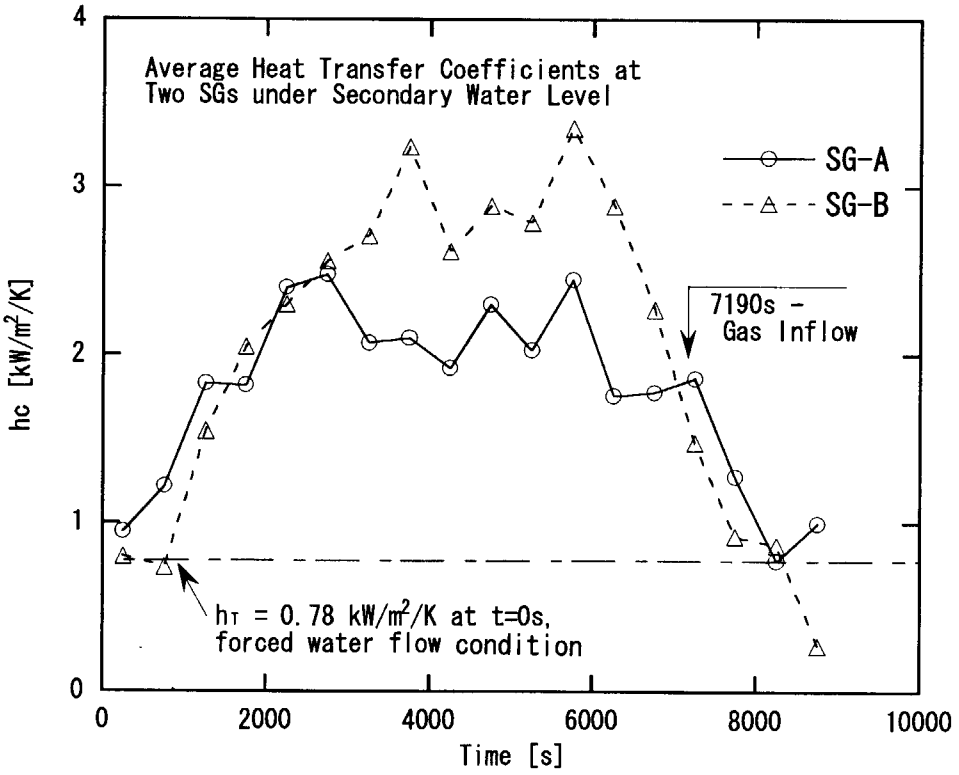

Fig.4.2.4 Average heat transfer coefficients at SG U-tubes below secondary water level in depressurization process

Appendix－A Measurement List of Experiment SB－PV－03 and Instrumentation Locations

A list of available measurements for experiment SB-PV-03 and related instrumentation locations are presented below in Table A.1 and Figs. A.1 through A.16, respectively. Precise description of the measurement system is shown in Reference [1].

List of Table and Figures

Appendix－B Measurement List and Configuration Data for Primary Mass Estimation

A measurement list and configuration data base are presented in Appendix-B for estimation of primary coolant mass distribution described in Section 4.2.1. Figure B.1 shows a mass distribution map both for the primary and SG secondary systems at initial state in experiment SB-PV-03.

List of Table and Figures

Appendix－C Estimation of Secondary Fluid Mass and SG Heat Transfer

Contents

List of Tables and Figures

C.1 Introduction to Secondary Mass and Energy Estimation

A model to estimate a total primary-to-secondary heat transfer rate at SG U-tubes was developped and applied to the ROSA-V/LSTF experiment, SB-PV-03. Appendix-C presents both models to estimate secondary mass inventory (Section C.2) and total heat transfer rate at each SG (Section C.3) with their uncertainty analyses and related data bases. Estimation of the regional fluid masses in the SG secondary system is necessary not only to check mass balance between remaining fluid mass change during a time period and a net discharged mass from the secondary system during the same period, but also to estimate regional fluid enthalpy. It is shown in this analysis that uncertainties of the fluid masses both for the RV steam flows and secondary coolant masses in two SGs have the largest influences on an uncertainty of the total heat removal rate.

The previous SG heat transfer model descrived in Reference 12 was revised here (1) to use the mass inventory estimation model for the secondary system, (2) to improve the steam mass calculation passed through the main steam line, relief valve (RV) line or safety valve (SV) line by excluding the valve closure time periods, (3) to use mass flow data consistent with the secondary mass inventory change, (4) to estimate an average heat transfer coefficient at U-tube inner surfaces during the SG depressurization action and (5) to introduce uncertainty analyses for both mass and energy calculation models.

Table C.1 (1) through (3) shows measurement data lists for estimation of fluid mass and enthalpy in each steam and feedwater flow, those remaining in the secondary fluid systems and metal stored heat both in the U-tube walls and SG vessel walls with their representative regional range. Table C.2 shows configurational data base in a form of elevation and cumulated fluid volumes above bottom level for all SG secondary regions. The regional volumes and average flow areas in boiler regions of SG-A and SG-B are slightly different while their fluid volumes in the downcomer regions are the same.

C.2 Estimation of Secondary Fluid Mass

C.2.1 Estimation of Regional Fluid Masses

A total mass inventory (M [kg]) in each SG secondary system is calculated as a sum of regional fluid masses (M_i [kg]) in region (i), which are determined at each time by using a collapsed water level (L_i [m]) as,

$$M = \Sigma M_i \ , \tag{C.1}$$

$$M_i = \rho_{Gi} V_{oi} + (\rho_{Li} - \rho_{Gi}) V_{Li} \ , \tag{C.2}$$

$$V_{Li} = \text{Function } (L_i) \ , \tag{C.3}$$

$$L_i = (DP_i/g - \rho_{Gi} h_i) / (\rho_{Li} - \rho_{Gi}) \ , \tag{C.4}$$

where ρ_{Li} and ρ_{Gi} [kg/m^3] are liquid and gas phase densities calculated from steam tables with the pressure and average temperature data (Table C.1 (2)), V_{Li} [m^3] is a liquid volume determined as a function of the collapsed water level L_i using the configuration data base (Table C.2), V_{oi} [m^3] is a total regional volume, h_i [m] is a height of the region, DP_i [Pa] is a DP data and g is the gravitational constant.

A total mass inventory at the initial condition (t = 0 s) of experiment SB-PV-03 was estimated as a sum of regional masses for each SG, i.e., M_o = 2552.1 kg for SG-A and 2555.9 kg for SG-B, respectively (refer Table 4.2-2) .

C.2.2 Uncertainty Estimation

Uncertainty of the total coolant mass in each SG secondary side is analyzed here considering mass uncertainties based on regional volume distribution in the secondary side and those caused by variation of thermal properties such as fluid density during the experiment transient (a pressure range from 7.4－1.3 MPa in experiment SB-PV-03), i.e., both uncertain factors varying in time and space in addition to uncertainties of measurement data.

An uncertainty of the regional fluid mass ($\triangle M_i$) can be derived from equation (C.2) as a sum of uncertainties of steam density ($\triangle \rho_{Gi}$), density difference between gas and liquid $\{\triangle(\rho_{Li} - \rho_{Gi})\}$, and liquid volume ($\triangle V_{Li}$), which depend on measurement uncertainties of the pressure, temperatures and liquid levels. The nominal accuracy of secondary pressure is $\triangle P = \pm 0.0539$ MPa, those of temperatures are $\triangle T = \pm 2.63$ K and those of DP and levels are listed in Table A.1.

The uncertainty of liquid volume is dependent on an uncertainty of liquid level ($\triangle L_i$) due to equation (C.3) and $\triangle L_i$ can be derived from equation (C.4) with a simplified form shown below in case of water level formation (i.e., $DP_i/g \gg \rho_{Gi} h_i$) at saturated condition in which fluid density uncertainties are dependent only on pressure uncertainty as,

$$\triangle L_i/L_i = \pm\sqrt{[\{\triangle DP_i/DP_i\}^2 + \{\triangle(\rho_{Li} - \rho_{Gi})/(\rho_{Li} - \rho_{Gi})\}^2]} \ , \tag{C.5}$$

where the second term of equation (C.5) was within ± 0.39 % during the depressurization process (1000－9000s) of the experiment SB-PV-03, and was significantly smaller than the first term which was within ± 7.9 % for all regions except for the steam dome region in which no water level formed. Thus, equation (C.5) can be simplified as,

$$\triangle L_i = (\triangle DP_i / DP_i) \times L_i = \triangle DP_i / \{(\rho_{Li} - \rho_{Gi}) g\} \ . \qquad (C.6)$$

Thus, an uncertainty of regional mass of $\triangle M_i$ can be given by using maximum values of $\triangle L_i$, $\triangle \rho_{Gi}$, $(\rho_{Li} - \rho_{Gi})$ and $\triangle(\rho_{Li} - \rho_{Gi})$ during a time period of (1000－9000 s) and a maximum flow area of $A_{i,max}$ in region (i) as,

$$\triangle M_i = \pm\sqrt{[\{\triangle \rho_{Gi} \times V_{oi}\}^2 + \{(\rho_{Li} - \rho_{Gi}) \times A_{i,max} \times \triangle L_i\}^2 + \{\triangle(\rho_{Li} - \rho_{Gi}) \times V_{Li}\}^2]} \ . \qquad (C.7)$$

Table C.3 shows mass uncertainties of secondary regions in both SGs calculated by this uncertainty estimation method in comparison with initial masses. An uncertainty of fluid mass in the steam dome (Boiler region (11) in Table C.3 was estimated by using $V_{Li} = 0.0\,m^3$ for equation (C.7) accounting no water level formation.

Concludingly, a total mass uncertainty ($\triangle M_j$ [kg], j = A, B) for the SG secondary system was derived as,

$$\triangle M_j = \pm\sqrt{[\Sigma_i (\triangle M_{ij})^2]} \ , \qquad (C.8)$$

and $\triangle M = \pm 65.8$ kg for SG-A and ± 66.6 kg for SG-B, respectively. These uncertainties correspond to ±2.6 % of the initial coolant masses in both SGs.

C.3 Estimation of SG Heat Removal Rate and Heat Transfer Coefficient

C.3.1 Heat Transfer Model at SGs

A total heat transferred from the primary system to secondary system (Q_{Uj} [kJ]), i.e., a total heat removed at each SG during some time period of $\triangle t$ [s] can be estimated from the experiment data shown in Table C.1 by using an equation of,

$$Q_{Uj} = Q_{Dj} - Q_{Fj} + \triangle Q_{Hj} - V_j \times \triangle P_j + \triangle Q_{Tj} - \triangle Q_{Wj} + Q_{Lj} \quad (j = A, B) \ , \qquad (C.9)$$

where Q_{Dj} is an enthalpy of steam flows discharged through the steam line including the RV steam flow, Q_{Fj} is an enthalpy of the feedwater flow, $\triangle Q_{Hj}$ is an enthalpy increase in all secondary fluid regions, $V_j \times \triangle P_j$ is an external work during a pressure decrease of $\triangle P_j$ [kPa] with a total volume of V_j [m^3], $\triangle Q_{Tj}$ is an increase of metal stored heat in all U-tubes, $\triangle Q_{Wj}$ is a decrease of metal stored heat in all SG vessel walls and others, and Q_{Lj} is an environmental heat loss from all wall outer surfaces. This equation is derived from energy balance at three domains as shown below.

(1) Energy Balance at SG U-tubes

Figure C.1 (1) illustrates an energy balance at a part of SG U-tubes during secondary depressurization action. Namely, a heat (Q_{Uj} [kJ], j=A, B) transfered from the primary fluid to all U-tube inner surfaces during a time period of $\triangle t$ [s] (=t2－t1) is equal to a sum of metal stored heat increase ($\triangle Q_{Tj}$ [kJ]) in all U-tube walls and a heat (Q_{Sj} [kJ]) transfered from all U-tube outer surfaces to the secondary fluid as,

$$Q_{Uj} = Q_{Sj} + \triangle Q_{Tj} \ . \tag{C.10}$$

The stored heat increase $\triangle Q_{Tj}$ is estimated as a sum of regional stored heat increase at region (i) as,

$$\triangle Q_{Tj} = \Sigma_i \triangle Q_{Tij} \ , \tag{C.11}$$

$$\triangle Q_{Tij} = M_{ij} \times C_{Pij} \times (TW_{ij,t2} - TW_{ij,t1}), \tag{C.12}$$

where M_{ij} [kg] is a metal mass at region (i) shown in Table C.1 (3), C_{Pij} [kJ/kg/K] is an average specific energy of the metal wall of which average temperature increases from $TW_{ij,t1}$ [K] to $TW_{ij,t2}$ [K]. The specific heat for the U-tube materials is shown in Table C.4 and representative temperatures for each U-tube region are listed in Table C.1 (3) to derive an average temperature (TW_{ij}) in the region (i).

(2) Energy Balance at Vessel Walls and Others

Figure C.1 (2) illustrates an energy balance at a part of SG vessel walls and others during secondary depressurization action. Namely, a decreased stored heat ($\triangle Q_{Wj}$ [kJ]) in all metal parts is equal to a sum of a heat transfered from all metal surfaces to the secondary fluid (Q_{Wj} [kJ]) and an environmental heat loss through all vessel outer surfaces (Q_{Lj} [kJ]) during a time period of $\triangle t$ as,

$$\triangle Q_{Wj} = Q_{Wj} + Q_{Lj} \ . \tag{C.13}$$

The stored heat decrease $\triangle Q_{Wj}$ is estimated as a sum of regional stored heat decreases at region (i) as,

$$\triangle Q_{Wj} = \Sigma_i \triangle Q_{Wij} , \quad (C.14)$$

$$\triangle Q_{Wij} = M_{ij} \times C_{Pij} \times (TW_{ij,t2} - TW_{ij,t1}), \quad (C.15)$$

where M_{ij}, C_{Pij} and TW_{ij} are metal mass, specific heat and average wall temperatures of the SG vessel walls and others as shown in Table C.1 (3) and Table C.4. A total heat loss at the SG outer surfaces ($Q_{Lj} = Q_{HL,j} \times \triangle t$) was estimated by using a function of heat loss rate (Q_{HL} [kW]) given by the SG inside temperature as shown in Table C.5.

(3) Energy Balance in Secondary Fluid System

Figure C.1 (3) illustrates an energy balance in the SG secondary fluid during the secondary depressurization action. Namely, an energy increase in all secondary fluid in a time period of $\triangle t$ is balanced with a net enthalpy inflow at the steam and feed-water lines and heat inflows from the U-tube outer walls and SG vessel wall inner walls as,

$$\triangle Q_{Hj} - V_j \times \triangle P_j = Q_{Fj} - Q_{Dj} + Q_{Sj} + Q_{Wj} , \quad (C.16)$$

$$\triangle Q_{Hj} = \Sigma_i \triangle Q_{Hij} , \quad (C.17)$$

where $\triangle Q_{Hj}$ [kJ] is a sum of regional fluid enthalpies ($\triangle Q_{Hij}$) which is estimated by a next equation with the regional measurement data (Table C.1 (2)) and the configuration data base (Table C.2) as in the mass inventory estimation (Section C.2) as,

$$\triangle Q_{Hij} = (\rho_{Lij} \times h_{Lij} \times V_{Lij} + \rho_{Gij} \times h_{Gij} \times V_{Gij})_{t2} - (\rho_{Lij} \times h_{Lij} \times V_{Lij} + \rho_{Gij} \times h_{Gij} \times V_{Gij})_{t1} , \quad (C.18)$$

$$V_{Gij} = V_{oij} - V_{Lij} , \quad (C.19)$$

V [m^3] is a total secondary side volume, V_{Li} and V_{Gi} [m^3] are regional water volume and steam volume, h_{Li} and h_{Gi} [kJ/kg] are specific enthalpies of water and steam, respectively.

The enthalpy of steam flows (Q_{Dj} [kJ]) is a sum of enthalpy flows at the main steam line (Q_{Mj} [kJ]), RV line (Q_{Rj} [kJ]) and SV line (Q_{Vj} [kJ]) during a time period of $\triangle t$ ($= \Sigma_k \triangle t_k$) at each SG (j = A, B) as,

$$Q_{Mj} = \Sigma_k W_{Mjk} \times h_{Gjk} \times \triangle t_k \ , \quad (C.20)$$

$$Q_{Rj} = \Sigma_k W_{Rjk} \times h_{Gjk} \times \triangle t_k \ , \quad (C.21)$$

$$Q_{Vj} = \Sigma_k W_{Vjk} \times h_{Gjk} \times \triangle t_k \ , \quad (C.22)$$

$$Q_{Dj} = Q_{Mj} + Q_{Rj} + Q_{Vj} \ , \quad (C.23)$$

where W_{Mj} [kg/s] is a mass flow rate at the main steam line, W_{Rj} [kg/s] is a mass flow rate at the RV line, W_{Vj} [kg/s] is a mass flow rate at the SV line, and Σ_k means a time integration during the time period of $\triangle t$. These steam flow rates are set to zero for each valve closure period.

The enthalpy of feedwater flow (Q_{Fj} [kJ]) is similarly calculated as,

$$Q_{Fj} = \Sigma_k W_{Fjk} \times h_{Ljk} \times \triangle t_k \ , \quad (C.24)$$

where W_{Fj} [kg/s] is a mass flow rate of the main feedwater or auxiliary feedwater.

(4) Modification for Over-estimated RV Steam Mass Flow

In the experiment SB-PV-03, the RV steam flow rates showed some zero shifts at two SGs (see FE 27 in Fig. 4.1.8) and it caused large discrepancy in the secondary mass balance as shown in Section 4.2.2 (1). A corrected steam mass flow rate (W_{Rj}* [kg/s]) can be given by subtracting excess steam mass flow rate of $\triangle W_{Sj}$ [kg/s] which is derived from an average excess fluid mass compared with a decreased secondary fluid mass during the depressurization period (1000－9000 s) as,

$$W_{Rj}^* = W_{Rj} - \triangle W_{Sj} \ , \quad (C.25)$$

$$\triangle W_{Sj} = \{(\Sigma_k W_{Rjk} \times \triangle t_k - \Sigma_k W_{Fjk} \times \triangle t_k) - (M_{j,\,1000s} - M_{j,\,9000s})\} / 8000 \ , \quad (C.26)$$

where Σ_k means time integration for this period. Thus, $\triangle W_{Sj}$ was estimated as 0.0921 kg/s for SG-A and 0.0518 kg/s for SG-B, respectively.

By introducing W_{Rj}* instead of W_{Rj} in equation (C.21), modification of the enthalpy of steam flows (Q_{Dj}) can be conducted, which is consistent with the secondary fluid mass inventory.

(5) Total Heat Removal Rate and Condensed Water Flow Rate

Finally, the heats transfered from U-tubes (Q_{Sj}) and SG vessel walls (Q_{wj}) into secondary fluid given in the equations (C.10) and (C.13), respectively, are introduced to the equation (C.16) to derive the equation (C.9). A sum of Q_{UA} and Q_{UB} gives a total

heat (Q_U [kJ]) removed from the primary fluid to both secondary sides, and an average value of this removed heat during a time period of $\triangle t$ gives an average total heat removal rate ($Q_U/\triangle t$ [kW]), which can be compared with the core power (Q_C [kW]) in the SG depressurization process on the view point of effectiveness of this AM action to cool the primary loops.

$$Q_U = Q_{UA} + Q_{UB} \tag{C.27}$$

$$Q_U/\triangle t = Q_{UA}/\triangle t + Q_{UB}/\triangle t \tag{C.28}$$

A total heat removal rate during each time period can be used to estimate an average mass flow rate of the condensed water (W_C [kg/s]) at all U-tube inner surfaces with an average latent heat of steam, q_L [kJ/kg], at a middle time of period ($\triangle t$) as,

$$W_C = (Q_U/\triangle t)/q_L \ . \tag{C.29}$$

This mass flow rate is equivalent to a total volumetric steam flow rate of V_S [m^3/s] flowed into two SGs by using average value of saturated steam density of ρ'' [kg/m^3] in the time period as,

$$V_S = W_C/\rho'' \ . \tag{C.30}$$

(6) Average Heat Transfer Coefficient under Secondary Water Level

By using each SG heat removal rate ($Q_{Uj}/\triangle t$ [kW]) at each SG ($j = A, B$), an average heat transfer coefficient (h_{Tj} [kW/m^2/K]) at all U-tube inner surfaces (A_{Tj} [m^2]) can be defined during a time period of $\triangle t$ as,

$$h_{Tj} = (Q_{Uj}/\triangle t)/\{A_{Tj} \times (T_P - T_{Sj})\} \ , \tag{C.31}$$

where T_P [K] is a saturation temperature in the primary system (represented by RC 200) and T_{Sj} [K] is a secondary saturation temperature (RC 202 for SG-A or 203 for SG-B).

On the other hand, an average steam condensation heat transfer coefficient at U-tubes below the secondary water level (h_{Cj} [kW/m^2/K]) can be approximated by assuming that an SG heat removal rate above the secondary water level is negligiblly small compared with that below the secondary water level as in the SG depressurization process of the experiment SB-PV-03 (super-heated steam conditions were observed both in the U-tubes and secondary sides at the regions above the secondary water level). Thus an average value of h_{Cj} in a time period of $\triangle t$ can be approximated as,

$$h_{cj} = (Q_{Uj}/\triangle t)/\{A_{cj} \times (T_p - T_{sj})\} \ , \qquad (C.32)$$

where A_{cj} [m^2] is an U-tube inner surface area at the region under secondary water level, in which steam condensation phenomena is observed.

C.3.2 Uncertainty Estimation

An uncertainty of the total heat removed at each SG ($\triangle Q_{Uj}$ [kJ]) can be given as a sum of uncertainties of the terms in equation (C.9) as,

$$\triangle Q_{Uj} = \pm\sqrt{[\ (\triangle Q_{Dj})^2 + (\triangle Q_{Fj})^2 + \{\triangle(\triangle Q_{Hj})\}^2 + \{\triangle(V_j \times \triangle P_j)\}^2 + \{\triangle(\triangle Q_{Tj})\}^2 + \{\triangle(\triangle Q_{Wj})\}^2 + (\triangle Q_{Lj})^2\ ]} \ . \qquad (C.33)$$

Estimation of these unsertainty terms during a time period of $\triangle t$ [s] is shown below.

(1) Uncertainties of Enthalpy in Steam and Feedwater Flows

In the secondary depressurization process of the experiment SB-PV-03 (1000 - 9000 s), there are no steam flows through the main steam line and SV line but RV line. There is also no main feedwater flow but the AFW flow in the same process. Thus, uncertainties of enthalpies of these RV steam flow and AFW flow are estimated as follows. Equations (C.21) and (C.25) are reformed by using fluid masses (M_G or M_F [kg]) accounted in a time period of $\triangle t$ and average fluid enthalpies ($h_{G,AVE}$ or $h_{L,AVE}$ [kJ/kg]) as,

$$Q_{Dj} = \Sigma_k\ W_{Rjk}^* \times h_{Gjk} \times \triangle t_k = h_{Gj,AVE} \times M_{Gj} \ , \qquad (C.34)$$

$$M_{Gj} = \Sigma_k\ W_{Rjk}^* \times \triangle t_k \ , \qquad (C.35)$$

$$Q_{Fj} = \Sigma_k\ W_{Fjk} \times h_{Ljk} \times \triangle t_k = h_{Lj,AVE} \times M_{Fj} \ , \qquad (C.36)$$

$$M_{Fj} = \Sigma_k\ W_{Fjk} \times \triangle t_k \ . \qquad (C.37)$$

Thus, relative uncertainties of Q_{Dj} and Q_{Fj} can be given in a form of,

$$\triangle Q_{Dj}/Q_{Dj} = \pm\sqrt{[(\triangle h_{Gj}/h_{Gj,AVE})^2 + (\triangle M_{Gj}/M_{Gj})^2]} \ , \qquad (C.38)$$

$$\triangle Q_{Fj}/Q_{Fj} = \pm\sqrt{[(\triangle h_{Lj}/h_{Lj,AVE})^2 + (\triangle M_{Fj}/M_{Fj})^2]} \ , \qquad (C.39)$$

by using uncertainties of enthalpies ($\triangle h_{Gj}$, $\triangle h_{Lj}$) and masses ($\triangle M_{Gj}$, $\triangle M_{Fj}$). The relative uncertainty of steam enthalpy during the period (1000 - 9000 s) and that of AFW enthalpy in a period (1000 - 2753 s) were estimated in correspondence to the accuracies of pressure (±0.0539 MPa) and fluid temperatures (±2.63 K) as

$\triangle h_{Gj}/h_{Gj,AVE} = \pm 0.6\,\%$ for steam flow ,
$\triangle h_{Lj}/h_{Lj,AVE} = \pm 7.0\,\%$ for AFW flow .

The higher relative uncertainty of the AFW enthalpy is due to low specific enthalpy of the low temperature water (T = 310 K).

On the other hand, relative uncertainties of these masses were estimated using the mass flow accuracies of $\triangle W_R = \pm 0.07$ kg/s and $\triangle W_F = \pm 0.05$ kg/s for their maximum masses passed in a time period of $\triangle t = 500$ s as,

$\triangle M_{Gj}/M_{Gj} = (\pm 0.07 \times 500\,\text{kg})/(329\,\text{kg}) = \pm 10.6\,\%$ for SG-A ,
$\triangle M_{Gj}/M_{Gj} = (\pm 0.07 \times 500\,\text{kg})/(341\,\text{kg}) = \pm 10.3\,\%$ for SG-B ,
$\triangle M_{Fj}/M_{Fj} = (\pm 0.05 \times 500\,\text{kg})/(299\,\text{kg}) = \pm\ 8.4\,\%$ for SG-A ,
$\triangle M_{Fj}/M_{Fj} = (\pm 0.05 \times 500\,\text{kg})/(381\,\text{kg}) = \pm\ 6.6\,\%$ for SG-B .

Thus, the relative uncertainties of Q_{Dj} and Q_{Fj} were approximated as,

$\triangle Q_{Dj} / Q_{Dj} = \pm 10.6\,\%$ for SG-A, $\pm 10.3\,\%$ for SG-B , (C. 40)
$\triangle Q_{Fj} / Q_{Fj} = \pm 10.9\,\%$ for SG-A, $\pm\ 9.6\,\%$ for SG-B . (C. 41)

Maximum enthalpy flows at RV and AFW lines during 500 s were estimated for the depressurization process as, $Q_{DA} = 7.69 \times 10^5$ kJ, $Q_{DB} = 8.73 \times 10^5$ kJ, $Q_{FA} = 4.6 \times 10^4$ kJ, $Q_{FB} = 6.4 \times 10^4$ kJ, respectively. Therefore, uncertainties of these enthalpies are derived as,

$\triangle Q_{DA} = \pm 8.15 \times 10^4$ kJ for SG-A , (C. 42)
$\triangle Q_{DB} = \pm 8.99 \times 10^4$ kJ for SG-B , (C. 43)
$\triangle Q_{FA} = \pm 0.50 \times 10^4$ kJ for SG-A , (C. 44)
$\triangle Q_{FB} = \pm 0.61 \times 10^4$ kJ for SG-B . (C. 45)

(2) Uncertainty of Secondary Fluid Energy

Uncertainty of the external work $\{\triangle(V_j \times \triangle P_j),\ j = A, B\}$ due to the pressure accuracy (± 0.0539 MPa) is estimated for both SGs with total secondary volume of $V_j = 7.0\,\text{m}^3$ as,

$\triangle(V_j \times \triangle P_j) = \pm 3.8 \times 10^2$ kJ . (C. 46)

A total uncertainty of all secondary fluid enthalpy (Q_H) at each time is given as a sum of uncertainties of the regional fluid enthalpies as,

$$\triangle(Q_{Hi}) = \pm\sqrt{[\ \Sigma_i\{\triangle(Q_{Hij})\}^2]}\ , \tag{C.47}$$

where $\triangle(Q_{Hij})$ can be estimated for each secondary region (i) with similar manners as in the fluid mass uncertainty estimation shown in Section C.2.2. Namely, $\triangle M_i$ in equation (C.7) is replaced to $\triangle(Q_{Hi})$ by replacing fluid density (ρ) to ($\rho \times h$) at each SG as,

$$\begin{aligned}\triangle(Q_{Hi}) = \pm\sqrt{[\ \{V_{0i}\times\triangle(\rho_{Gi}\times h_{Gi})\}^2+\{(\rho_{Li}\times h_{Li}-\rho_{Gi}\times h_{Gi})\times A_{i,max}\times\triangle L_i\}^2}\\ +\{\triangle(\rho_{Li}\times h_{Li}-\rho_{Gi}\times h_{Gi})\times V_{Li}\}^2\ ]\ .\end{aligned} \tag{C.48}$$

Table C.6 shows a result of enthalpy uncertainty in each SG secondary region, which was calculated by estimating uncertainty of each term in equation (C.48) during each 500 s in the depressurization process (1000－9000 s), and is compared with initial fluid enthalpy in each region. In the steam dome of boiler region (11), the third term in the root of equation (C.48) is set to zero as a result of no water level formation. It is shown that a total uncertainty of secondary fluid enthalpy is

$\triangle(Q_{Hi}) = \pm 6.26\times10^4$ kJ, $\pm$ 1.7% of the initial fluid enthalpy for SG-A ,
$\triangle(Q_{Hi}) = \pm 6.33\times10^4$ kJ, $\pm$ 1.8% of the initial fluid enthalpy for SG-B .

Thus, an uncertainty of a total fluid enthalpy difference ($\triangle(\triangle Q_{Hi})$ [kJ]) during each 500 s can be derived by multiplying $\sqrt{2}$ for these $\triangle(Q_{Hi})$ as,

$$\triangle(\triangle Q_{Hi}) = \pm 8.85\times10^4\ \text{kJ},\quad \text{for SG-A}\ , \tag{C.49}$$
$$\triangle(\triangle Q_{Hi}) = \pm 8.95\times10^4\ \text{kJ},\quad \text{for SG-B}\ , \tag{C.50}$$

and these uncertainties are used for the uncertainty estimation of the total heat removal rates.

It should be noted that the second term in the root of equation (C.48) is influencially large due to the large uncertainty of water level ($\triangle L_i$) compared with other uncertain factors. The first term is negligibly small compared with the second term. The third term is approximately less than 14% of the second term in most regions except for the boiler region (2) where the third term was approximately 24% of the second term. Therefore, it is possible to approximate $\triangle(Q_{Hi})$ by neglecting the first term in equation (C.48).

(3) Uncertainties of Metal Stored Heats

Uncertainty of a total metal stored heat change during a time period of $\triangle t$ is given by a sum of each regional stored heat change ($\triangle(\triangle Q_{Ti})$ for U-tubes and $\triangle(\triangle Q_{wi})$ for SG vessel wall or others) as,

$$\triangle(\triangle Q_T) = \pm\sqrt{[\ \Sigma_i\{\triangle(\triangle Q_{Ti})\}^2]} \tag{C.51}$$

$$\triangle(\triangle Q_w) = \pm\sqrt{[\ \Sigma_i\{\triangle(\triangle Q_{wi})\}^2]}\ , \tag{C.52}$$

and the metal masses and specific heats for SG-A and SG-B are almost the same.

By the equations (C.12) and (C.15), uncertainties of regional stored heat change at each SG consist of three terms, i.e., an uncertainty of regional metal mass ($\triangle M_i$), that of metal specific heat at constant pressure ($\triangle C_{Pi}$), and that of metal temperature change $\triangle(TW_{i,\,t2}-TW_{i,\,t1})$. As the former two terms have significantly small relative uncertainties compared with a relative uncertainty of the third term, an uncertainty of the regional metal stored heat can be represented only by the third term in the next form of,

$$\triangle(\triangle Q_{Ti}) = M_i \times C_{Pi} \times \triangle(TW_{i,\,t2}-TW_{i,\,t1})\ , \tag{C.53}$$

$$\triangle(\triangle Q_{wi}) = M_i \times C_{Pi} \times \triangle(TW_{i,\,t2}-TW_{i,\,t1})\ . \tag{C.54}$$

In the experiment SB-PV-03, the U-tube metal temperatures decreased approximately 100 K during the depressurization process (1000－9000 s), i.e., 6.25 K during 500 s in average. On the other hand, an uncertainty of this metal temperature change of 6.25 K, which was measured by the same thermocouple, can be less than an accuracy of the temperature ($\pm$ 2.75 K) guaranteed for a wider measurement range of (270-720 K) than this temperature change as,

magnitude of $\triangle(TW_{i,\,t2}-TW_{i,\,t1}) < 2.75$ K for U-tubes .and tube-sheets and
magnitude of $\triangle(TW_{i,\,t2}-TW_{i,\,t1}) < 2.63$ K for SG vessel walls and others.

These temperature accuracies are introduced to equations (C.53) and (C.54) as a maximum uncertainties of the metal temperature changes. Thus, an uncertainty of regional metal stored heat change during each 500 s was estimated as shown in Table C.7. Uncertainties of total metal stored heat change for the U-tubes and SG walls were estimated for both SGs as,

$$\triangle(\triangle Q_{Tj}) = \pm\ 3.1\times10^3\ \mathrm{kJ}\ , \tag{C.55}$$

$$\triangle(\triangle Q_{Wj}) = \pm 1.10\times10^{4}\ \mathrm{kJ}\ . \tag{C.56}$$

(4) Uncertainties of Environmental Heat Loss

Uncertainty of environmental heat loss ($\triangle Q_{HLj}$ [kW]) at each SG was experimentally estimated in the reference [14] as,

$$\triangle Q_{HLA} = \pm 5.17\ \mathrm{kW}\ \text{for SG-A}\ ,$$
$$\triangle Q_{HLB} = \pm 3.11\ \mathrm{kW}\ \text{for SG-B}\ .$$

Thus, uncertainties of $\triangle Q_{Lj}$ [kJ] at both SGs during $\triangle t = 500$ s can be derived as,

$$\triangle Q_{LA} = \triangle Q_{HLA}\times\triangle t = \pm 2.6\times10^{3}\ \mathrm{kJ}\ \text{for SG-A}\ , \tag{C.57}$$
$$\triangle Q_{LB} = \triangle Q_{HLB}\times\triangle t = \pm 1.6\times10^{3}\ \mathrm{kJ}\ \text{for SG-B}\ . \tag{C.58}$$

(5) Uncertainties of Total Heat Removal Rate and Heat Transfer Coefficient

By using the uncertainty values estimated above for all terms in equation (C.33), uncertainties of total heat ($\triangle Q_{Uj}$ [kJ]) removed at two SGs in a time period of 500 s can be given as follows with relative magnitudes to the largest term for comparison,

$$\triangle Q_{UA} = \pm\sqrt{[\ (\triangle Q_{DA})^2+(\triangle Q_{FA})^2+\{\triangle(\triangle Q_{HA})\}^2+\{\triangle(V_A\times\triangle P_A)\}^2+\{\triangle(\triangle Q_{TA})\}^2}$$
$$+\{\triangle(\triangle Q_{WA})\}^2+(\triangle Q_{LA})^2\ ]$$

$$= [\pm\sqrt{\ \{(8.15)^2+(0.50)^2+(8.85)^2+(0.04)^2+(0.31)^2+(1.1)^2+(0.26)^2\}\ }]\times10^{4}$$
$$(\ 0.848\ :\ 0.003\ :\ 1.000\ :\ 0.00002\ :\ 0.001\ :\ 0.015\ :\ 0.001\ )$$

$$= \pm 1.21\times10^{5}\ \mathrm{kJ}\ , \tag{C.59}$$

and similarly for SG-B as,

$$\triangle Q_{UB} = [\pm\sqrt{\ \{(8.99)^2+(0.61)^2+(8.95)^2+(0.04)^2+(0.31)^2+(1.1)^2+(0.16)^2\}\ }]\times10^{4}$$
$$(\ 1.000\ :\ 0.005\ :\ 0.991\ :\ 0.00002\ :\ 0.001\ :\ 0.015\ :\ 0.0003\ )$$

$$= \pm 1.28\times10^{5}\ \mathrm{kJ}\ . \tag{C.60}$$

An uncertainty of average total heat removal rate at each SG in a time period of $\triangle t$ can be derived from the uncertainty of $\triangle Q_{Uj}$ as,

$$\triangle Q_{UA}/\triangle t = \pm 242\ \mathrm{kW}\ \text{for SG-A}\ , \tag{C.61}$$

$$\triangle Q_{UB}/\triangle t = \pm 256\,kW \text{ for SG-B}\ , \tag{C.62}$$

and an uncertainty of average total heat transfer rate at two SGs is given as,

$$\triangle Q_U/\triangle t = \pm\sqrt{[\,\{\triangle Q_{UA}/\triangle t\}^2+\{\triangle Q_{UB}/\triangle t\}^2]} = \pm 352\,kW\ . \tag{C.63}$$

An uncertainty of the total mass flow rate of condensed water (W_C [kg/s]) in equation (C.29) can be derived accounting only uncertainty of $\triangle(Q_U/\triangle t)$ with a maximum latent heat of $q_{L.max} = 1970.7$ kJ/kg during the depressurization process (1000－9000 s) as,

$$\triangle W_C = (\triangle Q_U/\triangle t)/q_{L.max} = \pm 0.18\,kg/s\ . \tag{C.64}$$

An uncertainty of the average heat transfer coefficients defined in equation (C.31) for all U-tube walls can be estimated accounting an uncertainty of the average heat removal rate ($\triangle Q_{Uj}/\triangle t$ [kW]), that of the heat transfer area of $\triangle A_{Tj}$ [m^2] and those of the saturation temperature difference between the primary and secondary systems $\{\triangle(T_P-T_{Sj})$ [K]$\}$ as,

$$\triangle h_{Tj}/h_{Tj} = \pm\sqrt{[\,\{\triangle(Q_{Uj}/\triangle t)/(Q_{Uj}/\triangle t)\}^2+(\triangle A_{Tj}/A_{Tj})^2+\{\triangle(T_P-T_{Sj})/(T_P-T_{Sj})\}^2]}\ , \tag{C.65}$$

$$\triangle A_{Tj}/A_{Tj} = \triangle L_{Cj}/L_{Cj}\ , \tag{C.66}$$

where $\triangle L_{Cj}/L_{Cj}$ is a relative uncertainty of the secondary water level and j = A, B. It the case of experiment SB-PV-03, the first term of equation (C.65) was less than 1.0 for most time periods and the second term was far less than 1.0 due to the water level accuracy of $\triangle L_{Cj} = \pm 0.38$ m. As to the third term, however, the temperature difference between the primary and secondary systems was less than 4.0 K in most cases in the SG depressurization process (refer Tables 4.2-6 (1) and (2)), and it was significantly smaller than magnitude of the saturation temperature accuracies ($\triangle T_P = \pm 17.64$ K for RC 200 and $\triangle T_S = \pm 7.82$ K for RC 202 and RC 203 in Reference [1]). Therefore, the relative uncertainty of $\triangle h_{Tj}/h_{Tj}$ was not only strongly dependent on the third term but also more than 100 % in most cases. Consequently, the heat transfer coefficient estimated for LSTF experiments with SG depressurization action has only meanings on the view point of qualitative change during the experiment.

Table A.1 List of available measurements for experiment SB-PV-03 (1/20)

SEQ No.	Function ID.	Tagname	Location	Range		Unit	Uncertainty	
				LO	HI		±ABS.	±%FR
1	TE 1	TE010A-HLA	HLA Vessel-Side CPT	270	720	K	2.75	0.61
2	TE 2	TE010B-HLA	HLA Vessel-Side CPT	270	720	K	2.75	0.61
3	TE 3	TE010C-HLA	HLA Vessel-Side CPT	270	720	K	2.75	0.61
4	TE 4	TE010D-HLA	HLA Vessel-Side CPT	270	720	K	2.75	0.61
5	TE 5	TE010E-HLA	HLA Vessel-Side CPT	270	720	K	2.75	0.61
6	TE 6	TE020C-HLA	HLA Pipe Top	270	720	K	2.75	0.61
7	TE 7	TE020D-HLA	HLA Pipe Bottom	270	720	K	2.75	0.61
8	TE 8	TE030C-HLA	HLA Pipe Top	270	720	K	2.75	0.61
9	TE 10	TE040A-HLA	HLA SG-Side CPT	270	720	K	2.75	0.61
10	TE 11	TE040B-HLA	HLA SG-Side CPT	270	720	K	2.75	0.61
11	TE 12	TE040C-HLA	HLA SG-Side CPT	270	720	K	2.75	0.61
12	TE 13	TE040D-HLA	HLA SG-Side CPT	270	720	K	2.75	0.61
13	TE 14	TE040E-HLA	HLA SG-Side CPT	270	720	K	2.75	0.61
14	TE 15	TE050C-LSA	LSA Upflow Leg	270	720	K	2.75	0.61
15	TE 16	TE070C-CLA	CLA Pipe Top	270	720	K	2.75	0.61
16	TE 17	TE070D-CLA	CLA Pipe Bottom	270	720	K	2.75	0.61
17	TE 18	TE080C-CLA	CLA Pipe Top	270	720	K	2.75	0.61
18	TE 20	TE090A-CLA	CLA Vessel-Side CPT	270	720	K	2.75	0.61
19	TE 21	TE090B-CLA	CLA Vessel-Side CPT	270	720	K	2.75	0.61
20	TE 22	TE090C-CLA	CLA Vessel-Side CPT	270	720	K	2.75	0.61
21	TE 23	TE090D-CLA	CLA Vessel-Side CPT	270	720	K	2.75	0.61
22	TE 24	TE090E-CLA	CLA Vessel-Side CPT	270	720	K	2.75	0.61
23	TE 25	TE100-HLA	HLA-CLA Average	270	720	K	2.75	0.61
24	TE 27	TE150B-HLB	HLB Vessel-Side CPT	270	720	K	2.75	0.61
25	TE 28	TE150C-HLB	HLB Vessel-Side CPT	270	720	K	2.75	0.61
26	TE 29	TE150D-HLB	HLB Vessel-Side CPT	270	720	K	2.75	0.61
27	TE 30	TE150E-HLB	HLB Vessel-Side CPT	270	720	K	2.75	0.61
28	TE 31	TE160C-HLB	HLB Pipe Top	270	720	K	2.75	0.61
29	TE 32	TE160D-HLB	HLB Pipe Bottom	270	720	K	2.75	0.61
30	TE 33	TE170C-HLB	HLB Pipe Top	270	720	K	2.75	0.61
31	TE 35	TE180A-HLB	HLB SG-Side CPT	270	720	K	2.75	0.61
32	TE 36	TE180B-HLB	HLB SG-Side CPT	270	720	K	2.75	0.61
33	TE 37	TE180C-HLB	HLB SG-Side CPT	270	720	K	2.75	0.61
34	TE 38	TE180D-HLB	HLB SG-Side CPT	270	720	K	2.75	0.61
35	TE 39	TE180E-HLB	HLB SG-Side CPT	270	720	K	2.75	0.61
36	TE 40	TE190C-LSB	LSB Upflow Leg	270	720	K	2.75	0.61
37	TE 41	TE210C-CLB	CLB Pipe Top	270	720	K	2.75	0.61
38	TE 42	TE210D-CLB	CLB Pipe Bottom	270	720	K	2.75	0.61
39	TE 43	TE220C-CLB	CLB Pipe Top	270	720	K	2.75	0.61
40	TE 46	TE230B-CLB	CLB Vessel-Side CPT	270	720	K	2.75	0.61
41	TE 47	TE230C-CLB	CLB Vessel-Side CPT	270	720	K	2.75	0.61
42	TE 48	TE230D-CLB	CLB Vessel-Side CPT	270	720	K	2.75	0.61
43	TE 49	TE230E-CLB	CLB Vessel-Side CPT	270	720	K	2.75	0.61
44	TE 50	TE240-HLB	HLB-CLB Average	270	720	K	2.75	0.61
45	TE 51	TE270C-PR	PZR Spray Line	270	720	K	2.75	0.61
46	TE 52	TE280C-PR	PZR Surge Line	270	720	K	2.75	0.61
47	TE 55	TE430-SGA	SGA Feedwater Line	270	670	K	2.63	0.66
48	TE 56	TE440-SGA	SGA Main Steam Line	270	670	K	2.63	0.66
49	TE 57	TE450-SGA	SGA Relief Valve Line	270	670	K	2.63	0.66
50	TE 59	TE470-SGB	SGB Feedwater Line	270	670	K	2.63	0.66
51	TE 60	TE480-SGB	SGB Main Steam Line	270	670	K	2.63	0.66
52	TE 61	TE490-SGB	SGB Relief Valve Line	270	670	K	2.63	0.66
53	TE 63	TE510-SH	MSL Steam Header	270	670	K	2.63	0.66
54	TE 64	TE520-JC	JC Hot Water	270	670	K	2.63	0.66
55	TE 65	TE530-JC	PF Suction Line	270	670	K	2.63	0.66
56	TE 66	TE540-JC	JC Spray Water	270	670	K	2.63	0.66
57	TE 67	TE550-JC	JC Steam Vent Line	270	670	K	2.63	0.66
58	TE 68	TE431-SGA	SGA Downcomer A	270	670	K	2.63	0.66
59	TE 69	TE432-SGA	SGA Downcomer B	270	670	K	2.63	0.66
60	TE 70	TE433-SGA	SGA Downcomer C	270	670	K	2.63	0.66
61	TE 71	TE434-SGA	SGA Downcomer D	270	670	K	2.63	0.66
62	TE 72	TE471-SGB	SGB Downcomer A	270	670	K	2.63	0.66
63	TE 73	TE472-SGB	SGB Downcomer B	270	670	K	2.63	0.66
64	TE 74	TE473-SGB	SGB Downcomer C	270	670	K	2.63	0.66
65	TE 75	TE474-SGB	SGB Downcomer D	270	670	K	2.63	0.66
66	TE 76	TE560C-BU	Break Upstream	270	720	K	2.63	0.66
67	TE 77	TE560D-BU	Break Upstream	270	720	K	2.63	0.66
68	TE 78	TE570C-BU	RSV Spool Piece, Outlet Side	270	720	K	2.63	0.66
69	TE 79	TE570D-BU	RSV Spool Piece, Outlet Side	270	720	K	2.63	0.66
70	TE 80	TE580C-BU	Break Orif. Upstream Top	270	720	K	2.63	0.66
71	TE 81	TE580D-BU	Break Orif. Upstream Bottom	270	720	K	2.63	0.66
72	TE 82	TE590C-BU	Break Orif. Downstream Top	270	720	K	2.63	0.66
73	TE 83	TE590D-BU	Break Orif. Downstream Bottom	270	720	K	2.63	0.66
74	TE 84	TE600-ST	ST Inlet Line	270	470	K	2.3	1.15
75	TE 85	TE610-ST	ST Top Region	270	470	K	2.3	1.15
76	TE 86	TE620-ST	ST Middle Region	270	470	K	2.3	1.15
77	TE 87	TE630-ST	ST Bottom Region	270	470	K	2.3	1.15
78	TE 88	TE640-ST	ST Spray Line	270	470	K	2.3	1.15
79	TE 89	TE650-ACC	Acc-Cold Tank Bottom	270	470	K	2.3	1.15
80	TE 90	TE660-ACC	Acc-Cold Tank Top	270	470	K	2.3	1.15
81	TE 91	TE670-ACC	Acc-Cold Line to CLA	270	470	K	2.3	1.15
82	TE 92	TE680-ACC	Acc-Cold Line to CLB	270	470	K	2.3	1.15

Table A.1 (Cont'd) (2/20)

SEQ No.	Function ID.	Tagname	Location	Range		Unit	Uncertainty	
				LO	HI		±ABS.	±%FR
83	TE 94	TE700-ACH	Acc-Hot Tank Top	270	570	K	2.42	0.81
84	TE 95	TE710-ACH	Acc-Hot Line to CLA	270	570	K	2.42	0.81
85	TE 96	TE720-ACH	Acc-Hot Line to CLB	270	570	K	2.42	0.81
86	TE 97	TE730-HLA	HLA ECCS Nozzle	270	670	K	2.63	0.66
87	TE 98	TE740-LSA	LSA ECCS Nozzle	270	670	K	2.63	0.66
88	TE 99	TE750-CLA	CLA ECCS Nozzle	270	670	K	2.63	0.66
89	TE 100	TE760-HLB	HLB ECCS Nozzle	270	670	K	2.63	0.66
90	TE 101	TE770-LSB	LSB ECCS Nozzle	270	670	K	2.63	0.66
91	TE 102	TE780-CLB	CLB ECCS Nozzle	270	670	K	2.63	0.66
92	TE 103	TE790-PV	PV Bottom ECCS Nozzle	270	670	K	2.63	0.66
93	TE 104	TE800-PV	PV Top ECCS Nozzle	270	670	K	2.63	0.66
94	TE 112	TE880-RWST	RWST Lower Region	270	370	K	2.37	2.37
95	TE 113	TE890-RWST	RWST Middle Region	270	370	K	2.37	2.37
96	TE 115	TE-E066F-PV	Upper Head Bottom	270	970	K	3.49	0.5
97	TE 117	TE-E075F-PV	Upper Head Middle	270	970	K	3.49	0.5
98	TE 118	TE-W075F-PV	Upper Head Middle	270	970	K	3.49	0.5
99	TE 119	TE-E081F-PV	Upper Head Top	270	970	K	3.49	0.5
100	TE 120	TE-W081F-PV	Upper Head Top	270	970	K	3.49	0.5
101	TE 121	TE-E080H-PV	CR Guide Tube Top	270	970	K	3.49	0.5
102	TE 122	TE-W080H-PV	CR Guide Tube Top	270	970	K	3.49	0.5
103	TE 123	TE-E049F-PV	Upper Plenum Bottom	270	970	K	3.49	0.5
104	TE 125	TE-E055F-PV	Upper Plenum Middle	270	970	K	3.49	0.5
105	TE 126	TE-W055F-PV	Upper Plenum Middle	270	970	K	3.49	0.5
106	TE 127	TE-E060F-PV	Upper Plenum Top	270	970	K	3.49	0.5
107	TE 128	TE-W060F-PV	Upper Plenum Top	270	970	K	3.49	0.5
108	TE 129	TE-IN038-B09-UCP	Below Upper Core Plate	270	970	K	3.49	0.5
109	TE 130	TE-IN038-B11-UCP	Below Upper Core Plate	270	970	K	3.49	0.5
110	TE 131	TE-IN038-B01-UCP	Below Upper Core Plate	270	970	K	3.49	0.5
111	TE 132	TE-IN038-B03-UCP	Below Upper Core Plate	270	970	K	3.49	0.5
112	TE 133	TE-IN038-B05-UCP	Below Upper Core Plate	270	970	K	3.49	0.5
113	TE 134	TE-IN038-B07-UCP	Below Upper Core Plate	270	970	K	3.49	0.5
114	TE 135	TE-IN038-B21-UCP	Below Upper Core Plate	270	970	K	3.49	0.5
115	TE 136	TE-IN038-B23-UCP	Below Upper Core Plate	270	970	K	3.49	0.5
116	TE 137	TE-IN038-B02-UCP	Below Upper core Plate	270	970	K	3.49	0.5
117	TE 138	TE-IN038-B06-UCP	Below Upper Core Plate	270	970	K	3.49	0.5
118	TE 139	TE-IN038-B14-UCP	Below Upper Core Plate	270	970	K	3.49	0.5
119	TE 140	TE-IN038-B15-UCP	Below Upper Core Plate	270	970	K	3.49	0.5
120	TE 141	TE-IN038-B18-UCP	Below Upper Core Plate	270	970	K	3.49	0.5
121	TE 142	TE-IN038-B19-UCP	Below Upper Core Plate	270	970	K	3.49	0.5
122	TE 143	TE-IN038-B10-UCP	Below Upper Core Plate	270	970	K	3.49	0.5
123	TE 144	TE-IN038-B12-UCP	Below Upper Core Plate	270	970	K	3.49	0.5
124	TE 145	TE-IN038-B04-UCP	Below Upper Core Plate	270	970	K	3.49	0.5
125	TE 146	TE-IN038-B08-UCP	Below Upper Core Plate	270	970	K	3.49	0.5
126	TE 149	TE-EX040-B09-UCP	Above Upper Core Plate	270	970	K	3.49	0.5
127	TE 150	TE-EX040-B11-UCP	Above Upper Core Plate	270	970	K	3.49	0.5
128	TE 151	TE-EX040-B01-UCP	Above Upper Core Plate	270	970	K	3.49	0.5
129	TE 152	TE-EX040-B03-UCP	Above Upper Core Plate	270	970	K	3.49	0.5
130	TE 153	TE-EX040-B05-UCP	Above Upper Core Plate	270	970	K	3.49	0.5
131	TE 154	TE-EX040-B07-UCP	Above Upper Core Plate	270	970	K	3.49	0.5
132	TE 155	TE-EX040-B21-UCP	Above Upper Core Plate	270	970	K	3.49	0.5
133	TE 156	TE-EX040-B23-UCP	Above Upper Core Plate	270	970	K	3.49	0.5
134	TE 157	TE-EX040-B02-UCP	Above Upper Core Plate	270	970	K	3.49	0.5
135	TE 158	TE-EX040-B06-UCP	Above Upper Core Plate	270	970	K	3.49	0.5
136	TE 159	TE-EX040-B14-UCP	Above Upper Core Plate	270	970	K	3.49	0.5
137	TE 160	TE-EX040-B15-UCP	Above Upper Core Plate	270	970	K	3.49	0.5
138	TE 161	TE-EX040-B18-UCP	Above Upper Core Plate	270	970	K	3.49	0.5
139	TE 162	TE-EX040-B19-UCP	Above Upper Core Plate	270	970	K	3.49	0.5
140	TE 163	TE-EX040-B10-UCP	Above Upper Core Plate	270	970	K	3.49	0.5
141	TE 164	TE-EX040-B12-UCP	Above Upper Core Plate	270	970	K	3.49	0.5
142	TE 165	TE-EX040-B04-UCP	Above Upper Core Plate	270	970	K	3.49	0.5
143	TE 166	TE-EX040-B08-UCP	Above Upper Core Plate	270	970	K	3.49	0.5
144	TE 167	TE-EX040-B22-UCP	Above Upper Core Plate	270	970	K	3.49	0.5
145	TE 168	TE-EX040-B24-UCP	Above Upper Core Plate	270	970	K	3.49	0.5
146	TE 169	TE-IN-002B02-LCPP	Below Lower Core Plate	270	720	K	2.75	0.61
147	TE 171	TE-IN-002B06-LCPP	Below Lower Core Plate	270	720	K	2.75	0.61
148	TE 172	TE-IN-002B07-LCPP	Below Lower Core Plate	270	720	K	2.75	0.61
149	TE 174	TE-IN-002B11-LCPP	Below Lower Core Plate	270	720	K	2.75	0.61
150	TE 177	TE-IN-002B18-LCPP	Below Lower Core Plate	270	720	K	2.75	0.61
151	TE 178	TE-IN-002B20-LCPP	Below Lower Core Plate	270	720	K	2.75	0.61
152	TE 179	TE-IN-002B21-LCPP	Below Lower Core Plate	270	720	K	2.75	0.61
153	TE 184	TE-EX-000B07-LCPP	Above Lower Core Plate	270	720	K	2.75	0.61
154	TE 186	TE-EX-000B11-LCPP	Above Lower Core Plate	270	720	K	2.75	0.61
155	TE 189	TE-EX-000B18-LCPP	Above Lower Core Plate	270	720	K	2.75	0.61
156	TE 190	TE-EX-000B20-LCPP	Above Lower Core Plate	270	720	K	2.75	0.61
157	TE 191	TE-EX-000B21-LCPP	Above Lower Core Plate	270	720	K	2.75	0.61
158	TE 193	TE-N000C-DC	Downcomer EL.0.0m,North	270	720	K	2.75	0.61
159	TE 194	TE-S000C-DC	Downcomer EL.0.0m,South	270	720	K	2.75	0.61
160	TE 196	TE-W000C-DC	Downcomer EL.0.0m,West	270	720	K	2.75	0.61
161	TE 197	TE-N018C-DC	Downcomer EL.1.8m,North	270	720	K	2.75	0.61
162	TE 199	TE-E018C-DC	Downcomer EL.1.8m,East	270	720	K	2.75	0.61
163	TE 200	TE-W018C-DC	Downcomer EL.1.8m,West	270	720	K	2.75	0.61
164	TE 201	TE-N036C-DC	Downcomer EL.3.6m,North	270	720	K	2.75	0.61

Table A.1 (Cont'd) (3/20)

SEQ No.	Function ID.	Tagname	Location	Range		Unit	Uncertainty	
				LO	HI		±ABS.	±%FR
165	TE 202	TE-S036C-DC	Downcomer EL.3.6m,South	270	720	K	2.75	0.61
166	TE 203	TE-E036C-DC	Downcomer EL.3.6m,East	270	720	K	2.75	0.61
167	TE 204	TE-W036C-DC	Downcomer EL.3.6m,West	270	720	K	2.75	0.61
168	TE 206	TE-S060C-DC	Downcomer EL.6.0m,South	270	720	K	2.75	0.61
169	TE 208	TE-W060C-DC	Downcomer EL.6.0m,West	270	720	K	2.75	0.61
170	TE 209	TE-N055C-DC	Downcomer EL.5.5m,North	270	720	K	2.75	0.61
171	TE 210	TE-S055C-DC	Downcomer EL.5.5m,South	270	720	K	2.75	0.61
172	TE 211	TE-C-021-LP	Lower Plenum EL.-2.1m,C	270	720	K	2.75	0.61
173	TE 212	TE-C-018-LP	Lower Plenum EL.-1.8m,C	270	720	K	2.75	0.61
174	TE 213	TE-C-015-LP	Lower Plenum EL.-1.5m,C	270	720	K	3.73	0.83
175	TE 216	TE-C-006-LP	Lower Plenum EL.-0.6m,C	270	720	K	2.75	0.61
176	TE 217	TE-C-005-LP	Lower Plenum EL.-0.5m,C	270	720	K	2.75	0.61
177	TE 218	TE-C-003-LP	Lower Plenum EL.-0.3m,C	270	720	K	2.75	0.61
178	TE 220	TE-B18622	B18 Rod(6,2) Pos.2,Fluid	270	970	K	3.49	0.5
179	TE 221	TE-B18623	B18 Rod(6,2) Pos.3,Fluid	270	970	K	3.49	0.5
180	TE 222	TE-B18624	B18 Rod(6,2) Pos.4,Fluid	270	970	K	3.49	0.5
181	TE 223	TE-B18625	B18 Rod(6,2) Pos.5,Fluid	270	970	K	3.49	0.5
182	TE 226	TE-B18628	B18 Rod(6,2) Pos.8,Fluid	270	970	K	3.49	0.5
183	TE 227	TE-B18629	B18 Rod(6,2) Pos.9,Fluid	270	970	K	3.49	0.5
184	TE 256	TE-B09663	B09 Rod(6,6) Pos.3,Fluid	270	970	K	3.69	0.53
185	TE 257	TE-B09665	B09 Rod(6,6) Pos.5,Fluid	270	970	K	3.69	0.53
186	TE 258	TE-B09666	B09 Rod(6,6) Pos.6,Fluid	270	970	K	3.69	0.53
187	TE 260	TE-B09669	B09 Rod(6,6) Pos.9,Fluid	270	970	K	3.69	0.53
188	TE 277	TE-B14267	B14 Rod(2,6) Pos.7,Fluid	270	970	K	3.49	0.5
189	TE 278	TE-B14269	B14 Rod(2,6) Pos.9,Fluid	270	970	K	3.49	0.5
190	TE 279	TE-B15261	B15 Rod(2,6) Pos.1,Fluid	270	970	K	4.31	0.62
191	TE 280	TE-B15263	B15 Rod(2,6) Pos.3,Fluid	270	970	K	4.31	0.62
192	TE 281	TE-B15265	B15 Rod(2,6) Pos.5,Fluid	270	970	K	4.31	0.62
193	TE 282	TE-B15266	B15 Rod(2,6) Pos.6,Fluid	270	970	K	4.31	0.62
194	TE 283	TE-B15267	B15 Rod(2,6) Pos.7,Fluid	270	970	K	3.69	0.53
195	TE 284	TE-B15269	B15 Rod(2,6) Pos.9,Fluid	270	970	K	3.69	0.53
196	TE 291	TE-B15262	B15 Rod(2,6) Pos.2,Fluid	270	970	K	4.31	0.62
197	TE 292	TE-B15264	B15 Rod(2,6) Pos.4,Fluid	270	970	K	4.31	0.62
198	TE 293	TE-B15268	B15 Rod(2,6) Pos.8,Fluid	270	970	K	3.69	0.53
199	TE 294	TE-B23221	B23 Rod(2,2) Pos.1,Fluid	270	970	K	3.69	0.53
200	TE 295	TE-B23223	B23 Rod(2,2) Pos.3,Fluid	270	970	K	3.69	0.53
201	TE 296	TE-B23225	B23 Rod(2,2) Pos.5,Fluid	270	970	K	3.69	0.53
202	TE 297	TE-B23226	B23 Rod(2,2) Pos.6,Fluid	270	970	K	3.69	0.53
203	TE 298	TE-B23227	B23 Rod(2,2) Pos.7,Fluid	270	970	K	3.69	0.53
204	TE 299	TE-B23229	B23 Rod(2,2) Pos.9,Fluid	270	970	K	3.69	0.53
205	TE 300	TE-B20661	B20 Rod(6,6) Pos.1,Fluid	270	970	K	3.69	0.53
206	TE 301	TE-B20662	B20 Rod(6,6) Pos.2,Fluid	270	970	K	3.69	0.53
207	TE 302	TE-B20663	B20 Rod(6,6) Pos.3,Fluid	270	970	K	3.69	0.53
208	TE 303	TE-B20664	B20 Rod(6,6) Pos.4,Fluid	270	970	K	3.69	0.53
209	TE 305	TE-B20666	B20 Rod(6,6) Pos.6,Fluid	270	970	K	3.69	0.53
210	TE 306	TE-B20667	B20 Rod(6,6) Pos.7,Fluid	270	970	K	0	0
211	TE 307	TE-B20668	B20 Rod(6,6) Pos.8,Fluid	270	970	K	3.69	0.53
212	TE 308	TE-B20669	B20 Rod(6,6) Pos.9,Fluid	270	970	K	0	0
213	TE 309	TE-B22661	B22 Rod(6,6) Pos.1,Fluid	270	970	K	4.31	0.62
214	TE 310	TE-B22662	B22 Rod(6,6) Pos.2,Fluid	270	970	K	4.31	0.62
215	TE 311	TE-B22663	B22 Rod(6,6) Pos.3,Fluid	270	970	K	4.31	0.62
216	TE 312	TE-B22664	B22 Rod(6,6) Pos.4,Fluid	270	970	K	4.31	0.62
217	TE 313	TE-B22665	B22 Rod(6,6) Pos.5,Fluid	270	970	K	4.31	0.62
218	TE 314	TE-B22666	B22 Rod(6,6) Pos.6,Fluid	270	970	K	4.31	0.62
219	TE 315	TE-B22667	B22 Rod(6,6) Pos.7,Fluid	270	970	K	4.31	0.62
220	TE 316	TE-B22668	B22 Rod(6,6) Pos.8,Fluid	270	970	K	4.31	0.62
221	TE 317	TE-B22669	B22 Rod(6,6) Pos.9,Fluid	270	970	K	4.31	0.62
222	TE 318	TE-B24621	B24 Rod(6,2) Pos.1,Fluid	270	970	K	3.69	0.53
223	TE 319	TE-B24623	B24 Rod(6,2) Pos.3,Fluid	270	970	K	3.69	0.53
224	TE 320	TE-B24625	B24 Rod(6,2) Pos.5,Fluid	270	970	K	3.69	0.53
225	TE 321	TE-B24626	B24 Rod(6,2) Pos.6,Fluid	270	970	K	3.69	0.53
226	TE 322	TE-B24627	B24 Rod(6,2) Pos.7,Fluid	270	970	K	3.69	0.53
227	TE 323	TE-B24629	B24 Rod(6,2) Pos.9,Fluid	270	970	K	3.69	0.53
228	TE 324	TE-IN0641-SGA	SGA Inlet Plenum	270	720	K	2.75	0.61
229	TE 325	TE-IN0642-SGA	SGA Inlet Plenum	270	720	K	2.75	0.61
230	TE 326	TE-IN0643-SGA	SGA Inlet Plenum	270	720	K	2.75	0.61
231	TE 330	TE-IN0861-SGA	SGA U-Tube(1,IN) Pos.1	270	720	K	2.75	0.61
232	TE 331	TE-IN0862-SGA	SGA U-Tube(2,IN) Pos.1	270	720	K	2.75	0.61
233	TE 332	TE-IN0863-SGA	SGA U-Tube(3,IN) Pos.1	270	720	K	2.75	0.61
234	TE 333	TE-IN0864-SGA	SGA U-Tube(4,IN) Pos.1	270	720	K	2.75	0.61
235	TE 334	TE-IN0865-SGA	SGA U-Tube(5,IN) Pos.1	270	720	K	2.75	0.61
236	TE 335	TE-IN0866-SGA	SGA U-Tube(6,IN) Pos.1	270	720	K	2.75	0.61
237	TE 336	TE-EX0861-SGA	SGA U-Tube(1,EX) Pos.1	270	720	K	2.75	0.61
238	TE 337	TE-EX0862-SGA	SGA U-Tube(2,EX) Pos.1	270	720	K	2.75	0.61
239	TE 338	TE-EX0863-SGA	SGA U-Tube(3,EX) Pos.1	270	720	K	2.75	0.61
240	TE 339	TE-EX0864-SGA	SGA U-Tube(4,EX) Pos.1	270	720	K	2.75	0.61
241	TE 340	TE-EX0865-SGA	SGA U-Tube(5,EX) Pos.1	270	720	K	2.75	0.61
242	TE 341	TE-EX0866-SGA	SGA U-Tube(6,EX) Pos.1	270	720	K	2.75	0.61
243	TE 344	TE-IN0933-SGA	SGA U-Tube(3,IN) Pos.2	270	720	K	2.75	0.61
244	TE 345	TE-IN0934-SGA	SGA U-Tube(4,IN) Pos.2	270	720	K	2.75	0.61
245	TE 347	TE-IN0936-SGA	SGA U-Tube(6,IN) Pos.2	270	720	K	2.75	0.61
246	TE 348	TE-IN0991-SGA	SGA U-Tube(1,IN) Pos.3	270	720	K	2.75	0.61

Table A.1 (Cont'd) (4/20)

SEQ No.	Function ID.	Tagname	Location	Range		Unit	Uncertainty	
				LO	HI		±ABS.	±%FR
247	TE 349	TE-EX0991-SGA	SGA U-Tube(1,EX) Pos.3	270	720	K	2.75	0.61
248	TE 350	TE-IN0992-SGA	SGA U-Tube(2,IN) Pos.3	270	720	K	2.75	0.61
249	TE 351	TE-EX0992-SGA	SGA U-Tube(2,EX) Pos.3	270	720	K	2.75	0.61
250	TE 352	TE-IN0993-SGA	SGA U-Tube(3,IN) Pos.3	270	720	K	2.75	0.61
251	TE 353	TE-EX0993-SGA	SGA U-Tube(3,EX) Pos.3	270	720	K	2.75	0.61
252	TE 354	TE-IN0994-SGA	SGA U-Tube(4,IN) Pos.3	270	720	K	2.75	0.61
253	TE 355	TE-EX0994-SGA	SGA U-Tube(4,EX) Pos.3	270	720	K	2.75	0.61
254	TE 356	TE-IN0995-SGA	SGA U-Tube(5,IN) Pos.3	270	720	K	2.75	0.61
255	TE 358	TE-IN0996-SGA	SGA U-Tube(6,IN) Pos.3	270	720	K	2.75	0.61
256	TE 359	TE-EX0996-SGA	SGA U-Tube(6,EX) Pos.3	270	720	K	2.75	0.61
257	TE 360	TE-IN1051-SGA	SGA U-Tube(1,IN) Pos.4	270	720	K	2.75	0.61
258	TE 361	TE-IN1052-SGA	SGA U-Tube(2,IN) Pos.4	270	720	K	2.75	0.61
259	TE 362	TE-IN1053-SGA	SGA U-Tube(3,IN) Pos.4	270	720	K	2.75	0.61
260	TE 363	TE-IN1054-SGA	SGA U-Tube(4,IN) Pos.4	270	720	K	2.75	0.61
261	TE 364	TE-IN1055-SGA	SGA U-Tube(5,IN) Pos.4	270	720	K	2.75	0.61
262	TE 365	TE-IN1056-SGA	SGA U-Tube(6,IN) Pos.4	270	720	K	2.75	0.61
263	TE 366	TE-IN1121-SGA	SGA U-Tube(1,IN) Pos.5	270	720	K	2.75	0.61
264	TE 367	TE-EX1121-SGA	SGA U-Tube(1,EX) Pos.5	270	720	K	2.75	0.61
265	TE 368	TE-IN1122-SGA	SGA U-Tube(2,IN) Pos.5	270	720	K	2.75	0.61
266	TE 369	TE-EX1122-SGA	SGA U-Tube(2,EX) Pos.5	270	720	K	2.75	0.61
267	TE 372	TE-IN1124-SGA	SGA U-Tube(4,IN) Pos.5	270	720	K	2.75	0.61
268	TE 373	TE-EX1124-SGA	SGA U-Tube(4,EX) Pos.5	270	720	K	2.75	0.61
269	TE 374	TE-IN1125-SGA	SGA U-Tube(5,IN) Pos.5	270	720	K	2.75	0.61
270	TE 376	TE-IN1126-SGA	SGA U-Tube(6,IN) Pos.5	270	720	K	2.75	0.61
271	TE 377	TE-EX1126-SGA	SGA U-Tube(6,EX) Pos.5	270	720	K	2.75	0.61
272	TE 378	TE-IN1251-SGA	SGA U-Tube(1,IN) Pos.6	270	720	K	2.75	0.61
273	TE 379	TE-EX1251-SGA	SGA U-Tube(1,EX) Pos.6	270	720	K	2.75	0.61
274	TE 380	TE-IN1252-SGA	SGA U-Tube(2,IN) Pos.6	270	720	K	2.75	0.61
275	TE 381	TE-EX1252-SGA	SGA U-Tube(2,EX) Pos.6	270	720	K	2.75	0.61
276	TE 382	TE-IN1253-SGA	SGA U-Tube(3,IN) Pos.6	270	720	K	2.75	0.61
277	TE 383	TE-EX1253-SGA	SGA U-Tube(3,EX) Pos.6	270	720	K	2.75	0.61
278	TE 384	TE-IN1254-SGA	SGA U-Tube(4,IN) Pos.6	270	720	K	2.75	0.61
279	TE 385	TE-EX1254-SGA	SGA U-Tube(4,EX) Pos.6	270	720	K	2.75	0.61
280	TE 387	TE-EX1255-SGA	SGA U-Tube(5,EX) Pos.6	270	720	K	2.75	0.61
281	TE 389	TE-EX1256-SGA	SGA U-Tube(6,EX) Pos.6	270	720	K	2.75	0.61
282	TE 390	TE-IN1371-SGA	SGA U-Tube(1,IN) Pos.7	270	720	K	2.75	0.61
283	TE 392	TE-IN1372-SGA	SGA U-Tube(2,IN) Pos.7	270	720	K	2.75	0.61
284	TE 393	TE-EX1372-SGA	SGA U-Tube(2,EX) Pos.7	270	720	K	2.75	0.61
285	TE 395	TE-EX1373-SGA	SGA U-Tube(3,EX) Pos.7	270	720	K	2.75	0.61
286	TE 396	TE-IN1374-SGA	SGA U-Tube(4,IN) Pos.7	270	720	K	2.75	0.61
287	TE 397	TE-EX1374-SGA	SGA U-Tube(4,EX) Pos.7	270	720	K	2.75	0.61
288	TE 399	TE-EX1375-SGA	SGA U-Tube(5,EX) Pos.7	270	720	K	2.75	0.61
289	TE 400	TE-IN1376-SGA	SGA U-Tube(6,IN) Pos.7	270	720	K	2.75	0.61
290	TE 401	TE-EX1376-SGA	SGA U-Tube(6,EX) Pos.7	270	720	K	2.75	0.61
291	TE 402	TE-IN1501-SGA	SGA U-Tube(1,IN) Pos.8	270	720	K	2.75	0.61
292	TE 403	TE-EX1501-SGA	SGA U-Tube(1,EX) Pos.8	270	720	K	2.75	0.61
293	TE 404	TE-IN1502-SGA	SGA U-Tube(2,IN) Pos.8	270	720	K	2.75	0.61
294	TE 405	TE-EX1502-SGA	SGA U-Tube(2,EX) Pos.8	270	720	K	2.75	0.61
295	TE 406	TE-IN1503-SGA	SGA U-Tube(3,IN) Pos.8	270	720	K	2.75	0.61
296	TE 407	TE-EX1503-SGA	SGA U-Tube(3,EX) Pos.8	270	720	K	2.75	0.61
297	TE 408	TE-IN1504-SGA	SGA U-Tube(4,IN) Pos.8	270	720	K	2.75	0.61
298	TE 409	TE-EX1504-SGA	SGA U-Tube(4,EX) Pos.8	270	720	K	2.75	0.61
299	TE 410	TE-IN1505-SGA	SGA U-Tube(5,IN) Pos.8	270	720	K	2.75	0.61
300	TE 412	TE-IN1506-SGA	SGA U-Tube(6,IN) Pos.8	270	720	K	2.75	0.61
301	TE 414	TE-IN1632-SGA	SGA U-Tube(2,IN) Pos.9	270	720	K	2.75	0.61
302	TE 415	TE-EX1632-SGA	SGA U-Tube(2,EX) Pos.9	270	720	K	2.75	0.61
303	TE 416	TE-IN1633-SGA	SGA U-Tube(3,IN) Pos.9	270	720	K	2.75	0.61
304	TE 417	TE-EX1633-SGA	SGA U-Tube(3,EX) Pos.9	270	720	K	2.75	0.61
305	TE 418	TE-IN1634-SGA	SGA U-Tube(4,IN) Pos.9	270	720	K	2.75	0.61
306	TE 419	TE-EX1634-SGA	SGA U-Tube(4,EX) Pos.9	270	720	K	2.75	0.61
307	TE 420	TE-IN1635-SGA	SGA U-Tube(5,IN) Pos.9	270	720	K	2.75	0.61
308	TE 421	TE-EX1635-SGA	SGA U-Tube(5,EX) Pos.9	270	720	K	2.75	0.61
309	TE 422	TE-IN1701-SGA	SGA U-Tube(1,IN) Pos.10	270	720	K	2.75	0.61
310	TE 424	TE-IN1782-SGA	SGA U-Tube(2,IN) Pos.10	270	720	K	2.75	0.61
311	TE 426	TE-IN1863-SGA	SGA U-Tube(3,IN) Pos.11	270	720	K	2.75	0.61
312	TE 427	TE-IN1864-SGA	SGA U-Tube(4,IN) Pos.11	270	720	K	2.75	0.61
313	TE 429	TE-086C-SGA	SGA Boiling Section Pos.1	270	670	K	2.63	0.66
314	TE 430	TE-099C-SGA	SGA Boiling Section Pos.3	270	670	K	2.63	0.66
315	TE 431	TE-112C-SGA	SGA Boiling Section Pos.5	270	670	K	2.63	0.66
316	TE 432	TE-125C-SGA	SGA Boiling Section Pos.6	270	670	K	2.63	0.66
317	TE 433	TE-137C-SGA	SGA Boiling Section Pos.7	270	670	K	2.63	0.66
318	TE 434	TE-150C-SGA	SGA Boiling Section Pos.8	270	670	K	2.63	0.66
319	TE 435	TE-163C-SGA	SGA Boiling Section Pos.9	270	670	K	2.63	0.66
320	TE 436	TE-178C-SGA	SGA Boiling Section Pos.10	270	670	K	2.63	0.66
321	TE 437	TE-192F-SGA	SGA Boiling Section	270	670	K	2.63	0.66
322	TE 438	TE-208F-SGA	SGA Separator	270	670	K	2.63	0.66
323	TE 439	TE-192C-SGA	SGA Downcomer	270	670	K	2.63	0.66
324	TE 440	TE-208C-SGA	SGA Downcomer	270	670	K	2.63	0.66
325	TE 441	TE-223C-SGA	SGA Steam Dome	270	670	K	2.63	0.66
326	TE 442	TE-245C-SGA	SGA Steam Dome	270	670	K	2.63	0.66
327	TE 443	TE-IN0641-SGB	SGB Inlet Plenum	270	720	K	2.75	0.61
328	TE 444	TE-IN0642-SGB	SGB Inlet Plenum	270	720	K	2.75	0.61

Table A.1 (Cont'd) (5/20)

SEQ No.	Function ID.	Tagname	Location	Range		Unit	Uncertainty	
				LO	HI		±ABS.	±%FR
329	TE 445	TE-IN0643-SGB	SGB Inlet Plenum	270	720	K	2.75	0.61
330	TE 449	TE-IN0861-SGB	SGB U-Tube(1,IN) Pos.1	270	720	K	2.75	0.61
331	TE 450	TE-IN0862-SGB	SGB U-Tube(2,IN) Pos.1	270	720	K	2.75	0.61
332	TE 451	TE-IN0863-SGB	SGB U-Tube(3,IN) Pos.1	270	720	K	2.75	0.61
333	TE 452	TE-IN0864-SGB	SGB U-Tube(4,IN) Pos.1	270	720	K	2.75	0.61
334	TE 453	TE-IN0865-SGB	SGB U-Tube(5,IN) Pos.1	270	720	K	2.75	0.61
335	TE 454	TE-IN0866-SGB	SGB U-Tube(6,IN) Pos.1	270	720	K	2.75	0.61
336	TE 455	TE-EX0861-SGB	SGB U-Tube(1,EX) Pos.1	270	720	K	2.75	0.61
337	TE 456	TE-EX0862-SGB	SGB U-Tube(2,EX) Pos.1	270	720	K	2.75	0.61
338	TE 457	TE-EX0863-SGB	SGB U-Tube(3,EX) Pos.1	270	720	K	2.75	0.61
339	TE 458	TE-EX0864-SGB	SGB U-Tube(4,EX) Pos.1	270	720	K	2.75	0.61
340	TE 460	TE-EX0866-SGB	SGB U-Tube(6,EX) Pos.1	270	720	K	2.75	0.61
341	TE 461	TE-IN0931-SGB	SGB U-Tube(1,IN) Pos.2	270	720	K	2.75	0.61
342	TE 463	TE-IN0933-SGB	SGB U-Tube(3,IN) Pos.2	270	720	K	2.75	0.61
343	TE 464	TE-IN0934-SGB	SGB U-Tube(4,IN) Pos.2	270	720	K	2.75	0.61
344	TE 467	TE-IN0991-SGB	SGB U-Tube(1,IN) Pos.3	270	720	K	2.75	0.61
345	TE 468	TE-EX0991-SGB	SGB U-Tube(1,EX) Pos.3	270	720	K	2.75	0.61
346	TE 469	TE-IN0992-SGB	SGB U-Tube(2,IN) Pos.3	270	720	K	2.75	0.61
347	TE 470	TE-EX0992-SGB	SGB U-Tube(2,EX) Pos.3	270	720	K	2.75	0.61
348	TE 471	TE-IN0993-SGB	SGB U-Tube(3,IN) Pos.3	270	720	K	2.75	0.61
349	TE 472	TE-EX0993-SGB	SGB U-Tube(3,EX) Pos.3	270	720	K	2.75	0.61
350	TE 473	TE-IN0994-SGB	SGB U-Tube(4,IN) Pos.3	270	720	K	2.75	0.61
351	TE 474	TE-EX0994-SGB	SGB U-Tube(4,EX) Pos.3	270	720	K	2.75	0.61
352	TE 476	TE-EX0995-SGB	SGB U-Tube(5,EX) Pos.3	270	720	K	2.75	0.61
353	TE 477	TE-IN0996-SGB	SGB U-Tube(6,IN) Pos.3	270	720	K	2.75	0.61
354	TE 478	TE-EX0996-SGB	SGB U-Tube(6,EX) Pos.3	270	720	K	2.75	0.61
355	TE 479	TE-IN1051-SGB	SGB U-Tube(1,IN) Pos.4	270	720	K	2.75	0.61
356	TE 482	TE-IN1054-SGB	SGB U-Tube(4,IN) Pos.4	270	720	K	2.75	0.61
357	TE 486	TE-EX1121-SGB	SGB U-Tube(1,EX) Pos.5	270	720	K	2.75	0.61
358	TE 487	TE-IN1122-SGB	SGB U-Tube(2,IN) Pos.5	270	720	K	2.75	0.61
359	TE 488	TE-EX1122-SGB	SGB U-Tube(2,EX) Pos.5	270	720	K	2.75	0.61
360	TE 489	TE-IN1123-SGB	SGB U-Tube(3,IN) Pos.5	270	720	K	2.75	0.61
361	TE 490	TE-EX1123-SGB	SGB U-Tube(3,EX) Pos.5	270	720	K	2.75	0.61
362	TE 491	TE-IN1124-SGB	SGB U-Tube(4,IN) Pos.5	270	720	K	2.75	0.61
363	TE 492	TE-EX1124-SGB	SGB U-Tube(4,EX) Pos.5	270	720	K	2.75	0.61
364	TE 497	TE-IN1251-SGB	SGB U-Tube(1,IN) Pos.6	270	720	K	2.75	0.61
365	TE 498	TE-EX1251-SGB	SGB U-Tube(1,EX) Pos.6	270	720	K	2.75	0.61
366	TE 499	TE-IN1252-SGB	SGB U-Tube(2,IN) Pos.6	270	720	K	2.75	0.61
367	TE 502	TE-EX1253-SGB	SGB U-Tube(3,EX) Pos.6	270	720	K	2.75	0.61
368	TE 503	TE-IN1254-SGB	SGB U-Tube(4,IN) Pos.6	270	720	K	2.75	0.61
369	TE 504	TE-EX1254-SGB	SGB U-Tube(4,EX) Pos.6	270	720	K	2.75	0.61
370	TE 505	TE-IN1255-SGB	SGB U-Tube(5,IN) Pos.6	270	720	K	2.75	0.61
371	TE 506	TE-EX1255-SGB	SGB U-Tube(5,EX) Pos.6	270	720	K	2.75	0.61
372	TE 507	TE-IN1256-SGB	SGB U-Tube(6,IN) Pos.6	270	720	K	2.75	0.61
373	TE 508	TE-EX1256-SGB	SGB U-Tube(6,EX) Pos.6	270	720	K	2.75	0.61
374	TE 509	TE-IN1371-SGB	SGB U-Tube(1,IN) Pos.7	270	720	K	2.75	0.61
375	TE 510	TE-EX1371-SGB	SGB U-Tube(1,EX) Pos.7	270	720	K	2.75	0.61
376	TE 511	TE-IN1372-SGB	SGB U-Tube(2,IN) Pos.7	270	720	K	2.75	0.61
377	TE 514	TE-EX1373-SGB	SGB U-Tube(3,EX) Pos.7	270	720	K	2.75	0.61
378	TE 515	TE-IN1374-SGB	SGB U-Tube(4,IN) Pos.7	270	720	K	2.75	0.61
379	TE 516	TE-EX1374-SGB	SGB U-Tube(4,EX) Pos.7	270	720	K	2.75	0.61
380	TE 517	TE-IN1375-SGB	SGB U-Tube(5,IN) Pos.7	270	720	K	2.75	0.61
381	TE 518	TE-EX1375-SGB	SGB U-Tube(5,EX) Pos.7	270	720	K	2.75	0.61
382	TE 519	TE-IN1376-SGB	SGB U-Tube(6,IN) Pos.7	270	720	K	2.75	0.61
383	TE 520	TE-EX1376-SGB	SGB U-Tube(6,EX) Pos.7	270	720	K	2.75	0.61
384	TE 523	TE-IN1502-SGB	SGB U-Tube(2,IN) Pos.8	270	720	K	2.75	0.61
385	TE 525	TE-IN1503-SGB	SGB U-Tube(3,IN) Pos.8	270	720	K	2.75	0.61
386	TE 526	TE-EX1503-SGB	SGB U-Tube(3,EX) Pos.8	270	720	K	2.75	0.61
387	TE 527	TE-IN1504-SGB	SGB U-Tube(4,IN) Pos.8	270	720	K	2.75	0.61
388	TE 528	TE-EX1504-SGB	SGB U-Tube(4,EX) Pos.8	270	720	K	2.75	0.61
389	TE 529	TE-IN1505-SGB	SGB U-Tube(5,IN) Pos.8	270	720	K	2.75	0.61
390	TE 530	TE-EX1505-SGB	SGB U-Tube(5,EX) Pos.8	270	720	K	2.75	0.61
391	TE 532	TE-EX1506-SGB	SGB U-Tube(6,EX) Pos.8	270	720	K	2.75	0.61
392	TE 533	TE-IN1632-SGB	SGB U-Tube(2,IN) Pos.9	270	720	K	2.75	0.61
393	TE 534	TE-EX1632-SGB	SGB U-Tube(2,EX) Pos.9	270	720	K	2.75	0.61
394	TE 535	TE-IN1633-SGB	SGB U-Tube(3,IN) Pos.9	270	720	K	2.75	0.61
395	TE 536	TE-EX1633-SGB	SGB U-Tube(3,EX) Pos.9	270	720	K	2.75	0.61
396	TE 537	TE-IN1634-SGB	SGB U-Tube(4,IN) Pos.9	270	720	K	2.75	0.61
397	TE 538	TE-EX1634-SGB	SGB U-Tube(4,EX) Pos.9	270	720	K	2.75	0.61
398	TE 539	TE-IN1635-SGB	SGB U-Tube(5,IN) Pos.9	270	720	K	2.75	0.61
399	TE 540	TE-EX1635-SGB	SGB U-Tube(5,EX) Pos.9	270	720	K	2.75	0.61
400	TE 544	TE-IN1785-SGB	SGB U-Tube(5,IN) Pos.10	270	720	K	2.75	0.61
401	TE 546	TE-IN1864-SGB	SGB U-Tube(4,IN) Pos.11	270	720	K	2.75	0.61
402	TE 548	TE-086C-SGB	SGB Boiling Section Pos.1	270	670	K	2.63	0.66
403	TE 549	TE-099C-SGB	SGB Boiling Section Pos.3	270	670	K	2.63	0.66
404	TE 550	TE-112C-SGB	SGB Boiling Section Pos.5	270	670	K	2.63	0.66
405	TE 551	TE-125C-SGB	SGB Boiling Section Pos.6	270	670	K	2.63	0.66
406	TE 552	TE-137C-SGB	SGB Boiling Section Pos.7	270	670	K	2.63	0.66
407	TE 553	TE-150C-SGB	SGB Boiling Section Pos.8	270	670	K	2.63	0.66
408	TE 554	TE-163C-SGB	SGB Boiling Section Pos.9	270	670	K	2.63	0.66
409	TE 555	TE-178C-SGB	SGB Boiling Section Pos.10	270	670	K	2.63	0.66
410	TE 556	TE-192F-SGB	SGB Boiling Section	270	670	K	2.63	0.66

Table A.1 (Cont'd) (6/20)

SEQ No.	Function ID.	Tagname	Location	Range		Unit	Uncertainty	
				LO	HI		±ABS.	±%FR
411	TE 557	TE-208F-SGB	SGB Separator	270	670	K	2.63	0.66
412	TE 558	TE-192C-SGB	SGB Downcomer	270	670	K	2.63	0.66
413	TE 559	TE-208C-SGB	SGB Downcomer	270	670	K	2.63	0.66
414	TE 560	TE-223C-SGB	SGB Steam Dome	270	670	K	2.63	0.66
415	TE 561	TE-245C-SGB	SGB Steam Dome	270	670	K	2.63	0.66
416	TE 565	TE-980	(Reference Temperature)	0	50	℃	0.14	0.29
417	TE 566	TE-981	(Reference Temperature)	0	50	℃	0.14	0.29
418	TE 567	TE-982	(Reference Temperature)	0	50	℃	0.14	0.29
419	TE 568	TE-983	(Reference Temperature)	0	50	℃	0.14	0.29
420	TE 569	TE-984	(Reference Temperature)	0	50	℃	0.14	0.29
421	TE 570	TE-985	(Reference Temperature)	0	50	℃	0.14	0.29
422	TE 571	TE986	(Reference Temperature)	0	50	℃	0.14	0.29
423	TE 572	TE-990	(Reference Temperature)	0	50	℃	0.14	0.29
424	TE 573	TE-991	(Reference Temperature)	0	50	℃	0.14	0.29
425	TE 574	TE-992	(Reference Temperature)	0	50	℃	0.14	0.29
426	TE 575	TE-993	(Reference Temperature)	0	50	℃	0.14	0.29
427	TE 576	TE-994	(Reference Temperature)	0	50	℃	0.14	0.29
428	TE 577	TE-995	(Reference Temperature)	0	50	℃	0.14	0.29
429	TE 578	TE-996	(Reference Temperature)	0	50	℃	0.14	0.29
430	TE 579	TE-997	(Reference Temperature)	0	50	℃	0.14	0.29
431	TE 584	TE672-ACC	Acc-Cold Line to CLA	270	470	K	2.3	1.15
432	TE 588	TE711-ACH	Acc-Hot Line to HLA	270	720	K	2.75	0.61
433	TE 595	TE724-ACH	Acc-Hot Line to CLB	270	570	K	2.42	0.81
434	TE 607	TE011B-HLA	HLA Spool Piece Side	270	720	K	2.75	0.61
435	TE 609	TE012C-HLA	HLA Spool Piece Top	270	720	K	2.75	0.61
436	TE 610	TE012D-HLA	HLA Spool Piece Bottom	270	720	K	2.75	0.61
437	TE 613	TE051C-LSA	LSA Spool Piece West	270	720	K	2.75	0.61
438	TE 615	TE052-LSA	LSA Spool Piece	270	720	K	2.75	0.61
439	TE 616	TE071A-CLA	CLA Spool Piece Top	270	720	K	2.75	0.61
440	TE 619	TE072C-CLA	CLA Spool Piece Top	270	720	K	2.75	0.61
441	TE 620	TE072D-CLA	CLA Spool Piece Bottom	270	720	K	2.75	0.61
442	TE 624	TE152C-HLB	HLB Spool Piece Top	270	720	K	2.75	0.61
443	TE 625	TE152D-HLB	HLB Spool Piece Bottom	270	720	K	2.75	0.61
444	TE 628	TE191C-LSB	LSB Spool Piece East	270	720	K	2.75	0.61
445	TE 630	TE192-LSB	LSB Spool Piece	270	720	K	2.75	0.61
446	TE 634	TE212C-CLB	CLB Spool Piece Top	270	720	K	2.75	0.61
447	TE 635	TE212D-CLB	CLB Spool Piece Bottom	270	720	K	2.75	0.61
448	TE 644	TE571C-BU	RSV Spool Piece, Inlet Side	270	720	K	2.75	0.61
449	TE 645	TE571D-BU	RSV Spool Piece, Inlet Side	270	720	K	2.75	0.61
450	TE 651	TE591C-BU	Break Spool Piece	270	720	K	2.75	0.61
451	TE 652	TE591D-BU	Break Spool Piece	270	720	K	2.75	0.61
452	TE 662	TE-N-006-DC	PV Downcomer DTT North	270	720	K	2.75	0.61
453	TE 663	TE-S-006-DC	PV Downcomer DTT South	270	720	K	2.75	0.61
454	TE 664	TE-E-006-DC	PV Downcomer DTT East	270	720	K	2.75	0.61
455	TE 665	TE-W-006-DC	PV Downcomer DTT West	270	720	K	2.75	0.61
456	TE 707	TE-121E-UHDP	PLR-UH-9 Oil Outlet	270	720	K	2.75	0.61
457	TE 709	TE-121B-UHDP	PLR-UH-9 EL. 7.6m	270	720	K	2.75	0.61
458	TE 710	TE-121C-UHDP	PLR-UH-9 EL. 8.2m	270	720	K	2.75	0.61
459	TE 711	TE-E071C-DC	Downcomer EL.7.1m,East	270	720	K	2.75	0.61
460	TE 712	TE-W071C-DC	Downcomer EL.7.1m,West	270	720	K	2.75	0.61
461	TE 713	TE-E067C-DC	Downcomer EL.6.7m,East	270	720	K	2.75	0.61
462	TE 715	TE-951-CS	Oil Inlet-Main	270	720	K	2.75	0.61
463	TE 716	TE-952-CS	Oil Outlet-Main	270	720	K	2.75	0.61
464	TE 717	TE-953-CS	Oil HX Outlet	270	720	K	2.75	0.61
465	TE 718	TE-B05221	B05 Rod(2,2) Pos.1,Fluid	270	970	K	3.69	0.53
466	TE 719	TE-B05223	B05 Rod(2,2) Pos.3,Fluid	270	970	K	3.69	0.53
467	TE 720	TE-B05225	B05 Rod(2,2) Pos.5,Fluid	270	970	K	3.69	0.53
468	TE 721	TE-B05226	B05 Rod(2,2) Pos.6,Fluid	270	970	K	3.69	0.53
469	TE 723	TE-B05229	B05 Rod(2,2) Pos.9,Fluid	270	970	K	3.69	0.53
470	TE 724	TE-B07221	B07 Rod(2,2) Pos.1,Fluid	270	1470	K	5.31	0.44
471	TE 725	TE-B07223	B07 Rod(2,2) Pos.3,Fluid	270	1470	K	5.31	0.44
472	TE 726	TE-B07225	B07 Rod(2,2) Pos.5,Fluid	270	1470	K	5.31	0.44
473	TE 727	TE-B07226	B07 Rod(2,2) Pos.6,Fluid	270	1470	K	5.31	0.44
474	TE 728	TE-B07227	B07 Rod(2,2) Pos.7,Fluid	270	1470	K	5.31	0.44
475	TE 729	TE-B07229	B07 Rod(2,2) Pos.9,Fluid	270	1470	K	5.31	0.44
476	TE 730	TE-EX0650-SGA	SGA Outlet Plenum	270	720	K	2.75	0.61
477	TE 731	TE-EX0680-SGA	SGA Outlet Plenum	270	720	K	2.75	0.61
478	TE 732	TE-EX0720-SGA	SGA Outlet Plenum	270	720	K	2.75	0.61
479	TE 733	TE-EX0650-SGB	SGB Outlet Plenum	270	720	K	2.75	0.61
480	TE 734	TE-EX0680-SGB	SGB Outlet Plenum	270	720	K	2.75	0.61
481	TE 735	TE-EX0720-SGB	SGB Outlet Plenum	270	720	K	2.75	0.61
482	TE 736	TE810-PJ	HPI (PJ) Flow to CLA	270	370	K	2.37	2.37
483	TE 739	TE275C-PR	PZR Spray Inlet Nozzle	270	720	K	2.75	0.61
484	TE 752	TE293-ACH	ACC-Hot Top Gas Line	270	720	K	2.75	0.61
485	TE 780	TE687X-ACH	Acc-Hot Tank Fluid DL.6570	270	720	K	2.75	0.61
486	TE 803	TE-A99	(Reference Temperature)	270	320	K	0.51	1.02
487	TE 804	TE-A98	(Reference Temperature)	270	320	K	0.51	1.02
488	TE 854	TE-NP053F-PV	PV UP North Peri. EL.5299	270	630	K	3.05	0.85
489	TE 855	TE-NP055F-PV	PV UP North Peri. EL.5503	270	630	K	3.05	0.85
490	TE 856	TE-NP057F-PV	PV UP North Peri. EL.5706	270	630	K	3.05	0.85
491	TE 857	TE-NP059F-PV	PV UP North Peri. EL.5938	270	630	K	3.05	0.85
492	TE 858	TE-EP047F-PV	PV UP East Peri. EL.4672	270	630	K	3.05	0.85

Table A.1 (Cont'd) (7/20)

SEQ No.	Function ID.	Tagname	Location	Range		Unit	Uncertainty	
				LO	HI		±ABS.	±%FR
493	TE 859	TE-EP053F-PV	PV UP East Peri. EL.5299	270	630	K	3.05	0.85
494	TE 860	TE-EP055F-PV	PV UP East Peri. EL.5503	270	630	K	3.05	0.85
495	TE 861	TE-EP057F-PV	PV UP East Peri. EL.5706	270	630	K	3.05	0.85
496	TE 862	TE-EP059F-PV	PV UP East Peri. EL.5938	270	630	K	3.05	0.85
497	TE 863	TE-SP047F-PV	PV UP South Peri. EL.4672	270	630	K	3.05	0.85
498	TE 864	TE-SP053F-PV	PV UP South Peri. EL.5299	270	630	k	3.05	0.85
499	TE 865	TE-SP055F-PV	PV UP South Peri. EL.5503	270	630	K	3.05	0.85
500	TE 866	TE-SP057F-PV	PV UP South Peri. EL.5706	270	630	K	3.05	0.85
501	TE 867	TE-SP059F-PV	PV UP South Peri. EL.5938	270	630	K	3.05	0.85
502	TE 868	TE-WP047F-PV	PV UP West Peri. EL.4672	270	630	K	3.05	0.85
503	TE 869	TE-WP053F-PV	PV UP West Peri. EL.5299	270	630	K	3.05	0.85
504	TE 870	TE-WP055F-PV	PV UP West Peri. EL.5503	270	630	K	3.05	0.85
505	TE 871	TE-WP057F-PV	PV UP West Peri. EL.5706	270	630	K	3.05	0.85
506	TE 872	TE-WP059F-PV	PV UP West Peri. EL.5938	270	630	K	3.05	0.85
507	TE 873	TE-EM053F-PV	PV UP East Middle EL.5299	270	630	K	3.05	0.85
508	TE 874	TE-EM057F-PV	PV UP East Middle EL.5706	270	630	K	3.05	0.85
509	TE 875	TE-WM053F-PV	PV UP West Middle EL.5299	270	630	K	3.05	0.85
510	TE 876	TE-WM057F-PV	PV UP West Middle EL.5706	270	630	K	3.05	0.85
511	TE 877	TE-WC047F-PV	PV UP West Center EL.4672	270	630	K	3.05	0.85
512	TE 878	TE-WC053F-PV	PV UP West Center EL.5299	270	630	K	3.05	0.85
513	TE 879	TE-WC055F-PV	PV UP West Center EL.5503	270	630	K	3.05	0.85
514	TE 880	TE-WC057F-PV	PV UP West Center EL.5706	270	630	K	3.05	0.85
515	TE 881	TE-WC059F-PV	PV UP West Center EL.5938	270	630	K	3.05	0.85
516	TE 882	TE-EC047F-PV	PV UP East Center EL.4672	270	630	K	3.05	0.85
517	TE 883	TE-EC053F-PV	PV UP East Center EL.5299	270	630	K	3.05	0.85
518	TE 884	TE-EC055F-PV	PV UP East Center EL.5503	270	630	K	3.05	0.85
519	TE 885	TE-EC057F-PV	PV UP East Center EL.5706	270	630	K	3.05	0.85
520	TE 886	TE-EC059F-PV	PV UP East Center EL.5938	270	630	K	3.05	0.85
521	TE 888	TE-E037C-DC	DC East EL.3662	270	630	K	3.05	0.85
522	TE 891	TE-W037C-DC	DC West EL.3662	270	630	K	3.05	0.85
523	TE 893	TE-EN040C-DC	DC East-North EL.4037	270	630	K	3.05	0.85
524	TE 894	TE-E040C-DC	DC East EL.4037	270	630	K	3.05	0.85
525	TE 895	TE-ES040C-DC	DC East-South EL.4037	270	630	K	3.05	0.85
526	TE 896	TE-WN040C-DC	DC West-North EL.4037	270	630	K	3.05	0.85
527	TE 897	TE-W040C-DC	DC West EL.4037	270	630	K	3.05	0.85
528	TE 898	TE-WS040C-DC	DC West-South EL.4037	270	630	K	3.05	0.85
529	TE 899	TE-W042C-DC	DC West EL.4210	270	630	K	3.05	0.85
530	TE 900	TE-E042C-DC	DC East EL.4210	270	630	K	3.05	0.85
531	TE 901	TE-SW045C-DC	DC South-West EL.4497	270	630	K	3.05	0.85
532	TE 902	TE-NE045C-DC	DC North-East EL.4497	270	630	K	3.05	0.85
533	TE 903	TE-N045C-DC	DC North EL.4497	270	630	K	3.05	0.85
534	TE 904	TE-NW045C-DC	DC North-West EL.4497	270	630	K	3.05	0.85
535	TE 905	TE-S045C-DC	DC South EL.4497	270	630	K	3.05	0.85
536	TE 906	TE-SE045C-DC	DC South-East EL.4497	270	630	K	3.05	0.85
537	TE 907	TE-NE051C-DC	DC North-East EL.5074	270	630	K	3.05	0.85
538	TE 908	TE-N051C-DC	DC North EL.5074	270	630	K	3.05	0.85
539	TE 909	TE-NW051C-DC	DC North-West EL.5074	270	630	K	3.05	0.85
540	TE 910	TE-SW051C-DC	DC South-West EL.5074	270	630	K	3.05	0.85
541	TE 911	TE-S051C-DC	DC South EL.5074	270	630	K	3.05	0.85
542	TE 912	TE-SE051C-DC	DC South-East EL.5074	270	630	K	3.05	0.85
543	TE 913	TE-N054C-DC	DC North EL.5363	270	630	K	3.05	0.85
544	TE 914	TE-S054C-DC	DC South EL.5363	270	630	K	3.05	0.85
545	TE 921	HTE-C046-PV	Heated TC, EL.4597	270	1270	K	4.55	0.46
546	TE 922	TE-C046-PV	HTC Fluid, EL.4597	270	1270	K	4.55	0.46
547	TE 924	TE-C051-PV	HTC Fluid, EL.5102	270	1270	K	4.55	0.46
548	TE 925	TE-C056-PV	HTC Fluid, EL.5606	270	1270	K	4.55	0.46
549	TE 926	HTE-C056-PV	Heated TC, EL.5606	270	1270	K	4.55	0.46
550	TE 958	TE194A-PR	PZR DL.2025	270	720	K	2.75	0.61
551	TE 960	TE194C-PR	PZR DL.5995	270	720	K	2.75	0.61
552	TE 961	TE194D-PR	PZR DL.7965	270	720	K	2.75	0.61
553	TE 962	TE194E-PR	PZR DL.9795	270	720	K	2.75	0.61
554	TE 963	TE194F-PR	PZR DL.11321	270	720	K	2.75	0.61
555	TE 964	TE-PR2	PZR HT	270	1470	K	5.31	0.44
556	TE 965	TE677-ACC	Acc-Cold Tank Fluid DL.6450	270	720	K	2.75	0.61
557	TE 968	TE-A81-ADS	RSV(1-3) Downstream	270	720	K	2.75	0.61
558	TE 1089	TE910-CWT	Cooling Water Tank	270	370	K	2.37	2.37
559	TE 1092	TE960-AIR	Atmospheric Temperature	170	370	K	2.3	1.15
560	TE 1093	TE961-AIR	Room Temperature	170	370	K	2.3	1.15
561	TE 1094	TC030D-HLA	HLA Fluid at Pipe Bottom	273	673	K	2.63	0.66
562	TE 1095	TC170D-HLB	HLB Fluid at Pipe Bottom	273	673	K	2.63	0.66
563	TE 1096	TC080D-CLA	CLA Fluid at Pipe Bottom	273	673	K	2.63	0.66
564	TE 1097	TC220D-CLB	CLB Fluid at Pipe Bottom	273	673	K	2.63	0.66
565	TE 1098	TC194B-PR	PZR Fluid	273	673	K	2.63	0.66
566	TE 1099	TC223D-SGA	SGA Steam Dome	273	673	K	2.63	0.66
567	TE 1100	TC223D-SGB	SGB Steam Dome	273	673	K	2.63	0.66
568	TE 1101	TC-E000C-DC	Downcomer EL.0.0m,East	273	673	K	2.63	0.66
569	TE 1102	TC-E060C-DC	Downcomer EL.6.0m,East	273	673	K	2.63	0.66
570	TE 1108	TE561C-BU	BU-1 Downstream Top	270	720	K	2.75	0.61
571	TE 1109	TE561D-BU	BU-1 Downstream Down	270	720	K	2.75	0.61
572	TE 1123	TE687A-ACH	Acc-Hot Tank Fluid DL.10	270	720	K	2.75	0.61
573	TE 1124	TE687B-ACH	Acc-Hot Tank Fluid DL.475	270	720	K	2.75	0.61
574	TE 1125	TE687C-ACH	Acc-Hot Tank Fluid DL.940	270	720	K	2.75	0.61

Table A.1 (Cont'd) (8/20)

SEQ No.	Function ID.	Tagname	Location	Range		Unit	Uncertainty	
				LO	HI		±ABS.	±%FR
575	TE 1126	TE687D-ACH	Acc-Hot Tank Fluid DL.1405	270	720	K	2.75	0.61
576	TE 1127	TE687E-ACH	Acc-Hot Tank Fluid DL.1870	270	720	K	2.75	0.61
577	TE 1128	TE687F-ACH	Acc-Hot Tank Fluid DL.2335	270	720	K	2.75	0.61
578	TE 1129	TE687G-ACH	Acc-Hot Tank Fluid DL.2800	270	720	K	2.75	0.61
579	TE 1130	TE687H-ACH	Acc-Hot Tank Fluid DL.3265	270	720	K	2.75	0.61
580	TE 1131	TE687I-ACH	Acc-Hot Tank Fluid DL.3275	270	720	K	2.75	0.61
581	TE 1132	TE687J-ACH	Acc-Hot Tank Fluid DL.3285	270	720	K	2.75	0.61
582	TE 1133	TE687K-ACH	Acc-Hot Tank Fluid DL.3295	270	720	K	2.75	0.61
583	TE 1134	TE687L-ACH	Acc-Hot Tank Fluid DL.3305	270	720	K	2.75	0.61
584	TE 1135	TE687M-ACH	Acc-Hot Tank Fluid DL.3315	270	720	K	2.75	0.61
585	TE 1136	TE687N-ACH	Acc-Hot Tank Fluid DL.3325	270	720	K	2.75	0.61
586	TE 1137	TE687O-ACH	Acc-Hot Tank Fluid DL.3335	270	720	K	2.75	0.61
587	TE 1138	TE687P-ACH	Acc-Hot Tank Fluid DL.3345	270	720	K	2.75	0.61
588	TE 1139	TE687Q-ACH	Acc-Hot Tank Fluid DL.3355	270	720	K	2.75	0.61
589	TE 1140	TE687R-ACH	Acc-Hot Tank Fluid DL.3820	270	720	K	2.75	0.61
590	TE 1141	TE687S-ACH	Acc-Hot Tank Fluid DL.4285	270	720	K	2.75	0.61
591	TE 1142	TE687T-ACH	Acc-Hot Tank Fluid DL.4750	270	720	K	2.75	0.61
592	TE 1143	TE687U-ACH	Acc-Hot Tank Fluid DL.5215	270	720	K	2.75	0.61
593	TE 1144	TE687V-ACH	Acc-Hot Tank Fluid DL.5680	270	720	K	2.75	0.61
594	TE 1145	TE687W-ACH	Acc-Hot Tank Fluid DL.6145	270	720	K	2.75	0.61
595	TE 1151	TE075A-CLA	CLA TC Rake	270	720	K	2.75	0.61
596	TE 1152	TE075B-CLA	CLA TC Rake	270	720	K	2.75	0.61
597	TE 1153	TE075C-CLA	CLA TC Rake	270	720	K	2.75	0.61
598	TE 1154	TE075D-CLA	CLA TC Rake	270	720	K	2.75	0.61
599	TE 1155	TE075E-CLA	CLA TC Rake	270	720	K	2.75	0.61
600	TE 1156	TE215A-CLB	CLB TC Rake	270	720	K	2.75	0.61
601	TE 1157	TE215B-CLB	CLB TC Rake	270	720	K	2.75	0.61
602	TE 1158	TE215C-CLB	CLB TC Rake	270	720	K	2.75	0.61
603	TE 1159	TE215D-CLB	CLB TC Rake	270	720	K	2.75	0.61
604	TE 1160	TE215E-CLB	CLB TC Rake	270	720	K	2.75	0.61
605	TE 1163	TE-H86-PGIT	Primary Side GDIS Tank	270	720	K	2.75	0.61
606	TE 1164	TE-H87-SGIT	Secondary Side GDIS Tank	270	720	K	2.75	0.61
607	TE 1165	TE970-DIS	Dis. Gas Sampling	270	470	K	2.3	1.15
608	TE 1166	TE-H10-GAS	Air Injection Line No.1	270	370	K	2.37	2.37
609	TE 1167	TE-H20-GAS	Air Injection Line No.2	270	370	K	2.37	2.37
610	TE 1168	TE-E030C-DC	DC East EL.3000	270	720	K	2.37	0.53
611	TE 1169	TE-S030C-DC	DC South EL.3000	270	720	K	2.37	0.53
612	TE 1170	TE-W030C-DC	DC West EL.3000	270	720	K	2.37	0.53
613	TE 1171	TE-N030C-DC	DC North EL.3000	270	720	K	2.37	0.53
614	TE 1172	TE-S037C-DC	DC South EL.3662	270	720	K	2.37	0.53
615	TE 1173	TE-N037C-DC	DC North EL.3662	270	720	K	2.37	0.53
616	DT 3	DTE030A-HLA	HLA Wall I/O	-150	150	K	2.9	0.97
617	DT 4	DTE030B-HLA	HLA Wall-Fluid	-150	150	K	2.9	0.97
618	DT 5	DTE050A-LSA	LSA Wall I/O	-150	150	K	2.9	0.97
619	DT 6	DTE050B-LSA	LSA Wall-Fluid	-150	150	K	2.9	0.97
620	DT 7	DTE060A-PCA	PCA Wall I/O	-150	150	K	2.9	0.97
621	DT 8	DTE070A-CLA	CLA Wall I/O	-150	150	K	2.9	0.97
622	DT 9	DTE070B-CLA	CLA Wall-Fluid	-150	150	K	2.9	0.97
623	DT 10	DTE080A-CLA	CLA Wall I/O	-150	150	K	2.9	0.97
624	DT 11	DTE080B-CLA	CLA Wall-Fluid	-150	150	K	2.9	0.97
625	DT 12	DTE100-HLA	HLA-CLA	-150	150	K	2.9	0.97
626	DT 13	DTE160A-HLB	HLB Wall I/O	-150	150	K	2.9	0.97
627	DT 14	DTE160B-HLB	HLB Wall-Fluid	-150	150	K	2.9	0.97
628	DT 15	DTE170A-HLB	HLB Wall I/O	-150	150	K	2.9	0.97
629	DT 16	DTE170B-HLB	HLB Wall-Fluid	-150	150	K	2.9	0.97
630	DT 17	DTE190A-LSB	LSB Wall I/O	-150	150	K	2.9	0.97
631	DT 18	DTE190B-LSB	LSB Wall-Fluid	-150	150	K	2.9	0.97
632	DT 19	DTE200A-PCB	PCB Wall I/O	-150	150	K	2.9	0.97
633	DT 20	DTE210A-CLB	CLB Wall I/O	-150	150	K	2.9	0.97
634	DT 21	DTE210B-CLB	CLB Wall-Fluid	-150	150	K	2.9	0.97
635	DT 22	DTE220A-CLB	CLB Wall I/O	-150	150	K	2.9	0.97
636	DT 23	DTE220B-CLB	CLB Wall-Fluid	-150	150	K	2.9	0.97
637	DT 24	DTE240-HLB	HLB-CLB	-150	150	K	2.9	0.97
638	DT 25	DTE270A-PR	PZR Spray Line Wall-Fluid	-150	150	K	2.9	0.97
639	DT 26	DTE280A-PR	PZR Surge Line Wall-Fluid	-150	150	K	2.9	0.97
640	DT 27	DTE-E-015A-PV	PV Wall I/O-E at L. Plenum	-150	150	K	2.9	0.97
641	DT 28	DTE-W-015A-PV	PV Wall I/O-W at L. Plenum	-150	150	K	2.9	0.97
642	DT 29	DTE-N000A-PV	PV Wall I/O-N at DC Bottom	-150	150	K	2.9	0.97
643	DT 30	DTE-S000A-PV	PV Wall I/O-S at DC Bottom	-150	150	K	2.9	0.97
644	DT 31	DTE-E000A-PV	PV Wall I/O-E at DC Bottom	-150	150	K	2.9	0.97
645	DT 32	DTE-W000A-PV	PV Wall I/O-W at DC Bottom	-150	150	K	2.9	0.97
646	DT 33	DTE-N018A-PV	PV Wall I/O-N at DC Middle	-150	150	K	2.9	0.97
647	DT 34	DTE-S018A-PV	PV Wall I/O-S at DC Middle	-150	150	K	2.9	0.97
648	DT 35	DTE-E018A-PV	PV Wall I/O-E at DC Middle	-150	150	K	2.9	0.97
649	DT 36	DTE-W018A-PV	PV Wall I/O-W at DC Middle	-150	150	K	2.9	0.97
650	DT 37	DTE-N036A-PV	PV Wall I/O-N at Upper DC	-150	150	K	2.9	0.97
651	DT 38	DTE-S036A-PV	PV Wall I/O-S at Upper DC	-150	150	K	2.9	0.97
652	DT 39	DTE-E036A-PV	PV Wall I/O-E at Upper DC	-150	150	K	2.9	0.97
653	DT 40	DTE-W036A-PV	PV Wall I/O-W at Upper DC	-150	150	K	2.9	0.97
654	DT 41	DTE-N060A-PV	PV Wall I/O-N at DC Top	-150	150	K	2.9	0.97
655	DT 42	DTE-S060A-PV	PV Wall I/O-S at DC Top	-150	150	K	2.9	0.97

Table A.1 (Cont'd) (9/20)

SEQ No.	Function ID.	Tagname	Location	Range		Unit	Uncertainty	
				LO	HI		±ABS.	±%FR
656	DT 43	DTE-E060A-PV	PV Wall I/O-E at DC Top	-150	150	K	2.9	0.97
657	DT 44	DTE-W060A-PV	PV Wall I/O-W at DC Top	-150	150	K	2.9	0.97
658	DT 45	DTE-E080A-PV	PV Wall I/O-E at DC Head	-150	150	K	2.9	0.97
659	DT 46	DTE-W080A-PV	PV Wall I/O-W at DC Head	-150	150	K	2.9	0.97
660	DT 47	DTE-N000B-PV	PV/DC Fluid at DC Bottom	-150	150	K	2.9	0.97
661	DT 48	DTE-S000B-PV	PV/DC Fluid at DC Bottom	-150	150	K	2.9	0.97
662	DT 50	DTE-W000B-PV	PV/DC Fluid at DC Bottom	-150	150	K	2.9	0.97
663	DT 51	DTE-N018B-PV	PV/DC Fluid at DC Middle	-150	150	K	2.9	0.97
664	DT 53	DTE-E018B-PV	PV/DC Fluid at DC Middle	-150	150	K	2.9	0.97
665	DT 54	DTE-W018B-PV	PV/DC Fluid at DC Middle	-150	150	K	2.9	0.97
666	DT 55	DTE-N036B-PV	PV/DC Fluid at Upper DC	-150	150	K	2.9	0.97
667	DT 56	DTE-S036B-PV	PV/DC Fluid at Upper DC	-150	150	K	2.9	0.97
668	DT 57	DTE-E036B-PV	PV/DC Fluid at Upper DC	-150	150	K	2.9	0.97
669	DT 58	DTE-W036B-PV	PV/DC Fluid at Upper DC	-150	150	K	2.9	0.97
670	DT 60	DTE-S060B-PV	PV/DC Fluid at DC Top	-150	150	K	2.9	0.97
671	DT 62	DTE-W060B-PV	PV/DC Fluid at DC Top	-150	150	K	2.9	0.97
672	DT 64	DTE-S000C-PV	CB/DC Fluid at DC Bottom	-150	150	K	2.9	0.97
673	DT 66	DTE-W000C-PV	CB/DC Fluid at DC Bottom	-150	150	K	2.9	0.97
674	DT 67	DTE-N018C-PV	CB/DC Fluid at DC Middle	-150	150	K	2.9	0.97
675	DT 69	DTE-E018C-PV	CB/DC Fluid at DC Middle	-150	150	K	2.9	0.97
676	DT 70	DTE-W018C-PV	CB/DC Fluid at DC Middle	-150	150	K	2.9	0.97
677	DT 71	DTE-N036C-PV	CB/DC Fluid at Upper DC	-150	150	K	2.9	0.97
678	DT 72	DTE-S036C-PV	CB/DC Fluid at Upper DC	-150	150	K	2.9	0.97
679	DT 74	DTE-W036C-PV	CB/DC Fluid at Upper DC	-150	150	K	2.9	0.97
680	DT 76	DTE-S060C-PV	CB/DC Fluid at DC Top	-150	150	K	2.9	0.97
681	DT 78	DTE-W060C-PV	CB/DC Fluid at DC Top	-150	150	K	2.9	0.97
682	DT 80	DTE-S000E-PV	CB Wall I/O at DC Bottom	-150	150	K	2.9	0.97
683	DT 81	DTE-E000E-PV	CB Wall I/O at DC Bottom	-150	150	K	2.9	0.97
684	DT 82	DTE-W000E-PV	CB Wall I/O at DC Bottom	-150	150	K	2.9	0.97
685	DT 87	DTE-N018E-PV	CB Wall I/O at DC Middle	-150	150	K	2.9	0.97
686	DT 88	DTE-S018E-PV	CB Wall I/O at DC Middle	-150	150	K	2.9	0.97
687	DT 89	DTE-E018E-PV	CB Wall I/O at DC Middle	-150	150	K	2.9	0.97
688	DT 90	DTE-W018E-PV	CB Wall I/O at DC Middle	-150	150	K	2.9	0.97
689	DT 95	DTE-N036E-PV	CB Wall I/O at Upper DC	-150	150	K	2.9	0.97
690	DT 96	DTE-S036E-PV	CB Wall I/O at Upper DC	-150	150	K	2.9	0.97
691	DT 101	DTE-E049E-PV	CB Wall I/O below Nozzle	-150	150	K	2.9	0.97
692	DT 103	DTE-N060E-PV	CB Wall I/O at DC Top	-150	150	K	2.9	0.97
693	DT 104	DTE-S060E-PV	CB Wall I/O at DC Top	-150	150	K	2.9	0.97
694	DT 105	DTE-E060E-PV	CB Wall I/O at DC Top	-150	150	K	2.9	0.97
695	DT 106	DTE-W060E-PV	CB Wall I/O at DC Top	-150	150	K	2.9	0.97
696	DT 107	DTE-040-B09-UCP	Fluid DT across UCP	-150	150	K	2.9	0.97
697	DT 108	DTE-040-B11-UCP	Fluid DT across UCP	-150	150	K	2.9	0.97
698	DT 109	DTE-040-B01-UCP	Fluid DT across UCP	-150	150	K	2.9	0.97
699	DT 110	DTE-040-B03-UCP	Fluid DT across UCP	-150	150	K	2.9	0.97
700	DT 111	DTE-040-B05-UCP	Fluid DT across UCP	-150	150	K	2.9	0.97
701	DT 112	DTE-040-B07-UCP	Fluid DT across UCP	-150	150	K	2.9	0.97
702	DT 113	DTE-040-B21-UCP	Fluid DT across UCP	-150	150	K	2.9	0.97
703	DT 114	DTE-040-B23-UCP	Fluid DT across UCP	-150	150	K	2.9	0.97
704	DT 115	DTE-040-B02-UCP	Fluid DT across UCP	-150	150	K	2.9	0.97
705	DT 116	DTE-040-B15-UCP	Fluid DT across UCP	-150	150	K	2.9	0.97
706	DT 117	DTE-040-B06-UCP	Fluid DT across UCP	-150	150	K	2.9	0.97
707	DT 118	DTE-040-B14-UCP	Fluid DT across UCP	-150	150	K	2.9	0.97
708	DT 119	DTE-040-B18-UCP	Fluid DT across UCP	-150	150	K	2.9	0.97
709	DT 120	DTE-040-B19-UCP	Fluid DT across UCP	-150	150	K	2.9	0.97
710	DT 121	DTE-040-B10-UCP	Fluid DT across UCP	-150	150	K	2.9	0.97
711	DT 122	DTE-040-B12-UCP	Fluid DT across UCP	-150	150	K	2.9	0.97
712	DT 123	DTE-040-B04-UCP	Fluid DT across UCP	-150	150	K	2.9	0.97
713	DT 124	DTE-040-B08-UCP	Fluid DT across UCP	-150	150	K	2.9	0.97
714	DT 130	DTE-000-B07-LCP	In/Out Fluid across LCP	-150	150	K	1.665	0.555
715	DT 132	DTE-000-B11-LCP	In/Out Fluid across LCP	-150	150	K	1.665	0.555
716	DT 135	DTE-000-B18-LCP	In/Out Fluid across LCP	-150	150	K	1.665	0.555
717	DT 136	DTE-000-B20-LCP	In/Out Fluid across LCP	-150	150	K	1.665	0.555
718	DT 137	DTE-000-B21-LCP	In/Out Fluid across LCP	-150	150	K	1.665	0.555
719	DT 139	DTE-086A-SGA	SGA Wall I/O Pos.1	-40	40	K	2.07	2.58
720	DT 140	DTE-137A-SGA	SGA Wall I/O Pos.7	-40	40	K	2.07	2.58
721	DT 141	DTE-178A-SGA	SGA Wall I/O Pos.10	-40	40	K	2.07	2.58
722	DT 142	DTE-223A-SGA	SGA Steam Dome Wall I/O	-40	40	K	2.07	2.58
723	DT 143	DTE-IN0861-SGA	SGA U-Tube(1,IN) Pos.1	-100	100	K	2.42	1.21
724	DT 144	DTE-EX0861-SGA	SGA U-Tube(1,EX) Pos.1	-100	100	K	2.42	1.21
725	DT 145	DTE-IN0862-SGA	SGA U-Tube(2,IN) Pos.1	-100	100	K	2.42	1.21
726	DT 146	DTE-EX0862-SGA	SGA U-Tube(2,EX) Pos.1	-100	100	K	2.42	1.21
727	DT 147	DTE-IN0863-SGA	SGA U-Tube(3,IN) Pos.1	-100	100	K	2.42	1.21
728	DT 148	DTE-EX0863-SGA	SGA U-Tube(3,EX) Pos.1	-100	100	K	2.42	1.21
729	DT 149	DTE-IN0991-SGA	SGA U-Tube(1,IN) Pos.3	-100	100	K	2.42	1.21
730	DT 150	DTE-EX0991-SGA	SGA U-Tube(1,EX) Pos.3	-100	100	K	2.42	1.21
731	DT 151	DTE-IN0992-SGA	SGA U-Tube(2,IN) Pos.3	-100	100	K	2.42	1.21
732	DT 152	DTE-EX0992-SGA	SGA U-Tube(2,EX) Pos.3	-100	100	K	2.42	1.21
733	DT 153	DTE-IN0993-SGA	SGA U-Tube(3,IN) Pos.3	-100	100	K	2.42	1.21
734	DT 154	DTE-EX0993-SGA	SGA U-Tube(3,EX) Pos.3	-100	100	K	2.42	1.21
735	DT 155	DTE-IN1121-SGA	SGA U-Tube(1,IN) Pos.5	-100	100	K	2.42	1.21
736	DT 156	DTE-EX1121-SGA	SGA U-Tube(1,EX) Pos.5	-100	100	K	2.42	1.21
737	DT 157	DTE-IN1122-SGA	SGA U-Tube(2,IN) Pos.5	-100	100	K	2.42	1.21

Table A.1 (Cont'd) (10/20)

SEQ No.	Function ID.	Tagname	Location	Range		Unit	Uncertainty	
				LO	HI		±ABS.	±%FR
738	DT 158	DTE-EX1122-SGA	SGA U-Tube(2,EX) Pos.5	-100	100	K	2.42	1.21
739	DT 161	DTE-IN1371-SGA	SGA U-Tube(1,IN) Pos.7	-100	100	K	2.42	1.21
740	DT 163	DTE-IN1372-SGA	SGA U-Tube(2,IN) Pos.7	-100	100	K	2.42	1.21
741	DT 164	DTE-EX1372-SGA	SGA U-Tube(2,EX) Pos.7	-100	100	K	2.42	1.21
742	DT 166	DTE-EX1373-SGA	SGA U-Tube(3,EX) Pos.7	-100	100	K	2.42	1.21
743	DT 167	DTE-IN1632-SGA	SGA U-Tube(2,IN) Pos.9	-100	100	K	2.42	1.21
744	DT 168	DTE-EX1632-SGA	SGA U-Tube(2,EX) Pos.9	-100	100	K	2.42	1.21
745	DT 169	DTE-IN1633-SGA	SGA U-Tube(3,IN) Pos.9	-100	100	K	2.42	1.21
746	DT 170	DTE-EX1633-SGA	SGA U-Tube(3,EX) Pos.9	-100	100	K	2.42	1.21
747	DT 171	DTE-IN1701-SGA	SGA U-Tube(1,IN) Pos.10	-100	100	K	2.42	1.21
748	DT 172	DTE-IN1782-SGA	SGA U-Tube(2,IN) Pos.10	-100	100	K	2.42	1.21
749	DT 173	DTE-IN1863-SGA	SGA U-Tube(3,IN) Pos.11	-100	100	K	2.42	1.21
750	DT 174	DTE-086A-SGB	SGB Wall I/O Pos.1	-40	40	K	2.07	2.58
751	DT 175	DTE-137A-SGB	SGB Wall I/O Pos.7	-40	40	K	2.07	2.58
752	DT 176	DTE-178A-SGB	SGB Wall I/O Pos.10	-40	40	K	2.07	2.58
753	DT 177	DTE-223A-SGB	SGB Steam Dome Wall I/O	-40	40	K	2.07	2.58
754	DT 178	DTE-IN0861-SGB	SGB U-Tube(1,IN) Pos.1	-100	100	K	2.42	1.21
755	DT 179	DTE-EX0861-SGB	SGB U-Tube(1,EX) Pos.1	-100	100	K	2.42	1.21
756	DT 180	DTE-IN0862-SGB	SGB U-Tube(2,IN) Pos.1	-100	100	K	2.42	1.21
757	DT 181	DTE-EX0862-SGB	SGB U-Tube(2,EX) Pos.1	-100	100	K	2.42	1.21
758	DT 182	DTE-IN0863-SGB	SGB U-Tube(3,IN) Pos.1	-100	100	K	2.42	1.21
759	DT 183	DTE-EX0863-SGB	SGB U-Tube(3,EX) Pos.1	-100	100	K	2.42	1.21
760	DT 184	DTE-IN0991-SGB	SGB U-Tube(1,IN) Pos.3	-100	100	K	2.42	1.21
761	DT 185	DTE-EX0991-SGB	SGB U-Tube(1,EX) Pos.3	-100	100	K	2.42	1.21
762	DT 186	DTE-IN0992-SGB	SGB U-Tube(2,IN) Pos.3	-100	100	K	2.42	1.21
763	DT 187	DTE-EX0992-SGB	SGB U-Tube(2,EX) Pos.3	-100	100	K	2.42	1.21
764	DT 188	DTE-IN0993-SGB	SGB U-Tube(3,IN) Pos.3	-100	100	K	2.42	1.21
765	DT 189	DTE-EX0993-SGB	SGB U-Tube(3,EX) Pos.3	-100	100	K	2.42	1.21
766	DT 191	DTE-EX1121-SGB	SGB U-Tube(1,EX) Pos.5	-100	100	K	2.42	1.21
767	DT 192	DTE-IN1122-SGB	SGB U-Tube(2,IN) Pos.5	-100	100	K	2.42	1.21
768	DT 193	DTE-EX1122-SGB	SGB U-Tube(2,EX) Pos.5	-100	100	K	2.42	1.21
769	DT 194	DTE-IN1123-SGB	SGB U-Tube(3,IN) Pos.5	-100	100	K	2.42	1.21
770	DT 195	DTE-EX1123-SGB	SGB U-Tube(3,EX) Pos.5	-100	100	K	2.42	1.21
771	DT 196	DTE-IN1371-SGB	SGB U-Tube(1,IN) Pos.7	-100	100	K	2.42	1.21
772	DT 197	DTE-EX1371-SGB	SGB U-Tube(1,EX) Pos.7	-100	100	K	2.42	1.21
773	DT 198	DTE-IN1372-SGB	SGB U-Tube(2,IN) Pos.7	-100	100	K	2.42	1.21
774	DT 201	DTE-EX1373-SGB	SGB U-Tube(3,EX) Pos.7	-100	100	K	2.42	1.21
775	DT 202	DTE-IN1632-SGB	SGB U-Tube(2,IN) Pos.9	-100	100	K	2.42	1.21
776	DT 203	DTE-EX1632-SGB	SGB U-Tube(2,EX) Pos.9	-100	100	K	2.42	1.21
777	DT 204	DTE-IN1633-SGB	SGB U-Tube(3,IN) Pos.9	-100	100	K	2.42	1.21
778	DT 205	DTE-EX1633-SGB	SGB U-Tube(3,EX) Pos.9	-100	100	K	2.42	1.21
779	DT 215	DTE-C046-PV	HTC Differential Temp	-150	150	K	2.9	0.97
780	TW 2	TWE030B-HLA	HLA Inner Surface	270	720	K	2.75	0.61
781	TW 3	TWE050B-LSA	LSA Inner Surface	270	720	K	2.75	0.61
782	TW 4	TWE060B-PCA	PCA Inner Surface	270	720	K	2.75	0.61
783	TW 5	TWE070B-CLA	CLA Inner Surface	270	720	K	2.75	0.61
784	TW 6	TWE080B-CLA	CLA Inner Surface	270	720	K	2.75	0.61
785	TW 7	TWE160B-HLB	HLB Inner Surface	270	720	K	2.75	0.61
786	TW 8	TWE170B-HLB	HLB Inner Surface	270	720	K	2.75	0.61
787	TW 9	TWE190B-LSB	LSB Inner Surface	270	720	K	2.75	0.61
788	TW 10	TWE200B-PCB	PCB Inner Surface	270	720	K	2.75	0.61
789	TW 11	TWE210B-CLB	CLB Inner Surface	270	720	K	2.75	0.61
790	TW 12	TWE220B-CLB	CLB Inner Surface	270	720	K	2.75	0.61
791	TW 13	TWE280B-PR	Pressurizer Surge Line	270	720	K	2.75	0.61
792	TW 14	TWE431A-SGA	SGA Downcomer A Wall	270	670	K	2.63	0.66
793	TW 15	TWE432A-SGA	SGA Downcomer B Wall	270	670	K	2.63	0.66
794	TW 16	TWE433A-SGA	SGA Downcomer C Wall	270	670	K	2.63	0.66
795	TW 17	TWE434A-SGA	SGA Downcomer D Wall	270	670	K	2.63	0.66
796	TW 18	TWE471A-SGB	SGB Downcomer A Wall	270	670	K	2.63	0.66
797	TW 19	TWE472A-SGB	SGB Downcomer B Wall	270	670	K	2.63	0.66
798	TW 20	TWE473A-SGB	SGB Downcomer C Wall	270	670	K	2.63	0.66
799	TW 21	TWE474A-SGB	SGB Downcomer D Wall	270	670	K	2.63	0.66
800	TW 22	TWE-E-015B-PV	PV Inner Surf. EL.-1.5m,E	270	720	K	2.75	0.61
801	TW 23	TWE-W-015B-PV	PV Inner Surf. EL.-1.5m,W	270	720	K	2.75	0.61
802	TW 24	TWE-N000B-PV	PV Inner Surf. EL.0.0m,N	270	720	K	2.75	0.61
803	TW 25	TWE-S000B-PV	PV Inner Surf. EL.0.0m,S	270	720	K	2.75	0.61
804	TW 26	TWE-E000B-PV	PV Inner Surf. EL.0.0m,E	270	720	K	2.75	0.61
805	TW 27	TWE-W000B-PV	PV Inner Surf. EL.0.0m,W	270	720	K	2.75	0.61
806	TW 28	TWE-N018B-PV	PV Inner Surf. EL.1.8m,N	270	720	K	2.75	0.61
807	TW 29	TWE-S018B-PV	PV Inner Surf. EL.1.8m,S	270	720	K	2.75	0.61
808	TW 30	TWE-E018B-PV	PV Inner Surf. EL.1.8m,E	270	720	K	2.75	0.61
809	TW 31	TWE-W018B-PV	PV Inner Surf. EL.1.8m,W	270	720	K	2.75	0.61
810	TW 32	TWE-N036B-PV	PV Inner Surf. EL.3.6m,N	270	720	K	2.75	0.61
811	TW 33	TWE-S036B-PV	PV Inner Surf. EL.3.6m,S	270	720	K	2.75	0.61
812	TW 34	TWE-E036B-PV	PV Inner Surf. EL.3.6m,E	270	720	K	2.75	0.61
813	TW 35	TWE-W036B-PV	PV Inner Surf. EL.3.6m,W	270	720	K	2.75	0.61
814	TW 36	TWE-N060B-PV	PV Inner Surf. EL.6.0m,N	270	720	K	2.75	0.61
815	TW 37	TWE-S060B-PV	PV Inner Surf. EL.6.0m,S	270	720	K	2.75	0.61
816	TW 38	TWE-E060B-PV	PV Inner Surf. EL.6.0m,E	270	720	K	2.75	0.61
817	TW 39	TWE-W060B-PV	PV Inner Surf. EL.6.0m,W	270	720	K	2.75	0.61
818	TW 40	TWE-E080B-PV	PV Inner Surf. EL.8.0m,E	270	720	K	2.75	0.61

Table A.1 (Cont'd) (11/20)

SEQ No.	Function ID.	Tagname	Location	Range		Unit	Uncertainty	
				LO	HI		±ABS.	±%FR
819	TW 41	TWE-W080B-PV	PV Inner Surf. EL.8.0m,W	270	720	K	2.75	0.61
820	TW 43	TWE-S000D-CB	CB Outer Surf. EL.0.0m,S	270	970	K	3.49	0.5
821	TW 44	TWE-E000D-CB	CB Outer Surf. EL.0.0m,E	270	970	K	3.49	0.5
822	TW 45	TWE-W000D-CB	CB Outer Surf. EL.0.0m,W	270	970	K	3.49	0.5
823	TW 50	TWE-N018D-CB	CB Outer Surf. EL.1.8m,N	270	970	K	3.49	0.5
824	TW 51	TWE-S018D-CB	CB Outer Surf. EL.1.8m,S	270	970	K	3.49	0.5
825	TW 52	TWE-E018D-CB	CB Outer Surf. EL.1.8m,E	270	970	K	3.49	0.5
826	TW 53	TWE-W018D-CB	CB Outer Surf. EL.1.8m,W	270	970	K	3.49	0.5
827	TW 57	TWE-W026D-CB	CB Outer Surf. EL.2.6m,W	270	970	K	3.49	0.5
828	TW 58	TWE-N036D-CB	CB Outer Surf. EL.3.6m,N	270	970	K	3.49	0.5
829	TW 59	TWE-S036D-CB	CB Outer Surf. EL.3.6m,S	270	970	K	3.49	0.5
830	TW 61	TWE-W036D-CB	CB Outer Surf. EL.3.6m,W	270	970	K	3.49	0.5
831	TW 62	TWE-N049D-CB	CB Outer Surf. EL.4.9m,N	270	970	K	3.49	0.5
832	TW 63	TWE-S049D-CB	CB Outer Surf. EL.4.9m,S	270	970	K	3.49	0.5
833	TW 64	TWE-E049D-CB	CB Outer Surf. EL.4.9m,E	270	970	K	3.49	0.5
834	TW 65	TWE-W049D-CB	CB Outer Surf. EL.4.9m,W	270	970	K	3.49	0.5
835	TW 66	TWE-N060D-CB	CB Outer Surf. EL.6.0m,N	270	970	K	3.49	0.5
836	TW 67	TWE-S060D-CB	CB Outer Surf. EL.6.0m,S	270	970	K	3.49	0.5
837	TW 68	TWE-E060D-CB	CB Outer Surf. EL.6.0m,E	270	970	K	3.49	0.5
838	TW 69	TWE-W060D-CB	CB Outer Surf. EL.6.0m,W	270	970	K	3.49	0.5
839	TW 70	TWE-N000E-CB	CB Inner Surf. EL.0.0m,N	270	970	K	3.49	0.5
840	TW 71	TWE-S000E-CB	CB Inner Surf. EL.0.0m,S	270	970	K	3.49	0.5
841	TW 72	TWE-E000E-CB	CB Inner Surf. EL.0.0m,E	270	970	K	3.49	0.5
842	TW 73	TWE-W000E-CB	CB Inner Surf. EL.0.0m,W	270	970	K	3.49	0.5
843	TW 78	TWE-N018E-CB	CB Inner Surf. EL.1.8m,N	270	970	K	3.49	0.5
844	TW 79	TWE-S018E-CB	CB Inner Surf. EL.1.8m,S	270	970	K	3.49	0.5
845	TW 80	TWE-E018E-CB	CB Inner Surf. EL.1.8m,E	270	970	K	3.49	0.5
846	TW 81	TWE-W018E-CB	CB Inner Surf. EL.1.8m,W	270	970	K	3.49	0.5
847	TW 86	TWE-N036E-CB	CB Inner Surf. EL.3.6m,N	270	970	K	3.49	0.5
848	TW 87	TWE-S036E-CB	CB Inner Surf. EL.3.6m,S	270	970	K	3.49	0.5
849	TW 88	TWE-E036E-CB	CB Inner Surf. EL.3.6m,E	270	970	K	3.49	0.5
850	TW 92	TWE-E049E-CB	CB Inner Surf. EL.4.9m,E	270	970	K	3.49	0.5
851	TW 94	TWE-N060E-CB	CB Inner Surf. EL.6.0m,N	270	970	K	3.49	0.5
852	TW 95	TWE-S060E-CB	CB Inner Surf. EL.6.0m,S	270	970	K	3.49	0.5
853	TW 96	TWE-E060E-CB	CB Inner Surf. EL.6.0m,E	270	970	K	3.49	0.5
854	TW 97	TWE-W060E-CB	CB Inner Surf. EL.6.0m,W	270	970	K	3.49	0.5
855	TW 108	TWE-063-B09-UCSP	UCSP L.Surf. EL.6.3m,B09	270	970	K	3.49	0.5
856	TW 109	TWE-065-B09-UCSP	UCSP U.Surf. EL.6.5m,B09	270	970	K	3.49	0.5
857	TW 110	TWE-E047G-UP	UP Str. Surf. EL.4.7m,East	270	970	K	3.49	0.5
858	TW 111	TWE-W047G-UP	UP Str. Surf. EL.4.7m,West	270	970	K	3.49	0.5
859	TW 112	TWE-E056G-UP	UP Str. Surf. EL.5.6m,East	270	970	K	3.49	0.5
860	TW 113	TWE-W056G-UP	UP Str. Surf. EL.5.6m,West	270	970	K	3.49	0.5
861	TW 114	TWE-080G-UH	UH Str. Surf. EL.8.0m,CTR	270	970	K	3.49	0.5
862	TW 154	TWE-B03436	B03 Rod(4,3) Pos.6	270	1470	K	5.31	0.44
863	TW 155	TWE-B03438	B03 Rod(4,3) Pos.8	270	1470	K	5.31	0.44
864	TW 217	TWE-B08222	B08 Rod(2,2) Pos.2	270	970	K	5.31	0.44
865	TW 218	TWE-B08224	B08 Rod(2,2) Pos.4	270	970	K	5.31	0.44
866	TW 219	TWE-B08225	B08 Rod(2,2) Pos.5	270	970	K	5.31	0.44
867	TW 220	TWE-B08226	B08 Rod(2,2) Pos.6	270	970	K	5.31	0.44
868	TW 222	TWE-B08228	B08 Rod(2,2) Pos.8	270	970	K	5.31	0.44
869	TW 225	TWE-B08435	B08 Rod(4,3) Pos.5	270	1470	K	5.31	0.44
870	TW 227	TWE-B08437	B08 Rod(4,3) Pos.7	270	1470	K	5.31	0.44
871	TW 236	TWE-B10442	B10 Rod(4,4) Pos.2	270	1470	K	5.31	0.44
872	TW 237	TWE-B10444	B10 Rod(4,4) Pos.4	270	1470	K	5.31	0.44
873	TW 239	TWE-B10447	B10 Rod(4,4) Pos.7	270	1470	K	5.31	0.44
874	TW 259	TWE-B12262	B12 Rod(2,6) Pos.2	270	970	K	5.31	0.44
875	TW 260	TWE-B12264	B12 Rod(2,6) Pos.4	270	970	K	5.31	0.44
876	TW 261	TWE-B12265	B12 Rod(2,6) Pos.5	270	970	K	5.31	0.44
877	TW 262	TWE-B12266	B12 Rod(2,6) Pos.6	270	970	K	5.31	0.44
878	TW 264	TWE-B12268	B12 Rod(2,6) Pos.8	270	970	K	5.31	0.44
879	TW 283	TWE-B13442	B13 Rod(4,4) Pos.2	270	1470	K	5.31	0.44
880	TW 284	TWE-B13444	B13 Rod(4,4) Pos.4	270	1470	K	5.31	0.44
881	TW 286	TWE-B13446	B13 Rod(4,4) Pos.6	270	1470	K	5.31	0.44
882	TW 287	TWE-B13447	B13 Rod(4,4) Pos.7	270	1470	K	5.31	0.44
883	TW 288	TWE-B13448	B13 Rod(4,4) Pos.8	270	1470	K	5.31	0.44
884	TW 339	TWE-B17445	B17 Rod(4,4) Pos.5	270	1470	K	5.31	0.44
885	TW 341	TWE-B17447	B17 Rod(4,4) Pos.7	270	1470	K	5.31	0.44
886	TW 391	TWE-B21662	B21 Rod(6,6) Pos.2	270	1470	K	5.31	0.44
887	TW 392	TWE-B21664	B21 Rod(6,6) Pos.4	270	1470	K	5.31	0.44
888	TW 394	TWE-B21666	B21 Rod(6,6) Pos.6	270	1470	K	5.31	0.44
889	TW 395	TWE-B21667	B21 Rod(6,6) Pos.7	270	1470	K	5.31	0.44
890	TW 409	TWE-B22441	B22 Rod(4,4) Pos.1	270	1470	K	5.31	0.44
891	TW 410	TWE-B22443	B22 Rod(4,4) Pos.3	270	1470	K	5.31	0.44
892	TW 411	TWE-B22445	B22 Rod(4,4) Pos.5	270	1470	K	5.31	0.44
893	TW 414	TWE-B22449	B22 Rod(4,4) Pos.9	270	1470	K	5.31	0.44
894	TW 457	TWE-IN0641-SGA	SGA Inlet Plenum	270	720	K	2.75	0.61
895	TW 459	TWE-IN0643-SGA	SGA Inlet Plenum	270	720	K	2.75	0.61
896	TW 463	TWE-086B-SGA	SGA Inner Surf. Pos.1	270	670	K	2.63	0.66
897	TW 464	TWE-137B-SGA	SGA Inner Surf. Pos.7	270	670	K	2.63	0.66
898	TW 465	TWE-178B-SGA	SGA Inner Surf. Pos.10	270	670	K	2.63	0.66
899	TW 466	TWE-223B-SGA	SGA Inner Surf.	270	670	K	2.63	0.66
900	TW 467	TWE-IN0861-SGA	SGA U-Tube(1,IN) Pos.1	270	720	K	2.75	0.61

Table A.1 (Cont'd) (12/20)

SEQ No.	Function ID.	Tagname	Location	Range		Unit	Uncertainty	
				LO	HI		±ABS.	±%FR
901	TW 468	TWE-EX0861-SGA	SGA U-Tube(1,EX) Pos.1	270	720	K	2.75	0.61
902	TW 469	TWE-IN0862-SGA	SGA U-Tube(2,IN) Pos.1	270	720	K	2.75	0.61
903	TW 470	TWE-EX0862-SGA	SGA U-Tube(2,EX) Pos.1	270	720	K	2.75	0.61
904	TW 471	TWE-IN0863-SGA	SGA U-Tube(3,IN) Pos.1	270	720	K	2.75	0.61
905	TW 472	TWE-EX0863-SGA	SGA U-Tube(3,EX) Pos.1	270	720	K	2.75	0.61
906	TW 473	TWE-IN0991-SGA	SGA U-Tube(1,IN) Pos.3	270	720	K	2.75	0.61
907	TW 474	TWE-EX0991-SGA	SGA U-Tube(1,EX) Pos.3	270	720	K	2.75	0.61
908	TW 475	TWE-IN0992-SGA	SGA U-Tube(2,IN) Pos.3	270	720	K	2.75	0.61
909	TW 476	TWE-EX0992-SGA	SGA U-Tube(2,EX) Pos.3	270	720	K	2.75	0.61
910	TW 477	TWE-IN0993-SGA	SGA U-Tube(3,IN) Pos.3	270	720	K	2.75	0.61
911	TW 478	TWE-EX0993-SGA	SGA U-Tube(3,EX) Pos.3	270	720	K	2.75	0.61
912	TW 479	TWE-IN1121-SGA	SGA U-Tube(1,IN) Pos.5	270	720	K	2.75	0.61
913	TW 480	TWE-EX1121-SGA	SGA U-Tube(1,EX) Pos.5	270	720	K	2.75	0.61
914	TW 481	TWE-IN1122-SGA	SGA U-Tube(2,IN) Pos.5	270	720	K	2.75	0.61
915	TW 482	TWE-EX1122-SGA	SGA U-Tube(2,EX) Pos.5	270	720	K	2.75	0.61
916	TW 483	TWE-IN1123-SGA	SGA U-Tube(3,IN) Pos.5	270	720	K	2.75	0.61
917	TW 484	TWE-EX1123-SGA	SGA U-Tube(3,EX) Pos.5	270	720	K	2.75	0.61
918	TW 485	TWE-IN1371-SGA	SGA U-Tube(1,IN) Pos.7	270	720	K	2.75	0.61
919	TW 486	TWE-EX1371-SGA	SGA U-Tube(1,EX) Pos.7	270	720	K	2.75	0.61
920	TW 487	TWE-IN1372-SGA	SGA U-Tube(2,IN) Pos.7	270	720	K	2.75	0.61
921	TW 488	TWE-EX1372-SGA	SGA U-Tube(2,EX) Pos.7	270	720	K	2.75	0.61
922	TW 489	TWE-IN1373-SGA	SGA U-Tube(3,IN) Pos.7	270	720	K	2.75	0.61
923	TW 490	TWE-EX1373-SGA	SGA U-Tube(3,EX) Pos.7	270	720	K	2.75	0.61
924	TW 491	TWE-IN1632-SGA	SGA U-Tube(2,IN) Pos.9	270	720	K	2.75	0.61
925	TW 492	TWE-EX1632-SGA	SGA U-Tube(2,EX) Pos.9	270	720	K	2.75	0.61
926	TW 493	TWE-IN1633-SGA	SGA U-Tube(3,IN) Pos.9	270	720	K	2.75	0.61
927	TW 494	TWE-EX1633-SGA	SGA U-Tube(3,EX) Pos.9	270	720	K	2.75	0.61
928	TW 495	TWE-IN1701-SGA	SGA U-Tube(1,IN) Pos.10	270	720	K	2.75	0.61
929	TW 496	TWE-IN1782-SGA	SGA U-Tube(2,IN) Pos.10	270	720	K	2.75	0.61
930	TW 497	TWE-IN1863-SGA	SGA U-Tube(3,IN) Pos.11	270	720	K	2.75	0.61
931	TW 498	TWE-IN0641-SGB	SGB Inlet Plenum	270	720	K	2.75	0.61
932	TW 499	TWE-IN0642-SGB	SGB Inlet Plenum	270	720	K	2.75	0.61
933	TW 500	TWE-IN0643-SGB	SGB Inlet Plenum	270	720	K	2.75	0.61
934	TW 504	TWE-086B-SGB	SGB Inner Surf. Pos.1	270	670	K	2.63	0.66
935	TW 505	TWE-137B-SGB	SGB Inner Surf. Pos.7	270	670	K	2.63	0.66
936	TW 506	TWE-178B-SGB	SGB Inner Surf. Pos.10	270	670	K	2.63	0.66
937	TW 507	TWE-223B-SGB	SGB Inner Surf.	270	670	K	2.63	0.66
938	TW 508	TWE-IN0861-SGB	SGB U-Tube(1,IN) Pos.1	270	720	K	2.75	0.61
939	TW 509	TWE-EX0861-SGB	SGB U-Tube(1,EX) Pos.1	270	720	K	2.75	0.61
940	TW 510	TWE-IN0862-SGB	SGB U-Tube(2,IN) Pos.1	270	720	K	2.75	0.61
941	TW 511	TWE-EX0862-SGB	SGB U-Tube(2,EX) Pos.1	270	720	K	2.75	0.61
942	TW 512	TWE-IN0863-SGB	SGB U-Tube(3,IN) Pos.1	270	720	K	2.75	0.61
943	TW 513	TWE-EX0863-SGB	SGB U-Tube(3,EX) Pos.1	270	720	K	2.75	0.61
944	TW 514	TWE-IN0991-SGB	SGB U-Tube(1,IN) Pos.3	270	720	K	2.75	0.61
945	TW 515	TWE-EX0991-SGB	SGB U-Tube(1,EX) Pos.3	270	720	K	2.75	0.61
946	TW 516	TWE-IN0992-SGB	SGB U-Tube(2,IN) Pos.3	270	720	K	2.75	0.61
947	TW 517	TWE-EX0992-SGB	SGB U-Tube(2,EX) Pos.3	270	720	K	2.75	0.61
948	TW 518	TWE-IN0993-SGB	SGB U-Tube(3,IN) Pos.3	270	720	K	2.75	0.61
949	TW 519	TWE-EX0993-SGB	SGB U-Tube(3,EX) Pos.3	270	720	K	2.75	0.61
950	TW 520	TWE-IN1121-SGB	SGB U-Tube(1,IN) Pos.5	270	720	K	2.75	0.61
951	TW 521	TWE-EX1121-SGB	SGB U-Tube(1,EX) Pos.5	270	720	K	2.75	0.61
952	TW 522	TWE-IN1122-SGB	SGB U-Tube(2,IN) Pos.5	270	720	K	2.75	0.61
953	TW 523	TWE-EX1122-SGB	SGB U-Tube(2,EX) Pos.5	270	720	K	2.75	0.61
954	TW 524	TWE-IN1123-SGB	SGB U-Tube(3,IN) Pos.5	270	720	K	2.75	0.61
955	TW 525	TWE-EX1123-SGB	SGB U-Tube(3,EX) Pos.5	270	720	K	2.75	0.61
956	TW 526	TWE-IN1371-SGB	SGB U-Tube(1,IN) Pos.7	270	720	K	2.75	0.61
957	TW 527	TWE-EX1371-SGB	SGB U-Tube(1,EX) Pos.7	270	720	K	2.75	0.61
958	TW 528	TWE-IN1372-SGB	SGB U-Tube(2,IN) Pos.7	270	720	K	2.75	0.61
959	TW 529	TWE-EX1372-SGB	SGB U-Tube(2,EX) Pos.7	270	720	K	2.75	0.61
960	TW 530	TWE-IN1373-SGB	SGB U-Tube(3,IN) Pos.7	270	720	K	2.75	0.61
961	TW 531	TWE-EX1373-SGB	SGB U-Tube(3,EX) Pos.7	270	720	K	2.75	0.61
962	TW 532	TWE-IN1632-SGB	SGB U-Tube(2,IN) Pos.9	270	720	K	2.75	0.61
963	TW 533	TWE-EX1632-SGB	SGB U-Tube(2,EX) Pos.9	270	720	K	2.75	0.61
964	TW 534	TWE-IN1633-SGB	SGB U-Tube(3,IN) Pos.9	270	720	K	2.75	0.61
965	TW 535	TWE-EX1633-SGB	SGB U-Tube(3,EX) Pos.9	270	720	K	2.75	0.61
966	TW 536	TWE-IN1701-SGB	SGB U-Tube(1,IN) Pos.10	270	720	K	2.75	0.61
967	TW 537	TWE-IN1782-SGB	SGB U-Tube(2,IN) Pos.10	270	720	K	2.75	0.61
968	TW 538	TWE-IN1863-SGB	SGB U-Tube(3,IN) Pos.11	270	720	K	2.75	0.61
969	TW 545	TWE270A-PR	PZR Spray Line Outer Surf.	270	720	K	2.75	0.61
970	TW 598	TWE-121D-UHDP	PLR-UH-9 Outer Surf.	270	970	K	3.49	0.5
971	TW 631	TWE-B01225	B01 Rod(2,2) Pos.5	270	1470	K	6.32	0.53
972	TW 635	TWE-B04221	B04 Rod(2,2) Pos.1	270	970	K	3.69	0.53
973	TW 638	TWE-B04226	B04 Rod(2,2) Pos.6	270	970	K	3.69	0.53
974	TW 640	TWE-B04229	B04 Rod(2,2) Pos.9	270	970	K	3.69	0.53
975	TW 649	TWE-B11225	B11 Rod(2,2) Pos.5	270	1470	K	6.32	0.53
976	TW 650	TWE-B11226	B11 Rod(2,2) Pos.6	270	1470	K	6.32	0.53
977	TW 653	TWE-B16221	B16 Rod(2,2) Pos.1	270	970	K	3.69	0.53
978	TW 654	TWE-B16223	B16 Rod(2,2) Pos.3	270	970	K	3.69	0.53
979	TW 656	TWE-B16226	B16 Rod(2,2) Pos.6	270	970	K	3.69	0.53
980	TW 658	TWE-B16229	B16 Rod(2,2) Pos.9	270	970	K	3.69	0.53
981	TW 667	TWE-246A-SGPHX	SGPHX Outer Surf. DL.3825	270	570	K	2.42	0.81
982	TW 668	TWE-246B-SGPHX	SGPHX Inner Surf. DL.3825	270	570	K	2.42	0.81

Table A.1 (Cont'd) (13/20)

SEQ No.	Function ID.	Tagname	Location	Range		Unit	Uncertainty	
				LO	HI		±ABS.	±%FR
983	TW 669	TWE-230A-SGPHX	SGPHX Outer Surf. DL.2138	270	570	K	2.42	0.81
984	TW 670	TWE-230B-SGPHX	SGPHX Inner Surf. DL.2138	270	570	K	2.42	0.81
985	TW 671	TWE-213A-SGPHX	SGPHX Outer Surf. DL.450	270	570	K	2.42	0.81
986	TW 672	TWE-213B-SGPHX	SGPHX Inner Surf. DL.450	270	570	K	2.42	0.81
987	TW 673	TWE-EN037B-PV	PV East-North EL.3662	270	630	K	3.05	0.85
988	TW 674	TWE-E037B-PV	PV East EL.3662	270	630	K	3.05	0.85
989	TW 676	TWE-EN040B-PV	PV East-Nouth EL.4037	270	630	K	3.05	0.85
990	TW 678	TWE-ES040B-PV	PV East-South EL.4037	270	630	K	3.05	0.85
991	TW 679	TWE-E042B-PV	PV East EL.4210	270	630	K	3.05	0.85
992	TW 680	TWE-WN037B-PV	PV West-North EL.3662	270	630	K	3.05	0.85
993	TW 681	TWE-W037B-PV	PV West EL.3662	270	630	K	3.05	0.85
994	TW 682	TWE-WS037B-PV	PV West-South EL.3662	270	630	K	3.05	0.85
995	TW 685	TWE-WS040B-PV	PV West-South EL.4037	270	630	K	3.05	0.85
996	TW 687	TWE-SW045B-PV	PV South-West EL.4497	270	630	K	3.05	0.85
997	TW 688	TWE-S045B-PV	PV South EL.4497	270	630	K	3.05	0.85
998	TW 689	TWE-SE045B-PV	PV South-East EL.4497	270	630	K	3.05	0.85
999	TW 690	TWE-SW051B-PV	PV South-West EL.5074	270	630	K	3.05	0.85
1000	TW 691	TWE-S051B-PV	PV South EL.5074	270	630	K	3.05	0.85
1001	TW 692	TWE-SE051B-PV	PV South-East EL.5074	270	630	K	3.05	0.85
1002	TW 693	TWE-S054B-PV	PV South EL.5363	270	630	K	3.05	0.85
1003	TW 694	TWE-NE045B-PV	PV North-East EL.4497	270	630	K	3.05	0.85
1004	TW 696	TWE-NW045B-PV	PV North-West EL.4497	270	630	K	3.05	0.85
1005	TW 697	TWE-NE051B-PV	PV North-East EL.5074	270	630	K	3.05	0.85
1006	TW 698	TWE-N051B-PV	PV North EL.5074	270	630	K	3.05	0.85
1007	TW 700	TWE-N054B-PV	PV North EL.5363	270	630	K	3.05	0.85
1008	TW 709	TWE-IN038B02-UCP	UCP L.Surf. EL.3.8m,B02	270	970	K	3.49	0.5
1009	TW 710	TWE-IN038B04-UCP	UCP L.Surf. EL.3.8m,B04	270	970	K	3.49	0.5
1010	TW 711	TWE-IN038B06-UCP	UCP L.Surf. EL.3.8m,B06	270	970	K	3.49	0.5
1011	TW 712	TWE-IN038B08-UCP	UCP L.Surf. EL.3.8m,B08	270	970	K	3.49	0.5
1012	TW 713	TWE-IN038B21-UCP	UCP L.Surf. EL.3.8m,B21	270	970	K	3.49	0.5
1013	TW 714	TWE-EX040B02-UCP	UCP U.Surf. EL.4.0m,B02	270	970	K	3.49	0.5
1014	TW 715	TWE-EX040B04-UCP	UCP U.Surf. EL.4.0m,B04	270	970	K	3.49	0.5
1015	TW 716	TWE-EX040B06-UCP	UCP U.Surf. EL.4.0m,B06	270	970	K	3.49	0.5
1016	TW 717	TWE-EX040B08-UCP	UCP U.Surf. EL.4.0m,B08	270	970	K	3.49	0.5
1017	TW 718	TWE-EX040B21-UCP	UCP U.Surf. EL.4.0m,B21	270	970	K	3.49	0.5
1018	TW 727	TWE-B03437	B03 Rod(4,3) Pos.7	270	1470	K	5.31	0.44
1019	TW 732	TWE-B08431	B08 Rod(4,3) Pos.1	270	1470	K	5.31	0.44
1020	TW 733	TWE-B08433	B08 Rod(4,3) Pos.3	270	1470	K	5.31	0.44
1021	TW 734	TWE-B08439	B08 Rod(4,3) Pos.9	270	1470	K	5.31	0.44
1022	TW 739	TWE-B10446	B10 Rod(4.4) Pos.6	270	1470	K	5.31	0.44
1023	TW 740	TWE-B10448	B10 Rod(4.4) Pos.8	270	1470	K	5.31	0.44
1024	TW 757	TWE-B17441	B17 Rod(4.4) Pos.1	270	1470	K	5.31	0.44
1025	TW 758	TWE-B17443	B17 Rod(4.4) Pos.3	270	1470	K	5.31	0.44
1026	TW 759	TWE-B17449	B17 Rod(4.4) Pos.9	270	1470	K	5.31	0.44
1027	TW 768	TWE-B22447	B22 Rod(4.4) Pos.7	270	1470	K	5.31	0.44
1028	TW 773	TWE211A-PR	PZR Wall DL.2025	270	720	K	2.75	0.61
1029	TW 774	TWE211B-PR	PZR Wall DL.4238	270	720	K	2.75	0.61
1030	TW 775	TWE211C-PR	PZR Wall DL.5995	270	720	K	2.75	0.61
1031	TW 776	TWE211D-PR	PZR Wall DL.7965	270	720	K	2.75	0.61
1032	TW 777	TWE211E-PR	PZR Wall DL.9795	270	720	K	2.75	0.61
1033	TW 778	TWE211F-PR	PZR Wall DL.11321	270	720	K	2.75	0.61
1034	TW 779	TWE678-ACC	Acc-Cold Tank Wall	270	720	K	2.75	0.61
1035	TW 780	TWE688-ACH	Acc-Hot Tank Wall	270	720	K	2.75	0.61
1036	TW 783	TWE-A80-ADS	RSV(1-3) Line	270	720	K	2.75	0.61
1037	TW 845	TWE111A-PR	PZR Outer Wall DL.-289	270	720	K	2.75	0.61
1038	TW 846	TWE115A-PR	PZR Outer Wall DL.105	270	720	K	2.75	0.61
1039	TW 847	TWE189A-PR	PZR Outer Wall DL.7219	270	720	K	2.75	0.61
1040	TW 848	TWE198A-PR	PZR Outer Wall DL.8417	270	720	K	2.75	0.61
1041	TW 849	TWE-022A-PV	PV Outer Wall EL.-2245	270	720	K	2.75	0.61
1042	TW 850	TWE-027A-PV	PV Outer Wall EL.-2657	270	720	K	2.75	0.61
1043	TW 851	TWE-028A-PV	PV Outer Wall EL.-2677	270	720	K	2.75	0.61
1044	TW 852	TWE731A-HLA	HLA Outer Wall	270	720	K	2.75	0.61
1045	TW 853	TWE078A-SGA	SGA Outer Wall DL.-161	270	670	K	2.63	0.66
1046	TW 854	TWE245A-SGA	SGA Outer Wall DL.16572	270	670	K	2.63	0.66
1047	TW 859	TWE-A82-ADS	RSV123 Spool Piece	270	720	K	2.75	0.61
1048	TW 860	TWE-A83-ADS	RSV1 Orifice	270	720	K	2.75	0.61
1049	TW 862	TWE-A84-ADS	RSV AOV81 Body Wall	270	720	K	2.75	0.61
1050	TW 863	TWE-A85-ADS	RSV AOV81 Outer Frame	270	720	K	2.75	0.61
1051	TW 864	TWE292-PR	PZR VP-Line Pipe Wall	270	720	K	2.75	0.61
1052	TW 865	TWE442-SGA	SGA 8B MSL Pipe Wall	270	570	K	2.42	0.81
1053	TW 866	TWE441-SGA	SGA 8B MSL Support	270	570	K	2.42	0.81
1054	TW 867	TWE444-SGA	SGA 3B MSL Pipe Wall	270	570	K	2.42	0.81
1055	TW 868	TWE445-SGA	SGA 3B MSL Support	270	570	K	2.42	0.81
1056	TW 869	TWE446-SGA	SGA MSIV Body Wall	270	570	K	2.42	0.81
1057	TW 870	TWE447-SGA	SGA MSIV Outer Frame	270	570	K	2.42	0.81
1058	TW 872	TWE572-BU	SGTR BU Line	270	570	K	2.42	0.81
1059	TW 873	TWE-B03432	B03 Rod(4.3) Pos.2	270	1470	K	6.32	0.53
1060	TW 874	TWE-B03434	B03 Rod(4.3) Pos.4	270	1470	K	6.32	0.53
1061	FE 1	FE010-HLA	HLA Leakage (Normal)	0	0.4	kg/s	0.01	1.54
1062	FE 2	FE020A-LSA	Primary Loop LSA (High)	0	90	kg/s	1.25	1.39
1063	FE 3	FE020B-LSA	Primary Loop LSA (Low)	0	15.81	kg/s	0.22	1.37

Table A.1 (Cont'd) (14/20)

SEQ No.	Function ID.	Tagname	Location	Range		Unit	Uncertainty	
				LO	HI		±ABS.	±%FR
1064	FE 4	FE150-HLB	HLB Leakage (Normal)	0	0.4	kg/s	0.01	1.54
1065	FE 5	FE160A-LSB	Primary Loop LSB (High)	0	90	kg/s	1.25	1.39
1066	FE 6	FE160B-LSB	Primary Loop LSB (Low)	0	15.81	kg/s	0.22	1.37
1067	FE 13	FE430-SGA	SGA Feedwater	0	4	kg/s	0.05	1.35
1068	FE 14	FE431-SGA	SGA Downcomer	0	7	kg/s	0.09	1.26
1069	FE 15	FE432-SGA	SGA Downcomer	0	7	kg/s	0.09	1.26
1070	FE 16	FE433-SGA	SGA Downcomer	0	7	kg/s	0.09	1.26
1071	FE 17	FE434-SGA	SGA Downcomer	0	7	kg/s	0.09	1.26
1072	FE 18	FE440-SGA	SGA Steam Line	0	5	kg/s	0.1	2.04
1073	FE 19	FE450-SGA	SGA Relief Valve Line	0	4	kg/s	0.07	1.82
1074	FE 21	FE470-SGB	SGB Feedwater	0	4	kg/s	0.05	1.35
1075	FE 22	FE471-SGB	SGB Downcomer	0	7	kg/s	0.09	1.26
1076	FE 23	FE472-SGB	SGB Downcomer	0	7	kg/s	0.09	1.26
1077	FE 24	FE473-SGB	SGB Downcomer	0	7	kg/s	0.09	1.26
1078	FE 25	FE474-SGB	SGB Downcomer	0	7	kg/s	0.09	1.26
1079	FE 26	FE480-SGB	SGB Steam Line	0	5	kg/s	0.1	2.04
1080	FE 27	FE490-SGB	SGB Relief Valve Line	0	4	kg/s	0.07	1.82
1081	FE 29	FE510-SH	Main-Steam Header	0	10	kg/s	0.22	2.16
1082	FE 33	FE570A-BU	Break Venturi (Hi)	0	10	kg/s	0.14	1.43
1083	FE 34	FE570B-BU	Break Venturi (Lo)	0	2.24	kg/s	0.08	3.5
1084	FE 37	FE650-ACC	Acc-Cold Flow to CLA	0	15	kg/s	0.19	1.25
1085	FE 40	FE680-ACH	Acc-Hot Flow to CLB	0	10	kg/s	0.21	2.15
1086	FE 41	FE730-PJ	HPI (PJ) Delivery (High)	0	2.2	kg/s	0.03	1.25
1087	FE 42	FE740-PJ	HPI (PJ) Flow to A (High)	0	1.4	kg/s	0.02	1.26
1088	FE 48	FE820-PL	RHR Outlet (High)	0	15	kg/s	0.24	1.62
1089	FE 49	FE830-PL	LPI Flow to CLA (High)	0	15	kg/s	0.24	1.62
1090	FE 50	FE840-PL	LPI Flow to CLB (High)	0	15	kg/s	0.24	1.62
1091	FE 51	FE900-EX	N2 Gas	0	0.15	kg/s	0.003	1.93
1092	FE 57	FE783-PH	HPI (PH) Flow to CLB	0	3	kg/s	0.05	1.54
1093	FE 61	FE841-PL	LPI Flow to CLB	0	12	kg/s	0.16	1.35
1094	FE 62	FE010B-HLA	HLA Leakage (Reverse)	0	0.4	kg/s	0.01	1.53
1095	FE 63	FE150B-HLB	HLB Leakage (Reverse)	0	0.4	kg/s	0.01	1.53
1096	FE 65	FE440B-SGA	SGA Main Steam Line (Low)	0	1	kg/s	0.02	2.04
1097	FE 66	FE451-SGA	SGA Turbine Bypass Flow	0	20	kg/s	0.36	1.82
1098	FE 67	FE480B-SGB	SGB Main Steam Line (Low)	0	1	kg/s	0.02	2.04
1099	FE 68	FE491-SGB	SGB Turbine Bypass Flow	0	20	kg/s	0.36	1.82
1100	FE 70	FE520-PAA	Aux. Feedwater A (High)	0	1.5	kg/s	0.02	1.23
1101	FE 71	FE520B-PAA	Aux. Feedwater A (Low)	0	1	kg/s	0.01	1.23
1102	FE 72	FE530B-PAB	Aux. Feedwater B (Low)	0	1	kg/s	0.01	1.23
1103	FE 73	FE730B-PJ	HPI (PJ) Delivery (low)	0	1.28	kg/s	0.02	1.23
1104	FE 74	FE740B-PJ	HPI (PJ) Flow to A (Low)	0	1.28	kg/s	0.02	1.24
1105	FE 78	FE820B-PL	RHR Outlet (Low)	0	5	kg/s	0.08	1.6
1106	FE 79	FE830B-PL	LPI Flow to CLA (Low)	0	5	kg/s	0.08	1.6
1107	FE 80	FE840B-PL	LPI Flow to CLB (Low)	0	3	kg/s	0.05	1.6
1108	PE 2	PE581-BU	Break Venturi	0	20	MPa	0.1077	0.54
1109	PE 3	PE010-SGA	SGA Inlet Plenum	0	20	MPa	0.1077	0.54
1110	PE 4	PE020-LSA	PCA Suction	0	20	MPa	0.1077	0.54
1111	PE 5	PE030-CLA	PCA Delivery	0	20	MPa	0.1077	0.54
1112	PE 6	PE150-SGB	SGB Inlet Plenum	0	20	MPa	0.1077	0.54
1113	PE 7	PE160-LSB	PCB Suction	0	20	MPa	0.1077	0.54
1114	PE 8	PE170-CLB	PCB Delivery	0	20	MPa	0.1077	0.54
1115	PE 9	PE290-PV	PV Upper Head	0	20	MPa	0.1077	0.54
1116	PE 10	PE280A-PV	PV Upper Plenum (High)	0	20	MPa	0.1077	0.54
1117	PE 11	PE280B-PV	PV Upper Plenum (Low)	0	5	MPa	0.0269	0.54
1118	PE 12	PE270-PV	PV Lower Plenum	0	20	MPa	0.1077	0.54
1119	PE 13	PE300A-PR	Pressurizer (High)	0	20	MPa	0.1077	0.54
1120	PE 14	PE300B-PR	Pressurizer (Low)	0	5	MPa	0.0269	0.54
1121	PE 19	PE430-SGA	SGA Steam Dome	0	10	MPa	0.0539	0.54
1122	PE 20	PE440-SGA	SGA Steam Line	0	10	MPa	0.0539	0.54
1123	PE 21	PE450-SGB	SGB Steam Dome	0	10	MPa	0.0539	0.54
1124	PE 22	PE460-SGB	SGB Steam Line	0	10	MPa	0.0539	0.54
1125	PE 23	PE470-SH	Main-Steam Header	0	10	MPa	0.0539	0.54
1126	PE 24	PE480-JC	Jet Condenser	0	10	MPa	0.0539	0.54
1127	PE 25	PE610-ST	Break Flow Supp. Tank	0	1	MPa	0.0032	0.32
1128	PE 28	PE580-BU	Break Orifice Upstream	0	20	MPa	0.1077	0.54
1129	PE 29	PE590-BU	Break Orifice Downstream	0	20	MPa	0.1077	0.54
1130	PE 30	PE600-ST	Break-Flow Blowdown Line	0	2	MPa	0.0064	0.32
1131	PE 31	PE650-ACC	Acc-Cold Tank	0	10	MPa	0.0539	0.54
1132	PE 32	PE660-ACH	Acc-Hot Tank	0	10	MPa	0.0539	0.54
1133	PE 35	PE011-HLA	HLA Spool Piece	0	20	MPa	0.1077	0.54
1134	PE 36	PE071-CLA	CLA Spool Piece	0	20	MPa	0.1077	0.54
1135	PE 37	PE151-HLB	HLB Spool Piece	0	20	MPa	0.1077	0.54
1136	PE 38	PE211-CLB	CLB Spool Piece	0	20	MPa	0.1077	0.54
1137	PE 43	PE571-BU	RSV123 Inlet	0	20	MPa	0.1118	0.56
1138	PE 44	PE591-BU	Break Spool Piece	0	20	MPa	0.1118	0.56
1139	PE 45	PE451-SGA	SGA Safety Valve Line S/P	0	10	MPa	0.1031	1.03
1140	PE 46	PE820-RHR	PL Delivery	0	20	MPa	0.1077	0.54
1141	PE 53	PE430B-SGA	SGA Steam Dome (Low)	0	1	MPa	0.0032	0.32
1142	PE 54	PE450B-SGB	SGB Steam Dome (Low)	0	1	MPa	0.0032	0.32
1143	PE 62	PE-A50-DVIA	PV-DCA ECCS Line	0	20	MPa	0.0641	0.32
1144	PE 63	PE-A51-DVIA	PV-DCA ECCS Line	0	20	MPa	0.0641	0.32

Table A.1 (Cont'd) (15/20)

SEQ No.	Function ID.	Tagname	Location	Range		Unit	Uncertainty	
				LO	HI		±ABS.	±%FR
1145	PE 64	PE-A55-DVIB	PV-DCB ECCS Line	0	20	MPa	0.0641	0.32
1146	PE 65	PE-A56-DVIB	PV-DCB ECCS Line	0	20	MPa	0.0641	0.32
1147	PE 66	PE-A80-ADS	RSV(1-3) Discharge Line	0	4	MPa	0.009	0.22
1148	PE 73	PE-A83-ADS	RSV3 R.O Downstream	0	20	MPa	0.1077	0.54
1149	PE 77	PE300C-PR	Pressurizer (Low)	0	0.7	MPa	0.0019	0.27
1150	PE 78	PE435-SGA	SGA Steam Dome	0	10	MPa	0.0224	0.22
1151	PE 79	PE455-SGB	SGB Steam Dome	0	10	MPa	0.0224	0.22
1152	MI 1	RE010-PCA	PCA (Rotational Speed)	0	70	rps	0.39	0.55
1153	MI 2	RE150-PCB	PCB (Rotational Speed)	0	70	rps	0.39	0.55
1154	MI 3	OPE270-PR	PZR Spray (HCV270)	0	100	%	0.54	0.54
1155	MI 4	OPE300A-PR	PZR Pressure (PCV300A)	0	100	%	0.54	0.54
1156	MI 5	OPE430-SGA	SGA Feedwater (FCV430)	0	100	%	0.54	0.54
1157	MI 6	OPE470-SGB	SGB Feedwater (FCV470)	0	100	%	0.54	0.54
1158	MI 7	OPE440-SGA	Turbine Bypass (FCV440)	0	100	%	0.54	0.54
1159	MI 8	OPE510-SH	Steam Flow (FCV510)	0	100	%	0.54	0.54
1160	MI 9	OPE820-PL	RHR Flow (FCV820)	0	100	%	0.54	0.54
1161	MI 11	VBE010-PCA	PCA (Vibration)	0	200	um	0.1	5.01
1162	MI 12	VBE150-PCB	PCB (Vibration)	0	200	um	0.1	5.01
1163	MI 13	TQE010-PCA	PCA (Torque)	0	100	Nm	1.6	1.6
1164	MI 14	TQE150-PCB	PCB (Torque)	0	100	Nm	1.6	1.6
1165	MI 15	AE010-PCA	PCA (Electric Current)	0	150	A	1.56	1.04
1166	MI 16	AE150-PCB	PCB (Electric Current)	0	150	A	1.56	1.04
1167	MI 17	WE270A-T	Total Core Power	0	16	MW	0.07	0.44
1168	MI 18	WE270B-M	Core Power (Mid. Flux)	0	2	MW	0.01	0.44
1169	MI 19	WE270C-H1	Core Power (High Flux 1)	0	4	MW	0.02	0.44
1170	MI 20	WE270D-H2	Core Power (High Flux 2)	0	4	MW	0.02	0.44
1171	MI 21	WE270E-L1	Core Power (Low Flux 1)	0	2	MW	0.01	0.44
1172	MI 22	WE270F-L2	Core Power (Low Flux 2)	0	2	MW	0.01	0.44
1173	MI 23	WE270G-L3	Core Power (Low Flux 3)	0	2	MW	0.01	0.44
1174	MI 24	WE280A-PR	PZR Proportional Heater	0	10	kW	0.04	0.39
1175	MI 25	WE280B-PR	PZR Base Heater	0	150	kW	0.59	0.39
1176	MI 26	WE010-PCA	PCA Power	0	30	kW	－	－
1177	MI 27	WE150-PCB	PCB Power	0	30	kW	－	－
1178	MI 29	WE020-HLA	HLA Heater Power	0	5	kW	0.01	1.5
1179	MI 30	WE030-LSA	LSA Heater Power	0	7.5	kW	0.01	1.5
1180	MI 31	WE040-CLA	CLA Heater Power	0	2	kW	0.003	1.5
1181	MI 32	WE160-HLB	HLB Heater Power	0	5	kW	0.01	1.5
1182	MI 33	WE170-LSB	LSB Heater Power	0	7.5	kW	0.01	1.5
1183	MI 34	WE180-CLB	CLB Heater Power	0	2	kW	0.003	1.5
1184	MI 35	WE271A-PV	PV Heater Power	0	15	kW	0.02	1.5
1185	MI 36	WE271B-PV	PV Heater Power	0	15	kW	0.02	1.5
1186	MI 37	WE271C-PV	PV Heater Power	0	15	kW	0.02	1.5
1187	MI 38	WE271D-PV	PV Heater Power	0	15	kW	0.02	1.5
1188	MI 39	WE430A-SGA	SGA Heater Power	0	4	kW	0.01	1.5
1189	MI 40	WE430B-SGA	SGA Heater Power	0	4	kW	0.01	1.5
1190	MI 41	WE430C-SGA	SGA Heater Power	0	4	kW	0.01	1.5
1191	MI 42	WE430D-SGA	SGA Heater Power	0	4	kW	0.01	1.5
1192	MI 43	WE440A-SGA	SGA Downcomer Heater Power	0	2	kW	0.003	1.5
1193	MI 44	WE440B-SGA	SGA Downcomer Heater Power	0	2	kW	0.003	1.5
1194	MI 45	WE440C-SGA	SGA Downcomer Heater Power	0	2	kW	0.003	1.5
1195	MI 46	WE440D-SGA	SGA Downcomer Heater Power	0	2	kW	0.003	1.5
1196	MI 47	WE290-PR	PZR Surge Line Heater Power	0	4	kW	0.01	1.5
1197	MI 48	WE300-PR	PZR Spray Line Heater Power	0	7.5	kW	0.01	1.5
1198	MI 49	WE450A-SGB	SGB Heater Power	0	4	kW	0.01	1.5
1199	MI 50	WE450B-SGB	SGB Heater Power	0	4	kW	0.01	1.5
1200	MI 51	WE450C-SGB	SGB Heater Power	0	4	kW	0.01	1.5
1201	MI 52	WE450D-SGB	SGB Heater Power	0	4	kW	0.01	1.5
1202	MI 53	WE460A-SGB	SGB Downcomer Heater Power	0	2	kW	0.003	1.5
1203	MI 54	WE460B-SGB	SGB Downcomer Heater Power	0	2	kW	0.003	1.5
1204	MI 55	WE460C-SGB	SGB Downcomer Heater Power	0	2	kW	0.003	1.5
1205	MI 56	WE460D-SGB	SGB Downcomer Heater Power	0	2	kW	0.003	1.5
1206	LE 1	LE270-PV	PV	0	11	m	0.29	2.68
1207	LE 2	LE280-PR	PZR Overall Level	0	11.24	m	0.25	2.22
1208	LE 3	LE430-SGA	SGA Wide Range	0	17	m	0.38	2.26
1209	LE 4	LE440-SGA	SGA Narrow Range	0	6	m	0.14	2.32
1210	LE 5	LE441-SGA	SGA Boiling Section	0	11	m	0.25	2.27
1211	LE 6	LE450-SGB	SGB Wide Range	0	17	m	0.38	2.26
1212	LE 7	LE460-SGB	SGB Narrow Range	0	6	m	0.14	2.32
1213	LE 8	LE461-SGB	SGB Boiling Section	0	11	m	0.25	2.27
1214	LE 9	LE470-JC	Jet Condenser	0	5.5	m	0.13	2.33
1215	LE 10	LE560-ST	ST Wide Range	0	12	m	0.27	2.26
1216	LE 11	LE570-ST	ST Low Level	0	4	m	0.09	2.25
1217	LE 12	LE580-ST	ST Middle Level	0	4	m	0.11	2.65
1218	LE 13	LE590-ST	ST High Level	0	4	m	0.11	2.65
1219	LE 14	LE650-ACC	Acc-Cold Tank	0	5.5	m	0.12	2.25
1220	LE 15	LE660-ACH	Acc-Hot Tank	0	5.5	m	0.15	2.65
1221	LE 16	LE820-PL	RHR	0	5	m	－	－
1222	LE 17	LE830-RWST	RWST Overall	0	10	m	－	－
1223	LE 18	LE442-SGA	SGA Downcomer	0	12	m	0.27	2.25
1224	LE 19	LE462-SGB	SGB Downcomer	0	12	m	0.27	2.25

Table A.1 (Cont'd) (16/20)

SEQ No.	Function ID.	Tagname	Location	Range		Unit	Uncertainty	
				LO	HI		±ABS.	±%FR
1225	LE 20	DLE270-PV	PV Overall	0	111.06	kPa	1.07	0.96
1226	LE 21	DLE280-PR	PZR Overall	0	113.63	kPa	0.48	0.42
1227	LE 22	DLE430-SGA	SGA Wide Range	0	171.64	kPa	0.69	0.4
1228	LE 23	DLE440-SGA	SGA Narrow-Range	0	60.58	kPa	0.57	0.93
1229	LE 24	DLE441-SGA	SGA Boiling Section	0	111.06	kPa	0.61	0.55
1230	LE 25	DLE442-SGA	SGA Downcomer	0	114.27	kPa	0.62	0.54
1231	LE 26	DLE450-SGB	SGB Wide Range	0	171.64	kPa	0.69	0.4
1232	LE 27	DLE460-SGB	SGB Narrow-Range	0	60.58	kPa	0.57	0.93
1233	LE 28	DLE461-SGB	SGB Boiling Section	0	111.06	kPa	0.61	0.55
1234	LE 29	DLE462-SGB	SGB Downcomer	0	114.27	kPa	0.62	0.54
1235	LE 30	DLE470-JC	JC	0	55.53	kPa	0.56	1.01
1236	LE 31	DLE560-ST	ST Overall Level	0	121.16	kPa	0.59	0.49
1237	LE 32	DLE570-ST	ST Lower Region	0	40.39	kPa	0.16	0.4
1238	LE 33	DLE580-ST	ST Middle Region	0	40.39	kPa	0.27	0.68
1239	LE 34	DLE590-ST	ST Upper Region	0	40.39	kPa	0.27	0.68
1240	LE 35	DLE650-ACC	Acc-Cold Tank	0	55.53	kPa	0.53	0.95
1241	LE 36	DLE660-ACH	Acc-Hot Tank	0	55.53	kPa	1.02	1.84
1242	LE 37	DLE820-PL	RHR	0	50.17	kPa	0.18	0.36
1243	LE 38	DLE830-RWST	RWST	0	196.14	kPa	0.55	0.28
1244	DP 1	DPE010-HLA	Upper Plenum - HLA Nozzle	-40	40	kPa	1.02	1.28
1245	DP 2	DPE020-HLA	HLA Nozzle - HLA Break	-40	40	kPa	1.02	1.28
1246	DP 4	DPE040-HLA	HLA Break - SGA Inlet	-40	40	kPa	1.02	1.28
1247	DP 5	DPE050A-SGA	SGA Inlet - Tube 3 Top	-150	50	kPa	2.03	1.02
1248	DP 6	DPE050B-SGA	SGA Inlet - Tube 2 Top	-150	50	kPa	2.03	1.02
1249	DP 7	DPE050C-SGA	SGA Inlet - Tube 1 Top	-150	50	kPa	2.03	1.02
1250	DP 8	DPE050D-SGA	SGA Inlet - Tube 4 Top	-150	50	kPa	2.03	1.02
1251	DP 9	DPE050E-SGA	SGA Inlet - Tube 5 Top	-150	50	kPa	2.03	1.02
1252	DP 10	DPE050F-SGA	SGA Inlet - Tube 6 Top	-150	50	kPa	2.03	1.02
1253	DP 11	DPE060A-SGA	SGA Outlet - Tube 3 Top	-150	50	kPa	2.03	1.02
1254	DP 12	DPE060B-SGA	SGA Outlet - Tube 2 Top	-150	50	kPa	2.03	1.02
1255	DP 13	DPE060C-SGA	SGA Outlet - Tube 1 Top	-150	50	kPa	2.03	1.02
1256	DP 14	DPE060D-SGA	SGA Outlet - Tube 4 Top	-150	50	kPa	2.03	1.02
1257	DP 15	DPE060E-SGA	SGA Outlet - Tube 5 Top	-150	50	kPa	2.03	1.02
1258	DP 16	DPE060F-SGA	SGA Outlet - Tube 6 Top	-150	50	kPa	2.03	1.02
1259	DP 17	DPE070-LSA	SGA Outlet - LSA Bottom	-80	80	kPa	1.08	0.67
1260	DP 18	DPE080-LSA	LSA Bottom - PCA Suction	-50	50	kPa	1.03	1.03
1261	DP 19	DPE090-PCA	PCA Suction - Delivery	-50	50	kPa	1.03	1.03
1262	DP 20	DPE100-CLA	PZR Spray Line	-200	200	kPa	2.21	0.55
1263	DP 21	DPE110-CLA	PCA Delivery - CLA Break	-50	50	kPa	1.03	1.03
1264	DP 22	DPE120-CLA	CLA Break - CLA Nozzle	-50	50	kPa	1.03	1.03
1265	DP 23	DPE130-CLA	CLA Nozzle - Downcomer	-50	50	kPa	1.03	1.03
1266	DP 24	DPE140-HLA	Upper Plenum - Downcomer	-30	30	kPa	1.01	1.69
1267	DP 25	DPE150-HLB	Upper Plenum - HLB Nozzle	-30	30	kPa	1.01	1.69
1268	DP 26	DPE160-HLB	HLB Nozzle - HLB Break	-30	30	kPa	1.01	1.69
1269	DP 27	DPE170-HLB	HLB Break - SGB Break	-30	30	kPa	1.01	1.69
1270	DP 28	DPE180-HLB	SGB Break - SGB Inlet	-30	30	kPa	1.01	1.69
1271	DP 29	DPE190A-SGB	SGB Inlet - Tube 3 Top	-150	50	kPa	2.03	1.02
1272	DP 30	DPE190B-SGB	SGB Inlet - Tube 2 Top	-150	50	kPa	2.03	1.02
1273	DP 31	DPE190C-SGB	SGB Inlet - Tube 1 Top	-150	50	kPa	3.96	1.98
1274	DP 32	DPE190D-SGB	SGB Inlet - Tube 4 Top	-150	50	kPa	3.96	1.98
1275	DP 33	DPE190E-SGB	SGB Inlet - Tube 5 Top	-150	50	kPa	3.96	1.98
1276	DP 34	DPE190F-SGB	SGB Inlet - Tube 6 Top	-150	50	kPa	3.96	1.98
1277	DP 35	DPE200A-SGB	SGB Outlet - Tube 3 Top	-150	50	kPa	3.96	1.98
1278	DP 36	DPE200B-SGB	SGB Outlet - Tube 2 Top	-150	50	kPa	3.96	1.98
1279	DP 37	DPE200C-SGB	SGB Outlet - Tube 1 Top	-150	50	kPa	3.96	1.98
1280	DP 38	DPE200D-SGB	SGB Outlet - Tube 4 Top	-150	50	kPa	3.96	1.98
1281	DP 39	DPE200E-SGB	SGB Outlet - Tube 5 Top	-150	50	kPa	3.96	1.98
1282	DP 40	DPE200F-SGB	SGB Outlet - Tube 6 Top	-150	50	kPa	3.96	1.98
1283	DP 41	DPE210-LSB	SGB Outlet - LSB Bottom	-80	80	kPa	1.08	0.67
1284	DP 42	DPE220-LSB	LSB Bottom - PCB Suction	-50	50	kPa	1.03	1.03
1285	DP 43	DPE230-PCB	PCB Suction - Delivery	-50	50	kPa	1.03	1.03
1286	DP 44	DPE240-CLB	PCB Delivery - CLB Break	-20	20	kPa	1.01	2.51
1287	DP 45	DPE250-CLB	CLB Break - CLB Nozzle	-20	20	kPa	1.01	2.51
1288	DP 46	DPE260-CLB	CLB Nozzle - Downcomer	-20	20	kPa	1.01	2.51
1289	DP 47	DPE270-PV	PV Bottom - Top	-100	400	kPa	4.12	0.82
1290	DP 48	DPE280-PV	PV Lower Plenum	-50	100	kPa	1.07	0.71
1291	DP 49	DPE290-PV	Lower Core Support Plate	-50	100	kPa	1.07	0.71
1292	DP 50	DPE300-PV	Core (EL-35 -3945)	-50	100	kPa	1.07	0.71
1293	DP 51	DPE320-PV	Upper Plenum	-50	100	kPa	1.07	0.71
1294	DP 52	DPE330-PV	Upper Head (EL.6135 - 9653)	-50	100	kPa	1.07	0.71
1295	DP 53	DPE310-PV	Upper Core Support Plate	-100	100	kPa	3.96	1.98
1296	DP 54	DPE350A-PV	CR Guide Tube Top Orifice	-100	100	kPa	3.96	1.98
1297	DP 55	DPE350B-PV	CR Guide Tube Top Orifice	-100	100	kPa	3.96	1.98
1298	DP 56	DPE360-PV	PV Downcomer Overall	-100	300	kPa	4.05	1.01
1299	DP 57	DPE370-PV	Lower Downcomer	-50	150	kPa	3.96	1.98
1300	DP 58	DPE380-PV	Upper Downcomer	-50	150	kPa	3.96	1.98
1301	DP 59	DPE390-PV	UP-DC Check Valve A	-50	100	kPa	1.12	0.56
1302	DP 62	DPE332-PV	Upper Head - Downcomer	-100	100	kPa	3.96	1.98
1303	DP 63	DPE331-PV	Upper Head	-100	100	kPa	3.96	1.98
1304	DP 67	DPE580A-BU	FE570A (Break Hi)	0	100	kPa	1.03	1.03
1305	DP 68	DPE580B-BU	FE570B (Break Lo)	0	5	kPa	0.32	6.33

Table A.1 (Cont'd) (17/20)

SEQ No.	Function ID.	Tagname	Location	Range		Unit	Uncertainty	
				LO	HI		±ABS.	±%FR
1306	DP 69	DPE590-BU	Break Venturi	0	500	kPa	4.12	0.82
1307	DP 70	DPE030B-HLA	PZR Surge Line (Low)	-300	300	kPa	2.48	0.41
1308	DP 71	DPE072-LSA	LSA (SG-Side)	0	45	kPa	0.34	0.75
1309	DP 72	DPE073-LSA	LSA (SG-Side)	-10	10	kPa	0.32	1.6
1310	DP 73	DPE074-LSA	LSA (SG-Side)	-10	10	kPa	0.32	1.6
1311	DP 74	DPE075-LSA	LSA (SG-Side)	-10	10	kPa	0.32	1.6
1312	DP 75	DPE076-LSA	LSA (SG-Side)	0	30	kPa	0.33	1.08
1313	DP 76	DPE212-LSB	LSB (SG-Side)	0	45	kPa	0.34	0.75
1314	DP 77	DPE213-LSB	LSB (SG-Side)	-10	10	kPa	0.32	1.6
1315	DP 78	DPE214-LSB	LSB (SG-Side)	-10	10	kPa	0.32	1.6
1316	DP 79	DPE215-LSB	LSB (SG-Side)	-10	10	kPa	0.32	1.6
1317	DP 80	DPE216-LSB	LSB (SG-Side)	0	30	kPa	0.33	1.08
1318	DP 81	DPE430-SGA	SGA Boiling Section	-30	0	kPa	0.33	1.08
1319	DP 82	DPE431-SGA	SGA Boiling Section	-30	0	kPa	0.33	1.08
1320	DP 83	DPE432-SGA	SGA Boiling Section	-30	0	kPa	0.33	1.08
1321	DP 84	DPE433-SGA	SGA Boiling Section	-30	0	kPa	0.33	1.08
1322	DP 85	DPE434-SGA	SGA Boiling Section	-30	0	kPa	0.33	1.08
1323	DP 86	DPE435-SGA	SGA Boiling Section	-30	0	kPa	0.33	1.08
1324	DP 87	DPE436-SGA	SGA Boiling Section	-30	0	kPa	0.33	1.08
1325	DP 88	DPE437-SGA	SGA Boiling Section	-30	0	kPa	0.33	1.08
1326	DP 89	DPE438-SGA	SGA Boiling Section	-30	0	kPa	0.33	1.08
1327	DP 90	DPE439-SGA	SGA Boiling Section	-30	0	kPa	0.33	1.08
1328	DP 91	DPE440-SGA	SGA Boiling Section	-40	0	kPa	0.33	0.83
1329	DP 92	DPE450-SGB	SGB Boiling Section	-30	0	kPa	0.33	1.08
1330	DP 93	DPE451-SGB	SGB Boiling Section	-30	0	kPa	0.33	1.08
1331	DP 94	DPE452-SGB	SGB Boiling Section	-30	0	kPa	0.33	1.08
1332	DP 95	DPE453-SGB	SGB Boiling Section	-30	0	kPa	0.33	1.08
1333	DP 96	DPE454-SGB	SGB Boiling Section	-30	0	kPa	0.33	1.08
1334	DP 97	DPE455-SGB	SGB Boiling Section	-30	0	kPa	0.33	1.08
1335	DP 98	DPE456-SGB	SGB Boiling Section	-30	0	kPa	0.33	1.08
1336	DP 99	DPE457-SGB	SGB Boiling Section	-30	0	kPa	0.33	1.08
1337	DP 100	DPE458-SGB	SGB Boiling Section	-30	0	kPa	0.33	1.08
1338	DP 101	DPE459-SGB	SGB Boiling Section	-30	0	kPa	0.33	1.08
1339	DP 102	DPE460-SGB	SGB Boiling Section	-40	0	kPa	0.33	0.83
1340	DP 103	DPE011-HLA	HLA Spool Piece	-10	10	kPa	0.32	1.6
1341	DP 104	DPE071-CLA	CLA Spool Piece	-10	10	kPa	0.32	1.6
1342	DP 105	DPE151-HLB	HLB Spool Piece	-10	10	kPa	0.32	1.6
1343	DP 106	DPE211-CLB	CLB Spool Piece	-10	10	kPa	0.32	1.6
1344	DP 107	DPE571-BU	RSV123 Inlet	0	200	kPa	1.12	0.56
1345	DP 108	DPE591-BU	Break Spool Piece	-100	100	kPa	1.12	0.56
1346	DP 109	DPE041-PR	PZR (DL.9795 - 11321)	-14.95	0	kPa	0.25	1.69
1347	DP 110	DPE042-PR	PZR (DL.7965 - 9795)	-17.93	0	kPa	0.23	1.27
1348	DP 111	DPE043-PR	PZR (DL.5995 - 7965)	-19.31	0	kPa	0.23	1.18
1349	DP 112	DPE044-PR	PZR (DL.4238 - 5995)	-17.22	0	kPa	0.23	1.32
1350	DP 113	DPE045-PR	PZR (DL.2025 - 4238)	-21.68	0	kPa	0.23	1.06
1351	DP 114	DPE046-PR	PZR (DL.80 - 2025)	-19.06	0	kPa	0.23	1.2
1352	DP 115	DPE101-PR	PZR-CLA	-200	200	kPa	1.3	0.32
1353	DP 116	DPE055A-SGA	SGA U-Tube I/O (High)	-30	30	kPa	0.29	0.49
1354	DP 117	DPE055B-SGA	SGA U-Tube I/O (Low)	-3	3	kPa	0.2	3.37
1355	DP 118	DPE195A-SGB	SGB U-Tube I/O (High)	-30	30	kPa	0.29	0.49
1356	DP 119	DPE195B-SGB	SGB U-Tube I/O (Low)	-3	3	kPa	0.2	3.37
1357	DP 120	DPE056-SGA	SGA Inlet Plenum	-40	40	kPa	1.02	1.28
1358	DP 122	DPE196-SGB	SGB Inlet Plenum	-40	40	kPa	0.48	0.6
1359	DP 123	DPE197-SGB	SGB Primary-Secondary	-1000	1000	kPa	9.44	0.47
1360	DP 133	DPE333-PV	Upper Head (EL.6634 - 8860)	-35	0	kPa	0.23	0.67
1361	DP 195	DPE081-LSA	HCV020 Inlet-Outlet	-40	60	kPa	0.56	0.56
1362	DP 196	DPE221-LSB	HCV160 Inlet-Outlet	-40	60	kPa	0.56	0.56
1363	MF 2	MFE011B-HLA	HLA Spool Piece Side	-10	10	V	-	-
1364	MF 3	MFE011C-HLA	HLA Spool Piece Bottom	-10	10	V	-	-
1365	MF 4	MFE051A-LSA	LSA Spool Piece East	-10	10	V	-	-
1366	MF 5	MFE051B-LSA	LSA Spool Piece South	-10	10	V	-	-
1367	MF 6	MFE051C-LSA	LSA Spool Piece West	-10	10	V	-	-
1368	MF 10	MFE151A-HLB	HLB Spool Piece Top	-10	10	V	-	-
1369	MF 13	MFE191A-LSB	LSB Spool Piece West	-10	10	V	-	-
1370	MF 14	MFE191B-LSB	LSB Spool Piece North	-10	10	V	-	-
1371	MF 15	MFE191C-LSB	LSB Spool Piece East	-10	10	V	-	-
1372	MF 17	MFE211B-CLB	CLB Spool Piece Side	-10	10	V	-	-
1373	MF 21	MFE021-HLA	SGA Inlet	-10	10	V	-	-
1374	MF 24	MFE191D-LSB	LSB Spool Piece South (Low)	-10	10	V	-	-
1375	DE 1	DE011A-HLA	HLA Spool Piece, Beam A	0	10	V	-	-
1376	DE 2	DE011B-HLA	HLA Spool Piece, Beam B	0	10	V	-	-
1377	DE 3	DE011C-HLA	HLA Spool Piece, Beam C	0	10	V	-	-
1378	DE 4	DE051A-LSA	LSA Spool Piece, Beam A	0	10	V	-	-
1379	DE 5	DE051B-LSA	LSA Spool Piece, Beam B	0	10	V	-	-
1380	DE 6	DE051C-LSA	LSA Spool Piece, Beam C	0	10	V	-	-
1381	DE 7	DE071A-CLA	CLA Spool Piece, Beam A	0	10	V	-	-
1382	DE 8	DE071B-CLA	CLA Spool Piece, Beam B	0	10	V	-	-
1383	DE 9	DE071C-CLA	CLA Spool Piece, Beam C	0	10	V	-	-
1384	DE 10	DE151A-HLB	HLB Spool Piece, Beam A	0	10	V	-	-
1385	DE 11	DE151B-HLB	HLB Spool Piece, Beam B	0	10	V	-	-

Table A.1 (Cont'd) (18/20)

SEQ No.	Function ID.	Tagname	Location	Range		Unit	Uncertainty	
				LO	HI		±ABS.	±%FR
1386	DE 12	DE151C-HLB	HLB Spool Piece, Beam C	0	10	V	-	-
1387	DE 13	DE191A-LSB	LSB Spool Piece, Beam A	0	10	V	-	-
1388	DE 14	DE191B-LSB	LSB Spool Piece, Beam B	0	10	V	-	-
1389	DE 15	DE191C-LSB	LSB Spool Piece, Beam C	0	10	V	-	-
1390	DE 16	DE211A-CLB	CLB Spool Piece, Beam A	0	10	V	-	-
1391	DE 17	DE211B-CLB	CLB Spool Piece, Beam B	0	10	V	-	-
1392	DE 18	DE211C-CLB	CLB Spool Piece, Beam C	0	10	V	-	-
1393	DE 19	DE052-LSA	PCA Suction	0	10	V	-	-
1394	DE 20	DE192-LSB	PCB Suction	0	10	V	-	-
1395	DE 21	DE281-PR	PZR Surge Line	0	10	V	-	-
1396	DE 27	DE451A-SGA	SGA Safety S/P Upper Beam	0	10	V	-	-
1397	DE 28	DE451B-SGA	SGA Safety S/P Center Beam	0	10	V	-	-
1398	DE 29	DE451C-SGA	SGA Safety S/P Bottom Beam	0	10	V	-	-
1399	DE 30	DE571A-BU	RSV123 Inlet, Beam A	0	10	V	-	-
1400	DE 31	DE571B-BU	RSV123 Inlet, Beam B	0	10	V	-	-
1401	DE 32	DE571C-BU	RSV123 Inlet, Beam C	0	10	V	-	-
1402	DE 33	DE591A-BU	Break Spool Piece, Beam A	0	10	V	-	-
1403	DE 34	DE591B-BU	Braek Spool Piece, Beam B	0	10	V	-	-
1404	DE 35	DE591C-BU	Break Spool Piece, Beam C	0	10	V	-	-
1405	DE 40	DE291-SGB	SGB Feedwater Line	0	10	V	-	-
*1406	CP 123	CPE-086C-SGA	SGA Boiling Section Pos.1	0	100	%	-	-
*1407	CP 124	CPE-099C-SGA	SGA Boiling Section Pos.3	0	100	%	-	-
*1408	CP 126	CPE-125C-SGA	SGA Boiling Section Pos.6	0	100	%	-	-
*1409	CP 237	CPE-112C-SGB	SGB Boiling Section Pos.5	0	100	%	-	-
*1410	CP 238	CPE-125C-SGB	SGB Boiling Section Pos.6	0	100	%	-	-
*1411	CP 240	CPE-150C-SGB	SGB Boiling Section Pos.8	0	100	%	-	-
*1412	CP 241	CPE-163C-SGB	SGB Boiling Section Pos.9	0	100	%	-	-
*1413	CP 243	CPE-192F-SGB	SGB Boiling Section Pos.12	0	100	%	-	-
*1414	CP 347	CPE-010A-HLA	HLA Vessel-Side CPT	0	100	%	-	-
*1415	CP 349	CPE-010C-HLA	HLA Vessel-Side CPT	0	100	%	-	-
*1416	CP 350	CPE-010D-HLA	HLA Vessel-Side CPT	0	100	%	-	-
*1417	CP 351	CPE-010E-HLA	HLA Vessel-Side CPT	0	100	%	-	-
*1418	CP 352	CPE-040A-HLA	HLA SG-Side CPT	0	100	%	-	-
*1419	CP 353	CPE-040B-HLA	HLA SG-Side CPT	0	100	%	-	-
*1420	CP 354	CPE-040C-HLA	HLA SG-Side CPT	0	100	%	-	-
*1421	CP 355	CPE-040D-HLA	HLA SG-Side CPT	0	100	%	-	-
*1422	CP 356	CPE-040E-HLA	HLA SG-Side CPT	0	100	%	-	-
*1423	CP 357	CPE-090A-CLA	CLA Vessel-Side CPT	0	100	%	-	-
*1424	CP 358	CPE-090B-CLA	CLA Vessel-Side CPT	0	100	%	-	-
*1425	CP 359	CPE-090C-CLA	CLA Vessel-Side CPT	0	100	%	-	-
*1426	CP 362	CPE-150A-HLB	HLB Vessel-Side CPT	0	100	%	-	-
*1427	CP 363	CPE-150B-HLB	HLB Vessel-Side CPT	0	100	%	-	-
*1428	CP 364	CPE-150C-HLB	HLB Vessel-Side CPT	0	100	%	-	-
*1429	CP 366	CPE-150E-HLB	HLB Vessel-Side CPT	0	100	%	-	-
*1430	CP 369	CPE-180C-HLB	HLB SG-Side CPT	0	100	%	-	-
*1431	CP 370	CPE-180D-HLB	HLB SG-Side CPT	0	100	%	-	-
*1432	CP 371	CPE-180E-HLB	HLB SG-Side CPT	0	100	%	-	-
*1433	CP 372	CPE-230A-CLB	CLB Vessel-Side CPT	0	100	%	-	-
*1434	CP 373	CPE-230B-CLB	CLB Vessel-Side CPT	0	100	%	-	-
*1435	CP 374	CPE-230C-CLB	CLB Vessel-Side CPT	0	100	%	-	-
*1436	CP 375	CPE-230D-CLB	CLB Vessel-Side CPT	0	100	%	-	-
*1437	CP 376	CPE-230E-CLB	CLB Vessel-Side CPT	0	100	%	-	-
1438	CP 512	BU-SIGNAL	BU Signal	0	100		-	-
1439	RC 2	MFE011B-HLA-EU	HLA Spool Piece, Side			kg/ms2	88	
1440	RC 3	MFE011C-HLA-EU	HLA Spool Piece, Bottom			kg/ms2	80	
1441	RC 4	MFE051A-LSA-EU	LSA Spool Piece, East			kg/ms2	-	
1442	RC 5	MFE051B-LSA-EU	LSA Spool Piece, South			kg/ms2	-	
1443	RC 6	MFE051C-LSA-EU	LSA Spool Piece, West			kg/ms2	-	
1444	RC 10	MFE151A-HLB-EU	HLB Spool Piece, Top			kg/ms2	83	
1445	RC 13	MFE191A-LSB-EU	LSB Spool Piece, West			kg/ms2	-	
1446	RC 14	MFE191B-LSB-EU	LSB Spool Piece, North			kg/ms2	-	
1447	RC 15	MFE191C-LSB-EU	LSB Spool Piece, East			kg/ms2	-	
1448	RC 17	MFE211B-CLB-EU	CLB Spool Piece, Side			kg/ms2	80	
1449	RC 19	MFE021-HLA-EU	SGA Inlet			kg/ms2	-	
1450	RC 22	MFE191D-LSB-EU	LSB Spool Piece, South (Low)			kg/ms2	-	
1451	RC 31	DE011A-HLA-EU	HLA Spool Piece, Beam A			kg/m3	27	
1452	RC 32	DE011B-HLA-EU	HLA Spool Piece, Beam B			kg/m3	20	
1453	RC 33	DE011C-HLA-EU	HLA Spool Piece, Beam C			kg/m3	22	
1454	RC 34	DE151A-HLB-EU	HLB Spool Piece, Beam A			kg/m3	27	
1455	RC 35	DE151B-HLB-EU	HLB Spool Piece, Beam B			kg/m3	20	
1456	RC 36	DE151C-HLB-EU	HLB Spool Piece, Beam C			kg/m3	22	
1457	RC 37	DE071A-CLA-EU	CLA Spool Piece, Beam A			kg/m3	94.8	
1458	RC 38	DE071B-CLA-EU	CLA Spool Piece, Beam B			kg/m3	94.8	
1459	RC 39	DE071C-CLA-EU	CLA Spool Piece, Beam C			kg/m3	94.8	
1460	RC 40	DE211A-CLB-EU	CLB Spool Piece, Beam A			kg/m3	94.8	
1461	RC 41	DE211B-CLB-EU	CLB Spool Piece, Beam B			kg/m3	94.8	
1462	RC 42	DE211C-CLB-EU	CLB Spool Piece, Beam C			kg/m3	94.8	
1463	RC 47	DAE-011-HLA	from RC 31,32,33			kg/m3	13	
1464	RC 49	DAE-151-HLB	from RC 34,35,36			kg/m3	13	
1465	RC 52	DAE-071-CLA	from RC 37,38,39			kg/m3	55.63	

Table A.1 (Cont'd) (19/20)

SEQ No.	Function ID.	Tagname	Location	Range		Unit	Uncertainty	
				LO	HI		±ABS.	±%FR
1466	RC 53	DAE-211-CLB	from RC 40,41,42			kg/m3	55.63	
1467	RC 56	DE051A-LSA-EU	LSA Spool Piece, Beam A			kg/m3	94.8	
1468	RC 57	DE051B-LSA-EU	LSA Spool Piece, Beam B			kg/m3	94.8	
1469	RC 58	DE051C-LSA-EU	LSA Spool Piece, Beam C			kg/m3	94.8	
*1470	RC 59	DE191A-LSB-EU	LSB Spool Piece, Beam A			kg/m3	94.8	
*1471	RC 60	DE191B-LSB-EU	LSB Spool Piece, Beam B			kg/m3	94.8	
*1472	RC 61	DE191C-LSB-EU	LSB Spool Piece, Beam C			kg/m3	94.8	
1473	RC 62	DE052-LSA-EU	PCA Suction			kg/m3	94.8	
1474	RC 63	DE192-LSB-EU	PCB Suction			kg/m3	94.8	
1475	RC 64	DE281-PR-EU	PZR Surge Line			kg/m3	94.8	
1476	RC 70	DE451A-SGA-EU	SGA Safety S/P Upper Beam			kg/m3	94.8	
1477	RC 71	DE451B-SGA-EU	SGA Safety S/P Center Beam			kg/m3	94.8	
1478	RC 72	DE451C-SGA-EU	SGA Safety S/P Bottom Beam			kg/m3	94.8	
1479	RC 73	DE591A-BU-EU	Break Spool Piece, Beam A			kg/m3	94.8	
1480	RC 74	DE591B-BU-EU	Break Spool Piece, Beam B			kg/m3	94.8	
1481	RC 75	DE591C-BU-EU	Break Spool Piece, Beam C			kg/m3	94.8	
1482	RC 105	DE451-AVG	from RC 70,71,72			kg/m3	55.68	
1483	RC 106	DE571-AVG	from RC 43,44,45			kg/m3	55.74	
1484	RC 110	FRE-051-LSA	from RC 4, 5, 6,56,57,58			kg/s	-	
1485	RC 111	FRE-191-LSB	from RC 13,14,15,59,60,61			kg/s	-	
1486	RC 112	DAE-051-LSA	from RC 56,57,58			kg/m3	-	
1487	RC 113	DAE-191-LSB	from RC 59,60,61			kg/m3	-	
1488	RC 120	DAE-051-LSA-TY	from RC 56,57,58			kg/m3	-	
1489	RC 121	DAE-191-LSB-TY	from RC 59,60,61			kg/m3	-	
1490	RC 122	DAE-571A-BU	from RC 43,44,45			kg/m3	-	
1491	RC 123	DAE-571B-BU	Same as RC 122			kg/m3	-	
1492	RC 124	DAE-591A-BU	from RC 73,74,75			kg/m3	-	
1493	RC 125	DAE-591B-BU	Same as RC 124			kg/m3	-	
1494	RC 132	DE591-AVG	from RC 73,74,75			kg/m3	55.62	
1495	RC 133	TWE-PCT	Peak Cladding Temp.			K	5.31	
1496	RC 134	TWE-PCTLOC	Location of PCT				-	
1497	RC 139	CL-CORE	Core (EL.-35 - 3945)			m	0.216	
1498	RC 140	CL-UP	Upper Plenum (EL.4060 - 6135)			m	0.197	
1499	RC 141	CL-UH	Upper Head (EL.6634 - 8860)			m	0.21	
1500	RC 142	CL-DC	Downcomer			m	0.746	
1501	RC 143	CL-HLA-SGA	HLA Riser Part			m	0.181	
1502	RC 144	CL-TUA-U3	SGA Tube 3 Inlet - Top			m	0.43	
1503	RC 145	CL-TUA-U2	SGA Tube 2 Inlet - Top			m	0.42	
1504	RC 146	CL-TUA-U1	SGA Tube 1 Inlet - Top			m	0.413	
1505	RC 147	CL-TUA-U4	SGA Tube 4 Inlet - Top			m	0.43	
1506	RC 148	CL-TUA-U5	SGA Tube 5 Inlet - Top			m	0.42	
1507	RC 149	CL-TUA-U6	SGA Tube 6 Inlet - Top			m	0.425	
1508	RC 150	CL-TUA-D3	SGA Tube 3 Outlet - Top			m	0.442	
1509	RC 151	CL-TUA-D2	SGA Tube 2 Outlet - Top			m	0.431	
1510	RC 152	CL-TUA-D1	SGA Tube 1 Outlet - Top			m	0.422	
1511	RC 153	CL-TUA-D4	SGA Tube 4 Outlet - Top			m	0.422	
1512	RC 154	CL-TUA-D5	SGA Tube 5 Outlet - Top			m	0.431	
1513	RC 155	CL-TUA-D6	SGA Tube 6 Outlet - Top			m	0.422	
1514	RC 156	CL-LSA-D	SGA Out.Plenum - LSA Bottom			m	0.207	
1515	RC 157	CL-LSA-U	LSA Bottom - PCA Suction			m	0.188	
1516	RC 158	CL-SGA-IPL	SGA Inlet Plenum			m	0.185	
1517	RC 159	CL-HLB-SGB	HLB Riser Part			m	0.179	
1518	RC 160	CL-TUB-U3	SGB Tube 3 Inlet - Top			m	0.445	
1519	RC 161	CL-TUB-U2	SGB Tube 2 Inlet - Top			m	0.433	
1520	RC 162	CL-TUB-U1	SGB Tube 1 Inlet - Top			m	0.73	
1521	RC 163	CL-TUB-U4	SGB Tube 4 Inlet - Top			m	0.74	
1522	RC 164	CL-TUB-U5	SGB Tube 5 Inlet - Top			m	0.734	
1523	RC 165	CL-TUB-U6	SGB Tube 6 Inlet - Top			m	0.73	
1524	RC 166	CL-TUB-D3	SGB Tube 3 Outlet - Top			m	0.951	
1525	RC 167	CL-TUB-D2	SGB Tube 2 Outlet - Top			m	0.74	
1526	RC 168	CL-TUB-D1	SGB Tube 1 Outlet - Top			m	0.735	
1527	RC 169	CL-TUB-D4	SGB Tube 4 Outlet - Top			m	0.747	
1528	RC 170	CL-TUB-D5	SGB Tube 5 Outlet - Top			m	0.74	
1529	RC 171	CL-TUB-D6	SGB Tube 6 Outlet - Top			m	0.735	
1530	RC 172	CL-LSB-D	SGB Out.Plenum - LSB Bottom			m	0.207	
1531	RC 173	CL-LSB-U	LSB Bottom - PCB Suction			m	0.188	
1532	RC 174	CL-SGB-IPL	SGB Inlet Plenum			kg	0.094	
1533	RC 175	MC-UH	Upper Head (EL.6634 - 8860)			kg	79.08	
1534	RC 176	MC-LSA-DW	SGA Out.Plenum+LSA Downflow			kg	42.68	
1535	RC 177	MC-LSB-DW	SGB Out.Plenum+LSB Downflow			kg	41.33	
1536	RC 178	MS-CORE	Core (EL.-35 - 3945)			kg	15.4	
1537	RC 179	MS-UP	Upper Plenum (EL.4060 - 6135)			kg	24.37	
1538	RC 180	MS-DC	Downcomer			kg	46.31	
1539	RC 181	MS-TUA-UP-AV	SGA Tubes Upflow side			kg	8.3	
1540	RC 182	MS-TUA-DW-AV	SGA Tubes Downflow side			kg	8.3	
1541	RC 183	MS-SGA-IPL	SGA Inlet Plenum			kg	27.81	
1542	RC 184	MS-LSA-UP	LSA Upflow side			kg	3.57	
1543	RC 185	MS-TUB-UP-AV	SGB Tubes Upflow side			kg	9.65	
1544	RC 186	MS-TUB-DW-AV	SGB Tubes Downflow side			kg	10.25	
1545	RC 187	MS-SGB-IPL	SGB Inlet Plenum			kg	14.61	
1546	RC 188	MS-LSB-UP	LSB Upflow side			kg	3.57	
1547	RC 189	MS-ACC	Acc-Cold Tank			kg	39.26	

Table A.1 (Cont'd) (20/20)

SEQ No.	Function ID.	Tagname	Location	Range		Unit	Uncertainty	
				LO	HI		±ABS.	±%FR
1548	RC 190	MS-ACH	Acc-Hot Tank			kg	74.26	
1549	RC 191	MS-ST	Break Flow Supp. Tank			kg	323.61	
1550	RC 192	DM-ACC	Acc-Cold Tank			kg/s	13.55	
1551	RC 193	DM-ACH	Acc-Hot Tank			kg/s	26.08	
1552	RC 194	IM-ST	Break Flow Supp. Tank			kg/s	3.35	
1553	RC 195	DM-RWST	RWST			kg/s	51.9	
1554	RC 196	LG-HLA	HLA Water Level			m	0.012	
1555	RC 197	LG-CLA	CLA Water Level			m	0.028	
1556	RC 198	LG-HLB	HLB Water Level			m	0.012	
1557	RC 199	LG-CLB	CLB Water Level			m	0.028	
1558	RC 200	TS-UP	Upper Plenum			K	17.64	
1559	RC 201	TS-PR	Pressurizer			K	17.64	
1560	RC 202	TS-SGA	Steam Generator-A			K	7.82	
1561	RC 203	TS-SGB	Steam Generator-B			K	7.82	
1562	RC 279	DE291-SGB-EU	SGB Feedwater Line			kg/m3		

* The experiment data is not qualified Good but Qualitative because it includes large uncertainty or undefined trend.

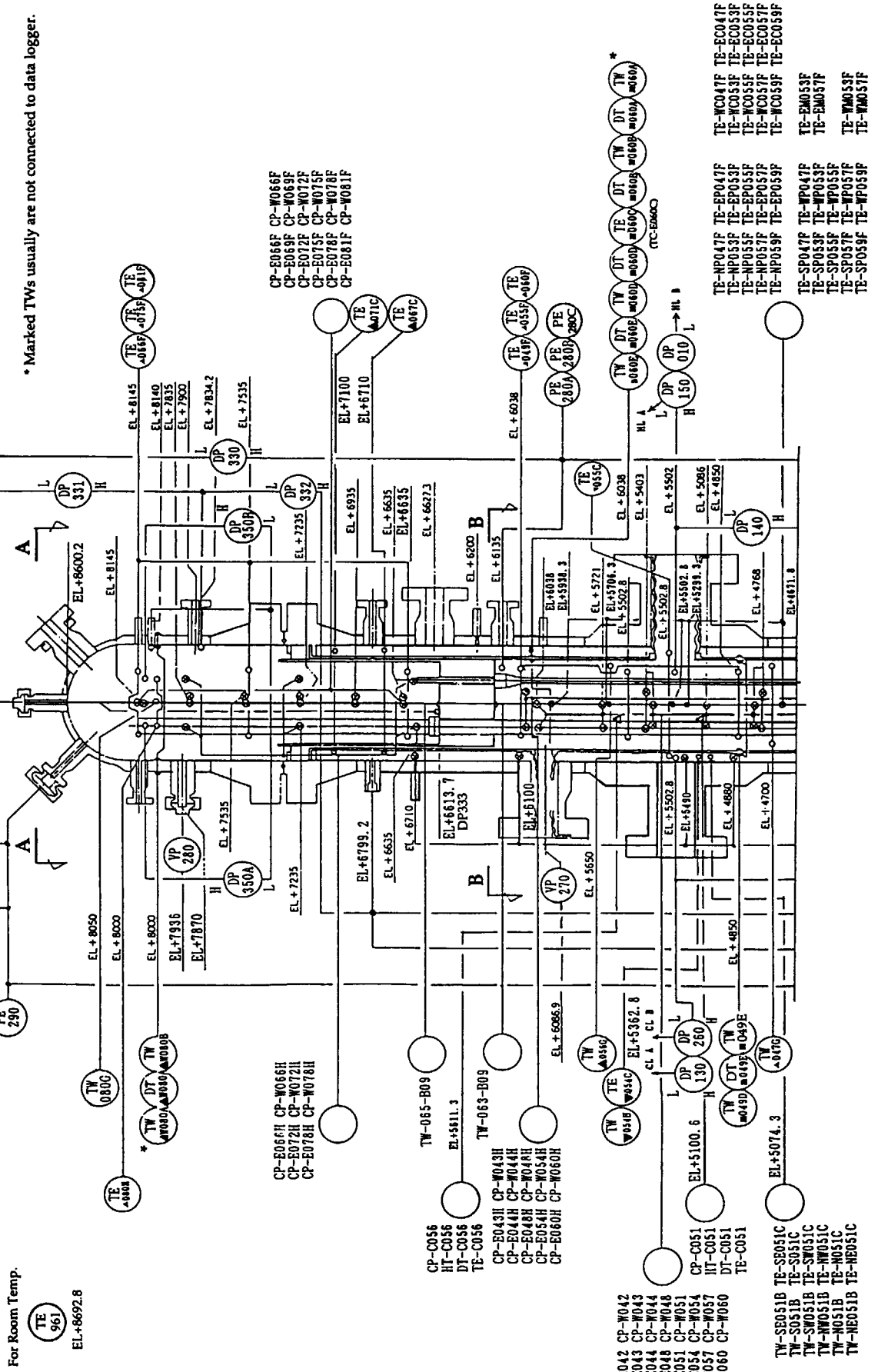

Fig. A. 1 Vertical locations of upper pressure vessel instruments

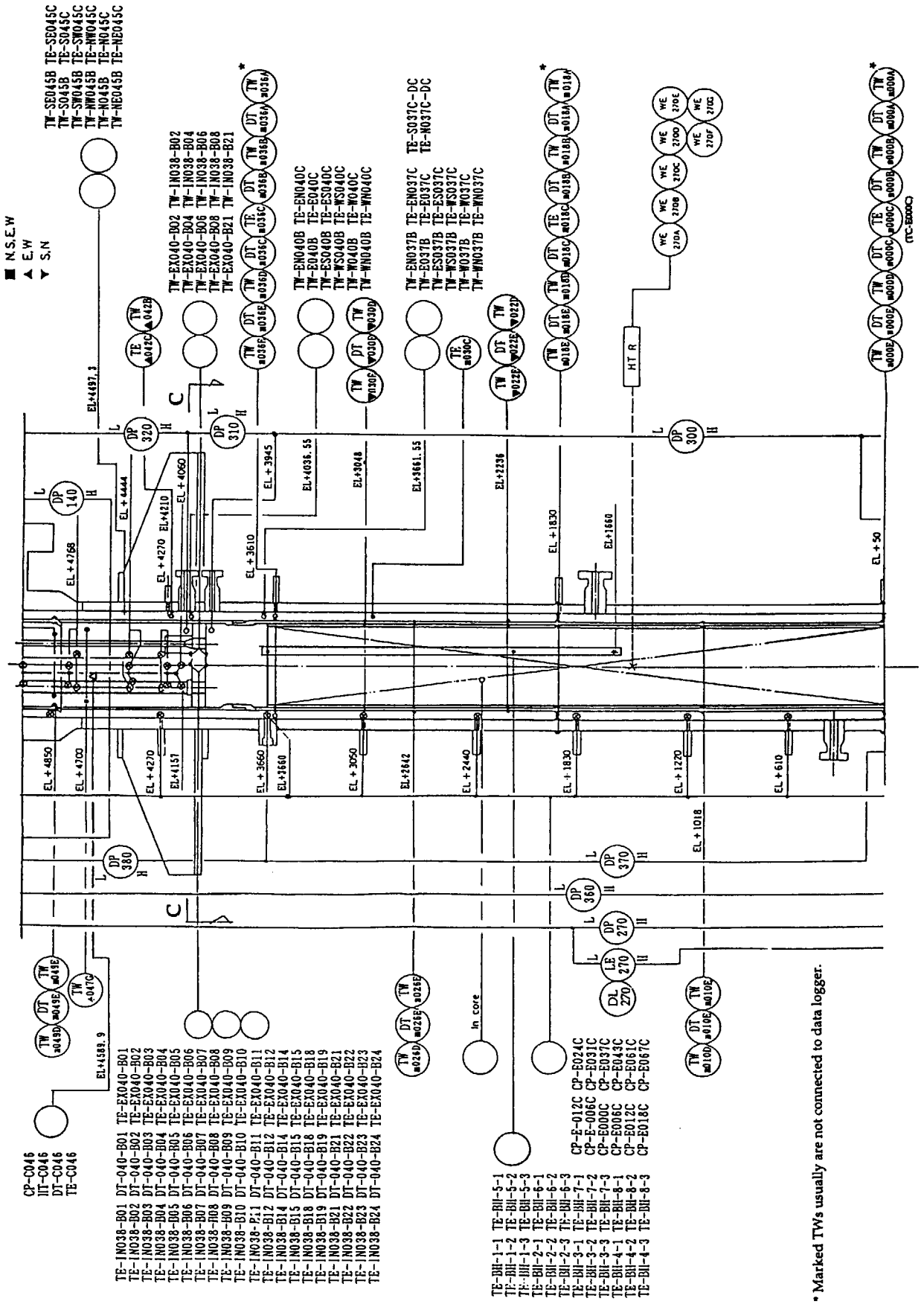

Fig. A. 2 Vertical locations of middle pressure vessel instruments (except for core)

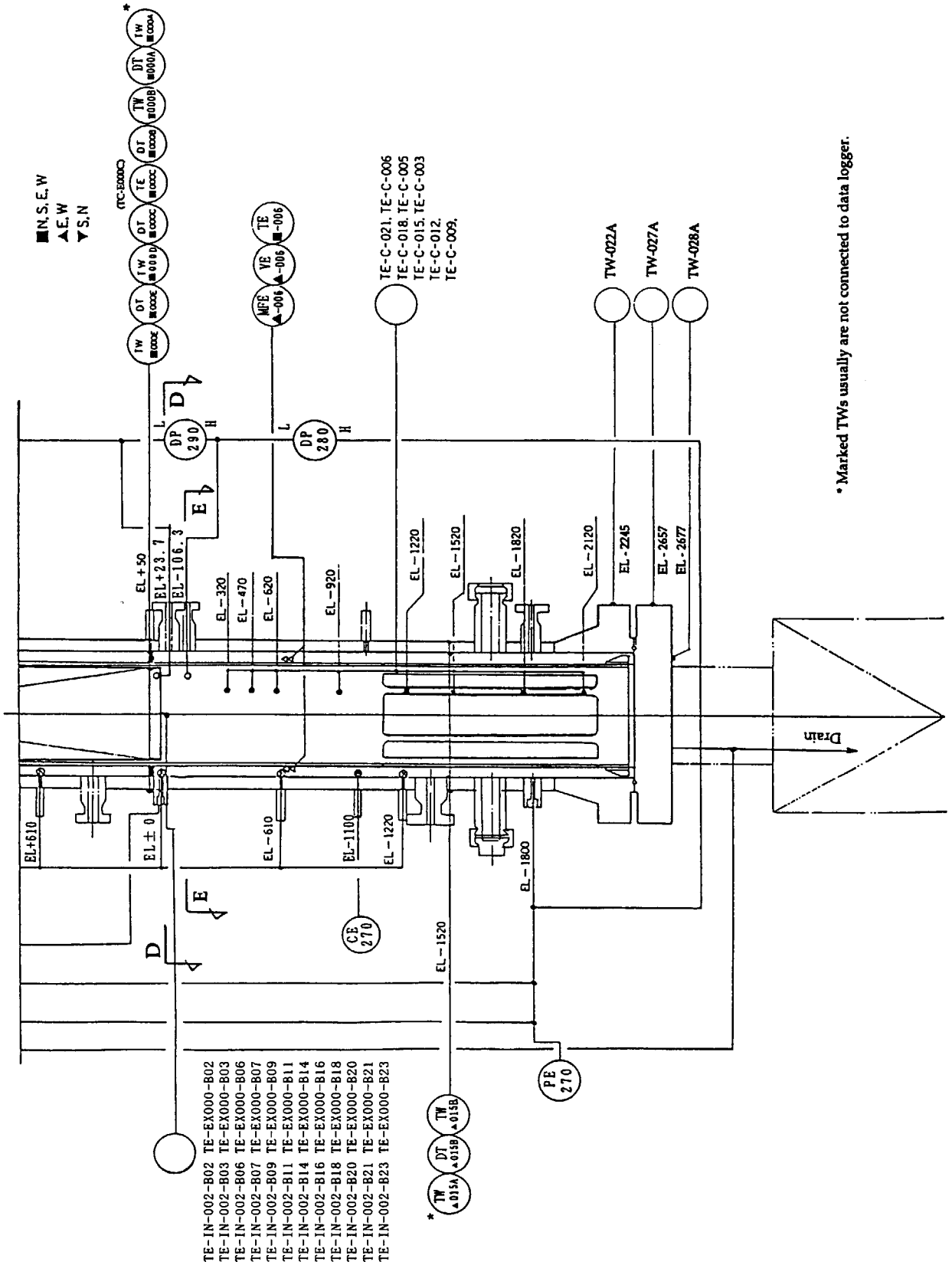

Fig. A. 3 Vertical locations of lower pressure vessel instruments

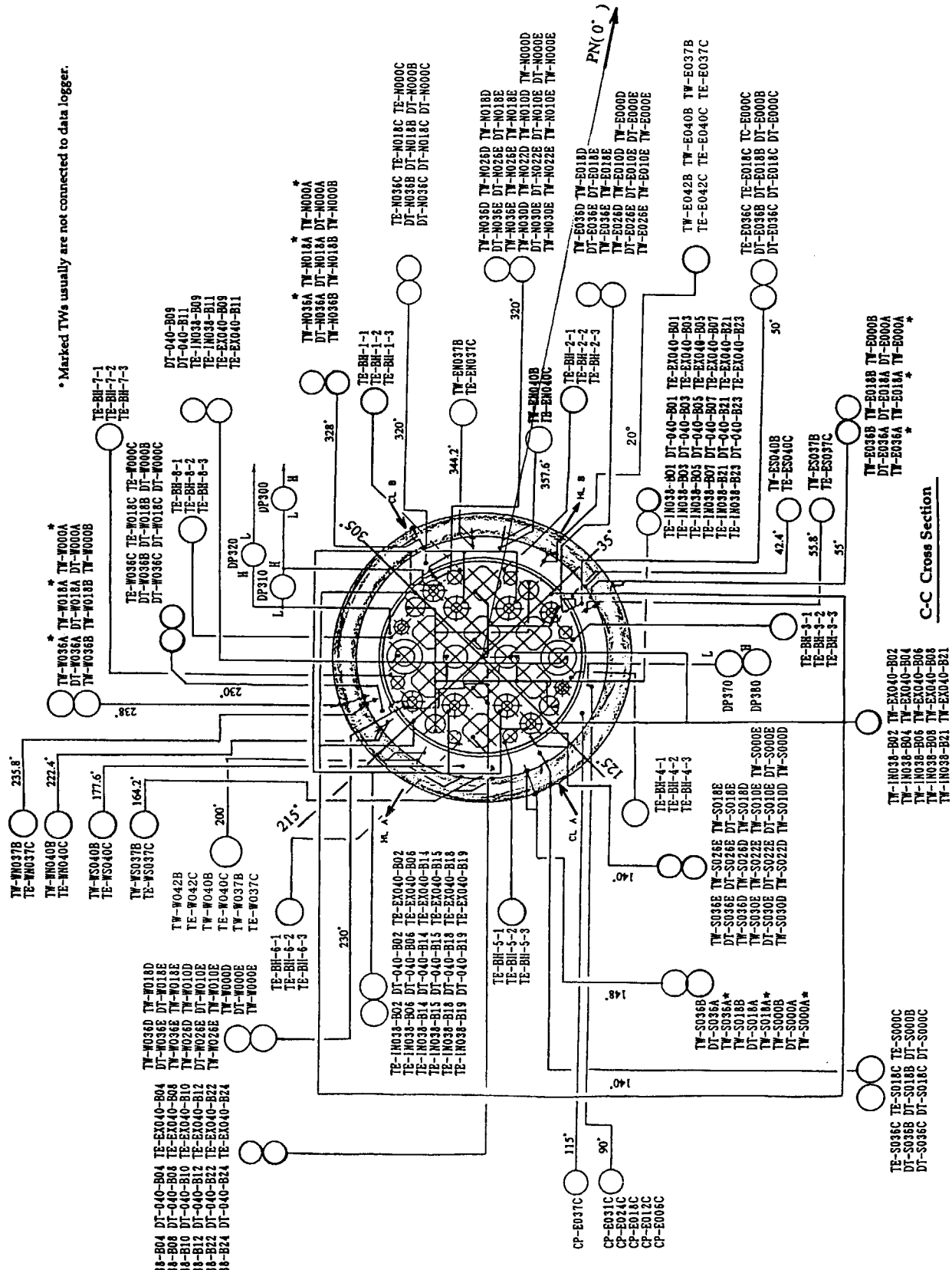

Fig. A. 4 Horizontal locations of upper plenum instruments including CETs

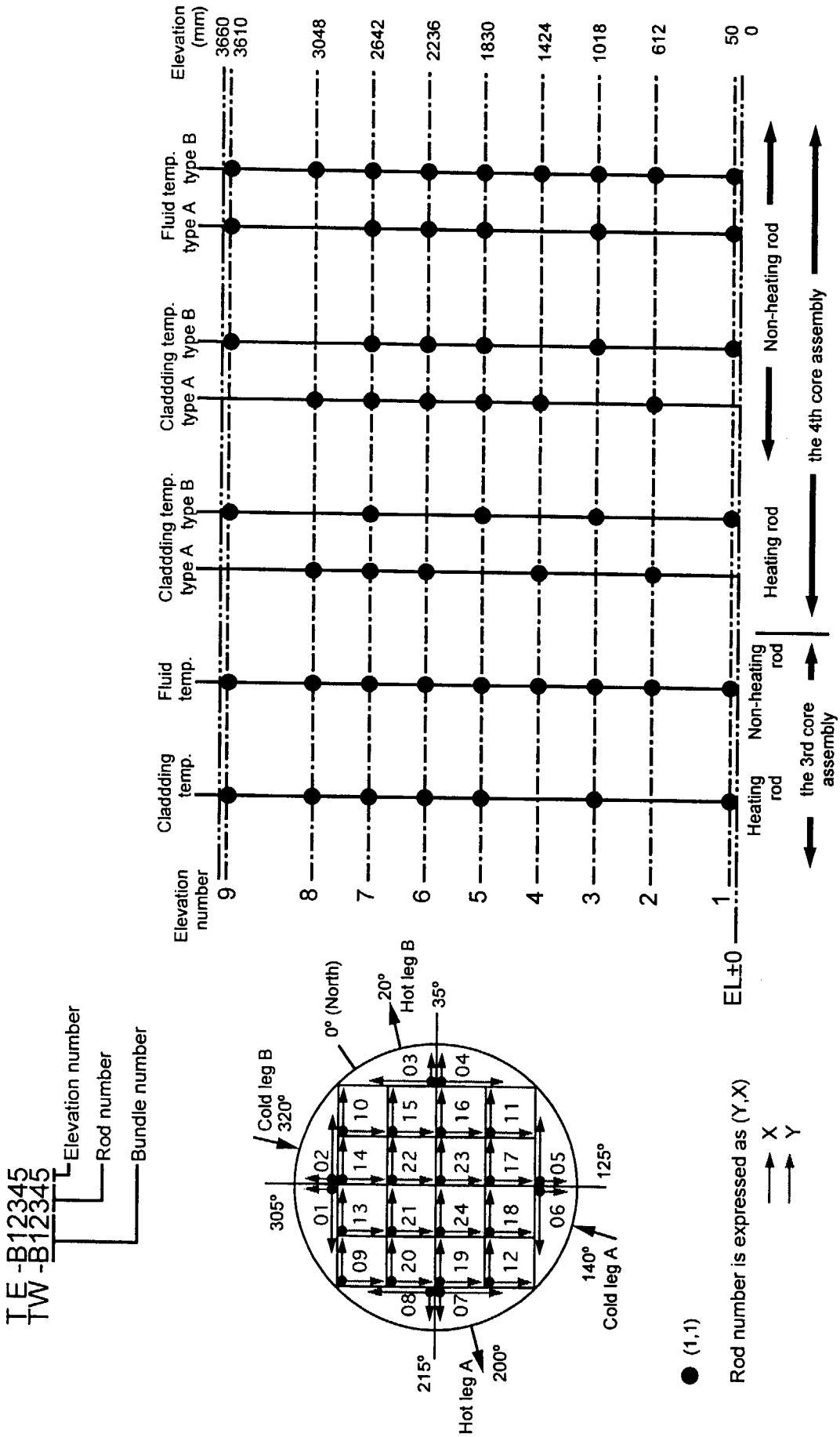

Fig. A. 5 Arrangement of thermocouple locations in core heater rod assembly

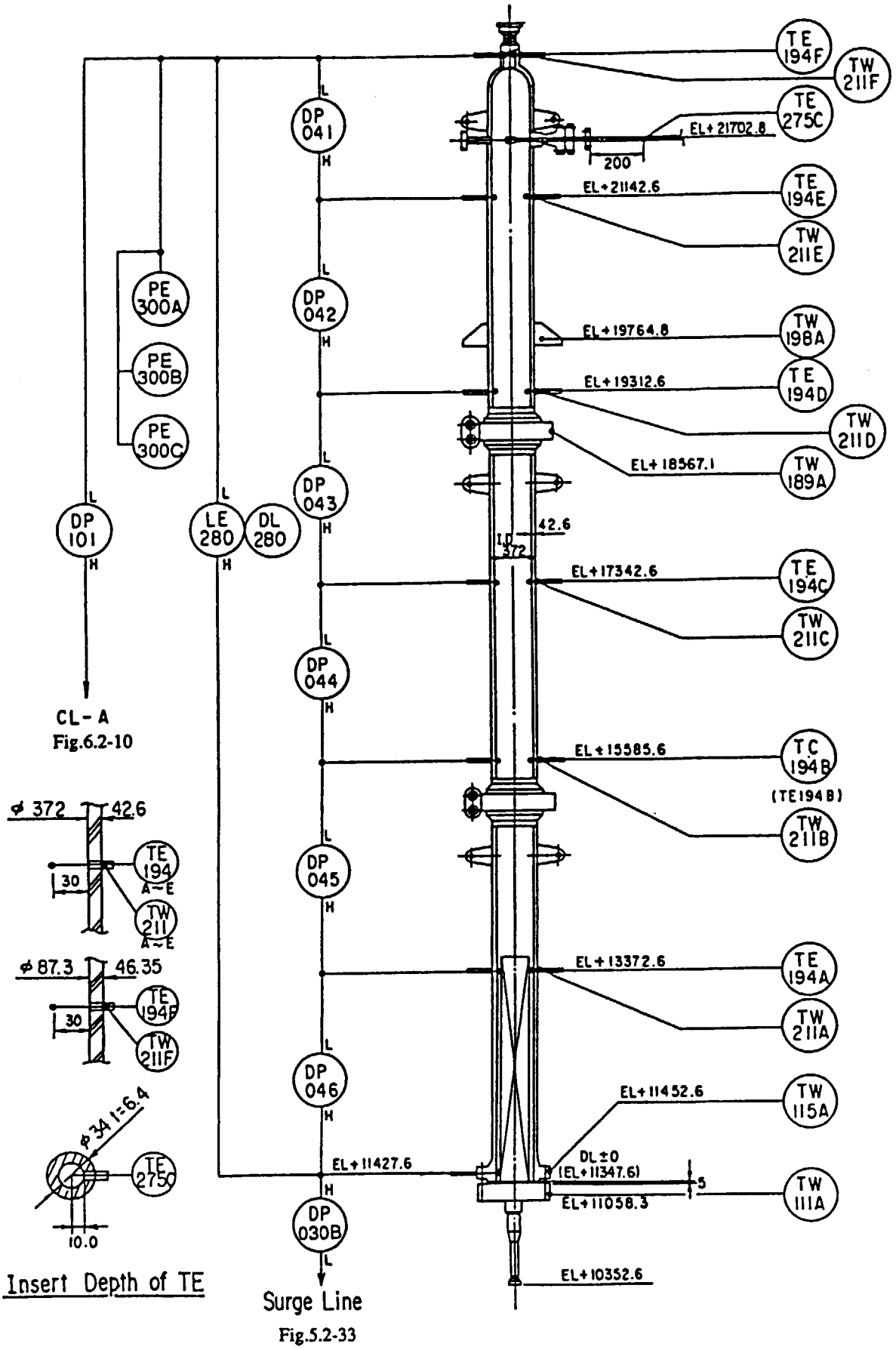

Fig. A. 6 Instrument locations for pressurizer

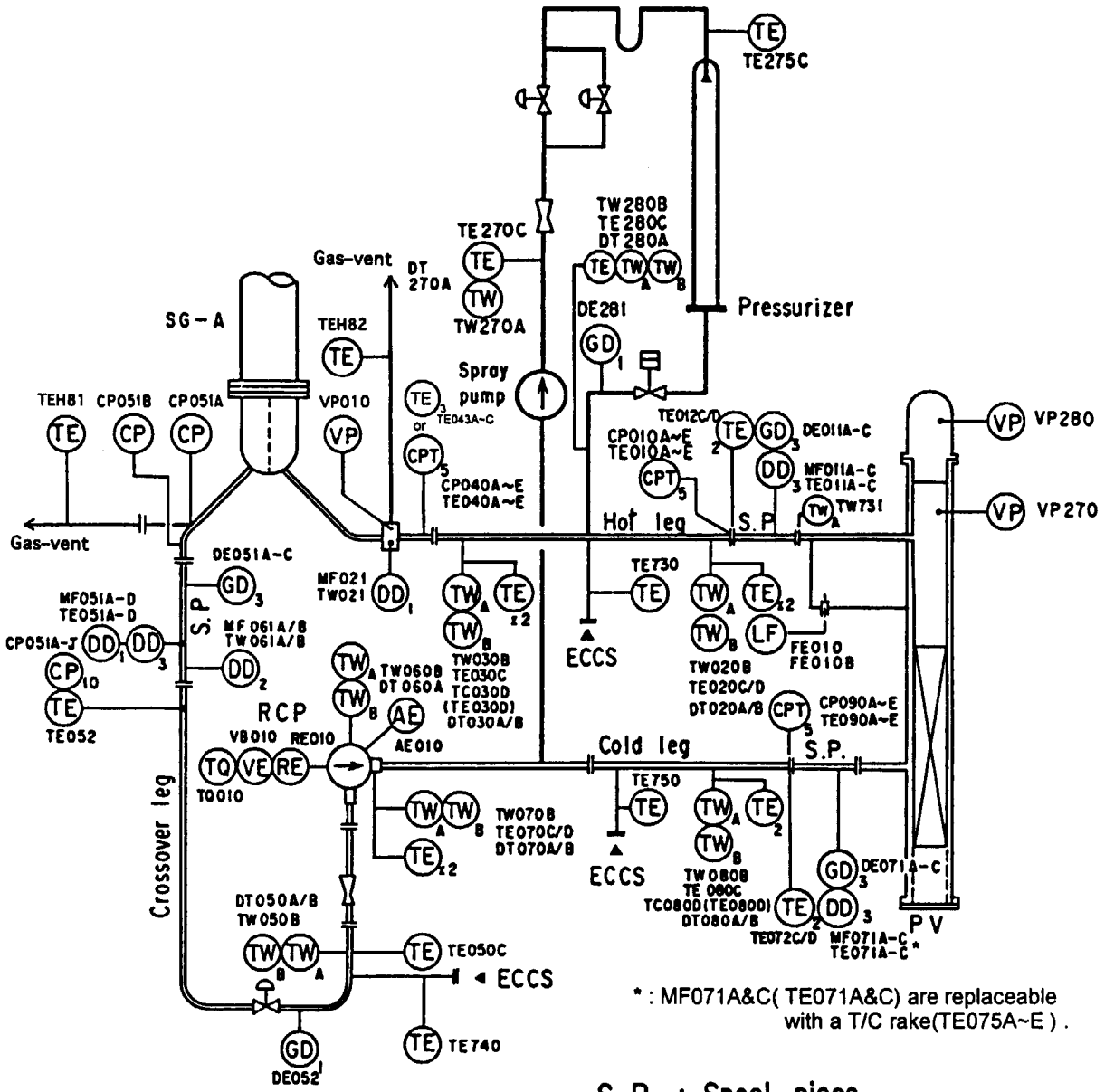

Fig. A. 7 Primary loop-A instrument locations for pressure, temperature, fluid density and others

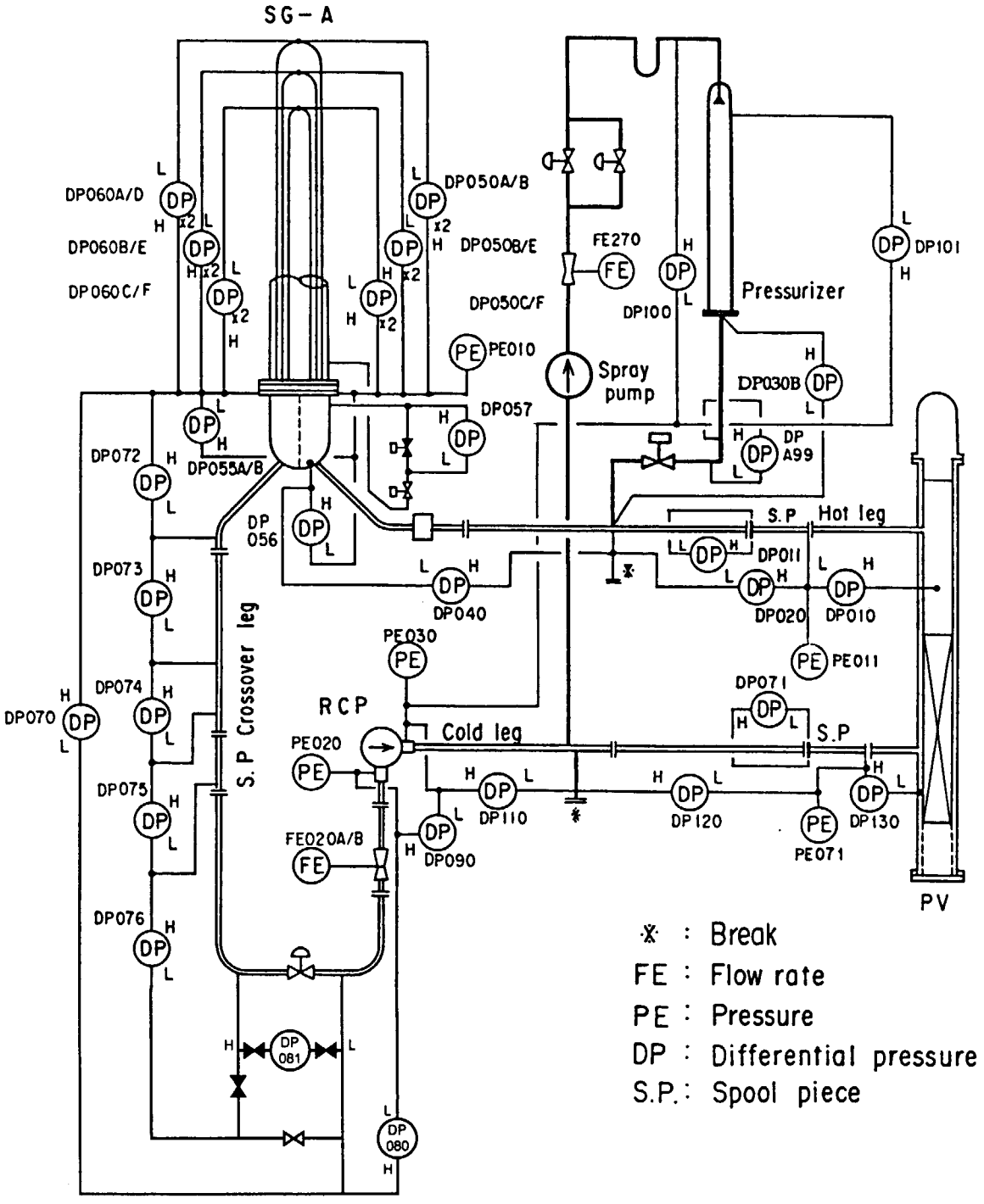

Fig. A. 8 Primary loop-A instrument locations for DP and flow-rate

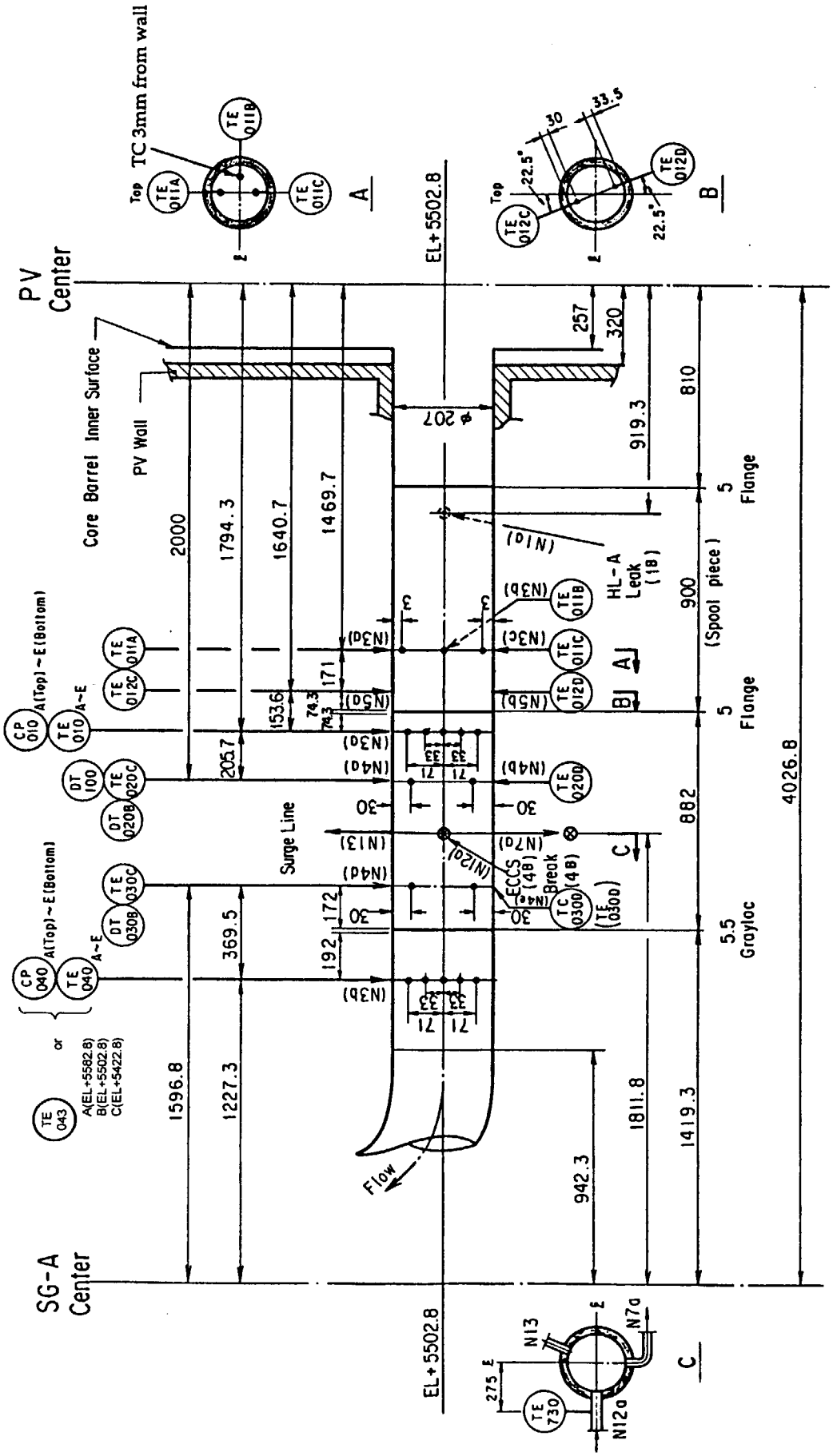

Fig.A.9 Detail of instrument locations in hot leg A

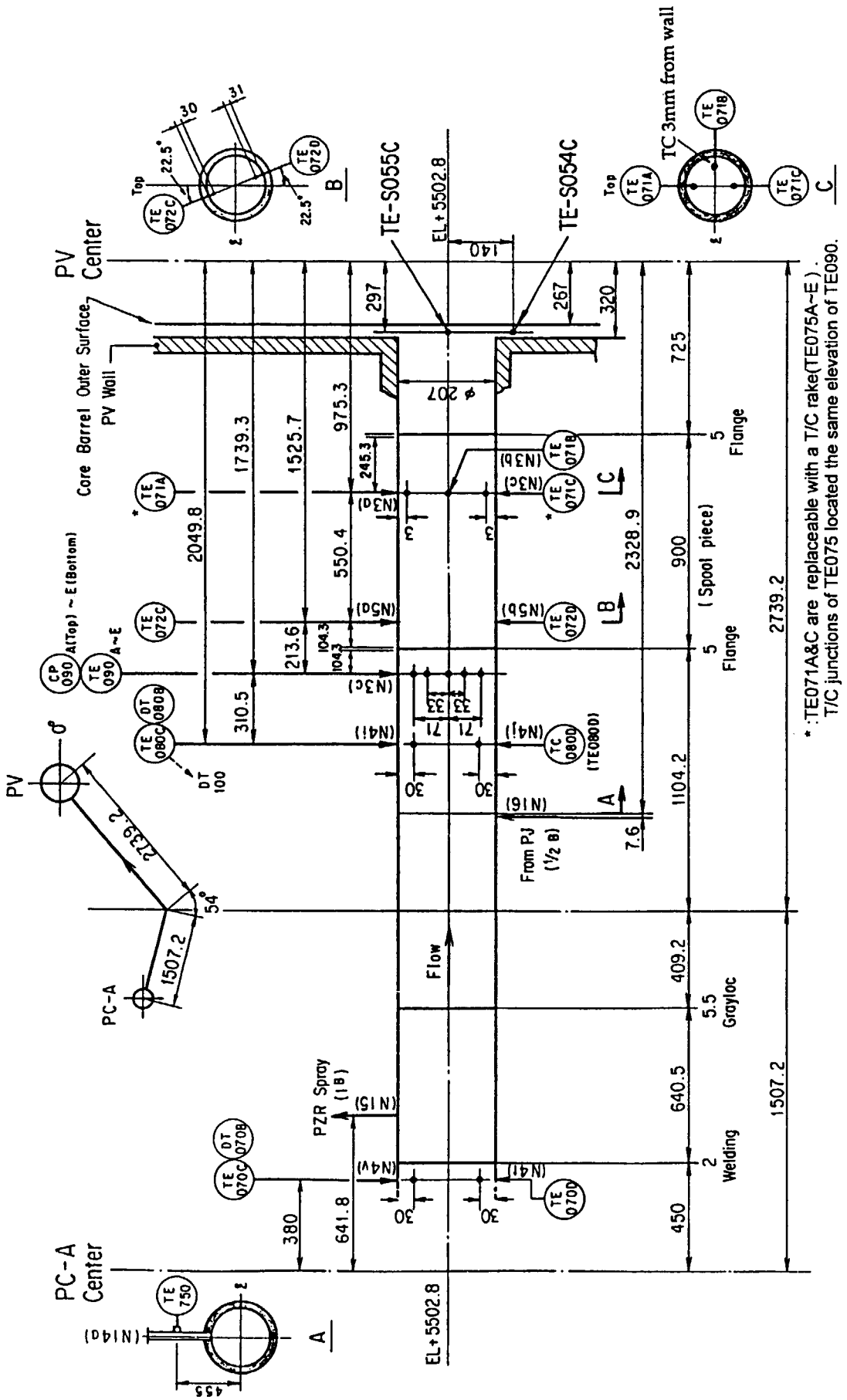

Fig. A. 10 Detail of instrument locations in cold leg A

VP : Video probe
GD_3 : 3 beams γ - densitometer
DD : Drag disk flow meter
CPT_5 : Conductance probe with TC
TC : Fluid temperature by resistance bulb
TE : Fluid temperature
TW_A : Outside wall temperature
TW_B : Inside wall temperature
RE : Rotation speed
VE : Pump oscillation
TQ : Pump torque
LF : Leakage flow meter

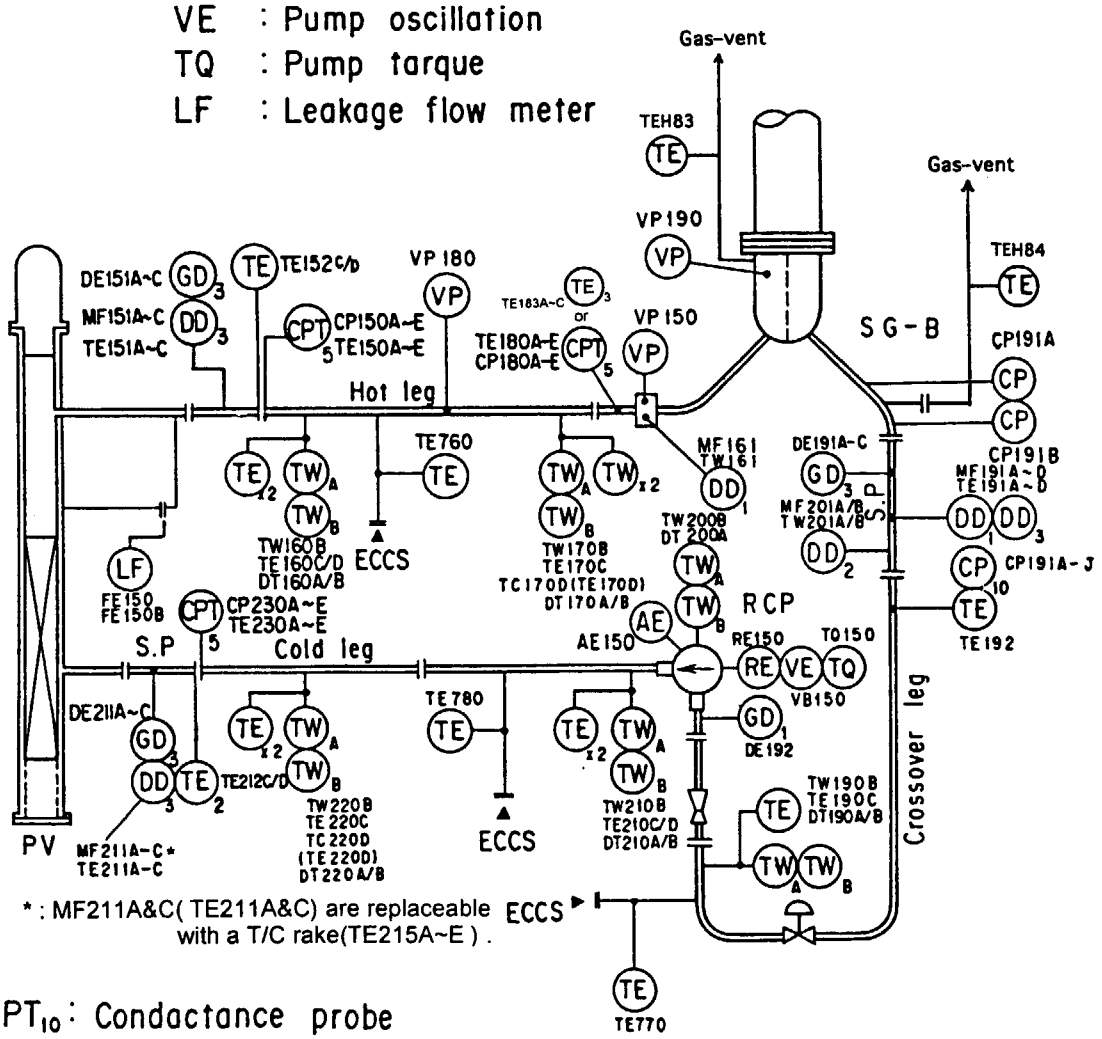

CPT_{10} : Condactance probe
AE : Electric current
ECCS : Emergency core cooling system
S.P. : Spool piece

Fig. A. 11 Primary loop-B instrument locations for pressure, temperature, fluid density and others

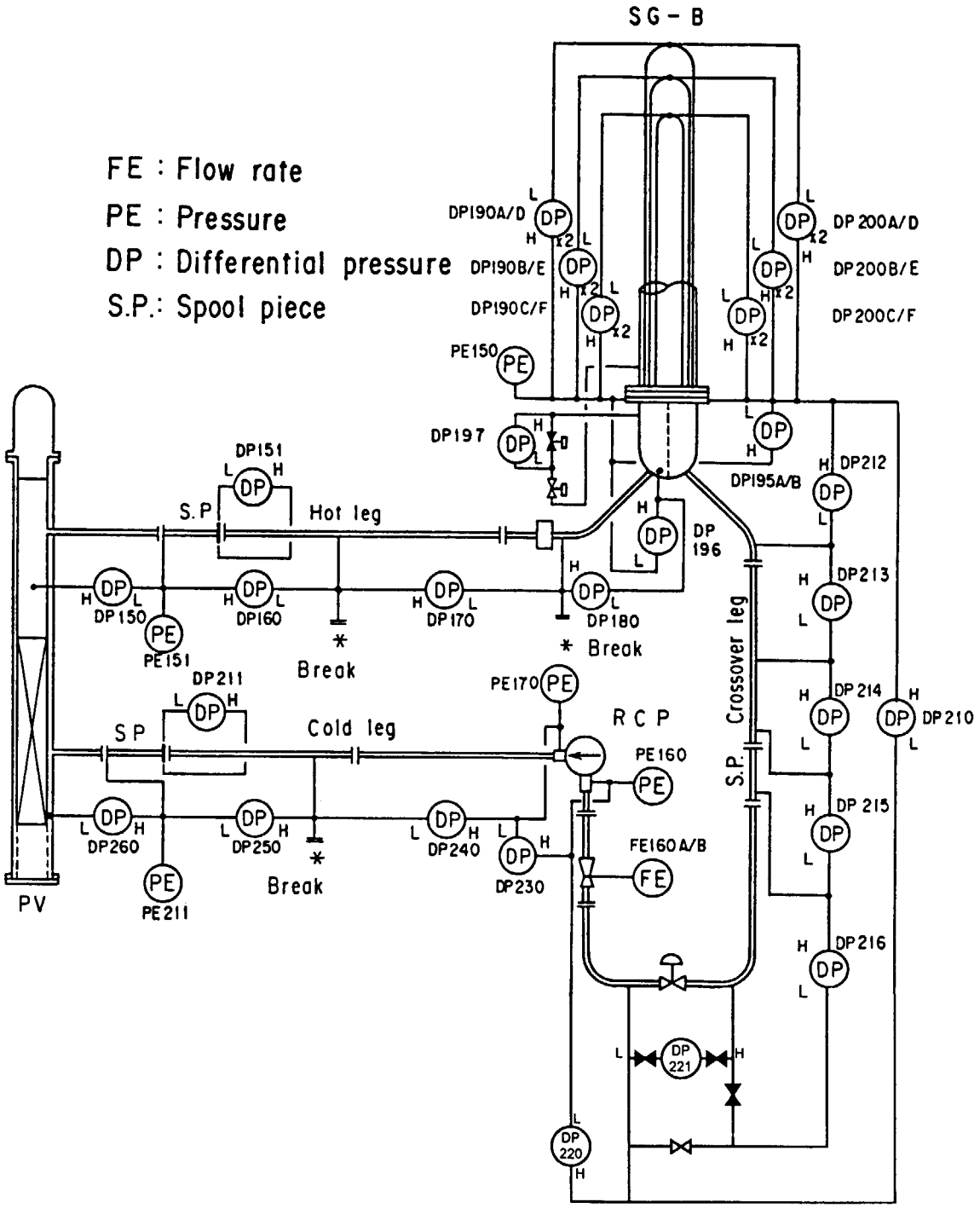

Fig. A. 12 Primary loop-B instrument locations for DP and flow-rate

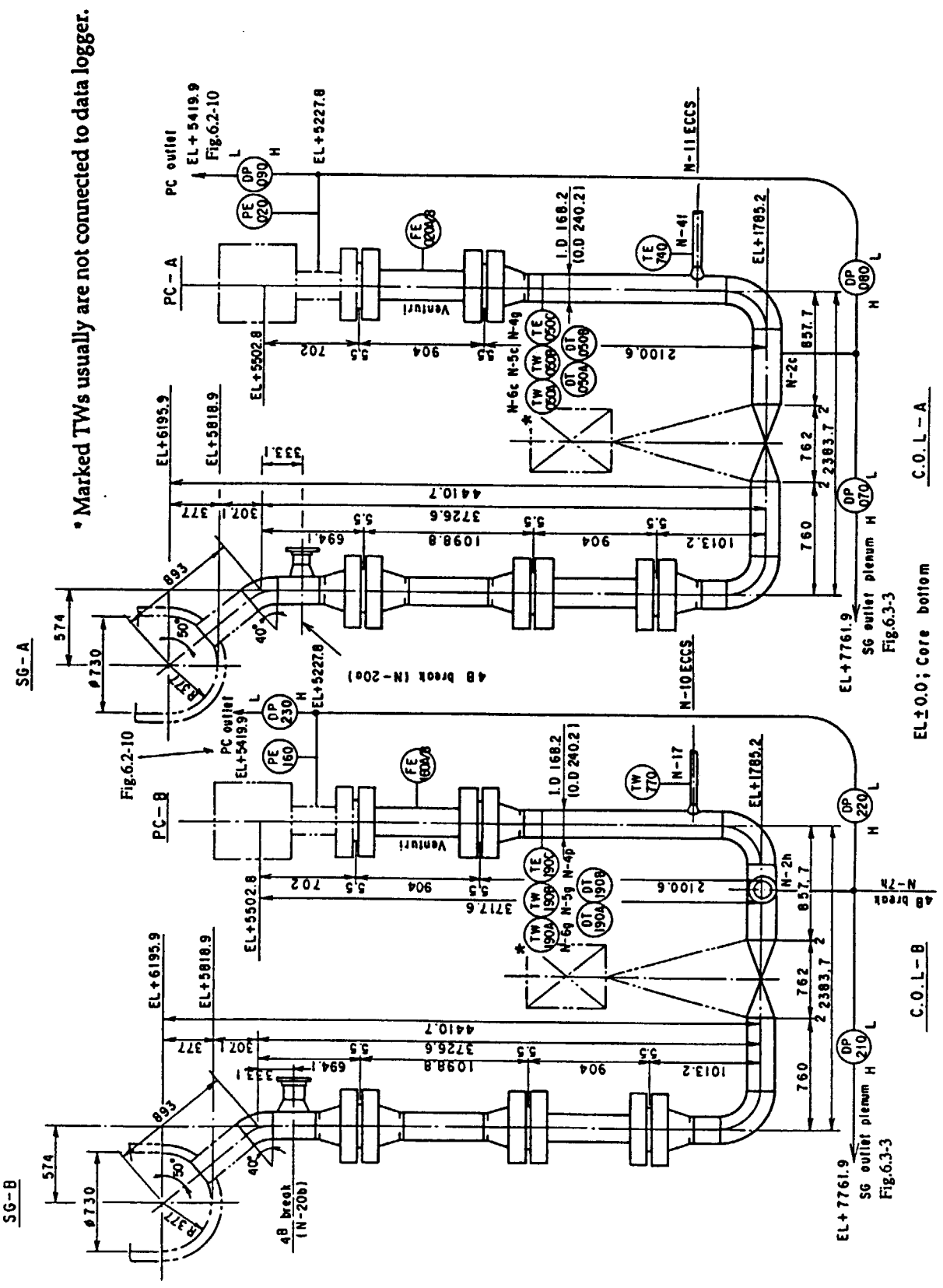

Fig. A. 13 Cross-over legs with instrumentation (Loop-seal region)

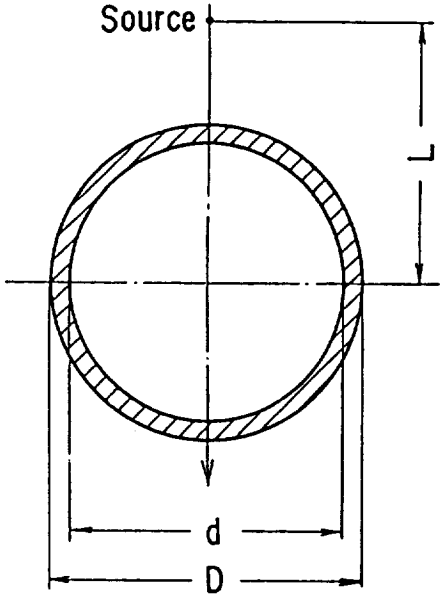

Single-beam densitometer

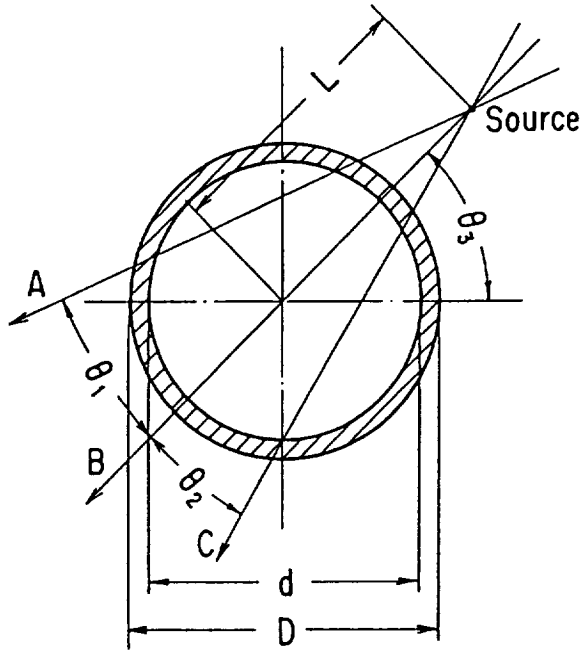

Three-beam densitometer

Function ID No.	Tag Name	D (mm)	d (mm)	L (mm)	Location Pipe Name/Direction
DE19	DE052	240.2	168.2	305.0	Loopseal A / Vertical
DE20	DE192	240.2	168.2	305.0	Loopseal B / Vertical
DE21	DE281	89.1	66.9	155.0	RZR Surge L. / Horiz.
DE40	DE291	89.1	66.9	-	SGB Feegwater line / Horiz.
DE41	DE321	457.2	372.0	-	PZR Body / Vertical

Function ID No.	Tag Name	D (mm)	d (mm)	L (mm)	θ1 (Deg.)	θ2 (Deg.)	θ3 (Deg.)	Location Pipe Name/Direction
DE1~3	DE011A~C	295.0	207.0	212.9	22.1	14.35	45.0	HLA / Horiz.
DE7~9	DE071A~C	295.0	207.0	212.9	22.1	14.35	45.0	CLA / Horiz.
DE10~12	DE151A~C	295.0	207.0	212.9	22.1	14.35	45.0	HLB / Horiz.
DE16~18	DE211A~C	295.0	207.0	212.9	22.1	14.35	45.0	CLB / Horiz.
DE4~6	DE051A~C	240.2	168.2	240.0	15..9	11.2		LSA / Vertical
DE13~15	DE191A~C	240.2	168.2	240.0	15..10	12.2		LSB / Vertical
DE27~29	DE451A~C	216.3	190.9	240.0	18.1	12.3	45.0	SGA / Horiz.
DE30~32	*DE571A~C	114.3	87.3	165.5	12.0	8.08	50.0	Break Unit
DE33~35	*DE591A~C	114.3	87.3	130.0	14.0	14.0	45.0	RSV1~3 / Horiz.

Note: DE571A~C was equipped ADS1~3 line and
DE591A~C was equipped breaj unit from Exp.AP-SG-01

Fig. A. 14 Gamma-densitometer setup, single-beam and three-beam types

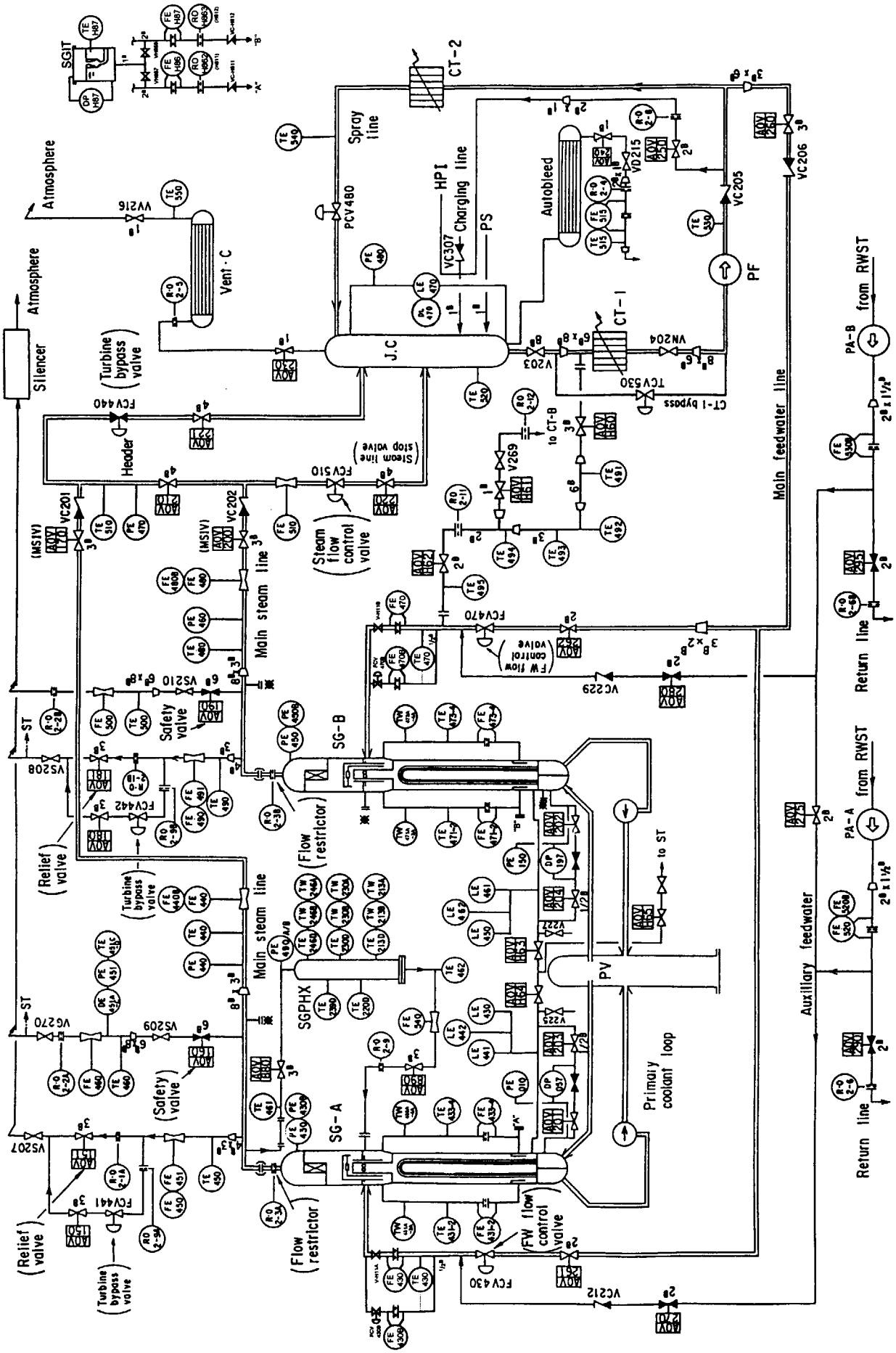

Fig. A. 15 Overview of piping and instrumentation for secondary coolant system

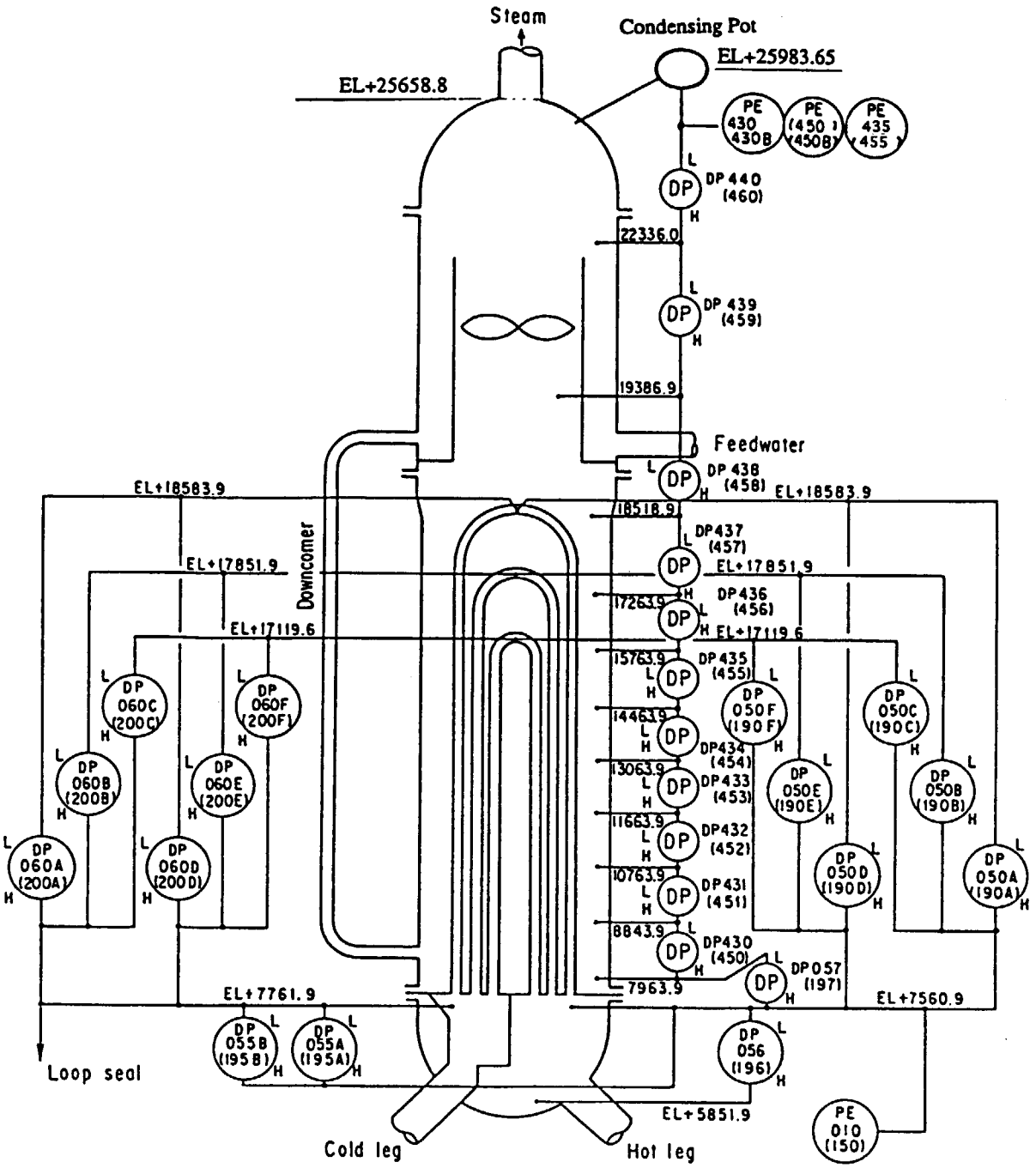

Note : Tag names in parenthesis are for SG-B.

Fig. A. 16 Location of pressure and DP measurements for SG-A/B

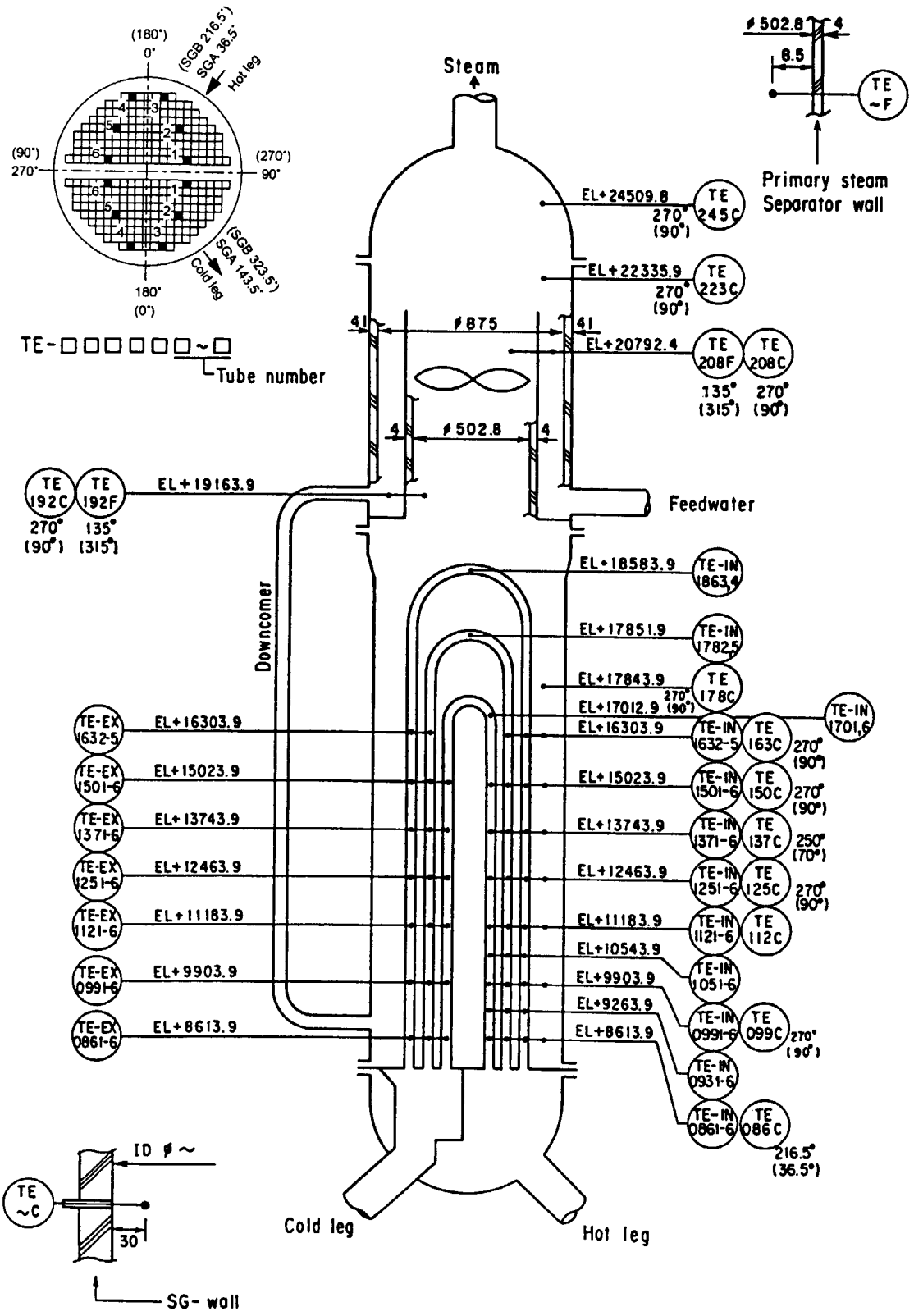

Fig. A. 17 Location of fluid temperature measurements for SG-A/-B

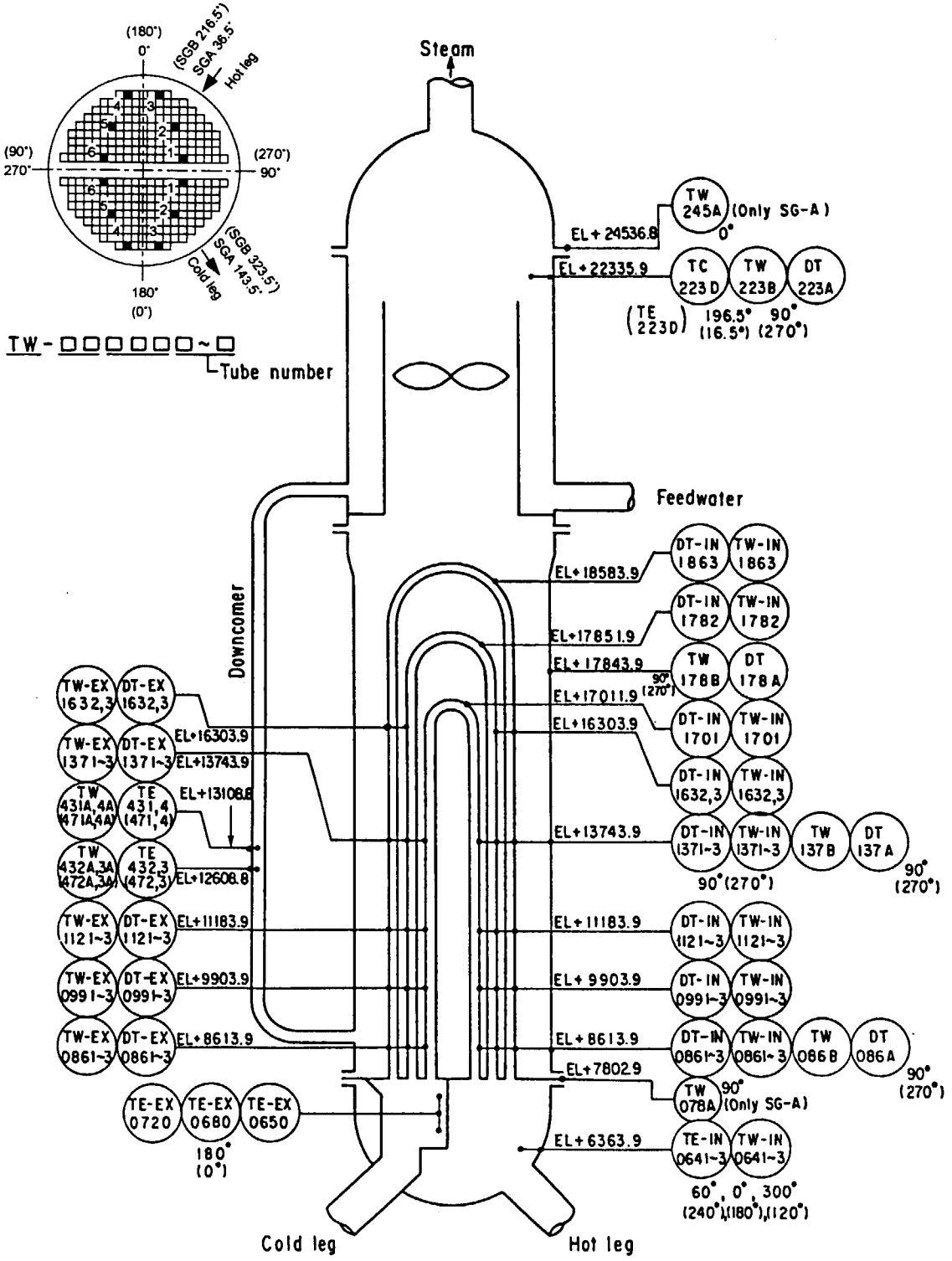

Fig. A. 18 Location of wall temperature and temperature difference measurements for SG-A/B

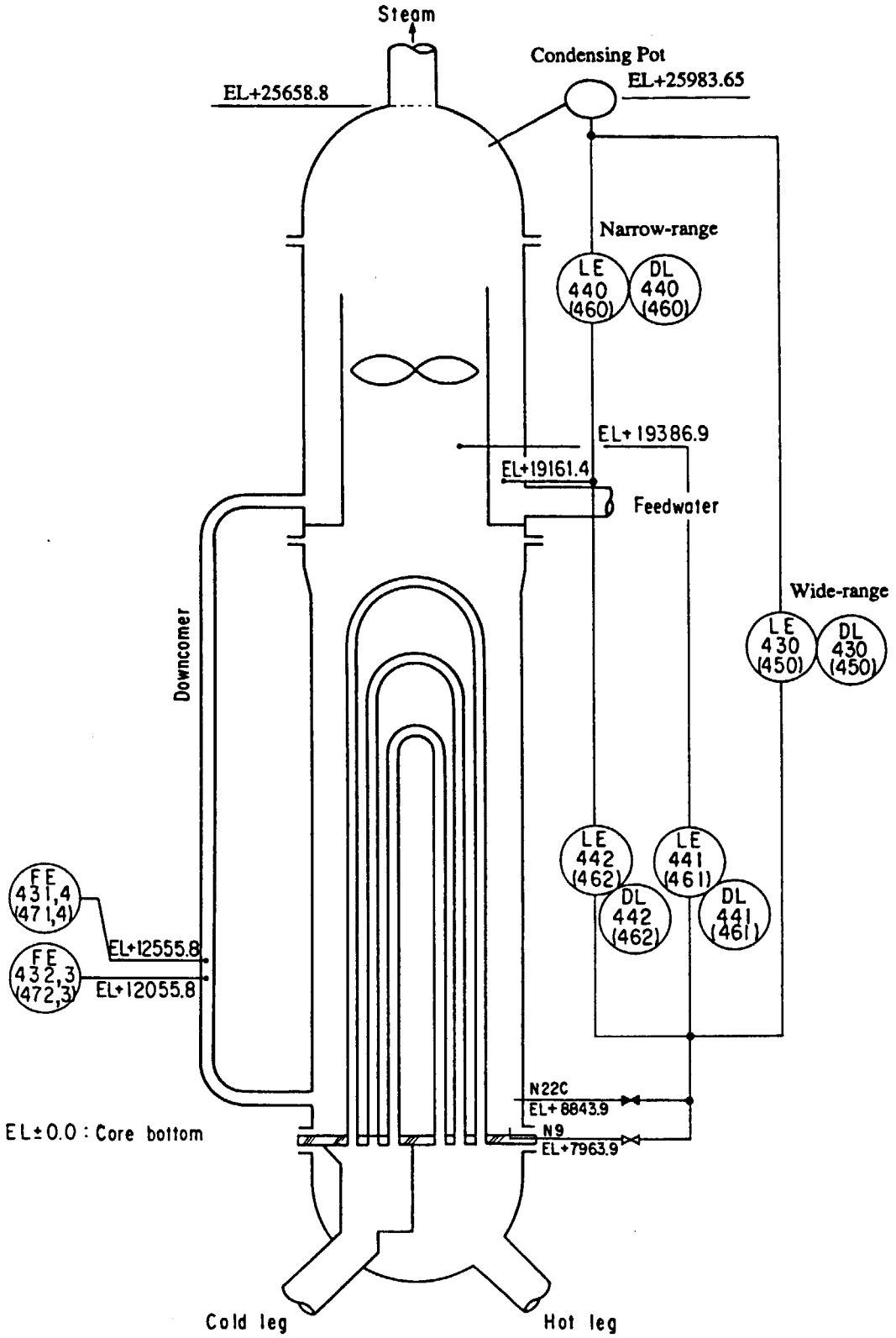

Note : Tag names in parenthesis are for SG-B.

Fig. A. 19 Liquid level and downcomer flowrate measurements for SG-A/B

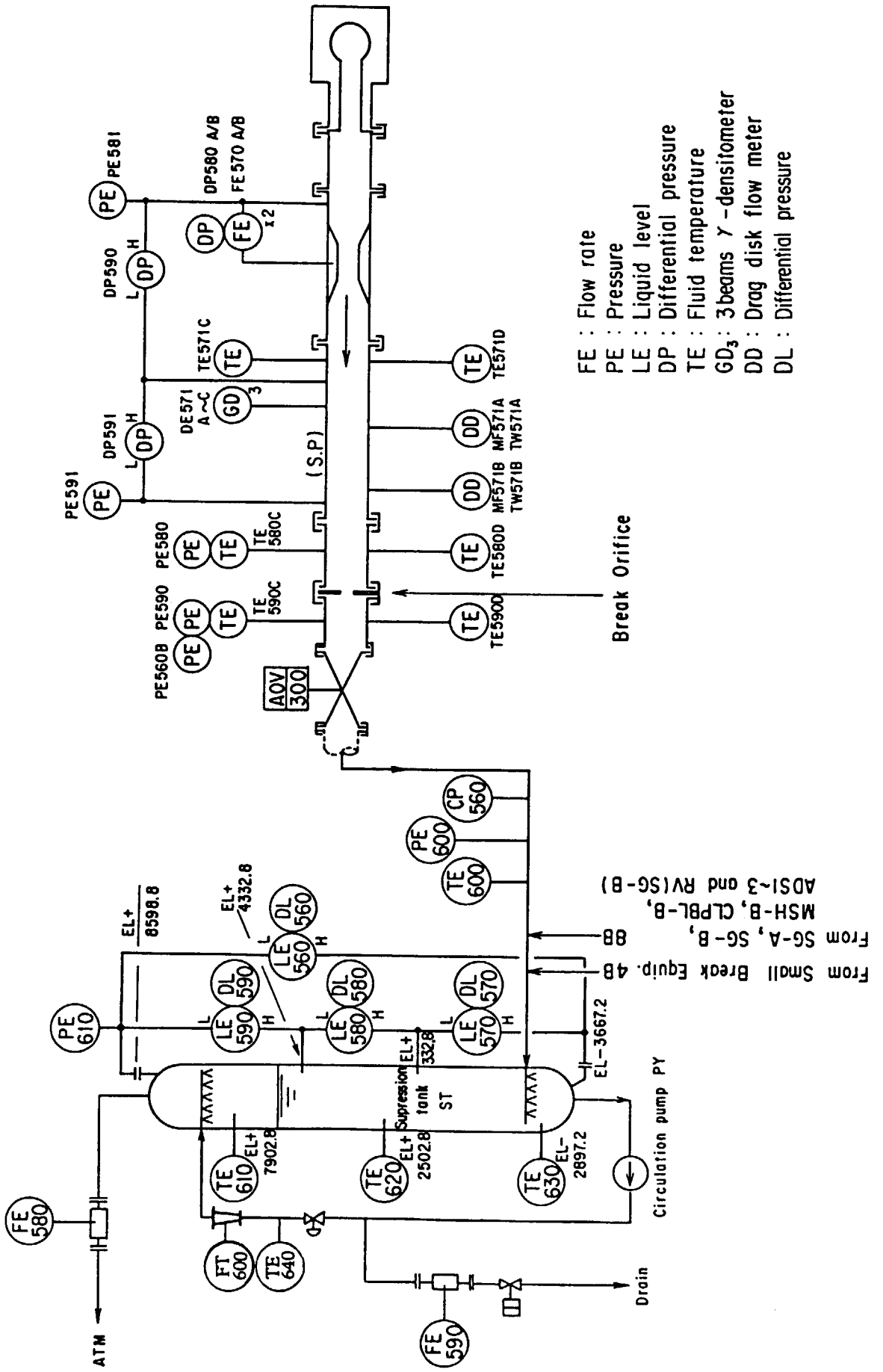

Fig. A. 20 Typical instrumentation for break unit and break flow storage tank

Table B.1 Measurement list for estimation of primary coolant mass inventory

Primary Region	Measurement ID List				Configuration		Initial
	Pres. PE	Dif.P DP/LE	Temperatures TE	Dens. RC	Height (m)	Volume (m^3)	Mass in SP3 (kg)
Pressure Vessel						2.7538	**1969.4**
Upper Head	9	DP 52	117, 118		3.518	0.4963	343.0
Upper Plenum	10	DP 51	125, 126		2.075	0.4950	327.9
Core	12	DP 50	274, 275, 276, 277		3.921	0.4477	316.7
Lower Plenum	12	DP 48	214, 215		1.655	0.3364	252.1
Downcomer	12	DP 56	193, 198, 203, 208		8.599	0.9784	729.6
Pressurizer						1.3320	**547.9**
PZR Vessel	13	LE 21	958, 960, 962		11.241	1.2955	520.2
Surge Line	13	DP 70	52		5.461	0.0365	27.7
SG-A U-tubes						0.86692	**630.7**
Type-1, Inlet	3	DP 7	330, 366, 390, 422		9.451	0.06032	42.8
Type-1, Outlet	3	DP 13	336, 367, 391		9.250	0.06032	44.8
Type-2, Inlet	3	DP 6	331, 368, 392, 424		10.103	0.22362	158.9
Type-2, Outlet	3	DP 12	337, 369, 393		9.902	0.22362	167.4
Type-3, Inlet	3	DP 5	332, 370, 394, 416		10.958	0.14952	105.6
Type-3, Outlet	3	DP 11	338, 371, 395		10.757	0.14952	111.3
SG-B U-tubes						0.86692	**630.8**
Type-1, Inlet	6	DP 31	449, 485, 509, 541		9.451	0.06032	42.6
Type-1, Outlet	6	DP 37	455, 486, 510		9.250	0.06032	44.8
Type-2, Inlet	6	DP 30	450, 487, 511, 544		10.103	0.22362	159.7
Type-2, Outlet	6	DP 36	456, 488, 512		9.902	0.22362	166.2
Type-3, Inlet	6	DP 29	451, 489, 545		10.958	0.14952	106.2
Type-3, Outlet	6	DP 35	457, 490, 514		10.757	0.14952	111.4
SG-A Inlet Side						0.4529	**302.6**
Inlet Plenum	3	DP120	324, 325, 326		1.709	0.4351	290.7
Inlet Pipe	3	DP 4	324, 325, 326		0.453	0.0178	11.9
SG-B Inlet Side						0.4549	**305.2**
Inlet Plenum	6	DP122	443, 444, 445		1.709	0.4371	293.3
Inlet Pipe	6	DP 28	443, 444, 445		0.453	0.0178	11.9
SG-A Outlet-LSA	4	DP 17	732, 615		6.061	0.3409	**254.0**
SG-B Outlet-LSB	7	DP 41	734, 630		6.061	0.3395	**253.0**
LSA-PCA, Pump	4	DP 18	15		3.527	0.0921	**68.7**
LSB-PCB, Pump	7	DP 42	40		3.527	0.0926	**69.1**
Hot Leg A	35		609, 610	31-33	0.207	0.1133	**75.1**
Hot Leg B	37		624, 625	34-36	0.207	0.1156	**76.8**
Cold Leg A	36		619, 620	37-39	0.207	0.1531	**114.2**
Cold Leg B	38		634, 635	40-42	0.207	0.1617	**120.5**
Loop A Total						2.01922	**1445.3**
Loop B Total						2.03122	**1455.3**
Primary Coolant System Total						8.1362	**5417.8**

Refer primary regions and mass distribution at initial state shown in Fig.B.1.

Table B.2 Regional volume related to elevation for LSTF primary coolant system

UPPER HEAD	
EL (m)	V (m3)
6.4742	0.0
6.63	0.0336
6.903	0.0728
7.207	0.1164
7.373	0.1511
8.033	0.3308
8.357	0.4308
8.6002	0.4963

UPPER PLENUM	
EL (m)	V (m3)
3.968	0.0
4.1926	0.0351
5.318	0.2459
5.9596	0.3765
6.1702	0.4950

CORE	
EL (m)	V (m3)
0.0	0.0
0.4575	0.0499
0.915	0.1009
1.3725	0.1525
1.83	0.2037
2.2875	0.2547
2.745	0.3030
3.2025	0.3527
3.66	0.4024
3.968	0.4477

LOWER PLENUM	
EL (m)	V (m3)
-2.357	0.0
-2.146	0.0330
-1.2588	0.1563
-0.552	0.2637
0.0	0.3364

DOWNCOMER	
EL (m)	V (m3)
-2.3570	0.0
-1.2588	0.1280
0.0	0.2706
0.4575	0.3149
0.915	0.3584
3.66	0.6207
3.968	0.6460
5.318	0.7808
5.9596	0.8364
6.1702	0.8564
7.196	0.9784

PRESSURIZER	
EL (m)	V (m3)
11.3426	0.0
13.5906	0.2361
15.5856	0.4520
17.3426	0.6430
19.3126	0.8562
21.1426	1.0551
22.6686	1.2955

SURGE LINE	
EL (m)	V (m3)
5.5028	0.0
6.9101	0.00663
8.5863	0.01252
9.4063	0.01620
9.5438	0.02665
9.6028	0.03078
11.3426	0.03650

SG-A U-TUBE(1,IN)	
EL (m)	V (m3)
7.6289	0.0
17.0688	0.05981
17.1196	0.06032

SG-A U-TUBE(1,EX)	
EL (m)	V (m3)
7.6289	0.0
17.0688	0.05981
17.1196	0.06032

SG-A U-TUBE(2,IN)	
EL (m)	V (m3)
7.6289	0.0
17.2196	0.21413
17.3029	0.21626
17.4859	0.21968
17.6689	0.22215
17.8519	0.22362

SG-A U-TUBE(2,EX)	
EL (m)	V (m3)
7.6289	0.0
17.2196	0.21413
17.3029	0.21626
17.4859	0.21968
17.6689	0.22215
17.8519	0.22362

SG-A U-TUBE(3,IN)	
EL (m)	V (m3)
7.6289	0.0
17.8216	0.14147
18.0349	0.14498
18.2179	0.14698
18.4009	0.14833
18.5839	0.14952

SG-A U-TUBE(3,EX)	
EL (m)	V (m3)
7.6289	0.0
17.8216	0.14147
18.0349	0.14498
18.2179	0.14698
18.4009	0.14833
18.5839	0.14952

Table B.2 (Cont'd)

SG-A INLET PLENUM	
EL (m)	V (m3)
5.8189	0.0
6.2819	0.1402
7.3819	0.3740
7.6319	0.4351

SG-A INLET PIPE	
EL (m)	V (m3)
5.3993	0.0
5.5028	0.0008
5.6063	0.0031
5.9224	0.0178

SG-A OUTLET PLENUM - LSA	
EL (m)	V (m3)
1.7011	0.0
1.8693	0.0330
5.5118	0.1168
5.9569	0.1294
7.3319	0.2912
7.6319	0.3409

SG-B U-TUBE(1,IN)	
EL (m)	V (m3)
7.6289	0.0
17.0688	0.05981
17.1196	0.06032

SG-B U-TUBE(1,EX)	
EL (m)	V (m3)
7.6289	0.0
17.0688	0.05981
17.1196	0.06032

SG-B U-TUBE(2,IN)	
EL (m)	V (m3)
7.6289	0.0
17.2196	0.21413
17.3029	0.21626
17.4859	0.21968
17.6689	0.22215
17.8519	0.22362

SG-B U-TUBE(2,EX)	
EL (m)	V (m3)
7.6289	0.0
17.2196	0.21413
17.3029	0.21626
17.4859	0.21968
17.6689	0.22215
17.8519	0.22362

SG-B U-TUBE(3,IN)	
7.6289	0.0
17.8216	0.14147
18.0349	0.14498
18.2179	0.14698
18.4009	0.14833
18.5839	0.14952

SG-B U-TUBE(3,EX)	
EL (m)	V (m3)
7.6289	0.0
17.8216	0.14147
18.0349	0.14498
18.2179	0.14698
18.4009	0.14833
18.5839	0.14952

SG-B INLET PLENUM	
EL (m)	V (m3)
5.8189	0.0
6.2819	0.1422
7.3819	0.3760
7.6319	0.4371

SG-B INLET PIPE	
EL (m)	V (m3)
5.3993	0.0
5.5028	0.0008
5.6063	0.0031
5.9224	0.0178

SG-B OUTLET PLENUM - LSB	
EL (m)	V (m3)
1.7011	0.0
1.8693	0.0330
5.5118	0.1180
5.9569	0.1306
7.3319	0.2898
7.6319	0.3395

HOT LEG A	
EL (m)	V (m3)
5.3993	0.0
5.6063	0.1133

HOT LEG B	
EL (m)	V (m3)
5.3993	0.0
5.6063	0.1156

COLD LEG A	
EL (m)	V (m3)
5.3993	0.0
5.6063	0.1531

COLD LEG B	
EL (m)	V (m3)
5.3993	0.0
5.6063	0.1617

LSA - PCA	
EL (m)	V (m3)
1.7011	0.0
1.8693	0.0107
2.2862	0.0217
5.3993	0.0921

LSB - PCB	
EL (m)	V (m3)
1.7011	0.0
1.8693	0.0119
2.2862	0.0229
5.3993	0.0926

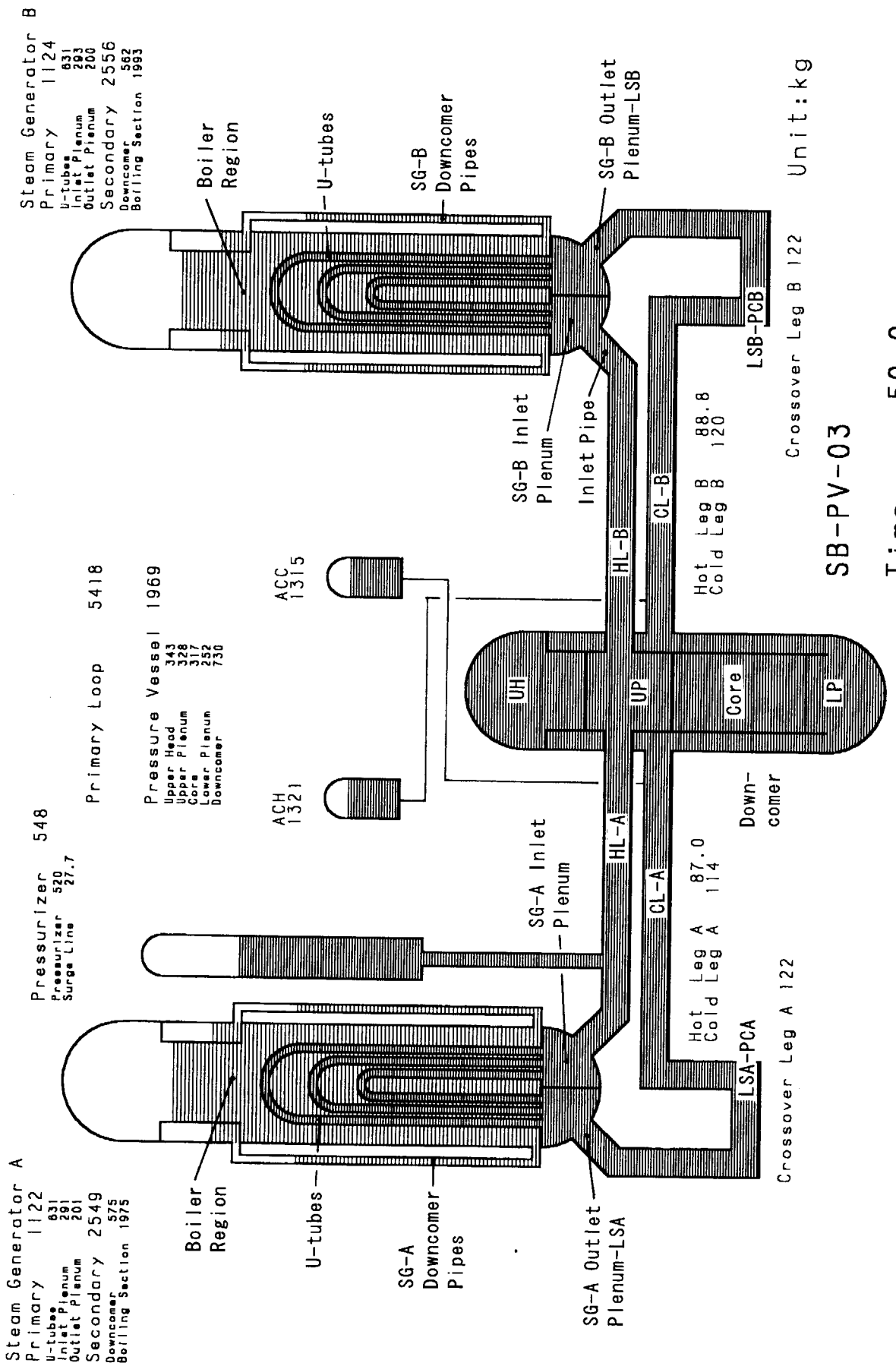

Fig. B. 1 Regional mass distribution map for primary and SG secondary systems at initial state of experiment SB-PV-03

Table C.1 Measurement list for secondary mass and energy estimation

(1) Measurement list for steam and feedwater flows

Item	Pressure	Flow Rate	Fluid Temp.
SG-A Secondary Side			
Main Steam Flow	PE 19	FE 18	TE 56
RV Line Flow	〃	FE 19	TE 57
SV Line Flow	〃	FE 20	TE 58
Feedwater Flow	〃	FE 13	TE 55
SG-B Secondary Side			
Main Steam Flow	PE 21	FE 26	TE 60
RV Line Flow	〃	FE 27	TE 61
SV Line Flow	〃	FE 28	TE 62
Feedwater Flow	〃	FE 21	TE 59

(2) Measurement list for fluid mass and energy estimation

Region	Elevation EL (m)*1	Volume (m^3)	Measurement ID		
			Pressure	Level/DP	Fluid Temp.
SG-A Sec. Side		6.9960			
Boiler (1)	7.964- 8.844	0.1958	PE 19	DP 81	TE 429
Boiler (2)	8.844-10.764	0.4351	〃	DP 82	TE 430
Boiler (3)	10.764-11.664	0.1979	〃	DP 83	TE 431
Boiler (4)	11.664-13.064	0.3082	〃	DP 84	TE 432
Boiler (5)	13.064-14.464	0.3092	〃	DP 85	TE 433
Boiler (6)	14.464-15.764	0.2880	〃	DP 86	TE 434
Boiler (7)	15.764-17.264	0.3472	〃	DP 87	TE 435
Boiler (8)	17.264-18.519	0.4572	〃	DP 88	TE 436
Boiler (9)	18.519-19.387	0.3768	〃	DP 89	TE 437
Boiler (10)	19.387-22.336	0.7431	〃	DP 90	TE 438
Boiler (11)	22.336-25.687	1.8604	〃	DP 91	TE 441, 442
Upper DC	19.115-21.881	1.0726	〃	LE 23	TE 439, 440
Lower DC	7.964-19.213	0.4045	〃	LE 25	TE 68 ～ 71
SG-B Sec. Side		7.0230			
Boiler (1)	7.964- 8.844	0.1958	PE 21	DP 92	TE 548
Boiler (2)	8.844-10.764	0.4326	〃	DP 93	TE 549
Boiler (3)	10.764-11.664	0.1981	〃	DP 94	TE 550
Boiler (4)	11.664-13.064	0.3125	〃	DP 95	TE 551
Boiler (5)	13.064-14.464	0.3109	〃	DP 96	TE 552
Boiler (6)	14.464-15.764	0.2867	〃	DP 97	TE 553
Boiler (7)	15.764-17.264	0.3540	〃	DP 98	TE 554
Boiler (8)	17.264-18.519	0.4783	〃	DP 99	TE 555
Boiler (9)	18.519-19.387	0.3783	〃	DP100	TE 556
Boiler (10)	19.387-22.336	0.7432	〃	DP101	TE 557
Boiler (11)	22.336-25.687	1.8555	〃	DP102	TE 560, 561
Upper DC	19.115-21.881	1.0726	〃	LE 27	TE 558, 559
Lower DC	7.964-19.213	0.4045	〃	LE 29	TE 72 ～ 75

Table C.1 (Cont'd)

(3) Measurement list for metal stored heat estimation

Region	Elevation EL (m)*1	Material*2	Weight (kg)	Measurement ID (Temperatures)
SG-A Secondary Side			21320	
U-tubes Part 1	7.964- 9.264	SS	598	TW 469, 470
U-tubes Part 2	9.264-10.544	〃	589	TW 475, 476
U-tubes Part 3	10.544-12.464	〃	883	TW 481, 482
U-tubes Part 4	12.464-15.024	〃	1178	TW 487, 488
U-tubes Part 5	15.024-18.584	〃	1284	TW 491, 492
U-tubes Total			4532	
Tube Sheet	7.632- 7.964	CS	1118	TE 324, TW 463
Lower Vessel Wall	7.964-10.544	〃	1823	TW 463, DT 139
Mid. Vessel Wall-1	10.544-15.024	〃	2644	TW 464, DT 140
Mid. Vessel Wall-2	15.024-18.584	〃	2430	TW 465, DT 141
Upper Vessel Wall	18.584-25.659	〃	6356	TW 466, DT 142
Steam Line Piping		SS	901	TE 442
Downcomer Piping		〃	787	TW 14 ～ 17
Internal Structure		〃	729	TE 442
Walls Total			16788	
SG-B Secondary Side			21320	
U-tubes Part 1	7.964- 9.264	SS	598	TW 510, 511
U-tubes Part 2	9.264-10.544	〃	589	TW 516, 517
U-tubes Part 3	10.544-12.464	〃	883	TW 522, 523
U-tubes Part 4	12.464-15.024	〃	1178	TW 528, 529
U-tubes Part 5	15.024-18.584	〃	1284	TW 532, 533
U-tubes Total			4532	
Tube Sheet	7.632- 7.964	CS	1118	TE 443, TW 504
Lower Vessel Wall	7.964-10.544	〃	1823	TW 504, DT 174
Mid. Vessel Wall-1	10.544-15.024	〃	2644	TW 505, DT 175
Mid. Vessel Wall-2	15.024-18.584	〃	2430	TW 506, DT 176
Upper Vessel Wall	18.584-25.659	〃	6356	TW 507, DT 177
Steam Line Piping		SS	901	TE 561
Downcomer Piping		〃	787	TW 18 ～ 21
Internal Structure		〃	729	TE 561
Walls Total			16788	

*1 Elevation above active core bottom (EL 0.0 m).
*2 CS:Carbon Steel, SS:Stainless Steel.

Table C.2 Configuration data base for SG secondary fluid system

(1) Boiler region of SG-A and SG-B

Part	Elev. EL (m)	SG-A Volume (m^3)	SG-A Area (m^2)	SG-B Volume (m^3)	SG-B Area (m^2)
1	7.964	0.0		0.0	
	8.844	0.1958	0.2225	0.1958	0.2225
2	8.844	0.0		0.0	
	10.764	0.4351	0.2266	0.4326	0.2253
3	10.764	0.0		0.0	
	11.664	0.1979	0.2199	0.1981	0.2201
4	11.664	0.0		0.0	
	13.064	0.3082	0.2201	0.3125	0.2232
5	13.064	0.0		0.0	
	14.464	0.3092	0.2209	0.3109	0.2221
6	14.464	0.0		0.0	
	15.764	0.2880	0.2215	0.2867	0.2205
7	15.764	0.0		0.0	
	16.937	0.2772	0.2363	0.2788	0.2377
	17.264	0.3472	0.2141	0.3540	0.2300
8	17.264	0.0		0.0	
	17.437	0.0392	0.2266	0.0440	0.2534
	17.687	0.1038	0.2584	0.1176	0.2944
	17.937	0.1814	0.3104	0.1962	0.3144
	18.187	0.2765	0.3804	0.2933	0.3884
	18.437	0.4098	0.5332	0.4296	0.5452
	18.519	0.4572	0.5780	0.4783	0.5939
9	18.519	0.0		0.0	
	18.687	0.0972	0.5786	0.0999	0.5946
	18.937	0.2328	0.5424	0.2345	0.5384
	19.115	0.3246	0.5157	0.3253	0.5101
	19.187	0.3388	0.1972	0.3395	0.1972
	19.387	0.3768	0.1900	0.3783	0.1940
10	19.387	0.0		0.0	
	19.687	0.0574	0.1913	0.0586	0.1953
	20.187	0.1467	0.1786	0.1469	0.1766
	20.687	0.2431	0.1928	0.2423	0.1908
	21.187	0.3275	0.1688	0.3277	0.1708
	21.687	0.4239	0.1928	0.4231	0.1908
	22.187	0.6534	0.4590	0.6526	0.4590
	22.336	0.7431	0.6020	0.7432	0.6081
11	22.336	0.0		0.0	
	22.687	0.2113	0.6020	0.2134	0.6080
	24.187	1.0843	0.5820	1.0764	0.5753
	25.687	1.8604	0.5174	1.8555	0.5194
Total		5.5189		5.5459	

(2) SG-A/B downcomer region

DC Part	Elev. EL (m)	SG-A/B Volume (m^3)	SG-A/B Area (m^2)
Up. DC	19.115	0.0	
	19.687	0.2265	0.3960
	20.187	0.4292	0.4054
	21.687	1.0130	0.3892
	21.881	1.0726	0.3072
Low. DC	7.964	0.0	
	8.964	0.0682	0.0682
	9.964	0.1091	0.0409
	16.964	0.3163	0.0296
	17.937	0.3451	0.0296
	18.187	0.3560	0.0436
	18.437	0.3687	0.0508
	18.937	0.3835	0.0296
	19.187	0.4012	0.0708
	19.213	0.4045	0.1269
Total		1.4771	

(3) SG-A/B total volume

Vol. (m^3)	SG-A	SG-B
	6.996	7.023

Table C.3 Uncertainty estimation for SG secondary fluid mass

Secondary Region	SG-A Secondary System			SG-B Secondary System		
	Initial State*		Uncer-tainty	Initial State*		Uncer-tainty
	Av. Temp. (K)	Mass M (kg)	ΔM (kg)	Av. Temp. (K)	Mass M (kg)	ΔM (kg)
Boiler (1)	552.62	147.5	± 9.64	554.72	146.7	± 9.64
〃 (2)	563.26	294.7	± 9.92	563.94	291.4	± 9.86
〃 (3)	563.21	114.7	± 9.53	563.11	113.2	± 9.55
〃 (4)	563.04	166.2	± 9.58	562.97	169.4	± 9.71
〃 (5)	563.69	161.6	± 9.61	562.89	162.8	± 9.67
〃 (6)	563.54	138.2	± 9.63	562.87	138.8	± 9.59
〃 (7)	563.84	178.4	± 10.29	562.75	174.9	± 10.35
〃 (8)	563.70	294.5	± 25.05	562.41	316.9	± 25.73
〃 (9)	562.78	184.5	± 25.05	562.89	191.8	± 25.74
〃 (10)	562.50	225.3	± 26.16	562.73	219.8	± 26.43
〃 (11)	563.64	74.3	± 26.04	562.97	72.0	± 26.30
Upper DC	554.88	330.5	± 30.71	557.38	314.6	± 30.71
Lower DC	551.77	241.7	± 10.49	552.41	243.6	± 10.49
Total		2552.1	± 65.84		2555.9	± 66.60
			(±2.6%)			(±2.6%)

* Initial pressures in steam domes of SG-A and SG-B at t=0 s are 7.3674 and 7.3965 MPa, respectively.

Table C.4 Specific heats for metal structures

SUS-316(*1)		Carbon Steel(*2)	
Temperature (K)	Spec. Heat (kJ/kg/K)	Temperature (K)	Spec. Heat (kJ/kg/K)
350.0	0.4794	348.0	0.486
400.0	0.5003	448.0	0.519
450.0	0.5192	498.0	0.528
500.0	0.5338	548.0	0.548
550.0	0.5443	598.0	0.569
600.0	0.5518	648.0	0.586
650.0	0.5577		

*1:Ref. [13], D698. *2:Ref. [1], Table A.2-5.

Table C.5 Experimental results on SG heat loss rate

SG In. Wall Temperature (K)	Total Heat Loss(*)	
	SG-A $Q_{HL,A}$ (kW)	SG-B $Q_{HL,B}$ (kW)
350.0	3.5	4.0
400.0	7.4	8.3
450.0	10.4	11.8
500.0	16.7	19.3
520.0	19.9	23.9
540.0	24.2	28.8
560.0	29.4	35.6

* Ref. [14].

Table C.6 Uncertainty estimation for SG fluid enthalpy

Secondary Region	SG-A Sec. System		SG-B Sec. System	
	Initial Enthalpy $Q_{H,I}$ (kJ)	Uncertainty of Q_H (kJ)	Initial Enthalpy $Q_{H,I}$ (kJ)	Uncertainty of Q_H (kJ)
Boiler (1)	1.819×10^5	$\pm\ 0.92\times10^4$	1.825×10^5	$\pm\ 0.92\times10^4$
〃 (2)	3.809 〃	± 1.01 〃	3.773 〃	± 1.01 〃
〃 (3)	1.500 〃	± 0.91 〃	1.484 〃	± 0.91 〃
〃 (4)	2.186 〃	± 0.94 〃	2.230 〃	± 0.95 〃
〃 (5)	2.132 〃	± 0.94 〃	2.149 〃	± 0.95 〃
〃 (6)	1.838 〃	± 0.94 〃	1.846 〃	± 0.93 〃
〃 (7)	2.356 〃	± 1.01 〃	2.322 〃	± 1.02 〃
〃 (8)	3.821 〃	± 2.37 〃	4.103 〃	± 2.43 〃
〃 (9)	2.449 〃	± 2.36 〃	2.540 〃	± 2.42 〃
〃 (10)	4.439 〃	± 2.53 〃	4.208 〃	± 2.56 〃
〃 (11)	2.017 〃	± 2.42 〃	1.994 〃	± 2.45 〃
Upper DC	4.508 〃	± 2.88 〃	4.362 〃	± 2.88 〃
Lower DC	3.023 〃	± 1.05 〃	3.052 〃	± 1.05 〃
Total	35.895 〃	± 6.26 〃	35.888 〃	± 6.33 〃
		(± 1.7 %)		(± 1.8 %)

Table C.7 Uncertainty estimation for SG metal stored heat

Metal Component	SG-A/B Secondary Systems		
	Component Metal Mass M (kg)	Accuracy of Temperature △T (K)	Uncertainty of Stored Heat* (kJ)
U-tube (1)	598	± 2.75	$\pm\ 0.88\times10^3$
〃 (2)	589	〃	± 0.86 〃
〃 (3)	883	〃	± 1.30 〃
〃 (4)	1173	〃	± 1.72 〃
〃 (5) Top	1284	〃	± 1.88 〃
〃 Total	4532		± 3.11 〃
Tube Sheet	1118	± 2.75	± 1.63 〃
Low. SG Wall	1823	± 2.63	± 2.54 〃
Mid.-1 Wall	2644	〃	± 3.69 〃
Mid.-2 Wall	2430	〃	± 3.39 〃
Up. SG Wall	6356	〃	± 9.09 〃
Steam Line	901	〃	± 1.28 〃
DC Lines	783	〃	± 1.10 〃
Internals	729	〃	± 1.03 〃
Vessel Total	16788		±10.99 〃
Total	21311		

* ΔQ_T for U-tubes and ΔQ_W for SG walls

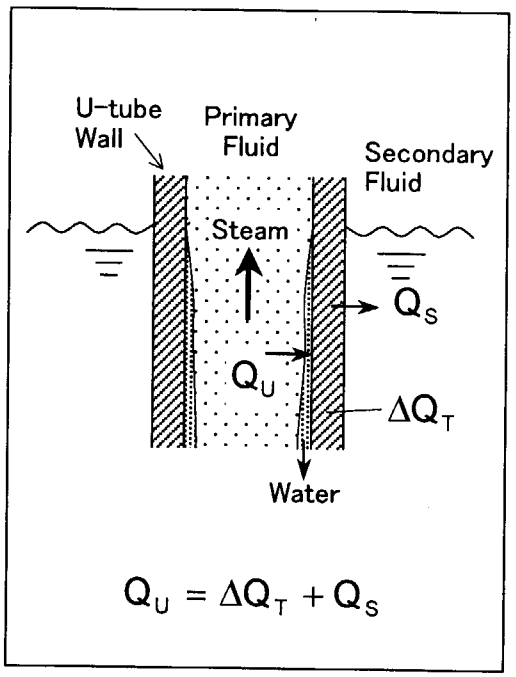

(1) Energy balance at U-tubes

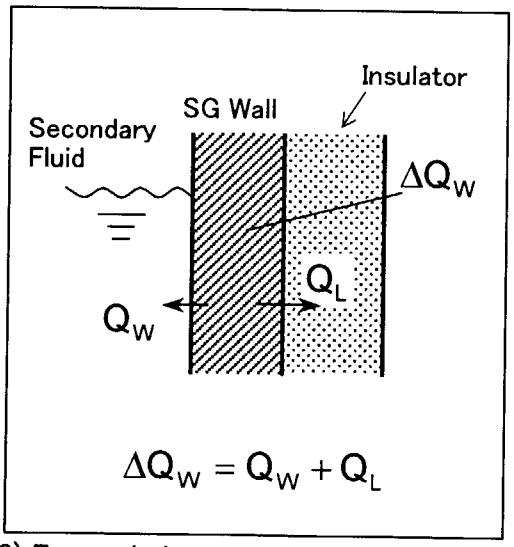

(2) Energy balance at SG vessel wall

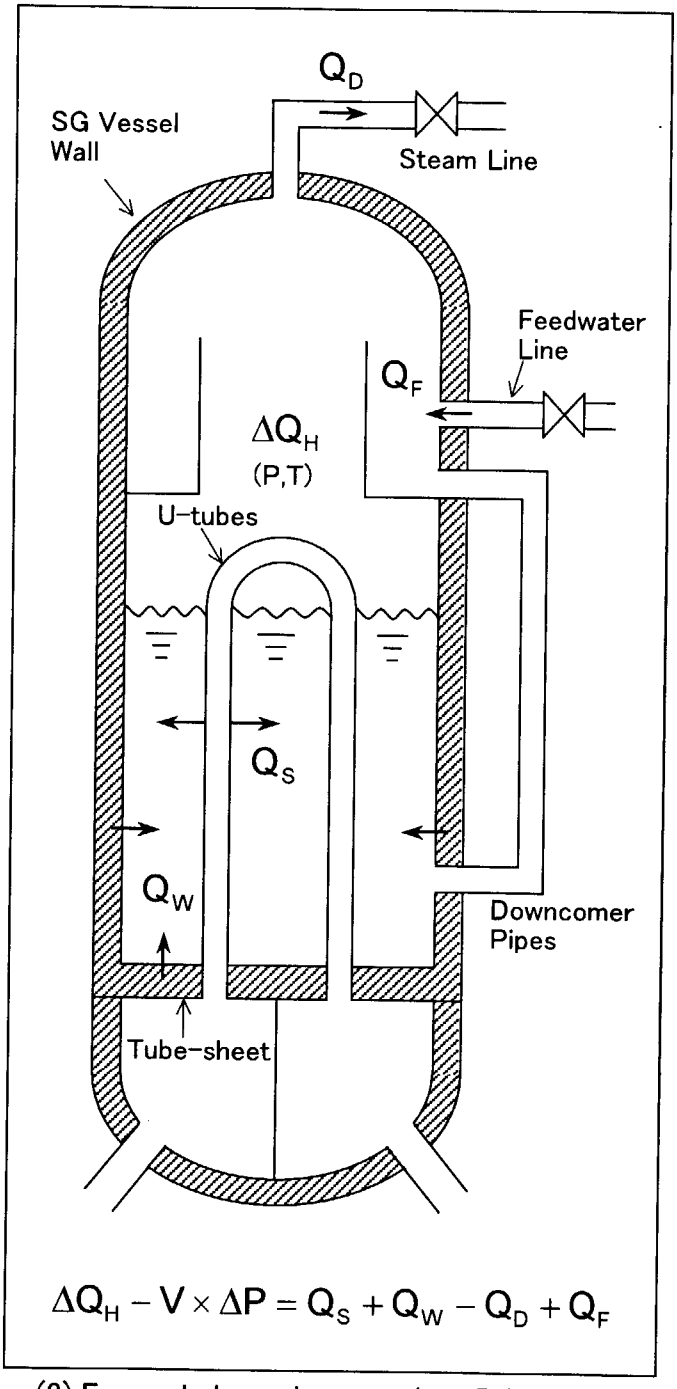

(3) Energy balance in secondary fluid system

$$Q_U = Q_D - Q_F + \Delta Q_H - V \times \Delta P + \Delta Q_T - \Delta Q_W + Q_L$$

Fig.C.1 Conception of heat transfer model for SG secondary system

国際単位系 (SI) と換算表

表 1　SI 基本単位および補助単位

量	名称	記号
長さ	メートル	m
質量	キログラム	kg
時間	秒	s
電流	アンペア	A
熱力学温度	ケルビン	K
物質量	モル	mol
光度	カンデラ	cd
平面角	ラジアン	rad
立体角	ステラジアン	sr

表 2　SI と併用される単位

名称	記号
分，時，日	min，h，d
度，分，秒	°，′，″
リットル	l，L
トン	t
電子ボルト	eV
原子質量単位	u

1 eV = 1.60218 × 10^{-19} J

1 u = 1.66054 × 10^{-27} kg

表 5　SI 接頭語

倍数	接頭語	記号
10^{18}	エクサ	E
10^{15}	ペタ	P
10^{12}	テラ	T
10^{9}	ギガ	G
10^{6}	メガ	M
10^{3}	キロ	k
10^{2}	ヘクト	h
10^{1}	デカ	da
10^{-1}	デシ	d
10^{-2}	センチ	c
10^{-3}	ミリ	m
10^{-6}	マイクロ	μ
10^{-9}	ナノ	n
10^{-12}	ピコ	p
10^{-15}	フェムト	f
10^{-18}	アト	a

表 3　固有の名称をもつ SI 組立単位

量	名称	記号	他の SI 単位による表現
周波数	ヘルツ	Hz	s^{-1}
力	ニュートン	N	m·kg/s^2
圧力，応力	パスカル	Pa	N/m^2
エネルギー，仕事，熱量	ジュール	J	N·m
工率，放射束	ワット	W	J/s
電気量，電荷	クーロン	C	A·s
電位，電圧，起電力	ボルト	V	W/A
静電容量	ファラド	F	C/V
電気抵抗	オーム	Ω	V/A
コンダクタンス	ジーメンス	S	A/V
磁束	ウェーバ	Wb	V·s
磁束密度	テスラ	T	Wb/m^2
インダクタンス	ヘンリー	H	Wb/A
セルシウス温度	セルシウス度	℃	
光束	ルーメン	lm	cd·sr
照度	ルクス	lx	lm/m^2
放射能	ベクレル	Bq	s^{-1}
吸収線量	グレイ	Gy	J/kg
線量当量	シーベルト	Sv	J/kg

表 4　SI と共に暫定的に維持される単位

名称	記号
オングストローム	Å
バーン	b
バール	bar
ガル	Gal
キュリー	Ci
レントゲン	R
ラド	rad
レム	rem

1 Å = 0.1 nm = 10^{-10} m

1 b = 100 fm^2 = 10^{-28} m^2

1 bar = 0.1 MPa = 10^5 Pa

1 Gal = 1 cm/s^2 = 10^{-2} m/s^2

1 Ci = 3.7 × 10^{10} Bq

1 R = 2.58 × 10^{-4} C/kg

1 rad = 1 cGy = 10^{-2} Gy

1 rem = 1 cSv = 10^{-2} Sv

（注）

1. 表 1 - 5 は「国際単位系」第 5 版，国際度量衡局 1985 年刊行による。ただし，1 eV および 1 u の値は CODATA の 1986 年推奨値によった。
2. 表 4 には海里，ノット，アール，ヘクタールも含まれているが日常の単位なのでここでは省略した。
3. bar は，JIS では流体の圧力を表わす場合に限り表 2 のカテゴリーに分類されている。
4. EC 閣僚理事会指令では bar，barn および「血圧の単位」mmHg を表 2 のカテゴリーに入れている。

換　算　表

力	N(=10^5 dyn)	kgf	lbf
	1	0.101972	0.224809
	9.80665	1	2.20462
	4.44822	0.453592	1

粘度　1 Pa·s(N·s/m^2) = 10 P(ポアズ)(g/(cm·s))

動粘度　1 m^2/s = 10^4 St(ストークス)(cm^2/s)

圧力	MPa(=10 bar)	kgf/cm^2	atm	mmHg(Torr)	lbf/in^2(psi)
	1	10.1972	9.86923	7.50062 × 10^3	145.038
	0.0980665	1	0.967841	735.559	14.2233
	0.101325	1.03323	1	760	14.6959
	1.33322 × 10^{-4}	1.35951 × 10^{-3}	1.31579 × 10^{-3}	1	1.93368 × 10^{-2}
	6.89476 × 10^{-3}	7.03070 × 10^{-2}	6.80460 × 10^{-2}	51.7149	1

エネルギー・仕事・熱量	J(=10^7 erg)	kgf·m	kW·h	cal(計量法)	Btu	ft·lbf	eV
	1	0.101972	2.77778 × 10^{-7}	0.238889	9.47813 × 10^{-4}	0.737562	6.24150 × 10^{18}
	9.80665	1	2.72407 × 10^{-6}	2.34270	9.29487 × 10^{-3}	7.23301	6.12082 × 10^{19}
	3.6 × 10^6	3.67098 × 10^5	1	8.59999 × 10^5	3412.13	2.65522 × 10^6	2.24694 × 10^{25}
	4.18605	0.426858	1.16279 × 10^{-6}	1	3.96759 × 10^{-3}	3.08747	2.61272 × 10^{19}
	1055.06	107.586	2.93072 × 10^{-4}	252.042	1	778.172	6.58515 × 10^{21}
	1.35582	0.138255	3.76616 × 10^{-7}	0.323890	1.28506 × 10^{-3}	1	8.46233 × 10^{18}
	1.60218 × 10^{-19}	1.63377 × 10^{-20}	4.45050 × 10^{-26}	3.82743 × 10^{-20}	1.51857 × 10^{-22}	1.18171 × 10^{-19}	1

1 cal = 4.18605 J (計量法)

= 4.184 J　(熱化学)

= 4.1855 J　(15 °C)

= 4.1868 J (国際蒸気表)

仕事率　1 PS (仏馬力)

= 75 kgf·m/s

= 735.499 W

放射能	Bq	Ci
	1	2.70270 × 10^{-11}
	3.7 × 10^{10}	1

吸収線量	Gy	rad
	1	100
	0.01	1

照射線量	C/kg	R
	1	3876
	2.58 × 10^{-4}	1

線量当量	Sv	rem
	1	100
	0.01	1

(86 年 12 月 26 日現在)

Experimental Study on Secondary Depressurization Action for PWR Vessel Bottom Small Break LOCA with HPI Failure and Gas Inflow (ROSA-V/LSTF Test SB-PV-03)